The Fatigue Resistance of Headed Shear Stud Connectors in Steel-Precast Composite Girders

by

Taylor Kenneth Porter

A thesis

presented to the University of Waterloo

in fulfillment of the

thesis requirement for the degree of

Master of Applied Science

in

Civil Engineering

Waterloo, Ontario, Canada, 2017

AUTHOR'S DECLARATION

I hereby declare that I am the sole author of this thesis. This is a true copy of the thesis, including any required final revisions, as accepted by my examiners.

I understand that my thesis may be made electronically available to the public.

ABSTRACT

Extensive research dating back to 1965 has been conducted on the fatigue performance of headed shear stud connectors in steel and cast-in-place composite girders. However, little research has been conducted specifically on the fatigue performance of headed shear stud connectors clustered into pockets. It seems that design provisions for pocketed shear connectors have been established assuming their performance is no different than that of continuous connectors, based on limited tests, terminated before failure, primarily on direct shear specimens that do not precisely model the loading that a shear connector is subjected to in a bridge girder.

This research study investigates the fatigue behaviour of continuous and grouped shear stud connectors for cast-in-place and precast deck applications, respectively. A total of six cast-in-place and six precast composite beams have been fabricated, instrumented, fatigued to failure, and monitored in order to generate new, valuable fatigue data. This data will improve the understanding of the fatigue behaviour of headed studs in composite beam specimens subjected to static and variable amplitude loading.

An autopsy program is implemented to further investigate the fatigue cracking behaviour of the shear connectors. The findings provide clear evidence that studs in precast application perform differently compared to cast-in-place as different fatigue cracking patterns were observed. Two non-linear finite element models have also been assembled in ABAQUS and compared to the results collected from the physical experiments. Additionally, a concrete shrinkage simulation is completed on the cast-in-place model to investigate its effect on the fatigue cracking behaviour. The results from this simulation are found to agree with the observed cracking patterns.

S-N regression analyses are completed to determine the mean regression curve corresponding to a 50% survival probability. In this analysis, the stress ranges assigned to the studs were determined utilizing three methods that introduced three levels of conservatism. In every case, the precast specimens were found to outperform the cast-in-place in terms of fatigue performance. The findings in this study propose that the cast-in-place and precast specimens have a greater conformity with a fatigue resistance curve defined by a Category D and Category C detail, respectively.

It is suggested that the design provisions governing the fatigue performance of shear connectors remains the same until a more intensive probabilistic approach is taken.

ACKNOWLEDGEMENTS

DEDICATION

I dedicate this M.A.Sc. thesis to my family and Fiancée for their continuous support, encouragement, and inspiration.

TABLE OF CONTENTS

LIST OF FIGURES

LIST OF TABLES

1 Introduction

1.1 Overview

Accelerated Bridge Construction (ABC) is a construction process that has gained popularity and interest over the past decade throughout North America. The idea behind ABC is to minimize traffic disruptions caused by the construction lane closures, to a considerable degree, by using modular bridge components and fast-tracking the construction process. The concept has been implemented by engineers to increase the overall efficiency and reduce the costs associated with disturbed traffic flow. Although the initial up-front cost of ABC is larger, when the social, environmental, and other secondary costs are factored in, ABC often results in the optimal solution. In 2013, a recent study conducted by the American Society of Civil Engineers estimated that $76 billion was required to address the one in nine structurally deficient bridges currently in service throughout the United States (ASCE, 2013). A similar study in 2016 was conducted by the Canadian Infrastructure Group, which estimated a $13 billion cost associated with the rehabilitation, replacement, and maintenance backlog for Canadian highway bridges with approximately 26% of Canada's bridge infrastructure reported as deficient (CIRC, 2016).

These reports expose the deteriorating bridge network across North America and the dire need for forward-thinking solutions, such as ABC and modular bridge design. The deteriorated bridge network that is present today can be attributed to the fact that bridges constructed in the past have been erected without corrosion resistant reinforcement, air-entrained concrete, and a proper maintenance schedule leading to an unforeseen amount of decay. The decay was further accelerated when de-icing agents, such as salt, became popular in the late sixties. In earlier bridge codes, the design life was never explicitly stated and a 50-year life was assumed. It was not until recently that the design life was increased to 75 years and explicitly stated in the Canadian Highway Bridge Design Code (CHBDC) (CSA S6, 2013), ensuring more durable structures, and reducing the unnecessarily high restoration costs that will be incurred in the future in the maturing highway network.

Since bridges are subject to transitory loads, the increase in design life to 75 years has had a direct effect on the fatigue performance of bridges, particularly, the headed shear studs found in composite bridges. Composite bridges consisting of a cast-in-place (CIP) concrete deck attached to steel girders via continuous shear studs present an efficient structural system that is widely popular across the North American highway network. Steel-concrete composite bridges utilize the CIP slab and steel girder primarily in compression and tension respectively, fully exploiting the strengths of these materials. Recent advancements in ABC have led to the construction of composite girders using prefabricated or precast concrete slabs with pockets at discrete locations for shear connectivity, expediting construction time and decreasing societal costs.

To date, there have been no reported structural failures due to connector fatigue. The issue with shear connectors is that their condition cannot be visually inspected or monitored in the field because they are fully encased in the concrete deck. The fact that there have been no failures due to fatigue may suggest that the current design code for steel-CIP composite girders is satisfactory, having been around since the 1930's. It may also suggest that engineers are using overly conservative methodologies to design for shear connector fatigue in newer structures. The application of precast deck slabs does not have a long enough history for reports of in-service connector fatigue failures to have come forward that might enable any direct comparisons in performance.

Extensive research dating back to 1965 has been conducted by researchers King & Toprac (1965), Slutter & Fisher (1966), and Oehlers & Foley (1985) on the fatigue performance of headed shear stud connectors in steel-CIP composite girders. However, little research has been conducted specifically on the fatigue performance of headed shear stud connectors clustered into pockets. Most of the results collected to date were either obtained using simplified testing methods that do not capture the full response and behaviour of a composite beam or the testing was terminated before failure. From the little research that has been completed with precast slabs, it has been assumed that composite girders with continuous and pocketed shear connectors behave in an identical manner.

The following subsections will discuss the research needs, objectives, and guide the reader with an overview of the organization of the remainder of the thesis report.

1.2 Research Needs

Several gaps were discovered following an evaluation of the existing literature and design codes, prompting a critical review of the current design provisions regarding the fatigue limit state of shear connectors in steel-concrete composite girders. Specifically:

- It seems that design provisions for pocketed shear connectors have been established assuming their performance is no different than that of continuous connectors, based on limited tests – terminated before failure – primarily on direct shear specimens that do not precisely model the loading that a shear connector is subjected to in a bridge girder.
- The CHBDC (CSA S6, 2014) provisions for continuous connectors in CIP construction have been established through a regression analysis completed on a large data set from push (direct shear) tests. These data contain over 130 data points assembled from a range of studies by various research groups, and contain inconsistencies in the testing techniques and failure criteria. It was assumed that these push-out tests represent a lower bound compared to beam tests, and thus the 50% failure line was utilized, closely resembling a Category D fatigue detail. Therefore, the regression line should be reviewed and established based on risk and reliability considerations to be consistent with the rest of the Code.
- Lastly, an investigation is required to address the effects of variable amplitude loading on fatigue performance and the effect of stud failure on the fatigue performance of adjacent studs. In North America, bridges are being constructed with approximately double the number of headed studs connectors compared to European and Japanese standards. Modifications to the current provisions could result in substantial cost savings.

1.3 Research Objectives

Given these gaps in the current state-of-practice, the objectives of this research are as follows:

- Study the fatigue behavior of continuous and grouped shear stud connectors for cast-in-place and precast deck applications, respectively using beam specimens subjected to variable amplitude loading.

- Confirm a novel instrumentation technique for indirectly detecting the failure of a stud.

- Perform finite element analyses (FEA) to validate the flexural and longitudinal shear responses by comparing the results to the experimental data obtained from the fatigue testing program.

- Investigate the effect of the method used for determining the stress range (e.g., elastic analysis, FEA, or using measured strain data) on the design S-N curve.

- Recommend new design S-N curves and/or procedures, based on this investigation.

1.4 Thesis Outline

This thesis has seven chapters. Chapter 2 begins with a literature review on the topic of steel-concrete composite beams. It briefly discusses the historic background and development, and then describes the differences between longitudinal shear connection and longitudinal shear interaction. The advantages and disadvantages between push-out and beam tests for studying the behaviour of shear studs are then discussed. Following this, the previous research conducted on the fatigue behaviour of headed shear studs in cast-in-place and precast applications is analyzed. Lastly, a detailed review of the design codes governing the design of shear connectors is presented.

Chapter 3 presents the design of the experimental program. Within this section the beam specimen geometry, construction materials, and instrumentation methodologies are described. In addition, the loading sequence and testing matrix are shown and the construction procedure employed in the fabrication of the beam specimens is discussed.

In Chapter 4, the experimental results pertaining to the static and fatigue testing are presented and discussed. This chapter also includes the findings of an autopsy program conducted once beam testing was complete.

Chapter 5 presents a non-linear finite element analysis (FEA) study of the test specimens conducted using the software ABAQUS. The details of the material inputs and steps taken to verify

the model are described. Lastly, a study investigating the effect of concrete shrinkage on the forces in the studs for cast-in-place members is completed.

Chapter 6 completes a log-log linear regression analysis on the fatigue data to establish fatigue resistance curves, also known as S-N curves, for the CIP and precast specimens. In the S-N analysis described in this chapter, three different approaches for determining the stress range, or S, are explored. The methodology for completing the log-log linear regressions is described and the results obtained from the regression analysis are plotted, discussed, and compared to the current code provisions governing the fatigue resistance of welded studs.

Chapter 7 concludes the thesis and details the significant findings of the research project. Recommendations for future work that would further enhance the understanding of shear connectors in steel-concrete composite bridges are also presented in this chapter.

2 Literature Review

This literature review provides a comprehensive survey of the significant research that has been conducted prior to this report and will also provide a foundation providing the justification the current research. Section 2.1 will introduce steel-concrete composite members as well as some of the basic concepts regarding shear connection and shear interaction. Later on in the section, push and beam tests will be introduced and differentiated. In Section 2.2, the previous research completed on the fatigue resistance and behaviour of shear connectors in composite members is summarized. In Section 2.3, the CHBDC provisions pertaining to the design of headed shear connectors is thoroughly examined.

2.1 Steel-Concrete Composite Members

2.1.1 Development

There are several benefits associated with steel-concrete composite members. It is known that concrete is stronger in compression and thin steel elements perform better in tension. Thus, composite members present the opportunity to optimally exploit these materials. Composite members also have increased lateral and flexural stiffness, resisting the lateral buckling of the compression flange and reducing the vertical deflection along the length respectively. These benefits are only attained when the top flange of the steel girder is fastened to the underside of the concrete slab producing an integrated structural member. This is made possible with a shear connection that serves two functions: to transmit longitudinal shear forces at the concrete-steel interface, and to tie the concrete slab to the steel beam, preventing any separation.

There are two methods commonly used in the construction of composite bridges. The most popular construction technique is one utilizing a cast-in-place (CIP) deck system. This construction procedure involves casting the concrete deck in-situ atop the steel girders, encasing the deck reinforcement and continuously welded shear connectors. In steel-CIP construction, the shear connection is typically achieved by welding headed studs or hot-rolled channels to the top of the steel flange prior to casting. Examples of the headed studs and channels used for shear connection are illustrated in Figures 2-1 and 2-2 respectively.

6

Figure 2-1: Exposed headed studs prior to the casting of the CIP concrete deck.

With the development of an arc-welding gun, shear studs have become the predominant form of mechanical connection due to the low economic cost and ease of installation, decreasing the attractiveness of steel channels. The performance of headed shear studs in composite bridge construction dates back to 1952 where Siess et al. conducted small and large scale tests on composite T-beams. Due to the difficulty of quantitatively measuring the forces acting on a stud in a beam test, researchers Slutter & Fisher (1966) began to utilize push-out tests, also called direct shear tests, to evaluate the ultimate and fatigue characteristics. Section 2.1.3 and 2.1.4 will discuss the advantages and disadvantages of push-out and beam tests more thoroughly.

(a)   (b)
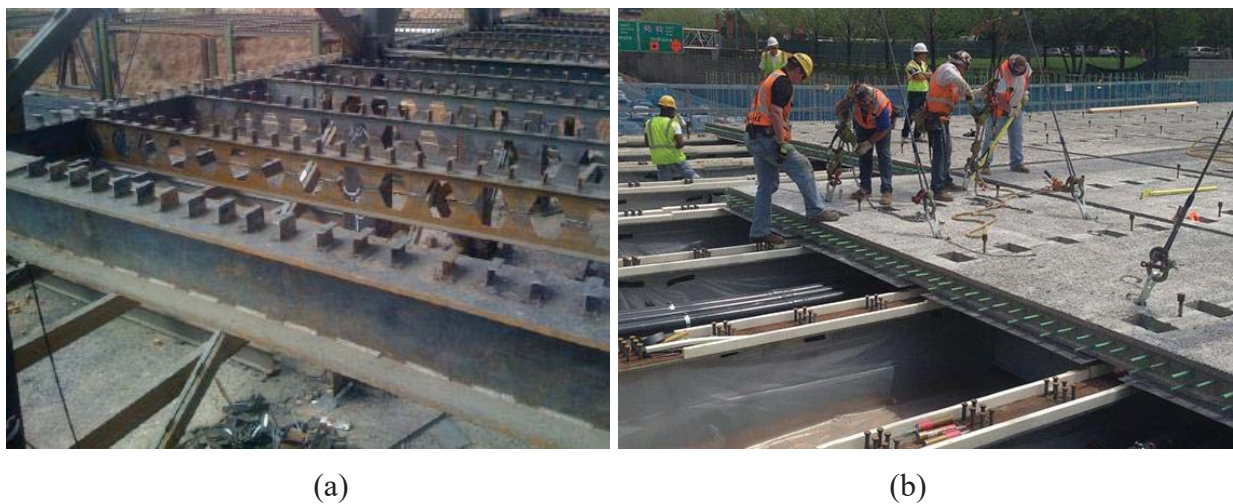
Figure 2-2: (a) Steel channels welded to the top of the steel flanges prior to casting (Shariati et al., 2011) (b) Construction of the Peoria Street Pedestrian Bridge in Chicago (PCI, 2015).

The second construction method of composite beams, which dates back to the 1970's, has been developed with ABC in mind and involves the use of prefabricated full depth deck panels in the place of classical CIP methods. The shear connection in a steel-precast section is often established with headed studs or bolts. When opting for headed studs, it is common to concentrate the studs at discrete clusters rather than continuously along the top flange of the girder. The prefabricated slabs are then cast with discrete pockets that align with the stud clusters as shown on the right in Figure 2-2. Once the precast slab is positioned, a high strength non-shrink grout is used to fill the pockets and establish the shear connection. This allows for a reduction in construction duration and overall costs compared to classical CIP construction while still maintaining the structural integrity at the ultimate limit state (ULS) of the girder. This has been demonstrated in the experimental programs conducted by Issa et al. (2008) and Huh et al. (2010).

An alternative for establishing a shear connection when using precast slabs is the use of bolted connections. Bolted connections present several advantageous properties over welded connections, where the first advantage being that the connection is weld-free. Typically, due to the weld detail on headed stud and channel connections, the fatigue limit state (FLS) governs over the ULS. Bolts, on the contrary, utilize a slip critical design where the frictional forces resulting from pretension resist the longitudinal shear at the interface. This results in a detail that is highly fatigue resistant since the bolt itself experiences no fluctuations in stress. Another advantage to bolts is the ease of deconstruction. If the bridge deck is ever damaged, comes to the end of its service life, or is only needed as a temporary solution (e.g., resource sector bridges), the removal of the deck slabs from the girders is as easy as removing the bottom nut from the underside of the top flange. Once removed, the slab can be hoisted away with a crane and either disposed of or salvaged depending on condition and needs of the bridge owner. Two typical details for bolted shear connection are illustrated in Figure 2-4.

Figure 2-3 depicts a high-tension friction-grip bolt assembly. This post-installed connector is installed after the precast slab is placed on top of the girder. The pretensioning procedure effectively applies tension along the length of the entire bolt and clamps the concrete deck to the top flange of the steel beam. Figure 2-3 also depicts a double nut bolt assembly. This bolt detail can be installed either before or after placement of the precast deck and the shear connection is

established once a high strength, non-shrink grout is used to fill the pockets. The pretension in the double nut bolt assembly is applied to only the portion of the bolt within the flange, restraining slip and preventing any bolt bearing in the hole (Kwon et al., 2010).

(a)   (b)
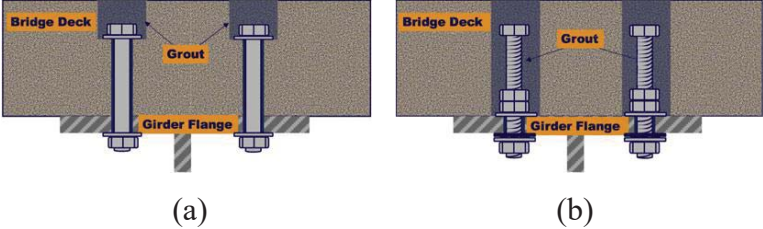
Figure 2-3: (a) High-tension friction-grip bolt assembly. (b) Double nut bolt assembly. (Kwon et al., 2010).

Connections by chemical adherence are a shear connection type that has been studied in the past decade. They transfer longitudinal shear through friction by adhesion between the steel and concrete deck to facilitate composite behaviour (Bowser, 2010). This type of shear connection has been researched by Dauner (2005), Thomann (2005, 2008), and Lebet (2008) with the hopes of developing a rapid alternative for installing precast slabs. The detail is presented in Figure 2-4. Direct shear testing completed on this connection found the performance to have a very high stiffness, however, demonstrated very low ductility. Despite the low ductility, Thomann and Lebet (2008) confirmed that composite sections with chemical adherence for shear connection can provide full plastic flexural resistance in both positive and negative moment regions.
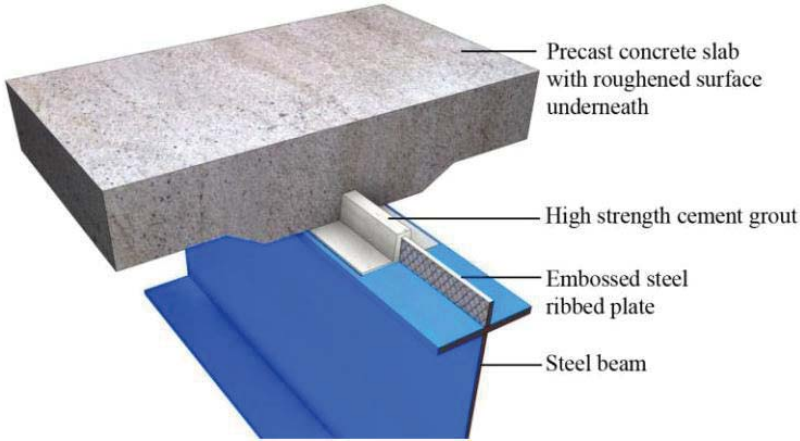
Figure 2-4: Detail of a chemically adhered shear connection (Papastergiou & Lebet, 2010).

9

2.1.2 Longitudinal Shear Connection versus Interaction

The following subsection discusses the concepts of longitudinal shear connection and interaction, as they are often mistakenly used synonymously when describing the behaviour of a composite section. In actuality, these two terms describe two different properties of composite behaviour.

The amount of longitudinal shear connection is directly related to the strength of the shear connection and quantifies the amount of shear force that can be transferred across the interface. A composite section that is constructed with a 100% shear connection, also known as a full shear connection, is a connection that can fully transfer the plastic capacity of either the slab or steel at the ultimate limit state (ULS). A partial shear connection, on the contrary, is one where the connection fails before the full plastic capacity of the composite section is reached. The degree of shear connection can be represented by η_{sc}, and is equal to the ratio of the total force that can be transmitted by the connection along the shear span to the lesser of the force found in the concrete slab or steel girder at the section's flexural plastic capacity. This behaviour can be described in Equation 2-1 and is illustrated in Figure 2-5:

$$\eta_{sc} = \frac{F_{sc}}{F_P} \tag{2-1}$$

where:

η_{sc}	=	the degree of shear connection [unitless],
F_{sc}	=	the force transmitted by the longitudinal shear connection [kN], and
F_P	=	the lesser force in either the concrete slab or steel girder at flexural plastic capacity [kN].
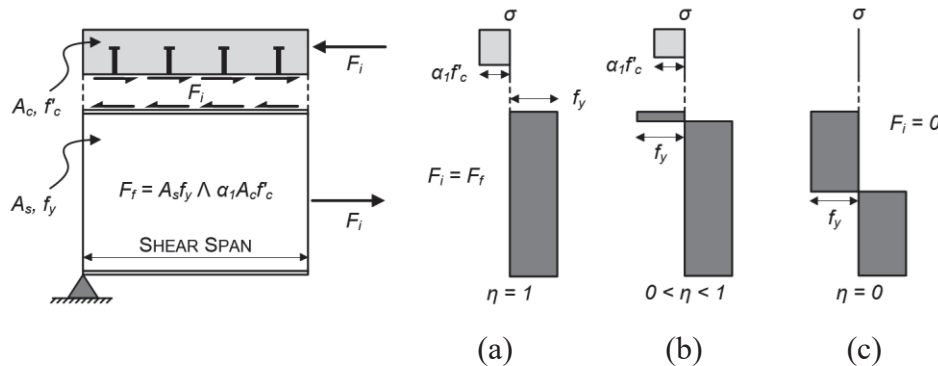
Figure 2-5: (a) Full, (b) partial, and (c) no shear connection plastic stress profiles.

10

Partially shear connected beams can provide economical solutions and have been implemented in the building industry since 1969. Depending on material properties and sectional geometries, sections with a 50% shear connection have been shown to retain upwards of 80% of their full moment capacity at ULS (Yura, Methvin, & Engelhardt, 2008). Although proven to be efficient, the use of partial shear connection in bridge girders is prohibited, as described in the current CHBDC (2014) and AASHTO (2016) codes.

The amount of longitudinal shear interaction is directly related to the stiffness of the shear connection and quantifies the amount of slip or change in strain at the steel-concrete interface. A composite section that contains 100% shear interaction, also known as full shear interaction, describes a connection that prohibits any strain discontinuity or slip at the steel-concrete interface. When a discontinuity at the interface is present, the degree of partial interaction can be quantified by the distance between the two neutral axis, h. This is illustrated in Figure 2-6, where the degree of shear interaction can be described by φ_{si} in Equation 2-2:
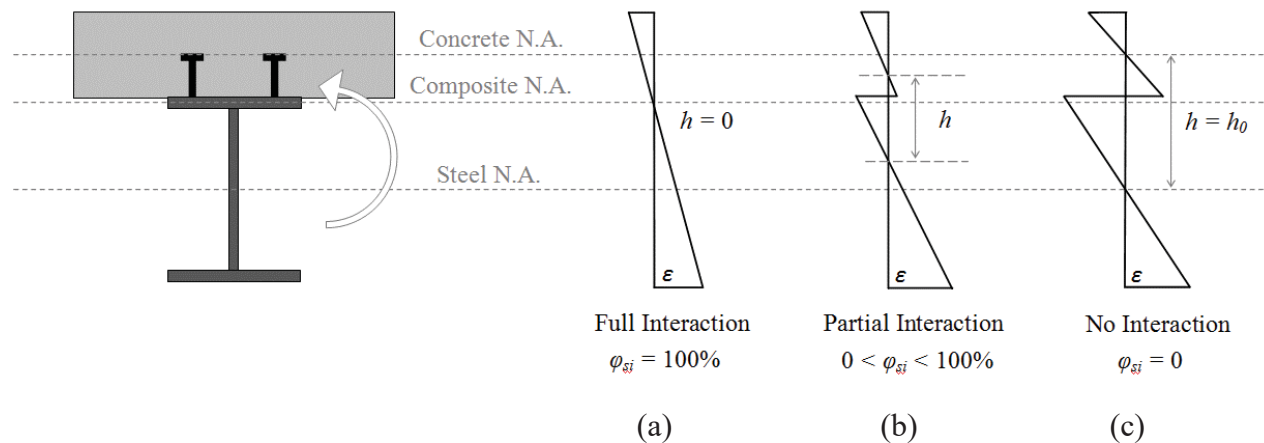
Figure 2-6: (a) Full, (b) partial, and (c) no shear interaction strain profiles.

$$\varphi_{si} = 1 - \frac{h}{h_0} \tag{2-2}$$

where:

φ_{si}	=	the degree of shear interaction [unitless],
h	=	the distance between the neutral axis for the concrete and steel [mm], and
h_0	=	the distance between the concrete and steel centroids [mm].

11

In reality, only chemically bonded composite sections, i.e., interfaces with full shear interaction, can carry load without requiring slip to engage the shear connection. Any interface via mechanical shear connection (headed studs, bolts, channels, etc.) will fall into the partial interaction case once the static friction between the steel flange and concrete slab is overcome. Once the shear flow overcomes the static friction, slip occurs and the displacement at the interface engages the mechanical shear connectors to provide the resistive force.

2.1.3 Push-out Tests Versus Beam Tests

Push-out tests, also called direct-shear tests, consist of a steel section with its two flanges sandwiched between two concrete slabs and made composite via embedded shear connectors. The specimens are symmetrically aligned along the beam's longitudinal and transverse centrelines and positioned in the vertical direction for monotonic (i.e., static) or fatigue testing. A typical push-out test specimen is illustrated in Figure 2-7.
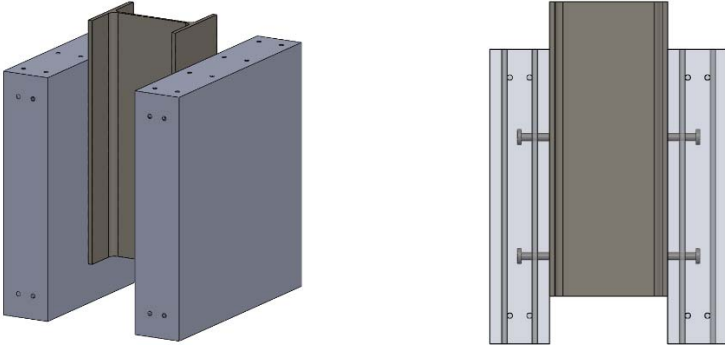
Figure 2-7: Typical push-out test specimen.

The test specimen has been designed with a slab on both sides of the steel section to create two shear interfaces, thus eliminating any load eccentricities when a downward load is applied to the top of the steel section. The force experienced by the shear connectors is calculated simply by dividing the total applied force by the total number of shear connectors. The push-out test procedure has been accepted as a standard test by past researchers to determine the ULS and FLS behaviour and performance of shear connectors in steel-concrete composite sections. The reason for this acceptance is because Slutter and Fisher (1966) reported, that there is little difference between beam tests and push-out tests and that push-out tests have a tendency to yield more

conservative results. It is the cost efficient and simplified nature of push-out tests that have made them a much more conventional alternative to beam tests in the previous years.

Typical modes of failure in cyclic push-out tests include fracture at the stud shank, failure at the flange heat affected zone, or the failure of the weld. The crack initiation location has been found to be dependent on the degree of initial geometric imperfection, the diameter of the stud, and the thickness of the flange to which it is attached (Yu-Hang et al. 2014). For push-out tests, the fatigue crack is typically found to initiate at the weld toe on the side that the transverse shear load is applied to the studs. Similar modes of failure have been recorded in beam tests, however, the fatigue crack has been found to initiate at the opposite side. Justifications for this behaviour have been accredited to concrete shrinkage, where the effect is greatest in the studs closest to the ends of the beam (King et al.1965). Schematics of typical fatigue crack failures for both push-out and beam tests are illustrated in Figure 2-8.

(a) (b)
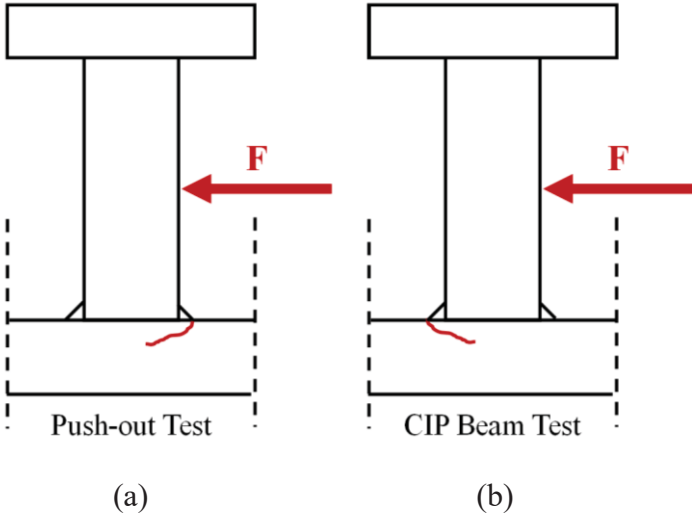
Figure 2-8: Typical fatigue failures for (a) push-out test and (b) beam test.

Various academic researchers including Oehlers (1985), Johnson (2000), and Yu-Hang (2014) have discussed the discrepancies that result from using push-out tests versus beam tests, including their limitations and modelling inaccuracies. In comparison to push-out tests, there exists a limited collection of fatigue test results collected from beam tests, many of which consist of run-outs terminated before failure. From this limited data set, the results generally show that the fatigue

performance of the headed studs is better in beam tests compared to push-out tests. It has been suggested that the real longitudinal shear force ranges acting on the shear connectors are lower than calculated for the following reasons:

- Longitudinal shear is initially resisted by bond until this bond is broken. Therefore, the connectors may experience no loading, in particular at the early stages of the fatigue testing, before and cyclic deterioration of this bond has occurred.

- Frictional forces along the steel-concrete interface reduce the amount of longitudinal shear transferred by the shear connectors.

- The calculations involve the use of a transformed sectional elastic analysis, which assumes complete interaction (i.e.,no slip) at the interface. Neglecting slip in the calculations results in a shear flow that is larger in magnitude.

- In the previous beams tests conducted by King & Toprac (1965), a loss of composite interaction was observed before failure. As the fatigue crack propagated, the headed studs became less stiff, which resulted in more slip at the interface. This condition, termed incremental slip, allowed for the connector forces to redistribute to studs with more stiffness and resulted in a less severe stress condition than computed from elastic theory. In push-out tests, the loading on the shear connectors is maintained at a reasonably constant level throughout the cycle life and thus represents a lower bound for failure (R. G. Slutter & Fisher, 1966).

Besides shear connectors experiencing lower than calculated longitudinal shear ranges in beam tests over push-out tests, there are several other differences between the two testing methods. Firstly, due to the actual and complex bending behaviour of a beam-test, the connectors may experience cyclic tensile forces from slab uplift and prying action. Secondly, the bending stresses in the top flange of the steel beam significantly affect the fatigue behaviour of the studs. This is dependent on the location of the neutral axis, placing the flange in either cyclic tension or compression around the root of the welded stud. Lastly, Oehlers & Foley (1985) revealed that the effect on the fatigue life of varying the maximum load, which may be the peak load or an overload, is much more important in beam tests. Variations in the maximum load have only a very small effect on the scatter of push-out test results. This trend is the result of beam tests having a larger number of shear connectors.

2.2   Fatigue Resistance of Shear Stud Connectors

2.2.1   General Fatigue

Fatigue is a phenomenon that progressively weakens a material under a repeated application of stress. There are three stages to the fatigue process: fatigue crack initiation, fatigue crack propagation, and finally brittle fracture or ductile rupture. All metals, including the fabricated steel used in structures, contain microflaws, inclusions, and internal discontinuities within the crystalline microstructure, which serve to facilitate the initiation and propagation of cracks. With each stress cycle, a sharp crack in a tension stress field causes a high stress concentration at the crack tip, resulting in the slip and plastic deformation in the material's crystalline bonds. Brittle fracture or ductile rupture occurs once the crack has propagated and reduced the cross-section sufficiently such that the uncracked portion can no longer transfer the applied forces. This failure mode can be catastrophic due to its sudden, brittle nature, and must be avoided and considered in design. A study conducted by Nussbaumer et al. (2008) demonstrated that fatigue is the cause for 38% of all recorded damages in railway and roadway bridges (Nussbaumer et al., 2008). Fortunately, fatigue is examined under the day-to-day service loading conditions and little history of serious failures have been recorded in the civil engineering practice (CSA S6.1, 2014).

There are three popular methods used for predicting the fatigue life of materials. They are the Stress-Life (S-N), Strain-life (ε-N), and Fracture Mechanics Methods. The S-N approach relates nominal stresses, *S*, to the number of cycles, *N*, in order to quantify the fatigue life. This is the method adopted by bridge engineers to design shear stud connectors due to the fact that nominal stresses can be easily determined, without the need of more complex calculations. In the S-N approach, the factors affecting fatigue crack growth under the application of cyclic loading are the stress ranges, the number of occurrences of each stress range, and the configuration of the detail (Fisher et al., 1970). It is essential to note that fatigue cracks grow only when there is a tensile stress range. When the fluctuation of stress is compressive, fatigue life is not a concern, unless the detail contains tensile residual stresses from a welding or fabrication process. It has been proven that cyclic compressive stresses will produce cracks in residual tensile locations and propagate until the crack tip exceeds the zone. Interestingly, fatigue life has been found to be independent of the grade of steel, primarily because of the presence of high tensile residual stresses resulting from

fabrication. Both physical testing and fracture mechanics have shown that the relationship between the stress range and the number of cycles is linear when represented on logarithmic scales (Fisher et al., 1997). Typically, the design curves are represented by Equation 2-3, which can be also manipulated into Equation 2-4 for a cleaner appearance:

$$\log N = \log M - m \log(\Delta\sigma_r)$$ (2-3)

$$N = M(\Delta\sigma_r)^{-m}$$ (2-4)

where:

N	=	the number of cycles,
$\Delta\sigma_r$	=	the tensile stress range [MPa or ksi], and
M, m	=	constants established from a regression analysis of test data.

The design curves defined by these equations require the input of a single tensile stress range. The output is the number of cycles at the given stress (constant amplitude) until failure. In reality however, cyclic stresses tend to vary in amplitude and the Palmgren-Miner's linear damage hypothesis for variable amplitude loading must be employed. This hypothesis/model determines an equivalent constant amplitude stress that would result in a fatigue life similar to the variable amplitude stress history. There are other models, which have been formulated by other academics, however, the Palmgren Miner's Rule (Equation 2-5) provides a simple model that contains enough accuracy for the purpose of design and application:

$$\sum_{i=1}^{k} \frac{n_i}{N_i} = D = 1$$ (2-5)

where:

n_i	=	the number of applied cycles at a given stress, in a spectrum,
N_i	=	the number of cycles to failure given a stress, determined from the S-N curve, and
D	=	the damage incurred.

Typically for design purposes, D, is set to 1. Thus $1/D$ is equal to the number of times the variable amplitude history can be repeated before failure. Palmgren-Miner's Rule has been criticized because it assumes that the sequence in which the loads in the spectrum are applied has no effect

on the fatigue life. This is not always true, e.g., if an overloading stress reversal causes plastic deformation, compressive residual stresses may result, reducing crack growth.

2.2.2   Shear Connectors in Cast-in-Place Slabs

The first set of experimental tests investigating the fatigue resistance of headed shear stud connectors in composite sections that has had an influential impact on today's design codes dates back to 1965. King, Slutter, & Driscoll (1965) were first to publish a laboratory titled "Fatigue Strength of ½" [12.7 mm] Diameter Stud Shear Connectors", which investigated the behaviour of 12 CIP composite sections under fatigue loading. Since this experimental program was state-of-the-art at the time, the parameters for achieving and guaranteeing stud failure due to fatigue were unknown. Therefore, the first four beams were constructed at a smaller scale (3.05 m [10 ft] in length) and were a part of a preliminary testing program, which aided in the experimental design for the remaining eight. The remainder of the eight beams were designed and constructed having a composite cross-section consisting of a W 310 mm x 39 kg/m [W 12" x 27lb/ft] steel beam with a concrete slab measuring 1200 mm wide and a depth of 100 mm [48" x 4"]. The yield and compressive strength for the steel and concrete were 228 MPa [33 ksi] and 21 MPa [3 ksi] respectively. The longitudinal shear connection was established utilizing 40 headed shear studs welded to the top of the steel flange, each with a diameter and height of 12.7 mm [0.5"] and 51 mm [2"] respectively. Each beam was simply supported, with a span of 4.57 m [15'], and loaded at two points via a spreader located at a distance of 229 mm [9"] on each side of the midspan (King et al., 1965).

Initially, a static test was conducted to the maximum load that was to be applied dynamically. If the chemical bond at the steel-concrete interface was not broken during the initial static test, cyclic loading took place at the same peak load level until bond breakage was noted. Once the bond was broken due to the cyclic loading, a second static test was completed to measure the deflection and interfacial slip of the composite beam prior to further cyclic loading. This technique was employed to gather initial static data without the effects of the chemical adhesion at the interface and ensured that the longitudinal shear was resisted mainly by the connectors during the actual cyclic testing. Following the initial static testing phase, constant amplitude cyclic loading at 4.2 hz was applied to the beams where the longitudinal shear stress ranged from 120 to 140 MPa [17.5 to 20.3 ksi].

Static loading tests were performed at regular intervals throughout the cyclic testing to collect deflection, interfacial slip, and strain gauge readings. From the data collected, King et al. (1965) determined that detecting connector failure from the trends in profile strain, deflection, and interfacial slip was insufficient to make any direct conclusions on the exact number of cycles to failure. The research group did, however, have success in determining the number of cycles until failure by measuring the change in local distortion strains at the studs. These strain gauges were installed on the underside of the top flange, directly beneath where the stud is located as shown in Figure 2-9. The resistive forces produced by the stud result in local bending stresses in the top flange and are sensitive to any changes in the stiffness/condition of the connector. King et al. (1965) found that once a crack forms and begins to propagate, the connection becomes less stiff, and the strains caused by the local distortions decrease in magnitude. For the purpose of defining a failure criterion, the number of cycles to failure for the beam was established once any of the local distortion strains reached a peak and started to descend. It was noted that the cracks initiated at the weld toe on the outside face, near the end of the beam, and propagated towards the midspan though the heat affected zone (HAZ). This phenomenon was explained by having fluctuating tensile stresses on the outside face due to the effects of concrete shrinkage.
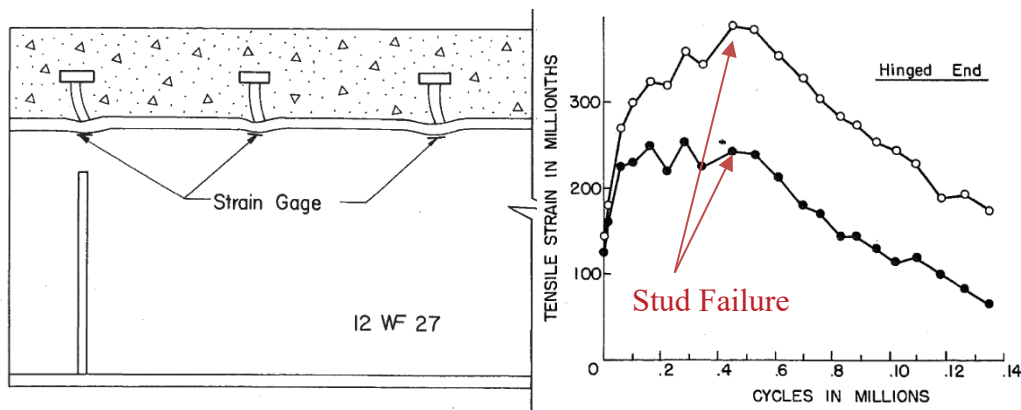
Figure 2-9: Local distortion strain gauge location and sample results (King et al., 1965).

It was concluded that connector failure due to fatigue was progressive in nature and began at the studs closest to the ends of the member. Due to the progressive failure, the results showed that the beam effectively maintained composite behaviour long after the initial failure of the first stud. This was proven by the subtle downward migration of the neutral axis location in the steel and small increases in interfacial slip as the testing continued.

18

Several months following the release of the research completed by King et al. (1965), a research group consisting of Toprac, Lehman, & Lew published an investigation on the "Fatigue strength of 3/4 Inch [19 mm] Studs in Lightweight Concrete" (Toprac et al., 1965). The purpose of this study was to determine if the shear stress range and maximum stress experienced by the studs had any effect on the stud's fatigue performance. The experiment was carried out utilizing a total of 14 CIP push-out specimens, which were loaded cyclically under constant amplitude loading. The test matrix varied the shear stress range and minimum stress at 69, 83, 97, 110, 124 MPa [10, 12, 14, 16, 18 ksi] and 14, 41, 69 MPa [2, 6, 10 ksi] respectively. The specimens were constructed with a W 200 mm x 71 kg/m [W 8" x 48 lb/ft] steel section, 508 mm [20"] in length, sandwiched between two concrete slabs measuring 610 mm [24"] wide, 508 mm [20"] long, and 152 mm [6"] thick. A total of eight headed studs were used in the shear connection with four welded to each flange in a rectangular orientation. In terms of instrumentation, dial gauges were utilized to measure interfacial slip and measurements were taken at set intervals over the fatigue life. Similar to King et al. (1965), strain gauges were also applied to the underside of the flanges, beneath the studs, to capture the local distortion caused by stud loading.

Upon completion of the testing program, Toprac et al. (1965) found that most of the stud fractures occurred in the HAZ rather than the stems, which was consistent with what King et al. (1965) experienced in their beam testing program. Toprac et al. (1965) also proposed that the interfacial slip cannot be directly related to the level of fatigue damage, however, during fatigue loading, a definite slip behaviour with respect to the number of cycles can be seen. This behaviour is illustrated in Figure 2-10, which initially displays a gradual increase of slip, followed by a plateau level, and ending in a sharp increase as the specimens reached failure. The sharp increase in slip behaviour is how Toprac et al. (1965) defined their failure criteria (complete failure), in contrast with King et al. (1965) who utilized the peaks found in the local distortion strain data (crack initiation).
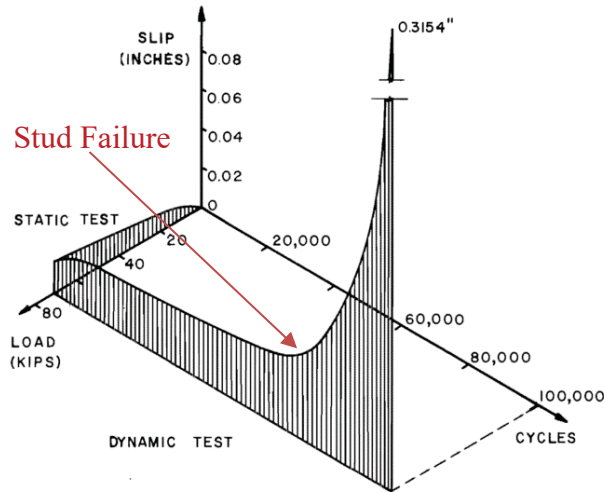
FIG.7.　LOAD−SLIP−CYCLES (SPECIMEN 220)

Figure 2-10: Load-slip-cycle plot cycled at 124 MPa [18 ksi] (Toprac, 1965).

From this study, it was concluded that the fatigue strength of headed studs used as shear connectors is independent of the maximum applied stress for any given stress range, and that the stress range has a significant effect on the fatigue life. It was also concluded that the S-N curve obtained based on the results of push-out specimens is always lower than the one obtained through beam tests, thus establishing a lower bound. This postulation was illustrated in Figure 2-11 where the solid and dashed lines represent previous beam and push-out test results, respectively. Figure 2-11 includes beam and push-out tests conducted by King et al. (1965) on 1/2" [12.7 mm] diameter studs, as well as the beam and push-out tests performed by Toprac et al. (1965) on 3/4" [19 mm] diameter studs.

The research discoveries and conclusions made by both King et al. (1965) and Toprac et al. (1965) were essential in the early development and understanding of the fatigue performance of shear stud connectors. They provided the fundamental background, which lead the team of researchers, R. G. Slutter and J. W. Fisher (1966) to conduct some of the most influential and impactful work on the fatigue performance of shear connectors to date. They claimed that the previous results gathered from composite beam tests included a considerable amount of variation due to the level of difficulty for assessing the fatigue damage during testing.

20
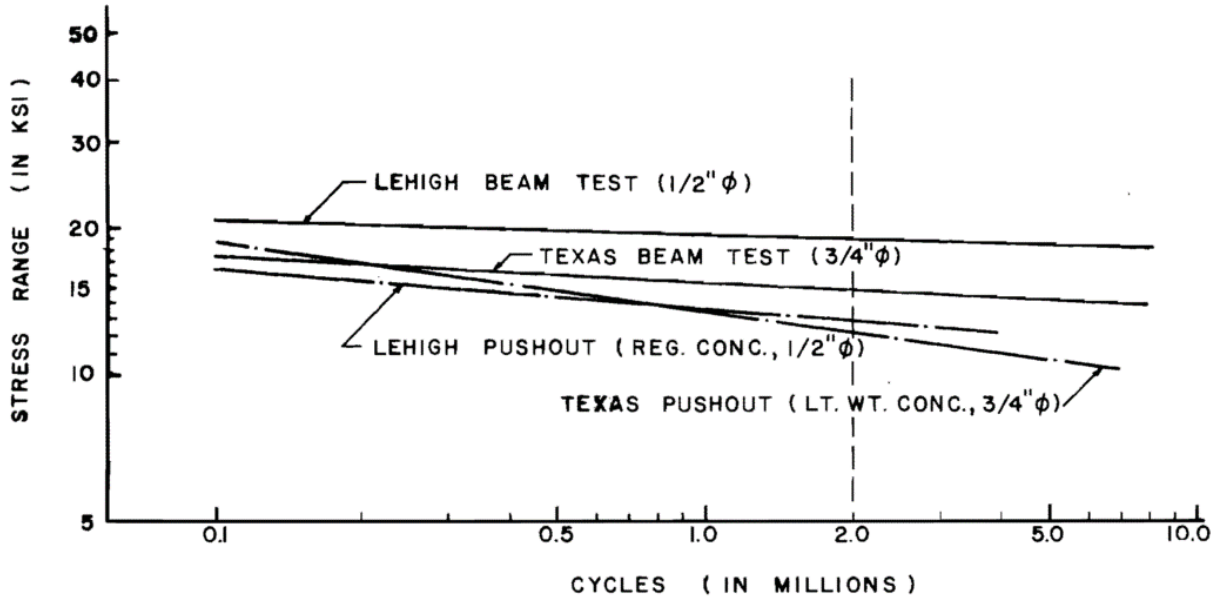
Figure 2-11: S-N results comparing beam and push-out tests including previous research conducted by King et al. (Toprac, 1965).

The failure of one or two connectors could not always be detected and did not significantly affect the beams performance as the longitudinal shear was redistributed to the other connectors. In contrast, push-out test failure was easily documented by the complete shearing of the slab from the steel. The amount of redistribution in push-out tests is negligible, and the load on the connectors could be evaluated easily since partial interaction and friction at the interface do not play a role. Considering these factors, as well as the economic feasibility of push-out tests compared to beams, Slutter and Fisher (1966) initiated an experimental investigation involving the fatigue testing of 35, 9, and 12 push-out specimens connected with 19 mm [3/4"] studs, 22 mm [7/8"] studs, and C 100 mm x 8 kg/m [C 4" x 5.4 lb/ft] channels respectively. The main experiment was designed to evaluate the stress range and the minimum stress at five and three levels, respectively. Based on the previous research of King et al. (1965) and Toprac et al. (1965), Slutter and Fisher (1966) suggested that the fatigue strength of the stud connectors can be represented by a semi-logarithmic mathematical model, which expresses the fatigue life, N, as a function of the stress range, S_r. A regression analysis of the test data yielded Equation 2-6 and Equation 2-7 for units of ksi and MPa, respectively.

$$\log N = 8.072 - 0.1753 S_r \ [ksi] \tag{2-6}$$

$$\log N = 8.072 - 0.02543 S_r \ [MPa] \tag{2-7}$$

21

Based on their experimental results, Slutter and Fisher (1966) concluded that the minimum stress had a negligible effect on fatigue life, however, the reversal of stress (i.e., application of cyclic stresses with a sign reversal, as opposed to a pulsing stress in one direction only) is significant and tends to increase the fatigue performance. Lastly, in establishing design criteria, they suggested that the spacing of the connectors should never exceed 610 mm [24"], as the connectors also perform the necessary function of holding the concrete slab in contact with the steel beam.

Future work completed by Oehlers and Foley (1985) included the regression analysis of 129 previous push-out tests, including 11 additional push-out tests conducted themselves. The linear regression was completed on the logarithm of both the number of cycles, N, and the ratio of the stress range, S_r, to the strength of the connector, P, represented in Equation 2-8:

$$\log N = 2.92 - 4.95\log\left(S_r / P\right) \tag{2-8}$$

Oehler and Foley (1985) also found that the cumulative damage (Miner-Palgrem) matched well for the 30-variable amplitude push-out tests analyzed in their work. They concluded that the peak load or an occasional overload does not affect the rate of fatigue crack propagation, but it does affect the endurance by limiting the amount of fatigue cracking that can occur before the stud fractures. Oehler also pointed out that the static strength of a stud is reduced once a crack is formed and continues to reduce while the crack propagates throughout the cyclic loading phase.

Recently, Zhang (2007) conducted a regression analysis on a large database of push-out test results. His research also found that a log-log relationship was best suited for the data set and concluded that the results closely approximated the fatigue detail Category D. This fatigue detail is typical in many North American design codes and expressed by Equation 2-9, which is manipulated into Equation 2-10 for comparison purposes:

$$S_r = \left(\frac{\gamma}{N}\right)^{\frac{1}{m}} \tag{2-9}$$

$$\log N = 11.858 - 3\log\left(S_r\right) \tag{2-10}$$

where:

γ	=	the fatigue life constant, taken as $721 \cdot 10^9$ for Category D, and
m	=	the slope of the fatigue detail, taken as 3.

Following the analysis of the push-out tests, Zhang collected a small database of beam tests. A comparison of the two data sets indicated that the design approach of using the mean regression of the push-out test data is conservative and appropriate.

A summary of the regression analyses completed by Slutter and Fisher (1966), Oehler and Foley (1985), and Zhang (2007) is graphically plotted in Figure 2-12 and is characterized by the green, blue, and red lines respectively. The regression curves are overlaid on top of a sample database consisting of push-out and beam tests results gathered from the literature (Slutter and Fisher (1966), Oehler and Foley, (1985), Zhang (2007)). At first glance it appears that the results for the beam tests, represented by the black squares, fall within the limits of the data cloud, bringing into question the assumption that push-out tests results represent a lower bound for fatigue behaviour. The reason for this is that the push-out test data, represented by the grey circles, corresponds with the complete failure of all the studs in a specimen. In contrast, the beam test data records failure when the first stud or stud pair has failed.
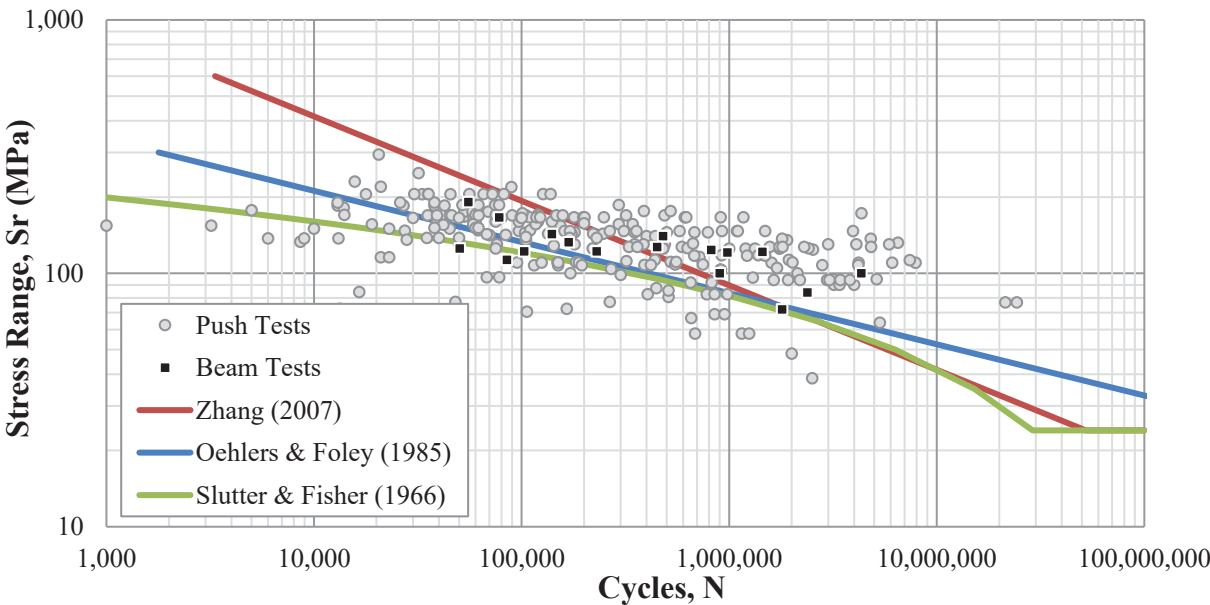
Figure 2-12: S-N plot summarizing the regression analyses completed by Slutter & Fisher (1966), Oehlers & Foley (1985), and Zhang (2007).

23

2.2.3 Precast

The implementation of full-depth precast panels in composite bridge construction is thought to be a positive development in terms of sustainable and cost efficiency. The precast panels are provided with grout pockets that accommodate for shear stud clusters, which are welded to the steel section. Once the slabs are positioned and levelled as per the design specifications, the pockets are filled with a non-shrink grout to establish the connection and provide the necessary composite action. The development of precast-steel composite girders represents a large step forward in regards to bridge construction technology, however, its potential has yet to be fully exploited. This is attributed to the assumption that precast composite girders behave identically to CIP composite girders, and therefore can be designed under the same code provisions.

One of the first studies that investigated the fatigue performance of precast-steel composite sections was completed by Shim et al. (2000). A total of nine precast-steel composite push-out test specimens were constructed as detailed in Figure 2-13, consisting of a H section of dimensions 300 x 300 mm and a concrete slab measuring 600, 700, and 220 mm wide, tall, and thick, respectively. A total of four headed studs, two welded to on each side of the flange, were used in this study measuring 150 mm in height and 19 mm in diameter. Once the precast slabs were cured for 28 days, they were positioned on either side of the steel section with a 20 mm haunch, and grouted with three different batches of mortar, having compressive strengths of 55, 61, and 71 MPa. Shim et al. (2000) tested the nine specimens under a sinusoidal load, targeting four shear stress ranges; 108, 125, 143 and 151 MPa.

Shim et al.'s (2000) fatigue results are represented in Figure 2-14 by the black squares. From these results, he established a semi-log relationship to represent the data and is expressed in Equation 2-11, which bears a resemblance to Equation 2-7 derived by Slutter and Fisher (1966):

$$\log N = 7.8869 - 0.021 S_r \; [MPa] \tag{2-11}$$

Based on his results, he suggested that further experiments are necessary to investigate the effect of the haunch on the fatigue performance of the shear connectors in the precast deck.
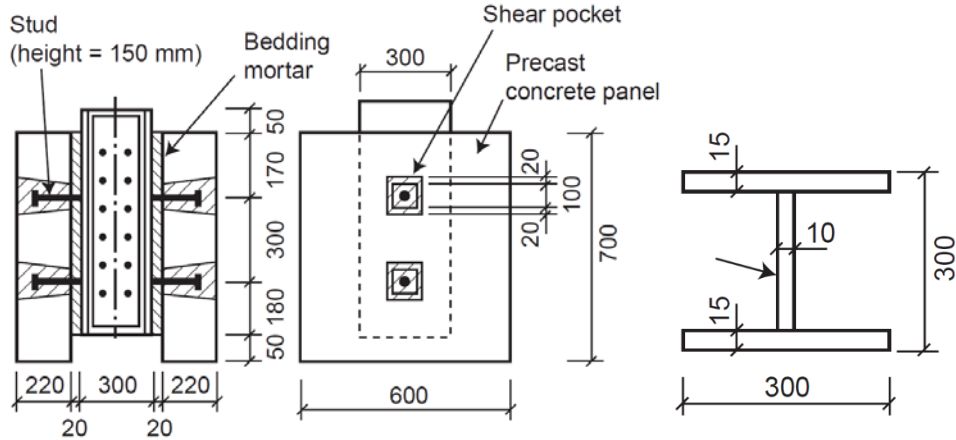
Figure 2-13: Details of the precast-steel composite push-out test specimen (Shim et al., 2000).
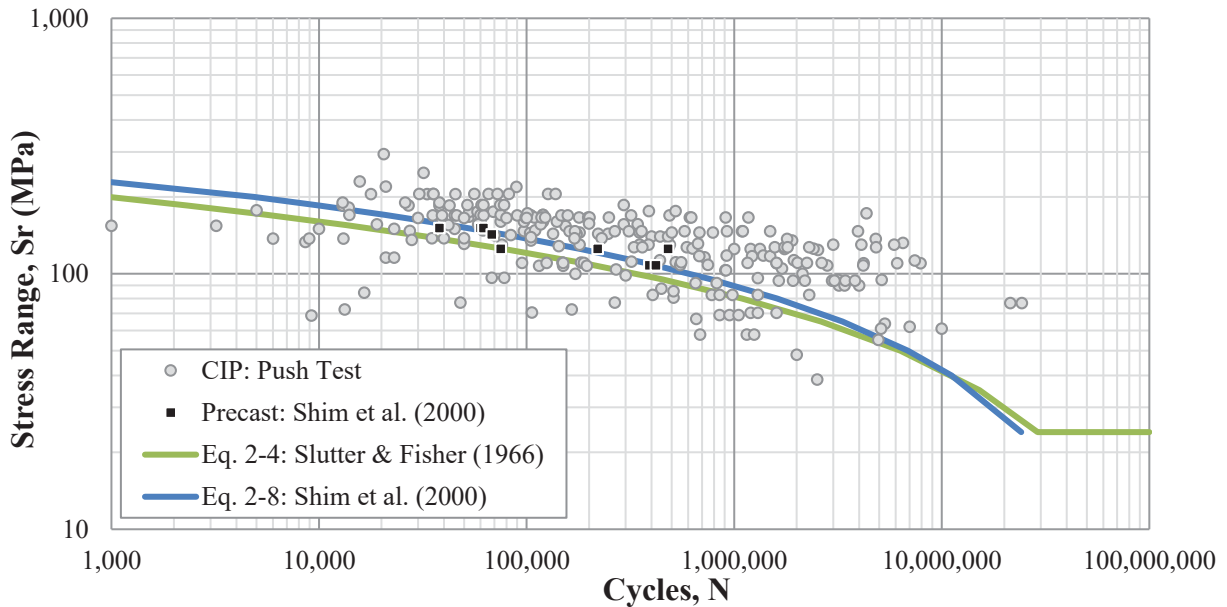
Figure 2-14: S-N plot illustrating the results from Shim et al. (2000).

Following the work of Shim et al. (2000), LaRose (2006) examined both experimental and analytical work on the performance of shear stud clusters in precast bridge deck panels. His experimental work consisted of 15 precast push-out test specimens constructed with circular grout pockets. Nine of his specimens were tested monotonically to determine the ultimate capacity of a stud cluster, and six were loaded cyclically followed by a monotonic loading to investigate the reduction in ultimate strength after fatigue loading. During the fatigue phase, the studs were loaded at a rate of 1 Hz to a stress range of 48 MPa, which corresponds to the endurance limit specified in the CHBDC (CSA S6, 2014). Three of the specimens were constructed with six studs per pocket

and the remaining three constructed with ten studs per pocket. Each of the specimens were then cycled to either 250,000, 500,000, or 750,000 cycles and loaded to failure. LaRose (2006) observed a reduction in the ultimate strength of the shear connectors with respect to the number of cycles, which he presented in the form of a linear trend. Complementing the experimental program, a parametric study on a 36 m bridge span designed according to the CHBDC and was completed using the commercial finite element software package STAAD.Pro. The investigation varied the longitudinal spacing of the shear stud clusters and studied the effects on deflection and the first mode of natural frequency. Based on the findings, it was suggested that the 600 mm spacing limit be increased to 1200 mm as the increase in deflection and decrease in natural frequency were minimal, amounting to 2% and 1%, respectively.

The Ministry of Transportation of Ontario (2010) published a paper titled "The Effect of Shear Stud Clusters in Composite Girder Design". This research was conducted by authors Huh, Lam, and Tharmabala in the hopes of determining the long-term reliability and effectiveness in maintaining composite action of stud clusters subject to cyclic loading. This goal was achieved by studying the ultimate flexural behaviour of four 4 m long beam specimens subject to 3 million fatigue cycles each. The specimens were constructed as per the drawings provided in Figure 2-15, which includes the geometrical layout of the stud clusters.
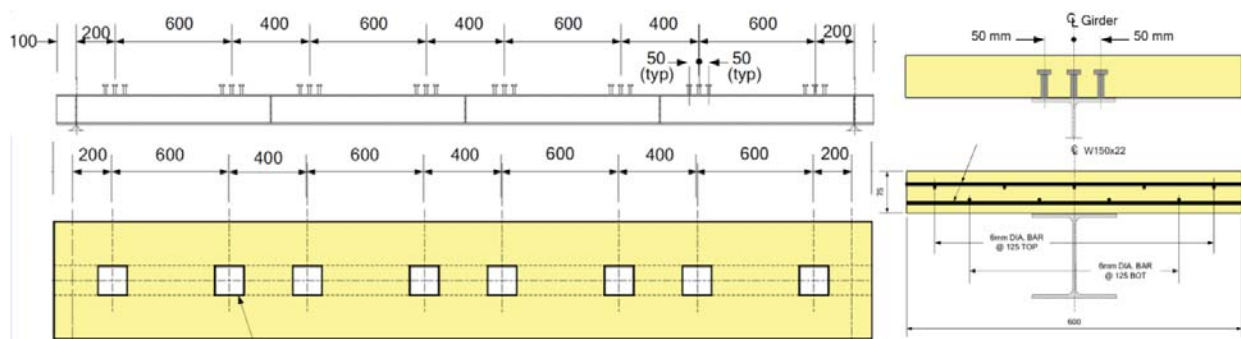
Figure 2-15: Precast-steel composite beam specimen geometry (Huh et al., 2010).

The behaviour of these four specimens (one CIP and three precast) was then compared to two beam tests, which were not subject to cyclic loading. The four beams subject to cyclic loading were initially loaded statically, and intermediate static loading tests were completed at the 1, 2, and 3 million cycle marks, to observe any gradual changes in load-deflection or strain behaviour.

The fatigue loading was completed at a rate of 0.8 Hz and a 30 kN load was applied as a single point load at midspan satisfying SLS load conditions, resulting in approximately a 40 MPa shear range. It was observed that the measurements remained uniform over the course of the fatigue loading, with the specimens having similar stiffness and strain properties as theory would calculate. This behaviour is expected, considering that the constant amplitude endurance limit for the stud weld detail is 48 MPa, suggesting that the studs did not incur any damage during the 3 million cycles. The failure mode under static loading was flexural yielding in the bottom flange of the steel beam at a load level well above the theoretical ultimate load. The testing concluded that shear stud clusters in precast-steel composite girders can provide the same level of composite action as a CIP-steel composite girder at the ULS, subsequent to the application of 3 million cyclic loads at a SLS load level.

Additional research on the fatigue and ultimate capacity of shear stud clusters has been completed by a team of researchers as a part of the National Cooperative Highway Research Program (NCHRP). Badie and his team have published numerous reports focusing on the advancement of rapid bridge deck replacement utilizing precast slabs with shear stud pockets. The first phase of the research was completed in 2010 with the objective of relaxing the stud cluster spacing limit, which at the time was prescribed to 610 mm [24"] in the American (AASHTO, 2007) and CHBDC (CSA S6, 2006) design codes. Initial push-out testing was completed on 16 precast specimens containing two groups of eight studs each. The first group was tested to examine the ultimate capacity and the second group was tested to study the ultimate capacity after cyclic loading. Other properties varied between specimen groups were the number of studs, stud cluster spacing, and the type of shear pocket confinement. The fatigue loading of the studs in the second group of specimens consisted of 2 million cycles with a shear range equal to the fatigue limit of a stud, corresponding to 24 MPa as prescribed by the AASHTO code (Badie et al., 2010). Results from the testing concluded that little change in the load-displacement relationship is caused by the fatigue loading, and that extending the spacing limitations of the stud clusters to 1220 mm [48"] is possible while maintaining full composite action. The researchers suggested that the push-out specimens are not as accurate as full-scale beams when modelling the true longitudinal shear as they do not provide the true shear and flexure interaction. Thus, they recommended the testing of

full-scale composite beams to investigate the behaviour of the studs when grouped in clusters spaced at 1220 mm [48"], leading to the second phase of the research.

Badie et al. (2011) completed the second phase of the NCHRP project with the objective of conducting full-scale steel-precast beam tests in order to determine the ultimate behaviour before and after cyclic loading when the stud cluster spacing limit is doubled to 1220 mm [48"]. The experiment consisted of two beams, each 9.75 m [32 ft] in length, and stud cluster spacing at 610 mm [2 ft] and 1220 mm [4 ft] for the first and second beam, respectively. A total of 62 headed studs with a diameter of 32 mm [1.25"] were welded to the top flange of the steel beam resulting in 16 and 8 discrete clusters for the two beams respectively. The precast slabs were constructed with 57 MPa [8.2 ksi] concrete at a depth of 203 mm [8"], a width of 1220 mm [4 ft], and situated on top of a W460x177 [W18x119] structural steel girder. The slab was positioned 25 mm [1"] above the steel to form a haunch when the pockets were filled in with a 66 MPa [9.6 ksi] commercial grade non-shrink grout. The beam layout and cross-section are illustrated in Figure 2-16. The beams were constructed with two different types of pocket confinement on each half of the beam. The pockets on one half were confined with closed ties, while the pockets on the other half were confined with a hollow structural section tube.
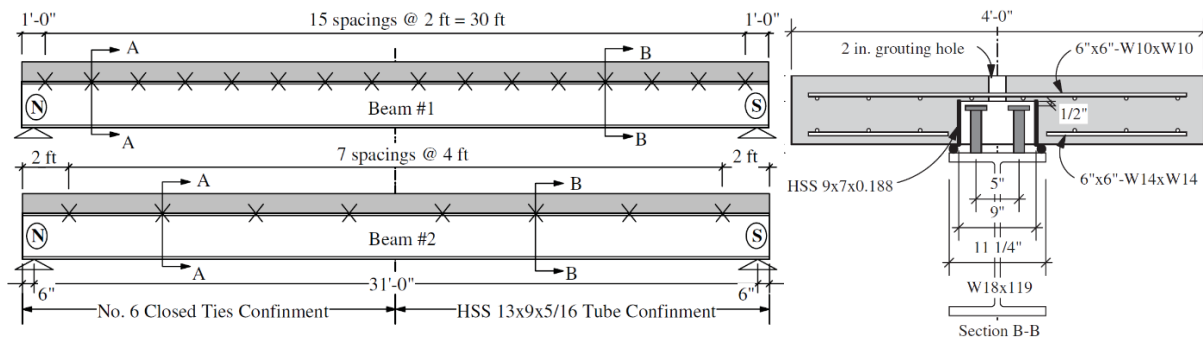
Figure 2-16: Beam specimen geometry and arrangement of stud clusters (Badie et al., 2011).

The beams were first tested with 2 million constant amplitude load cycles that resulted in a longitudinal shear stress range of 24 MPa [3.5 ksi]. Unfortunately, the second beam with the 1220 mm [48"] stud group spacing failed in fatigue at the bottom flange and the crack propagated up into the web at approximately 1.95 million cycles. The researchers stated that the cause for this was solely due to the fact that the steel beams were used in previous fatigue testing. Thus, a reduced span was utilized for ultimate testing. Once the beams were tested to their ultimate capacities, it

was concluded that the 1220 mm [48"] pocket spacing had no adverse effects on the beam's ultimate capacity after fatigue loading. Both beams demonstrated the same stiffness characteristics and the testing proved that modification of the current design specifications due to the extended spacing is not necessary.

A summary of the research work completed on steel-precast composite beams subject to cyclic loading is presented in Table 2-1. LaRose (2006), Huh et al. (2010), and Badie et al. (2011) ultimately all focused on the reduction in the ultimate strength under constant amplitude cyclic loading. Their work was essential in the understanding of stud cluster spacing at ULS, however, provided no useful data in defining the FLS for steel-precast constructed beams. Shim et al. is the only researcher that provides insight to the actual fatigue strength of shear connectors in steel-precast construction. This may be attributed to the fact that his results closely align with the results collected by Slutter and Fisher (1966) on steel-CIP push-out tests. As a result, the assumption was made that further testing on the FLS of shear studs in precast is not necessary because precast construction has no influence on the fatigue performance. This may hold true in smaller push-out test experiments where the true shear and flexure behaviour are not accurately modelled and the effect of concrete shrinkage is minimal. Since there has been no steel-precast beam testing that has resulted in a fatigue failure, it is necessary to fill the research void and provide scientific evidence as to whether or not the assumption of similarity holds true.

Table 2-1: Summary of the previous research completed on steel-precast composite specimens subject to cyclic loading.

Researcher	Shim et al. (2000)	LaRose (2006)	Huh et al. (2010)	Badie et al. (2010)	Badie et al. (2011)
Year	2000	2006	2010	2010	2011
Test Specimen Type	Push-Out	Push-Out	Beam	Push-Out	Beam
No. Precast Fatigue Specimens	9	6	3	8	2
Stress Range (MPa)	108 - 151	48	40	24	24
No. Cycles	40,000 - 500,000	250,000 - 750,000	3,000,000	2,000,000	2,000,000
Objective	Fatigue Failure	Reduction in ULS Strength due to Cyclic Loading			
Failure Type	FLS	ULS	ULS	ULS	ULS

2.3   Design Codes

In the current Canadian Highway Bridge Design Code (CHBDC) (CSA S6, 2014) governing steel-concrete composite girder design, shear studs are designed to satisfy both strength and fatigue requirements. To satisfy strength requirements at the ultimate limit state (ULS), the shear connection at the steel-concrete interface must be capable of developing the full plastic capacity of the steel cross-section, facilitating full composite action. To satisfy fatigue requirements at the fatigue limit state (FLS), the stress levels must be kept below an empirically determined threshold given an anticipated number of repeated cycles.

This discussion first provides insight to the ULS provisions set by the CHBDC (CSA S6, 2014)and then compares the Canadian provisions to the FLS provisions in other codes, including the American (AASHTO LRFD, 2014), Eurocode 4 (CEN, 2005), British (BSI, 1980), and Japanese (JSCE, 2009) codes. The CHBDC provides engineers with essential tools and regulatory provisions for the safe design of headed shear connectors in both full-depth cast-in-place and precast concrete deck panels. The headed shear stud connectors found in composite bridge girders resist both horizontal and vertical movements between the concrete slab and steel girder to achieve an efficient composite section, which satisfies the ultimate and fatigue limit state verifications.

2.3.1   Ultimate Limit State

The ultimate limit state (ULS) design for shear connection is a function of the connector, concrete, and grout strength; spacing; embedment; and clear concrete cover. The material requirements permit for the use of Type B studs that comply with metal arc welding procedures stated in CSA W59, Appendix H (2013). Type B studs require the material to consist of a ductile low carbon steel with a tensile and yield strength of 450 MPa and 350 MPa, respectively. The necessary flexibility and ductile behaviour permits a uniform distribution of forces along the connection nearing the ULS. The code requires that the minimum number of shear connectors, N, in each shear span, defined as a segment between points of maximum and zero moments at the ULS for both cast-in-place and precast composite girders shall be calculated in accordance with Clause 10.11.8.3:

$$N = P / q_r \qquad (2\text{-}12)$$

30

where P is the ultimate factored load capacity of the concrete slab or steel to be transferred by the shear connectors. When the plastic neutral axis is located in the concrete slab or steel section, P is calculated using Equation 2-13 or 2-14, respectively:

$$P = \varphi_s A_s F_y \tag{2-13}$$

$$P = 0.85 \varphi_c f'_c b_e t_c + \varphi_r A_r f_y \tag{2-14}$$

where:

φ_s	=	the material resistance factor for steel [unitless],
A_s	=	the area of the steel section [mm²],
F_y	=	the minimum specified yield stress of the steel girder [MPa],
φ_c	=	the material resistance factor for concrete [unitless],
f'_c	=	the compressive strength of the concrete [MPa],
b_e	=	the effective width of the concrete slab [mm],
t_c	=	the thickness of the concrete slab [mm],
φ_r	=	the material resistance factor for the steel reinforcement [unitless],
A_r	=	the area of steel reinforcement within b_e [mm²], and
f_y	=	the minimum specified yield stress of the reinforcing steel [MPa].

In the determination of the ultimate factored load capacity, P, the CHBDC utilizes several material resistance factors for the steel, concrete, and reinforcing bars as presented in the previous equations. Interestingly, the AASHTO LRFD specifies that the nominal strength of the structural materials are to be utilized. As a result, the CHBDC calculates more conservative design forces to be transferred, and as a result, lowers the required number of shear stud connectors at ULS. An explanation for this non-conservative approach is currently unavailable in the literature or the code commentary (LaRose, 2006).

The factored shear resistance of a single headed shear stud connector, q_r, was developed based on the experimental program conducted by Ollgaard et al. (1971). The program consisted of 48 two-slab push-out specimens to evaluate the capacity of headed shear stud connectors embedded in cast-in-place concrete slabs. The test results concluded that the capacity was predominantly influenced by the compressive strength and modulus of elasticity of the concrete. It was observed

that significant inelastic deformation had occurred before the stud sheared off or the concrete encasing the stud failed due to cracking.

For a single shear stud connector where the height to depth ratio is ≥ 4, the factored shear resistance, q_r, is calculated in accordance to Clause 10.11.8.3.1:

$$q_r = 0.5\varphi_{sc} A_{sc} \sqrt{f'_c E_c} \leq \varphi_{sc} F_u A_{sc} \qquad (2\text{-}15)$$

where:

φ_{sc}	=	the material resistance factor for the shear stud connector [unitless],
A_{sc}	=	the cross-sectional area of one shear stud connector [mm²],
f'_c	=	the uniaxial compressive strength of the concrete/grout encasing the shear stud [MPa],
E_c	=	the elastic modulus of the concrete/grout encasing the shear stud [MPa], and
F_u	=	the minimum specified tensile strength of the stud steel [MPa].

Although Ollgaard's experimental program was intended for the use of shear stud connectors in CIP concrete, the CHBDC permits the application of his work towards studs embedded in precast concrete. For precast-steel composite beams, values for f'_c and E_c are to be based on the values from the non-shrink grout filling the shear pockets. It is important to note that the grout strength utilized in the calculation is not permitted to be greater than 1.3 times the compressive strength of the precast concrete.

The AASHTO LRFD Bridge Design Specifications (AASHTO, 2014) treat the design of CIP and precast equally, and state that the maximum spacing between shear studs should not exceed 610 mm [24"]; a statement arbitrarily made by Slutter and Fisher (1966) as a design guideline. This guideline was implemented with no experimental justification, and claimed to be the maximum spacing to avoid slab-steel separation. Also, the statement was made on the basis of CIP slabs, where continuous rows of studs are used instead of stud clusters.

This problem was observed and addressed by the CAN/CSA S6 Code in 2010, where supplementary provisions were implemented to extend the spacing limit on shear stud clusters to

1200 mm. The foundation on which this provision was formulated can be attributed to the researchers Tadros and Baishya (1998), Issa et al. (2003), Elwood and LaRose (2006), Huh (2010), and Badie et al. (2010, 2011). Each of the researchers' work focused on the behaviour of precast-steel composite sections with the intension of making the system more efficient, by ultimately reducing the number of pockets along a bridge. As stated by Tadros and Baishya (1998), it is advantageous to reduce the number and size of the shear pockets as it:

- simplifies and accelerates the fabrication process and ultimately lowers fabrication costs,
- decreases the amount of in-situ grouting along a bridge deck, further reducing the construction costs by increasing construction speed,
- reduces reinforcement congestion by increasing space for transverse slab reinforcement and adding flexibility for the design engineer,
- alleviates the possibility of water penetration between grout and concrete interfaces, improving the durability of the system, and
- at the end of the slabs life, reduces the amount of saw cutting required for deck removal.

2.3.2 Fatigue Limit State

When designing the shear connection in steel-concrete composite girders, the FLS frequently governs over the ULS, resulting in an increase in the required number of shear connectors. Since bridges are required to have a minimum 75 year design life in the current North American Codes (CSA S6, 2014), the average daily truck traffic is extrapolated over this time period resulting in a high number of stress cycles. From an S-N design curve, the threshold of cyclic stress, given the number of cycles expected during the service life, can be determined and designed for appropriately.

Prior to the CHBDC code's revision in 2010, the FLS provisions for stud connectors abided by the experimental results on CIP push-out tests provided by Slutter and Fisher (1966) (Equation 2-7). This former approach utilized a semi-log relationship corresponding to the stress range and the logarithm of the fatigue life, the design approach still applied by the American AASHTO LRFD code (AASHTO, 2014). In addition, the mean regression curve, rather than the mean minus two standard deviations, was used in the place of the design curve. This method was deemed adequate recognizing the level conservatism employed when utilizing push-out tests to evaluate the fatigue

resistance. The commentary to the CHBDC recognized this conservatism and justified the design decision by stating that composite action due to friction at the steel-concrete interface contributes to a reduction in stress in the shear connectors at the service load level. Thus, making the use of push-out test results for fatigue design somewhat conservative.

In contrast, the adopted approach in the 2010 revision utilizes a log-log relationship typically represented by Equation 2-16:

$$F_{sr} = \left(\frac{\gamma}{N_c}\right)^{\frac{1}{m}} \geq \frac{F_{srt}}{2} \tag{2-16}$$

where:

F_{sr}	=	the fatigue stress range resistance of a member or detail [MPa],
γ	=	the fatigue life constant pertaining to a detail category found in Table 10.4 of the CHBDC,
N_c	=	the total number of design cycles calculated as: 365 y N_d ($ADTT_f$),
y	=	the design life (typically 75 years unless specified otherwise),
N_d	=	number of stress cycles experienced for each passage of a design truck as specified in Table 10.5 of the CHBDC,
$ADTT_f$	=	the forecasted single lane average daily truck traffic specified in Table 10.6 of the CHBDC,
m	=	a constant derived from regression analyses, taken as $m = 3$, and
F_{srt}	=	the constant amplitude threshold stress range pertaining to a detail category found in Table 10.4 of the CHBDC (CSA S6, 2014) [MPa].

The constant amplitude threshold stress range, F_{srt}, is the stress range below which a crack will not propagate for a certain detail category found in Table 10.4 of the CHBDC (CSA S6, 2014). If the stress range is below this threshold, then the detail is assumed (for practical purposes) to have an infinite fatigue life. In reality however, the stresses the bridge will experience over its design life are variable in amplitude, and have been found to occasionally be twice as great as calculated for the specified fatigue design load. Thus, to ensure a theoretically infinite life, the constant amplitude threshold is divided by 2 to provide the designer with a variable amplitude fatigue limit (VAFL)

stress range represented by the inequality in Equation 2-16. Figure 2-17 provides the S-N plot for the various fatigue detail categories prescribed in the CHBDC. The horizontal dashed lines represent the constant amplitude threshold for each of the categories.
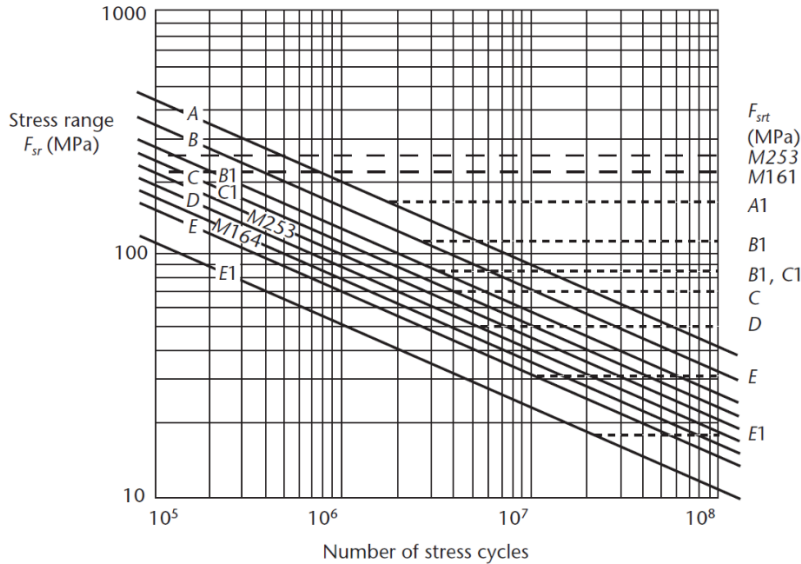
Figure 2-17: S-N plot for the different fatigue detail categories as defined in the CHBDC Commentary (CSA S6.1, 2014).

Zhang (2007) completed an investigation, which included a regression analysis on a large collection of push-out tests collected from the literature. The analysis concluded that the inventory of data could be well represented on a log stress range versus log fatigue life, and the mean regression line could be closely approximated by the fatigue Category D curve. Additionally, it was noted that detail Category D has the same constant amplitude fatigue limit (CAFL) as the previous value used for studs, i.e.,48 MPa, leaving it unchanged.

When designing the shear stud connectors for the FLS, the CHBDC (CSA S6, 2014) requires that both the base material and the stud connector satisfy Cl. 10.17.2.3 and Cl. 10.17.2.7, respectively. According to Table 10.4 in the CHBDC, the base metal weld fatigue resistance is prescribed as a detail Category C, amounting to a fatigue life constant, γ, and a constant amplitude threshold stress range, F_{srt}, as 1140×10^9 and 69 MPa, respectively. The 2010 revision incorporated Zhang's (2007) regression work and defined the fatigue resistance of a stud connector as a Category D fatigue detail, with a γ and F_{srt} of $721 \cdot 10^9$ and 48 MPa, respectively, governing over the base material

fatigue detail in all cases. It should also be noted that the design for headed studs in CIP and precast construction are identical, utilizing the same formulas and fatigue details.

An elastic analysis is utilized when calculating the fatigue resistance of shear stud connectors as prescribed in Cl. 10.17.2.7. The design check involves equating the fatigue resistance, F_{sr} (Equation 2-16), to the design shear stress range, τ_{rs}, calculated in Equation 2-17:

$$\tau_{rs} = 0.52 C_L \frac{V_{sc}Qs}{A_{sc}I_t n} \tag{2-17}$$

where:

τ_{rs}	=	the design shear stress range on the studs [MPa],
C_L	=	the modification factor for when anticipated loading is greater than a CL-625 design truck,
V_{sc}	=	the range of design shear force at the section being evaluated [N],
Q	=	the first moment of area of the transformed section at the interface of the steel and concrete [mm^3],
s	=	the shear stud group spacing [mm],
A_{sc}	=	the cross-sectional area of a shear stud [mm^2],
I_t	=	the moment of inertia of the transformed cross-section about the primary axis of bending [mm^4], and
n	=	the number of shear studs in the group at the cross-section being evaluated.

The design shear stress range, τ_{rs}, is calculated due to the passage of a single CL-625 design truck. Thus the 0.52 calibration factor found in Equation 2-17 accounts for the difference between the CL-625 design truck and the average/equivalent truck that is expected to cause the majority of the fatigue damage.

An analysis comparing the design provisions governing the fatigue performance of stud shear connectors in the CHBDC (CSA S6, 2014) to other design codes is presented in the following paragraphs. The additional design codes included in the analysis are the American (AASHTO, 2014), Eurocode 4 (CEN, 2005), British (BSI, 1980), and Japanese (JSCE, 2009) codes. Similar

to the CHBDC, the AASHTO and Eurocode 4 provisions are direct functions of the stress range and life. The British Standards and Japanese codes however, are dependent on the static strength of the studs, as described in each of the codes respectively. Therefore, material and geometrical properties are required to produce the curves, and for the purpose of the comparison, assumed as follows: height of the stud = 67 mm; diameter of the stud = 16 mm; compressive strength of the concrete = 45 MPa; and yield strength of the stud = 350 MPa. The various design curves are overlaid onto an S-N plot in Figure 2-18, which includes a cloud of push-out test and beam test data points collected from the literature (Slutter and Fisher (1966), Oehler and Foley (1985), Zhang (2007)). The solid black line, dashed green line, dashed red line, dashed purple line, and dashed blue line represents the American (AASHTO, 2014), Eurocode 4 (CEN, 2005), British (BSI, 1980), and Japanese (JSCE, 2009) codes, respectively.
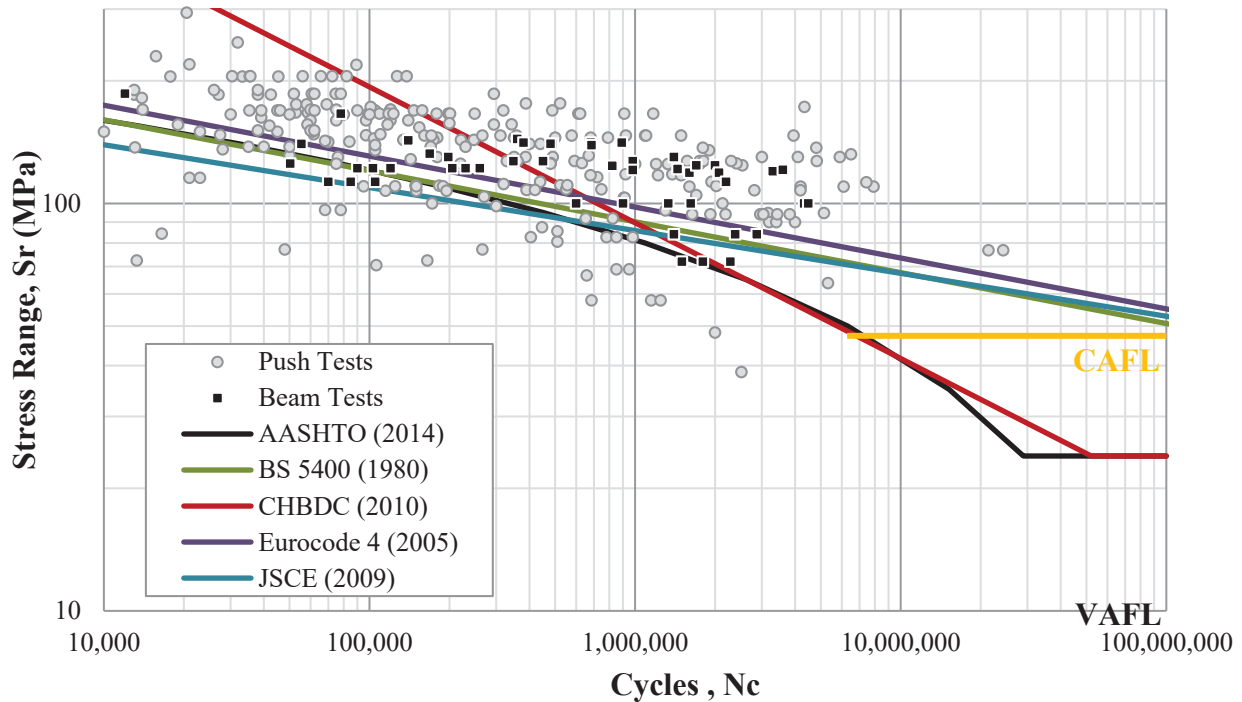
Figure 2-18: Global design provisions governing the fatigue of headed shear connectors.

According to the Table 10.6 in the CHBDC (CSA S6, 2014), the average daily truck traffic for a single lane, $ADDT_f$ for a Class A, B, C, and D highway are 4000, 1000, 250, and 50, correspondingly. The numbers of design cycles, N_c, that each class of highway must endure over its 75-year design life are summarized in Table 2-2. The load modelling aspect for determining the allowable stress ranges varies from code to code. Therefore, to facilitate this code comparison, it

is assumed that the codes determine the allowable stress ranges from Canadian truck traffic and the CL-625 design truck. The percentages provided in the lower portion of Table 2-2 quantify how much larger the maximum allowable stress range can be for a given code compared to the CHBDC, being directly related to the percentage decrease in the number of required studs.

Table 2-2: Global Design Code Comparison.

Design Code			CHBDC (2014)	AASHTO (2014)	BS 5400 (1980)	Eurocode 4 (2005)	JSCE (2009)
Class	ADTT	Nc	Maximum Allowable Stress Range (MPa)				
A	4000	109,500,000	24	24	50	55	52
B	1000	27,375,000	30	25	60	65	60
C	250	6,843,750	47	49	71	77	69
D	50	1,368,750	81	76	87	94	82
			Percent Larger than CHBDC (Decrease in Studs)				
A	4000	109,500,000	-	0%	109%	127%	116%
B	1000	27,375,000	-	-16%	101%	118%	102%
C	250	6,843,750	-	3%	50%	63%	47%
D	50	1,368,750	-	-6%	7%	17%	2%

Given the range of design cycles corresponding to each highway class, it is evident in the S-N plot in Figure 2-18 and comparative results in Table 2-2 that both the Canadian and American design provisions result in a similar number of required studs. For highway Classes A and B, the North American codes require approximately double the number of required studs compared to the others, as the maximum allowable stress range is approximately halved.

The AASHTO code, being semi-logarithmic, does not have a log-log slope, represented by m, as compared to the other codes. Instead, it follows a similar slope of the BS 5400, Eurocode 4, and JSCE codes in the range of 10,000 to 1,000,000 cycles. Past the 1,000,000 cycle mark, the AASHTO code corresponds well with the CHBDC, until each is limited by the variable amplitude fatigue limit of 24 MPa. Both the BS 5400 and Eurocode 4 design curves are defined with an m value equal to 8, while the JSCE and CHBDC hold values of 9.5 and 3 respectively. Johnson (2000) noted that for the residual fatigue life in existing bridges, if m is low, most of the fatigue damage is incurred by high frequency, low stress range producing trucks. On the other hand, if m is large, it is the heavy and rare loads that inflict the majority of the damage.

Once analyzed, the inconsistencies between the design standards governing the fatigue of headed stud shear connectors across the globe are clear. The main discrepancy between the codes is the slope, *m*, which varies between 3 in the CHBDC and 9.5 in the JSCE. This variability is not due to the test data, but rather on how the regression analysis of the test data is completed. Although these discrepancies may seem significant, there has been no reports of failures in the field. This is not because the existing methods are exceptional, but because the real stress ranges are conservatively less than those calculated by design (Johnson, 2000).

2.4   Summary

The literature review presented in this chapter provides a foundation on which the concerns formulated in the Research Needs Section 1.1 were assembled. Copious amounts of push-out test results are readily available for both CIP and precast construction methods, and the mean regression of this data has been found to correspond to a Category D fatigue detail in the CHBDC (Zhang, 2007). The mean regression line was chosen for design, rather than the mean minus two standard deviations, under the assumption that push-out tests provide conservative results. This conservatism has not yet been quantified and once determined, should be calibrated appropriately and included into the provisions. Other design codes, like the Eurocode 4 (CEN, 2005), British (BSI, 1980), and Japanese (JSCE, 2009) codes, can require approximately half the number of studs compared to the North American counterparts when assuming Canadian truck traffic. Additionally, it has been discussed that there currently is an absence of beam tests that have led to accurately reported connector failures. Of the beam tests that have led to reported connector failures, studies providing insight into the performance of the composite beam subsequent to the failure are currently not available and are essential when calibrating the code provisions considering the consequence of failure. Lastly, it remains the case that no fatigue tests conducted on steel-precast composite beams have resulted in shear connector failures. The investigations completed on steel-precast composite beams to date have focused on confirming the appropriateness of CIP design provisions, assuming that the construction method has no effect on the fatigue performance of shear connectors. Thus, as previously discussed, the effects of concrete shrinkage and friction at the steel-concrete interface must be investigated, as they may have a significant impact on the fatigue behaviour.

3 Experimental Design

This Chapter describes the experimental design of this research project. Firstly, the geometry, materials, and instrumentation chosen for each of the beam specimens are provided. Secondly, the loading sequence used to simulate in-service bridge loading on the specimens is described, along with the final beam testing matrix and program. Thirdly, the fabrication process utilized for the beam specimens is covered in detail. Lastly, details on the laboratory testing frame, data acquisition, hydraulics, and other equipment used in the testing procedure is identified.

3.1 Beam Specimen Geometry and Materials

A total of twelve simply supported beams were fabricated and tested for this research project, six of which utilize traditional CIP methods, and six that were constructed using precast slabs. Both the CIP and precast specimens had a span of 3 m and consisted of a W250x49 steel section connected to the underside of a 600 mm wide, 125 mm deep, 3 m long concrete slab as shown in Figure 3-1. Note that the steel beams extend an additional 100 mm from the centerline of the supports, resulting in a total length of 3.2 m. Additionally, the loading is applied in equal proportions by a load spreader at Points A and B, which are located 500 mm and 1000 mm from the west support, respectively.
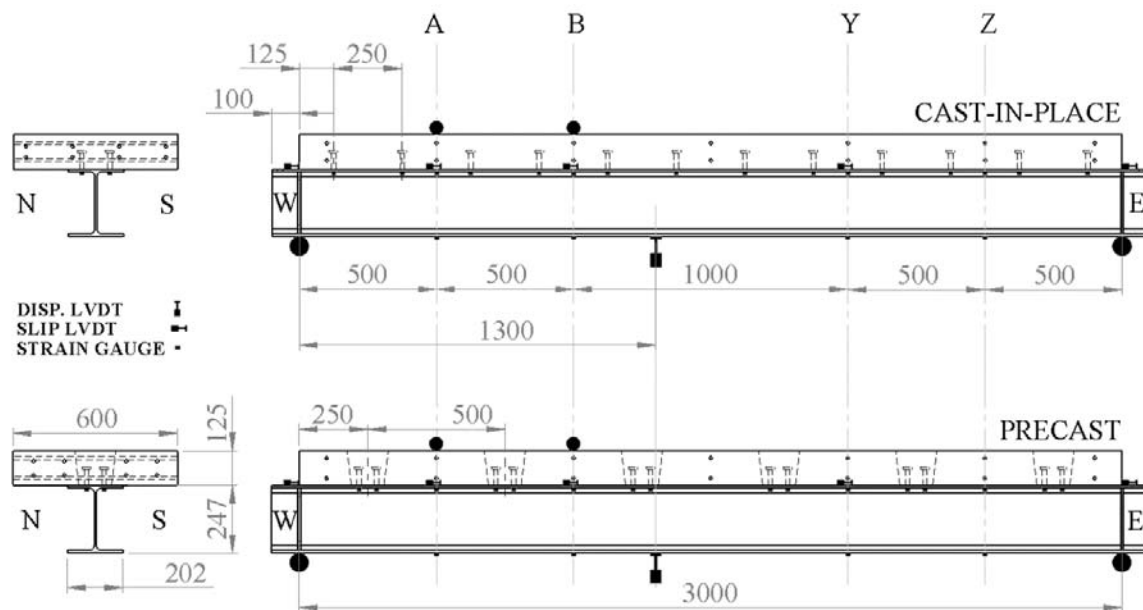
Figure 3-1: Beam specimen geometry and layout (dimensions in mm).

To prevent web buckling, 10 mm thick web stiffeners were welded onto the beam at the centrelines of the West and East supports. The grade of steel utilized for the W-section and web stiffeners was a 350W (350 MPa yield strength, weldable) steel conforming to the CAN/CSA G40.21-13 Structural Quality Steel guidelines (CSA G40.21, 2013). To aid in the hoisting and mobility of the specimens, four - 21 mm diameter holes were drilled through the top flange on each side of the web at each beam end, two on the west and east ends respectively.

To establish the shear connection between steel beams and concrete slabs, a total of 24 - Type B Nelson shear studs were arc-welded to the top flange of each specimen using a typical stud gun. Type B refers to the low carbon steel requirement facilitating ductile behaviour, resulting in a yield and ultimate strength of 350 MPa and 450 MPa respectively. The studs used in this experiment had a 16 mm shank diameter, 31.75 mm head diameter, and were 67 mm in height. For the CIP specimens, the studs were welded in pairs uniformly spaced at 250 mm. The precast specimens utilized six stud clusters spaced at 500 mm. Each cluster consisted of four studs in a square arrangement, spaced at 64 mm in the longitudinal and transverse directions.

The concrete slab was designed to be cast with a standard 40 MPa air entrained concrete provided by a local ready-mix supplier. Standard 10M carbon steel reinforcing bars were utilized in the longitudinal and transverse directions to control concrete shrinkage and cracking (see Appendix A). For the precast slabs, the pockets were formed with square wooden block-outs that were tapered to form a shear key. The pockets were 120 mm x 120 mm at the base and tapered up to 150 mm x 150 mm at the top of the slab. To establish the shear connection in the precast specimens, a high performance, high early strength, low shrinkage, pre-packaged concrete material provided by King Construction Products was utilized. The HP-S10 rapid hardening concrete product has been specified by the MTO for the application of infill strips and shear key pockets in prefabricated bridges, and has a 28-day compressive strength of 60 MPa.

Full fabrication drawings are provided in Appendix A, detailing the dimensions for each of the components not outlined in this section. A summary of the materials and geometry utilized in the design of the specimen's composite cross section is included in Table 3-1.

Table 3-1: Specimen Design Summary

Component / Attribute		Steel Beam W250x49	Rebar 10M	Studs Nelson 16 mm	Concrete Slab	Grout Pockets
Strength	f_y , f'_c (MPa)	350	400	350	40	60
Elastic Modulus	E (MPa)	200,000	200,000	200,000	27,770	32,460
Area	A (mm^2)	6,250	100	201	75,000	-
Depth	d (mm)	247	-	64	125	-
Width	b (mm)	202	11.3	16	600	-

The nomenclature for describing various locations along the beam, used throughout the remainder of the report for both the CIP and precast specimens, is as follows:

- The West and East ends correspond to the left and right supports in the figures.

- The Southern face of the beam is the face viewed in the figure.

- Studs are labelled from West to East (left to right), corresponding to Stud Pairs 1 through 12. The studs are then labelled as N1, S1, N2, S2, and etc.

- The precast specimens contain a total of 6 pockets. The pockets are labelled as P1 to P6 from West to East.

- Profile A, B, Y, and Z correspond to the cross sections of the composite beams at locations 500, 1000, 2000, and 2500 mm from the West support.

3.2 Loading Procedure and Test Matrix

3.2.1 Variable Amplitude Loading

Most fatigue tests on shear connectors conducted to date have been under constant amplitude loading conditions. The effects on fatigue performance of connector slip during infrequent overload cycles (i.e.,due to very heavy trucks or convoys) may be significant. For this reason, a variable amplitude loading history was used for the fatigue testing, simulating typical in-service loading for a bridge subjected to Ontario highway truck traffic. The foundation of the variable amplitude loading history utilized in this experiment was a study completed by the Ministry of Transportation Ontario (MTO) in 1995. This study involved surveying the weights of 10,198 trucks that were randomly selected while travelling on the road network. The results from this survey are presented in the form of a histogram in Figure 3-2.
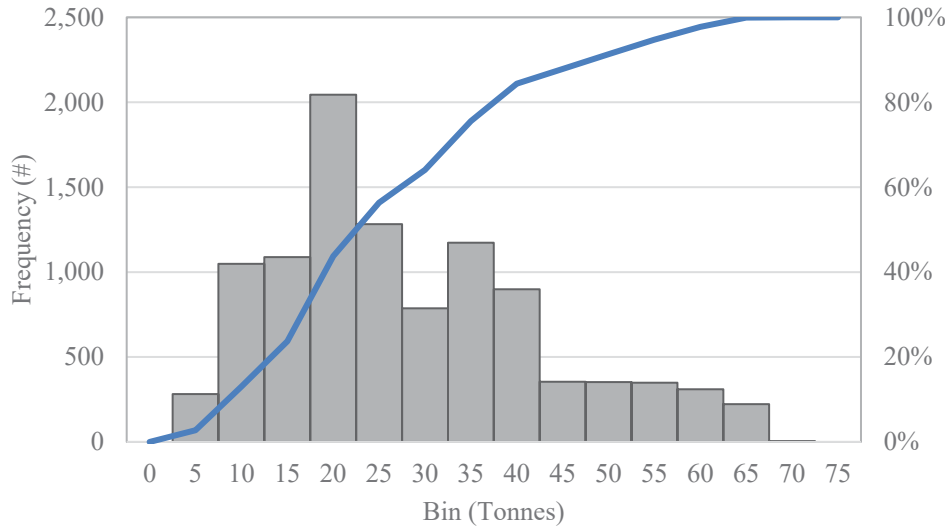
Figure 3-2: Ontario highway truck traffic surveyed by the MTO in 1995.

This data was condensed, randomized, and formatted as a sinusoidal variable amplitude loading history using a script in MATLAB. The procedure for condensing the data involved reducing the frequency of each bin by a factor of 10 (reducing the history length to 1,024 cycles). The frequencies were then rounded to their nearest integer and the data was randomized. Each cycle was represented by 30 discretized points, which produced a smooth sinusoidal curve. The original survey data and the modified bin sizes are provided in Table 3-2 for comparison, and a segment of the first 25 cycles from the randomized history is presented in Figure 3-3. It should be noted that in Figure 3-3, the negative sign on the load indicates a downward-acting load. In order to prevent impact loading on the specimen, a constant downward-acting load of 10 kN was maintained, which is why the load does not return to zero after each cycle.

Since the experiment utilizes a variable amplitude loading history, an equivalent stud load range was determined using the Palmgren-Miner's linear damage accumulation rule. In this way, it was found that the equivalent load range was 344 kN. The variable amplitude loading history was then scaled appropriately to achieve the predetermined target equivalent stress ranges (nominal shear stress the stud shear connectors) for each test specimen. Due to the unique off-centered loading arrangement of the spreader, the Stud Pairs 1 and 2 experience what will be called, the target stress range, while Stud Pairs 3 to 12 experience exactly one-third of the target stress range. A shear force diagram helpss illustrate this concept, as shown in Figure 3-4.

43

Table 3-2: Original and Modified Survey Data Frequencies

Bin (Tonnes)	Original No.	Modified No.	% of Original
0	0	0	-
5	282	28	9.9%
10	1,049	105	10.0%
15	1,088	109	10.0%
20	2,044	205	10.0%
25	1,282	128	10.0%
30	787	79	10.0%
35	1,173	118	10.1%
40	899	90	10.0%
45	354	36	10.2%
50	353	36	10.2%
55	349	35	10.0%
60	310	31	10.0%
65	223	23	10.3%
70	5	1	20.0%
75	0	0	-
Total Vehicles	10,198	1,024	10.0%
Equivalent Load (kN)	343	344	100.3%
Max Load (kN)	687	687	100.0%
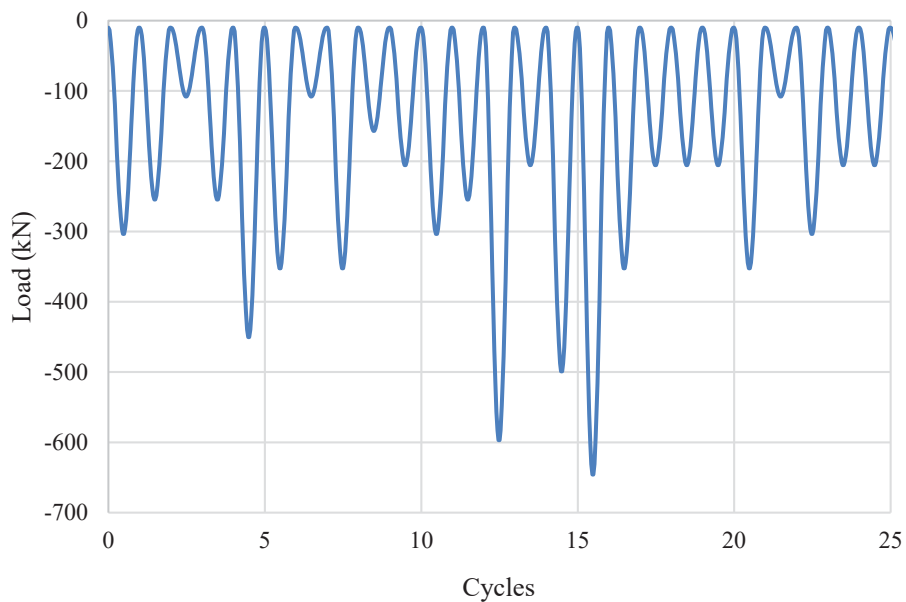
Figure 3-3: A sample of the modified variable amplitude loading created from the 1995 survey.
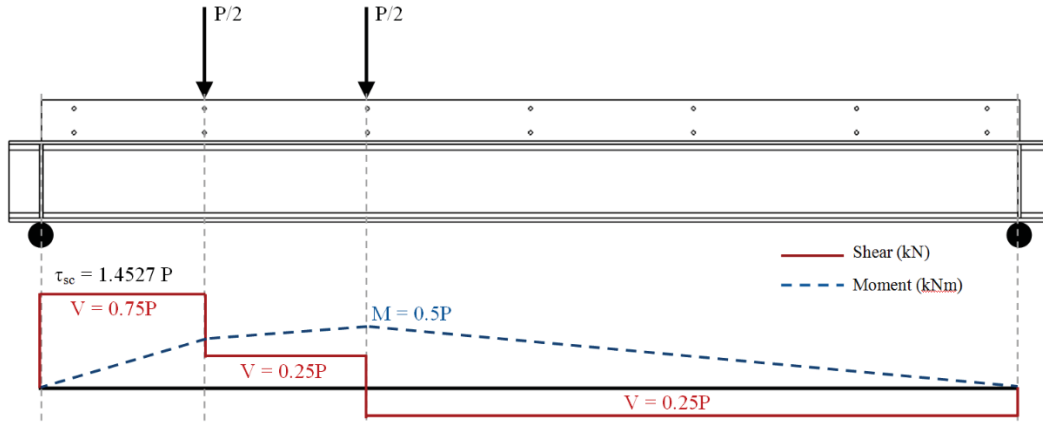
Figure 3-4: Shear force and bending moment diagrams for the test specimen.

The testing setup employs two-point loading, offset to create a varying interface shear profile along the beam span. This was done to allow the effects of connector failures on the neighbouring connector groups along the span to be studied. The loading offset was also implemented to apply a greater shear stress to Stud Pairs 1 and 2. The greater stress then governs where the fatigue failure will first occur, making monitoring much simpler.

The frequency at which the fatigue loading was applied ranged between 2 and 4 Hz, depending on the target load level. The data was collected utilizing peak detection software, which recorded the channel values when a peak in the cyclic loading was identified.

3.2.2 Static Loading

A static loading step was completed initially, and at the 100% and 1000% theoretical fatigue lives for each of the specimens. The initial static loading test was completed to break the chemical bond adhering the concrete to the top of the steel flange upon casting, and to collect data before any damage occurs from the subsequent cyclic loading phase. The data collected in the static tests included the strain profiles, max deflection, and interfacial slip. For comparison purposes, a load of 200 kN was selected as a standard load, corresponding to a 291 MPa stud stress in Stud Pairs 1 and 2. The 200 kN load was applied at a rate of 2 kN/s under load control conditions. The 200 kN load was then held statically for 5 seconds, followed by a 4 kN/s load retraction rate. The static loading history is graphically shown in Figure 3-5. Additionally, the data was collected at a rate of 2 Hz during each of the static tests.

45
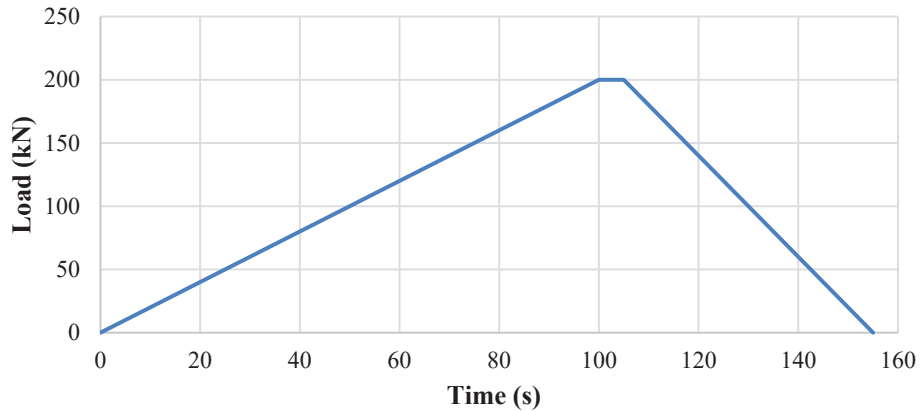
Figure 3-5: Static loading history.

3.2.3   Test Matrix

It was decided that the precast and CIP specimens would be tested together in pairs at the same equivalent target shear stress level. Each of the specimens was classified with a letter P or C, followed by a number, describing the type of specimen and the equivalent target stress range at which it was cycled. Six target stress ranges were established for testing as shown in the test matrix in Table 3-3. The first column in this table lists the target stress range in Stud Pairs 1 and 2. The second column provides the resultant stress for Stud Pairs 3 through 12, which is simply the target stress range divided by three. The third and fourth columns list the specimen names for the stress levels, comprising of one precast and one CIP beam. The fifth and last column provides the factor applied to the variable amplitude load history to hit the target stress range.

Table 3-3: Test Program Matrix

Eq. Stud Shear Stress (MPa)		Specimen Name		Modified Scale Factor
Studs 1-2 (Target)	Studs 3-12 (Target/3)	Precast	Cast-in-Place	
67	22	P067	C067	13.4%
100	33	P100	C100	20.0%
120	40	P120	C120	24.0%
140	47	P140	C140	28.0%
200	67	P200	C200	40.1%
300	100	P300	C300	60.1%

The peak load range in each variable amplitude loading history occurs once every 1,024 cycles and is approximately twice the magnitude of the equivalent load range. This implies that the peak

46

stress range in each segment would induce a stress two times higher than the equivalent (target) stress range. Therefore, the target stress ranges 200 and 300 MPa will result in a cyclic maximum stress range of 400 and 600 MPa, respectively, effectively yielding the connection. Testing at this high load level was undertaken for two reasons: 1) to help establish the slope of the S-N curve, and 2) to allow a relatively short test to be performed until a large number of studs had failed, in order to study the change in specimen failure after each stud failure.

3.3   Instrumentation

One challenge that the research team was presented with was developing an instrumentation approach that would both quantitatively and qualitatively describe the progression of stud failures during cyclic loading. The goal was to accurately capture this progression of stud failures and to determine the number of cycles to failure as accurately as possible, so that stress versus life (S-N) results could be plotted and compared to test data from previous studies. Complications arose from the fact that the studs cannot be instrumented directly in a way that doesn't either result in premature instrumentation damage during loading or altering the shear connector properties themselves. The fact that the stud is encased in concrete or grout also eliminates the possibility of visual inspection during the fatigue testing. To overcome this difficult task, several instrumentation methods were tried, including: applying strain gauges to the underside of the top flange directly under each stud, capturing a strain profile at discrete locations, and measuring interfacial slip between the slab and steel flange.

Several modifications were made to the instrumentation layout over the course of testing. As the data was analyzed, it was found that some of the techniques were redundant or did not provide any sufficient or conclusive data. As a result, the research team discontinued the use of these data channels and replaced them with gauges at other locations of possible interest. All of these changes occurred to the strain profiles and gauges located under the studs, while the slip and deflection transducers were left unchanged. This process was repeated until the instrumentation layout was established for the fifth specimen, which remained consistent with the subsequent specimens. This layout will be referred to henceforth as the general layout (Figure 3-1) and will be discussed exclusively in the remainder of this section, while the details regarding the modifications to the preliminary layouts are provided in Section 3.3.1.

Capturing the change in local strain under the stud provided a means of determining the time of fatigue crack initiation and subsequent stud failure. The measured strain is induced by the local distortion of the top flange due to the horizontal force resisted by the stud. Since the placement of these gauges largely affected the magnitude of the strain readings, only the general trend of the data was used in formulating the failure criterion, which was then used to determine the number of cycles to failure for each stud. Specifically, it was observed that the strains due to the local distortion of the top flange caused by the stud were seen to increase during fatigue cycling up until they reached a peak, after which they decreased. The number of cycles at which the peak strain occurred was then assumed to be the number of cycles to failure. This is a similar instrumentation approach taken by King et al. (1965). One of the secondary objectives of this research was to determine the accuracy of this instrumentation method and to confirm that these peaks in the local strain data correspond to a stud failure by autopsying the specimens after testing. The gauges were installed directly beneath the studs 50 mm or 69 mm from the outside edge of the flange for the CIP and precast members, respectively. An example illustrating the placement of these gauges on a precast specimen is shown in Figure 3-6.
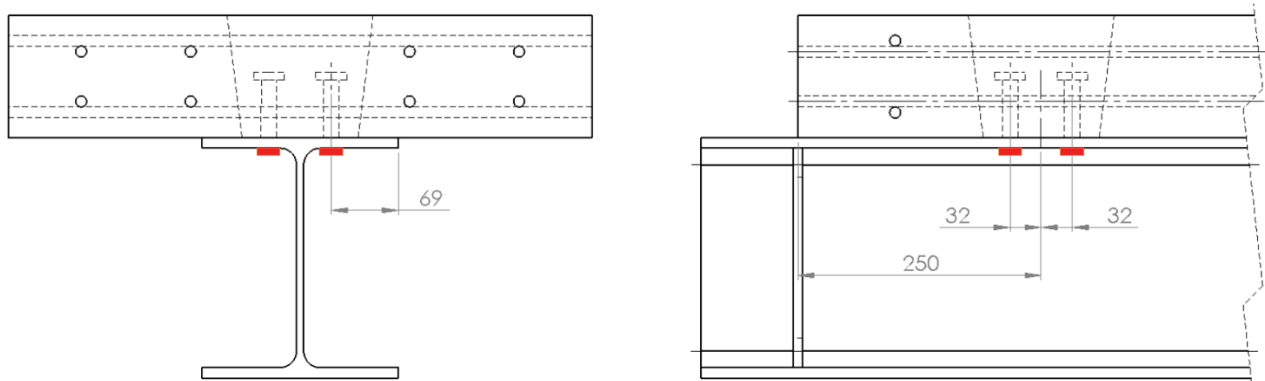
Figure 3-6: Example locations of the local distortion gauges for a precast specimen (N1, N2, S1, and S2).

Strain profiles were measured between shear pockets locations at Sections A, B, Y, and Z. By measuring the strain on the underside of the top and bottom flanges respectively, it is possible to calculate the horizontal axial force in the slab being transferred into the studs. It is expected that as the studs become increasingly fatigue damaged, the slab axial force should decrease and

approach zero when the studs have completely sheared off. This data provides information on the actual stress experienced by the studs over time and offers insight on the redistribution of stresses over the specimen's fatigue life. The 10 mm strain gauges were installed on a single side, measuring 69 mm from the edge of the flanges as illustrated in Figure 3-7.
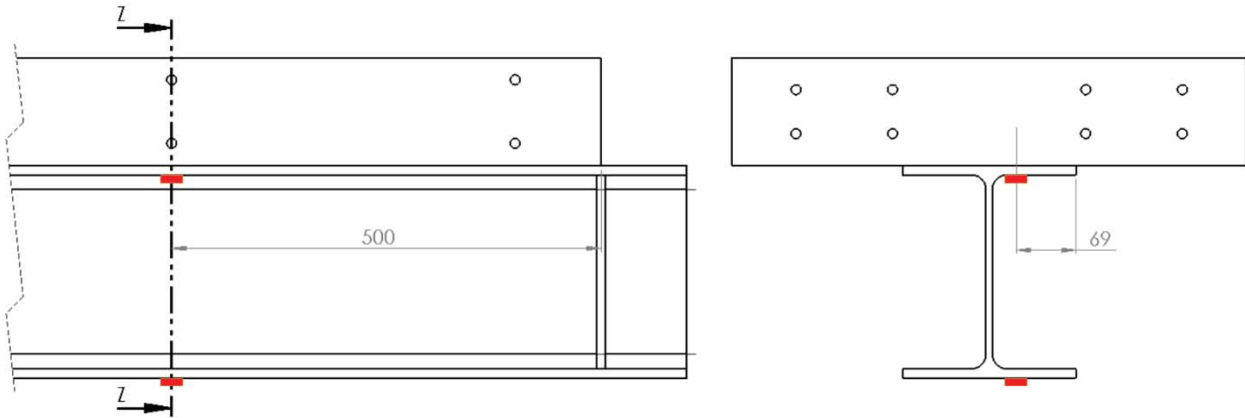
Figure 3-7: Example strain profile at Profile Z for both the precast and CIP specimens.

To capture the interfacial slip behaviour of the beams during fatigue testing, a set of 5 linear voltage displacement transducers (LVDTs) with a stroke of 10 mm were positioned at each of the beam's ends (W and E) and at profiles A, B, and Y. An additional LVDT (75 mm stroke) was positioned 1300 mm from the west support at the underside of the bottom flange to measure the maximum vertical deflection.

Additionally, a standard 10 mm strain gauge was installed on a steel plate and set beside the specimen to serve as a temperature control. If there was any fluctuation in temperature affecting the strain gauge results, it could thus be observed and the data could be corrected appropriately. Since only the trend of the local distortion gauge data, and not the actual magnitudes were used to identify stud failures, the effect of temperature on these gauges was not important. The profile gauges, however, may be affected by the influence of a temperature fluctuation.

3.3.1 Instrumentation Modifications

Many modifications to the instrumentation setup were implemented throughout the experimental program. To help summarize these modifications, Appendix B provides a chart that identifies all the locations instrumented for each beam. Note that Profile E, which has yet to be discussed and is located 250 mm from the West support, was removed after the fourth test on Specimen P200. The equipment that did not change throughout the experimental program included the interfacial slip and the maximum deflection LVDTs. The following list summarizes the other modifications made in each successive test in chronological order:

1. C140: The first beam specimen tested had local distortion gauges only installed at N1 and S1, and with seven strain gauges at Profiles E and B. The profiles included gauges located at the top of the concrete, top longitudinal reinforcing bar, bottom longitudinal reinforcing bar, bottom of concrete, underside of the top flange, mid-height of the web, and on the underside of the bottom flange.

2. P140: Local distortion gauges were added in the second beam test to Stud Pairs 2, 3, and 4. Gauges were also added to the top and bottom of the concrete at Profile A.

3. C200: The only change to the third beam included the substitution of the web mid-height strain gauge located at Profile E for a temperature control gauge.

4. P200: The fourth beam was overhauled with the removal of the two reinforcement strain gauges and the bottom of concrete gauges at Profile E, the removal of the bottom of concrete gauge at Profile B, and the installation of gauges to Profiles A, Y, and Z on the undersides of both the top and bottom flanges.

5. C300: The fifth beam tested had the rest of the gauges on Profile E removed (top of concrete and two steel gauges), as well as the top of concrete, top reinforcement bar, bottom reinforcement bar, and web mid-height gauge at Profile B. Local distortion gauges under Stud Pairs 9 through 12 were then installed.

6. P300: Stud Pairs 5 through 8 were additionally instrumented, with the exception of N7.

7. C100: No changes to the instrumentation were made.

8. P100: Slip 3 was removed.

9. C120: The strain gauges under Stud Pairs 5 through 8 were removed.

10. P120: No changes to the instrumentation were made

11. C067: The strain gauges under Stud Pairs 4, 9, 10 and 11 were removed.

12. P067: No changes to the instrumentation were made

3.4 Specimen Fabrication

This section provides information pertaining to the methodology employed in the fabrication of the composite beam specimens. Specifically, it outlines how the steel beams were prepared prior to casting, it explains the processes followed for the reinforcement and formwork assembly, and it provides information on the concrete casting and pocket grouting.

3.4.1 Steel Beam Preparation

Once the twelve 3200 mm W250x49 steel beams were delivered to the University of Waterloo, they were sent to the Engineering Machine Shop for fabrication. The fabrication work included drilling holes through the top flange and welding web stiffeners at the support locations. The holes drilled through the top flange were 21 mm diameter in size and provided locations in which hoisting equipment could be attached. A total of four holes were drilled into each beam – two at each beam end. The web stiffeners were fabricated from a 10 mm thick plate and welded to the beam at 100 mm from each end utilizing a 6 mm fillet weld.

A local metal fabricator, Ball Service Group Inc., completed the stud welding for the research group utilizing their own in house drawn arc stud welding equipment. The procedure followed the Metal Arc Welding provisions specified in Appendix H of the CAN/CSA W59 Code (CSA W59, 2013). A total of 24 Nelson Studs were welded to each of the specimens. For the CIP specimens, the studs were welded continuously along the top flange, spaced at 250 mm from one another. The precast specimens, however, utilized stud clusters spaced at 500 mm, with each cluster consisting of four studs, spaced 64 mm from one another in a rectangular pattern. The CIP and precast specimen weldments are both depicted on the left and right, respectively, in Figure 3-8. As a matter of standard practice, several studs were welded to a separate steel plate and bent over with a hammer to display the quality of the weld and ductility of the stud's material. This bend test is shown in Figure 3-9. Further fabrication details are provided in Appendix A.

51

Figure 3-8: Fabrication photos of the CIP and precast steel beams (left and right).

Figure 3-9: A stud after welding (left), and two studs that passed the bend test (right).

3.4.2 Formwork Construction

The specimens were cast in two batches, resulting in three CIP and three precast formwork assemblies being recycled for each cast. The general dimensions of both the CIP and precast slabs are 125 mm deep, 600 mm wide, and 3000 mm in length. The formwork was constructed utilizing a special 19 mm thick formply, which had once face manufactured to provide a smooth concrete finish. The CIP formwork was constructed around the steel beams, which laid flat on the foundation slab. This represented a shored construction method and was chosen due to its simplicity. It was predetermined by the research group that a non-shored construction method would not affect the experimental results substantially. Thus, the formwork needed to be elevated by the height of the beam (247 mm) to align with the top surface of the top flange. This shoring technique was completed utilizing standard 2" x 4" lumber that were cut to the required lengths. The precast slab formwork was laid flat on the ground and included wooden blockouts, which formed the pockets. The blockouts were tapered to have a square outside dimension of 120 mm that increased to 150 mm, resulting in approximately a 7º sloped shear key. Photographs of the formwork are provided in Figure 3-10 and Figure 3-11.

10M reinforcing bars were assembled to form the upper and lower rebar mats used in the slabs. Both the CIP and precast rebar mats were constructed with four 3000 mm longitudinal bars spaced at 170 mm on-center, and seven 600 mm transverse bars spaced at 500 mm on-center. These dimensions may have been altered slightly during construction for clearance and constructability purposes. The reinforcing steel cages were prepared off to the side and placed into the forms. Metal wire ties were used to keep the cages intact and ensure the bars did not migrate during concrete placement and vibration.

The initial instrumentation layout called for strain measurements along to top and bottom longitudinal bars at Profile E and B. As discussed previously, these strains were not recorded after the fourth test, as strains at other areas of interest were measured instead. Nonetheless, each beam was constructed with these four strain gauges applied to the longitudinal rebar. First, the location of application was ground down utilizing a pneumatic belt sander. The surface was then prepared as per the gauge manufacturer's instructions and the gauges were then applied. A buthyl rubber

product (SB Tape) was applied over the gauges, which were then wrapped with electrical tape. This barrier provided the necessary moisture and mechanical protection for the subsequent concrete casting. The wires leading off the gauges were threaded through polyethylene tubing (providing wire protection) and supported upwards in a vertical position. Photographs of this procedure are provided in Figure 3-12 and Figure 3-13.

Figure 3-10: Formwork for the precast (left) and CIP (right) specimens.

Figure 3-11: The precast formwork laid flat on the ground, while the CIP formwork was shored.

Figure 3-12: Longitudinal reinforcement strain gauge application.

Figure 3-13: Top and bottom longitudinal reinforcement strain gauges prepared with a protective coating of rubber SB tape and electrical tape. Also included is the tubing providing the wire protection.

3.4.3 Concrete Casting

Prior to casting, form oil was applied to all exposed edges. The concrete casting took place in two batches, with each cast resulting in three precast and three CIP concrete slabs. The concrete utilized for the slabs was provided by the local ready-mix supplier, Hogg Concrete, and was designed to have a 28-day strength of 40 MPa. Upon delivery, a standard slump test revealed that the concrete had approximately a 130 mm [5"] slump for the first cast, depicted in Figure 3-14. The second cast had a slump of 180 mm [7"], satisfying standard specifications. The concrete mix was also designed to have 5-8% air entrainment, satisfying the standard practice for Canadian bridges. Unfortunately, the research team was unable to measure the air entrainment in the mix because the testing equipment was sent for service at the time of the pour. Nonetheless, this information was insignificant for the purpose of the planned experimental testing. Approximately 20 cylinders were prepared for each cast to test throughout the curing process, and to determine the strength of the concrete before each fatigue test was initiated. The cylinder strengths were tested in the laboratory and the results are provided in Appendix C. The 28-day strengths for Cast 1 and Cast 2 were 43 MPa and 36 MPa, respectively.

The concrete was placed directly into the forms using a conveyor belt and vibrated to mitigate any honeycombing. The slabs were screeded to provide a level height of 125 mm, a magnesium float was used to smooth out the top surface of the concrete, and the final finish on the top of the concrete slabs was completed with a trowel tool. Additionally, embedded hoisting anchors were vibrated into two opposite corners of the precast slabs so that they could be maneuvered and lifted after casting, as identified in Figure 3-16.

The concrete was moist cured for 7 days by covering the slabs with water saturated burlap and a high-density polyethylene (HDPE) tarp. 28 days after the concrete was cured, the formwork was stripped and the beams were stacked.

Figure 3-14: 100 mm [4"] slump test results (first cast).

Figure 3-15: Concrete placement into a CIP specimen.
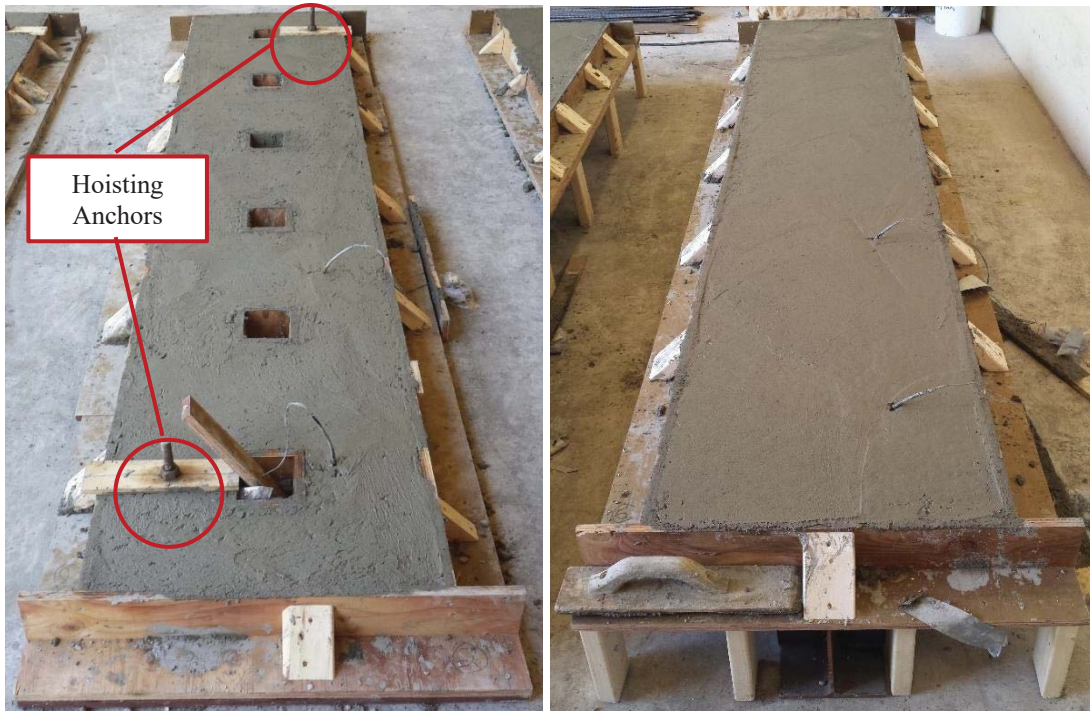
Figure 3-16: Trowel finished precast (left) and CIP (right) slabs prior to moist curing.

Figure 3-17: After 28 days the formwork was stripped from the slabs.

3.4.4   Stud Pocket Grouting

To establish the shear connection in the precast specimens, a high-performance, high-early strength, low shrinkage, pre-packaged concrete material provided by King Construction Products was utilized. The HP-S10 rapid hardening concrete product has been specified by the MTO for the application of infill strips and shear key pockets in prefabricated bridges. The product has a 12-hour and 28-day compressive strength of 20 MPa and 60 MPa, respectively.

The six steel beams were placed flat on the foundation slab and the precast slabs were hoisted and positioned on top as shown in Figure 3-18. The slabs were then carefully aligned to ensure symmetry about the beam's longitudinal and transverse centerlines. A total of five grout batches were mixed in a small-scale mechanical mixer. One batch consisted of two bags of premixed concrete and filled approximately eight pockets. Thus, most of the precast specimen were constructed with two different batches of grout. A total number of 20 cylinders were also cast, consisting of 4 cylinders per batch. The 4 and 28-day compressive strengths of the cylinders was found to be 45 and 57 MPa.
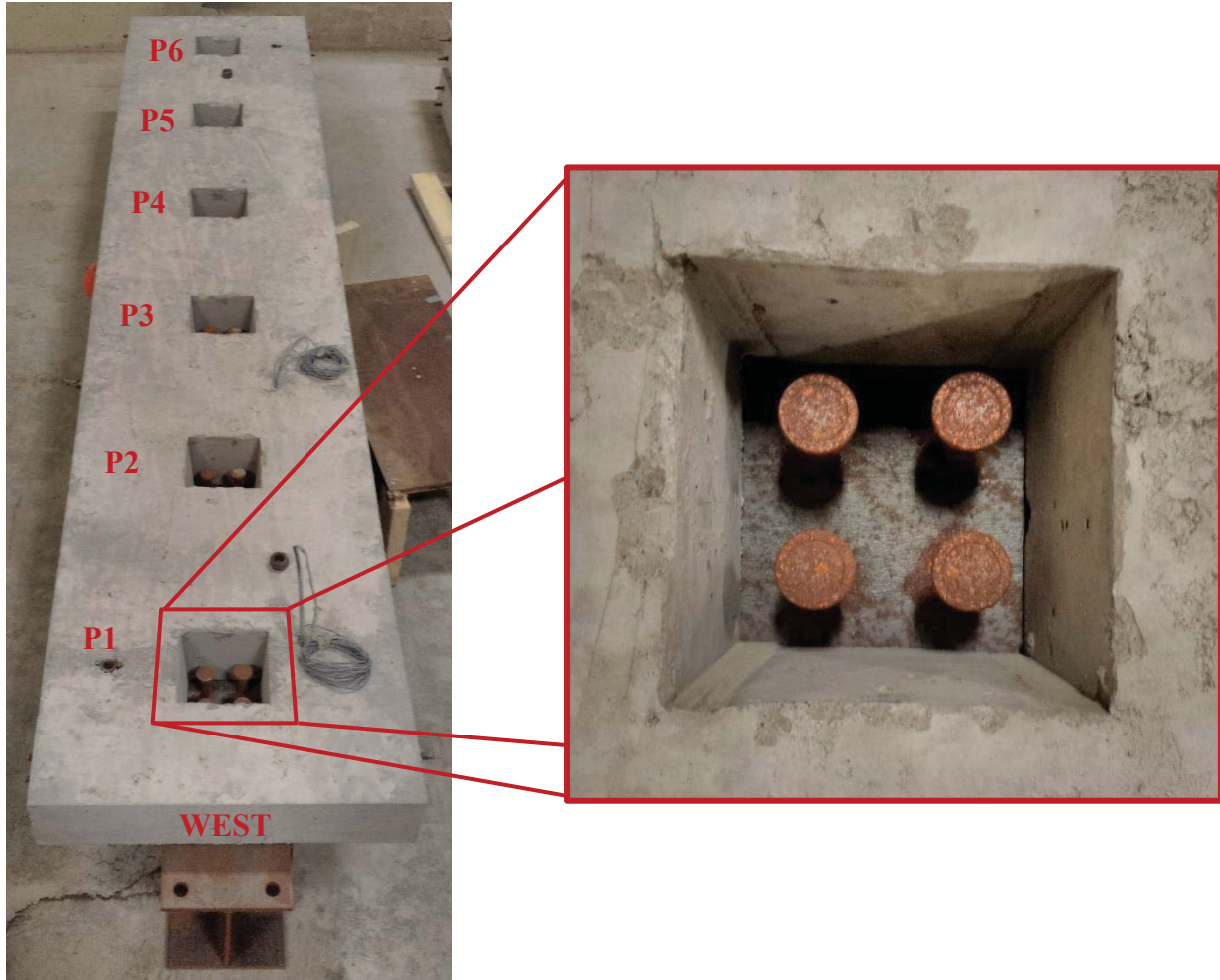
Figure 3-18: Precast slab positioned on top of the steel beam prior to grouting and establishing the shear connection.

Figure 3-19: Completed specimens: CIP (left), precast (right).

3.5 Laboratory Testing Frame and Data Acquisition

The laboratory frame and setup depicted in Figure 3-20 was utilized for the testing of the beam specimens. The testing frame utilizes a unidirectional hydraulic actuator that has a maximum capacity of 500 kN. The actuator is equipped with a load cell to measure the applied force and a LVDT to measure stroke. A spreader beam was attached to the bottom of the load cell to disperse the force between the two loading points equally. The loading points consisted of two pin connectors and a 2 mm thick neoprene pad. The neoprene pads ensured an equal force distribution over the loading point in the case of an uneven concrete surface.

Figure 3-20: Laboratory testing frame and setup.

The beams were simply supported on top of two pedestals located at the west and east ends. The support conditions consisted of two rollers and the pedestals were anchored into the foundation slab with bolts. To keep the roller supports from migrating during the fatigue testing, 25 mm thick backing plates were bolted into the top of the pedestals. Threaded rods were screwed vertically into the backing plates, which provided transverse migration control.

61

The actuator hydraulics were controlled by a Shore Western computer control system. The modified variable amplitude loading history discussed in Section 3.2.1 was uploaded to the system, and was then augmented according to the target shear stresses for each of the specimens. The data acquisition (DAQ) for both the fatigue and static testing was run off of a LabVIEW system design software by National Instruments. For the fatigue testing, data was recorded using peak detection algorithms. Whenever the software would detect a peak in the load, the data was collected and stored in a file. Afterwards, MATLAB and Excel were used to reduce and compile the data collected. The MATLAB program is discussed in further detail in Section 4.2.

4 Experimental Results

Chapter 4 reports the experimental results of the static and fatigue testing program. The static data presented in Section 4.1 includes the load-deflection behaviour, interfacial slip, and strain profile plots. The fatigue testing results in Section 4.2 present the change in deflection, interfacial slip, and local distortion data throughout the experimental fatigue program. Lastly, the autopsy program is presented in Section 4.3, including an investigation into the methodology of accurately confirming fatigue failures.

4.1 Static Testing Results

As described in Section 3.2.2, static loading cycles were performed prior to fatigue testing (referred throughout the rest of the chapter as 0%), and at the 100% and 1000% theoretical fatigue lives for each of the specimens to assess the effect of fatigue loading on the response of the beams. If the specimen fatigue life exceeded 1000% of their predicted life, an additional static load test was completed at the end of the fatigue testing. If the 1000% milestone was not reached, the final static test was completed at the conclusion of fatigue testing. Table 4-1 summarizes the timing of the static tests for each of the specimens throughout their respective fatigue lives. For comparison purposes, a load of 200 kN was selected as the standard static applied load for each specimen, corresponding to two 100 kN point loads applied at x = 500 mm and 1000 mm from the west support (Figure 3-4). The static loading resulted in a maximum transverse shear force of 150 kN (from x = 0 to 500 mm) and maximum bending moment of 100 kNm (at x = 1000 mm). Additionally, it was found during preliminary analysis that the maximum deflection occurred at approximately x = 1300 mm from the west support.

The measured static load-deflection and strain profile plots have been supplemented by including the theoretical behaviour for each specimen on the respective plots for the purpose of confirming and comparing the test results. The predicted behaviour was based on an elastic transformed section analysis of the composite section under several assumptions:

- The transformed section moment of inertia about the bending axis was calculated based on the assumption of strain continuity at the interface, implying full composite interaction.
- The moment of inertia includes the longitudinal reinforcement in the slab.

63

• The concrete slab is reduced in width by the modular ratio, n.

Table 4-1: Summary of when the static tests were completed for each specimen.

Specimen	Eq. Stress Range (MPa)	Theoretical Fatigue Life	Completed Static Tests			
C067	67	2,397,236	0%	100%	-	-
P067	67	2,397,236	0%	100%	-	-
C100	100	721,000	0%	100%	1000%	1300%
P100	100	721,000	0%	100%	1000%	-
C120	120	417,245	0%	100%	1000%	-
P120	120	417,245	0%	100%	1000%	-
C140	140	262,755	0%	100%	1000%	-
P140	140	262,755	0%	100%	1000%	-
C200	200	90,125	0%	100%	1000%	2000%
P200	200	90,125	0%	100%	1000%	-
C300	300	26,704	0%	100%	1000%	3000%
P300	300	26,704	0%	100%	1000%	3700%

The transformed section properties of the composite beams (based on the geometry detailed in Section 3.1) are summarized in Table 4-2, which includes the modular ratio, n, the transformed section centroid, y, transformed moment of inertia, I_t, transformed section modulus, S_t, and the first moment of area for the slab, Q.

Table 4-2: Transformed cross sectional properties

Modular Ratio	n	7.2
Centroid from Top	y (mm)	129.1
Transformed Moment of Inertia	I_t (mm^4)	2.23E+08
Transformed Section Modulus	S_t (mm^3)	9.19E+05
Moment of Area	Q (mm^3)	6.93E+05

The preceding calculations are based on the assumption of full composite behaviour of the section. In order to facilitate a full composite connection, it was determined that a total of 48 headed studs are required on each specimen when assuming a symmetrical applied loading pattern. Given that each of the specimens were fabricated with 24 headed studs suggests the composite beams utilized in the research program are in fact partially connected. Thus the specimens will demonstrate a load-deflection response that is less stiff than the full shear connection case (assuming full connection corresponds to full interaction). Therefore, the calculated bending stiffness based on full composite action must be modified to obtain a better estimation of the predicted composite

beam behaviour. This modification utilizes a provision for partial shear connection found in the Code requirements for steel buildings, CAN/CSA S16 (2014), as given by Equation 4-1. This provision provides an effective transformed moment of inertia, I_e, as a function of the degree of shear connectivity, p, transformed moment of inertia, I_t, and moment of inertia for the steel section alone, I_s.

$$I_e = I_s + 0.85 p^{0.25} (I_t - I_s) \qquad (4\text{-}1)$$

The degree of shear connectivity, p, has been defined previously in Section 2.1.3 (Equation 2-1) and the shear span is normally determined as the distance from zero to maximum moment. In a symmetrical and typical load case, this results in a shear span of L/2 (1500 mm), and a 50% degree of shear connection. However, due to the offset loading used in this experimental program, the governing shear span is reduced to 1000 mm, resulting in a 33% shear connection. Thus the modified moment of inertia for a 33% shear connected specimen is $I_e = 1.69 \cdot 10^8$ mm^4 corresponding to a flexural stiffness reduction of 25%.

4.1.1 Static Load-Deflection Results

The static load-deflection results (deflection measured at x = 1300 mm) have been plotted for each of the beam specimens in Appendix E1. Each plot compares the response at 0%, 100%, and the other subsequent static tests such that the change in stiffness over the course of the fatigue loading can be observed. Additionally, the predicted load-deflection response for a composite beam with full interaction, 33% shear connection, and a steel beam alone are overlaid onto the plots for comparison purposes. Due to the shear dominated loading pattern, the theoretical deflection responses also include for shear deformation. The deflection due to shear deformation was determined by applying the principal of virtual work on an elastic transformed section. As a result, the shear deformation was determined to account for 8%, 6%, and 13% of the total deflection for the full interaction, 33% partial shear connection, and steel beam only cases, respectively.

Sample plots are provided in Figures 4-1 through Figure 4-4 and include the load-deflection results from Specimens C140, P140, C300, and P300. The red, blue, and green dashed lines correspond to the 0%, 100%, and 1000% static tests, respectively. An additional dashed orange line can be found in the C300 and P300 test results and corresponds to the 3000% and 3700% static tests, respectively. For the C140 and P140 specimens, the beam stiffness did not change throughout the

fatigue testing. However, the load-deflection trends for the C300 and P300 specimens did display a significant decrease in stiffness over the course of fatigue loading. It is interesting to note that the response of Specimens C300 and P300 at 3000% and 3700%, respectively, did not behave in a linear fashion. First, the stiffness was similar to a steel beam during the initial loading phase, and increased in stiffness at an applied load of 25 kN. This type of behaviour may suggest that most of the studs have sheared off and a 25 kN load was required to engage the shear connection through mechanical action and bearing.
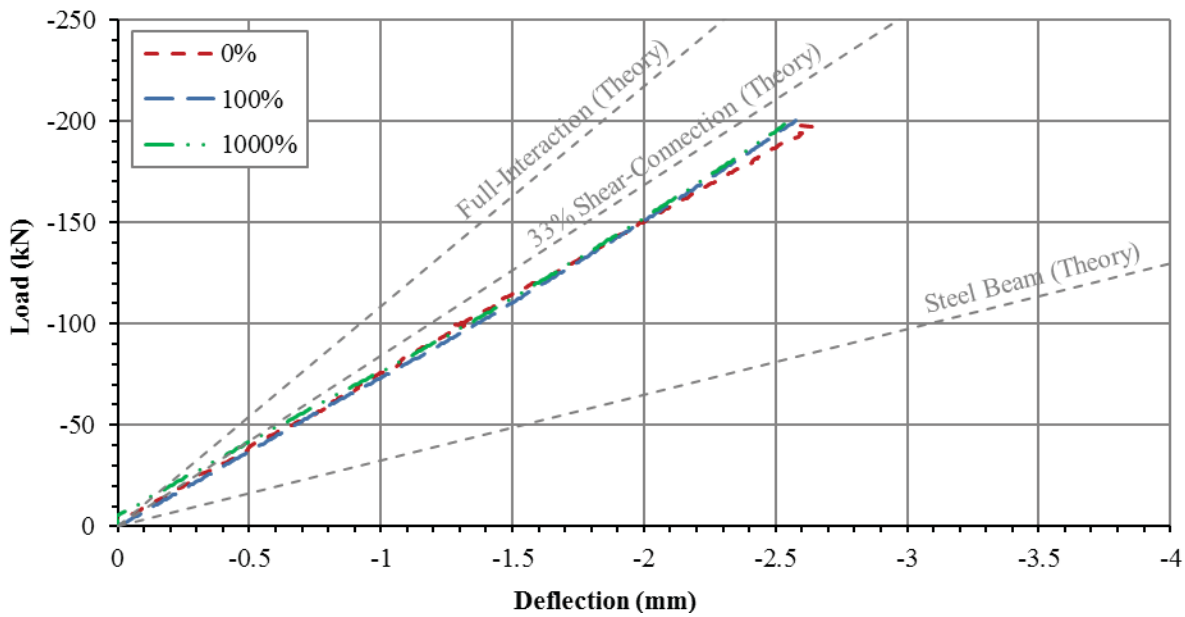
Figure 4-1: Load-deflection results for C140.

Table 4-3 provides a summary of the maximum static deflections at the 200 kN load level for each specimen at 0%, 100% and 1000% of their respective fatigue lives. Also included in the table are the differences in deflection for the 100% and 1000% in comparison to the initial static test, 0%.
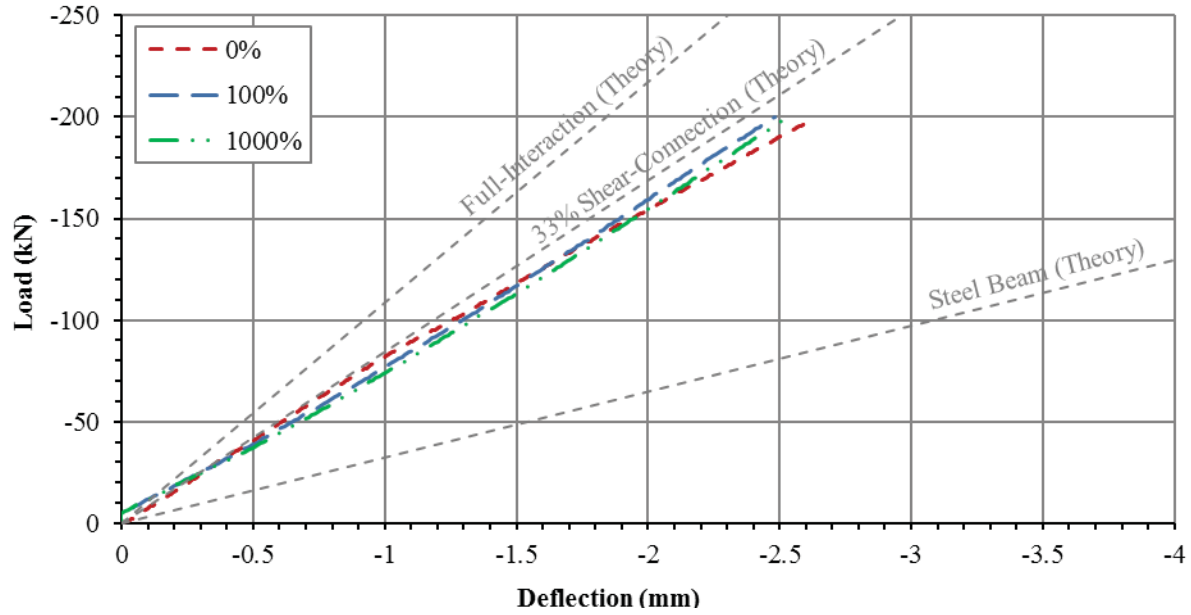
Figure 4-2: Load-deflection results for P140.
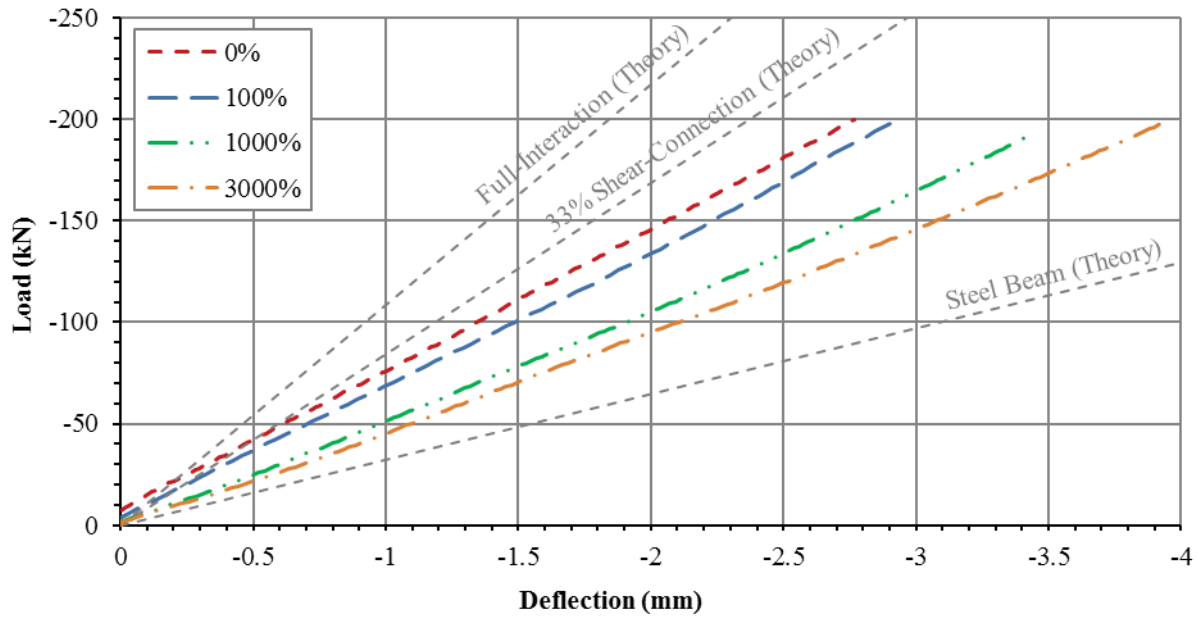
Figure 4-3: Load-Deflection Results for C300
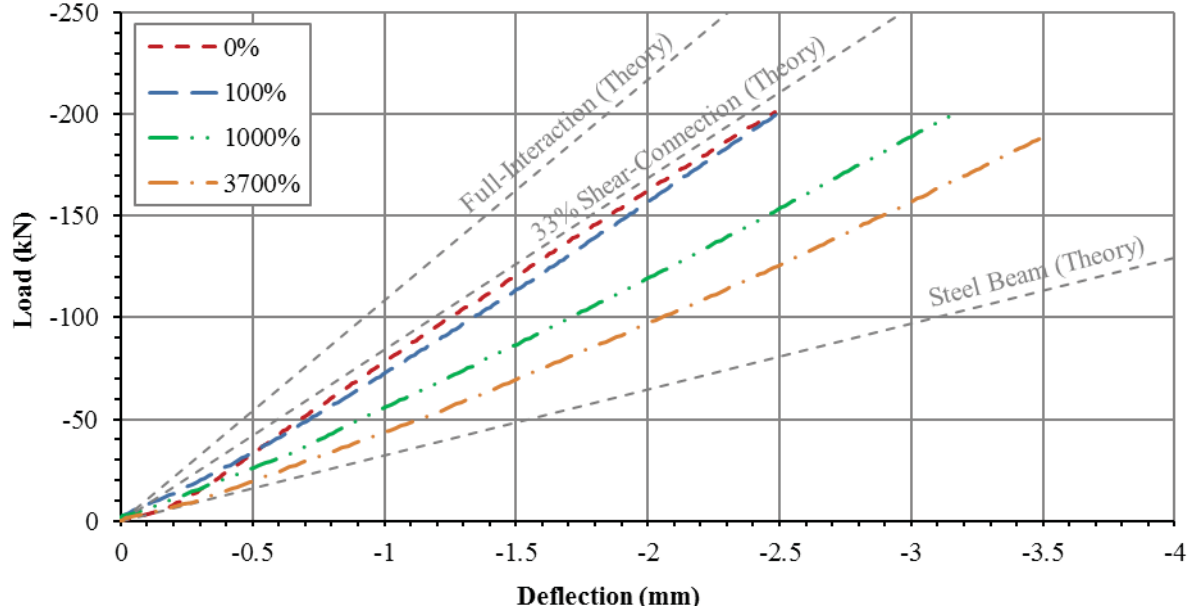
Figure 4-4: Load-deflection results for P300.

Table 4-3: Maximum Deflection Results.

Specimen	0% (mm)	100% (mm)	Change relative to 0%	1000% (mm)	Change relative to 0%
C067	-2.81	-2.45	-13%	-	-
P067	-2.77	-2.62	-5%	-	-
C100	-2.65	-2.41	-9%	-2.63	-1%
P100	-2.82	-2.54	-10%	-2.47	-12%
C120	-2.51	-2.41	-4%	-2.55	2%
P120	-2.65	-2.28	-14%	-2.32	-13%
C140	-2.62	-2.58	-2%	-2.53	-3%
P140	-2.64	-2.48	-6%	-2.54	-4%
C200	-2.64	-2.48	-6%	-2.89	10%
P200	-2.60	-2.72	5%	-2.94	13%
C300	-2.77	-2.93	6%	-3.41	23%
P300	-2.48	-2.49	0%	-3.15	27%
Average	-2.66				
Theory	-2.37				

The average deflection for the initial static testing was observed to be 2.66 mm for both the CIP and precast specimens. The theoretical deflection, including shear deformation, was calculated to be 2.37 mm, corresponding to a 12% difference from the initially observed data. A statistical

68

Student's t-test was performed on the initial CIP and precast deflection data set to determine whether the two are likely to have come from the same two underlying populations containing the same mean. Specifically, the test provides the likelihood that there is no difference between the initial CIP and precast deflection behaviour. The calculation was completed assuming a two-tailed distribution and homoscedasticity, resulting in a 94% probability.

Nine of the deflections observed at the 100% life and five of the deflections observed at the 1000% life were found to be smaller in magnitude than observed initially (i.e., at 0%), demonstrating a stiffer load-deflection response after fatigue loading. The stiffer static load response after fatigue loading may be due to several factures unrelated to actual specimen behaviour, including LVDT zeroing errors, possible migration of the LVDT core on the bottom flange, deterioration of the neoprene pads, or the wearing out of the rollers over the course of repeated loading.

An increase in deflection was observed in both the CIP and precast specimens at the 200 MPa and 300 MPa equivalent stress levels at the 1000% static tests. The C200, P200, C300, and P300 specimens exhibited a deflection that was 10%, 13%, 23% and 27% larger than the initial tests, respectively.

It was hypothesized that the deflection would increase over the onset of fatigue loading for all specimens. This assumption was formed on the basis of the shear connectors becoming less stiff due to fatigue cracking. As the fatigue cracks propagate and the connected area between the flange and the studs decrease, the degree of shear connection and shear interaction also decreases. The end result is an increased deflection due to an increase in beam curvature.

The results display a negligible increase in deflection for specimens that experienced an equivalent stress range of 67 MPa to 140 MPa. The specimens experiencing a 200 MPa or 300 MPa equivalent stress range did, however, experience a significant increase in deflection. It is important to note that these equivalent stress ranges are applied to only Stud Pairs 1 and 2 which make up 16.7% of the entire shear connection. The remaining Stud Pairs 3 to 12 are considered throughout the thesis as the secondary studs and experience an equivalent stress that is three times less than the primary studs. Due to the non-linearity of the log-log relationship between stress range and number of

69

cycles to failure the secondary studs in the 67MPa to 140 MPa loaded specimens experienced significantly less fatigue damage. Additionally, if any of the applied stress ranges were lower than the constant amplitude fatigue limit of 48 MPa, the studs theoretically received no fatigue damage for the given cycle.

4.1.2 Interfacial Slip

Interfacial slip data were recorded at five locations along the longitudinal axis of the beams, labelled as Slip 1 through 5 and located at x = 0, 500, 1000, 2000, and 3000 mm from the west support. The data are presented for all specimens in Appendix E2 in the form of load-slip and interfacial slip profiles plots. Representative results are shown for Specimen P140 in Figures 4-5 and Figure 4-6. In both figures, the 0%, 100%, and 1000% static tests are represented by the dashed red, blue, and green lines, respectively. The sign convention adopted for the load-slip and interfacial slip plots is positive when the slab slips to the west, and negative when the slab slips to the east, relative to the steel flange.

The initial static data illustrated in Figure 4-5 displays two types of nonlinear behaviour. The first is clearly demonstrated by Slip 1, Slip 2 and Slip 5 with trends that are negative in curvature, or concave down. The second is shown in Slip 4 and Slip 5 which demonstrate a tri-linear and bi-linear trend, respectively. The discontinuities likely occur due to the chemical bond breaking between the concrete and steel at the interface, resulting in a change in stiffness. From Slip 4 and Slip 5, it is evident that the load at which the breaks was approximately 85 kN.

Once the specimens experienced fatigue loading, changes in the load-lip behaviour became pronounced. Slip 1, Slip 2, and Slip 5 all demonstrated a trend that was positive in curvature (concave up) and resulted in interfacial slip values that were larger in magnitude compared to the initial static behavior (i.e., at 0%). It is hypothesized that the change in curvature is associated with concrete damage around the weld of the stud due to fatigue loading, allowing for more slip and resulting in an initial reduction in stiffness followed by stiffening once the concrete bearing on the stud is re-engaged.

Similar trends in the load-slip data are exhibited by the other test specimens, with Slip 1 experiencing the largest amount of slip. Since the longitudinal shear force was three times larger at the west support than the rest of the beam, Slip 1 saw the most dramatic changes in slip due to the fatigue damage. The recorded Slip 3 slip values were approximately zero which corresponds to the correct behaviour expected at the location of maximum moment. The 100% static tests results were similar to the initial results, however, once the specimens experienced significant fatigue damage (i.e., at 1000% of the predicted fatigue life), the slip increased noticeably. The direction in which Slip 3 began to slip as the number of load cycles increased was variable and not consistent throughout the specimen data. Both Slip 4 and Slip 5 appear to be good indicators of the force required to break the chemical bond between the concrete and the steel at the interface.

The interfacial slip profile for P140, plotted in Figure 4-6, represents the slip values recorded at the peak static load of 200 kN. Table 4-4 summarizes the results for Slip 1 (x = 0, west end of beam) for all of the specimens at the 0%, 100%, and 1000% tests, and also includes the slip increase compared to the 0% slip value. The interfacial slip profiles for the other specimens are found in Appendix E2, which also includes the summary tables for each slip location, similar to Table 4-4.

When considering the 0% slip values in Table 4-4, the average values for the CIP and precast specimens are 0.136 mm and 0.135 mm, respectively. A statistical Student's t-test was performed on the CIP and precast data set to determine whether the two are likely to have come from the same two underlying populations containing the same mean Specifically, the test provides the likelihood that there is no difference between the initial CIP and precast Slip 1 behaviour. The calculation was completed assuming a two-tailed distribution and homoscedasticity, resulting in a 97% probability.
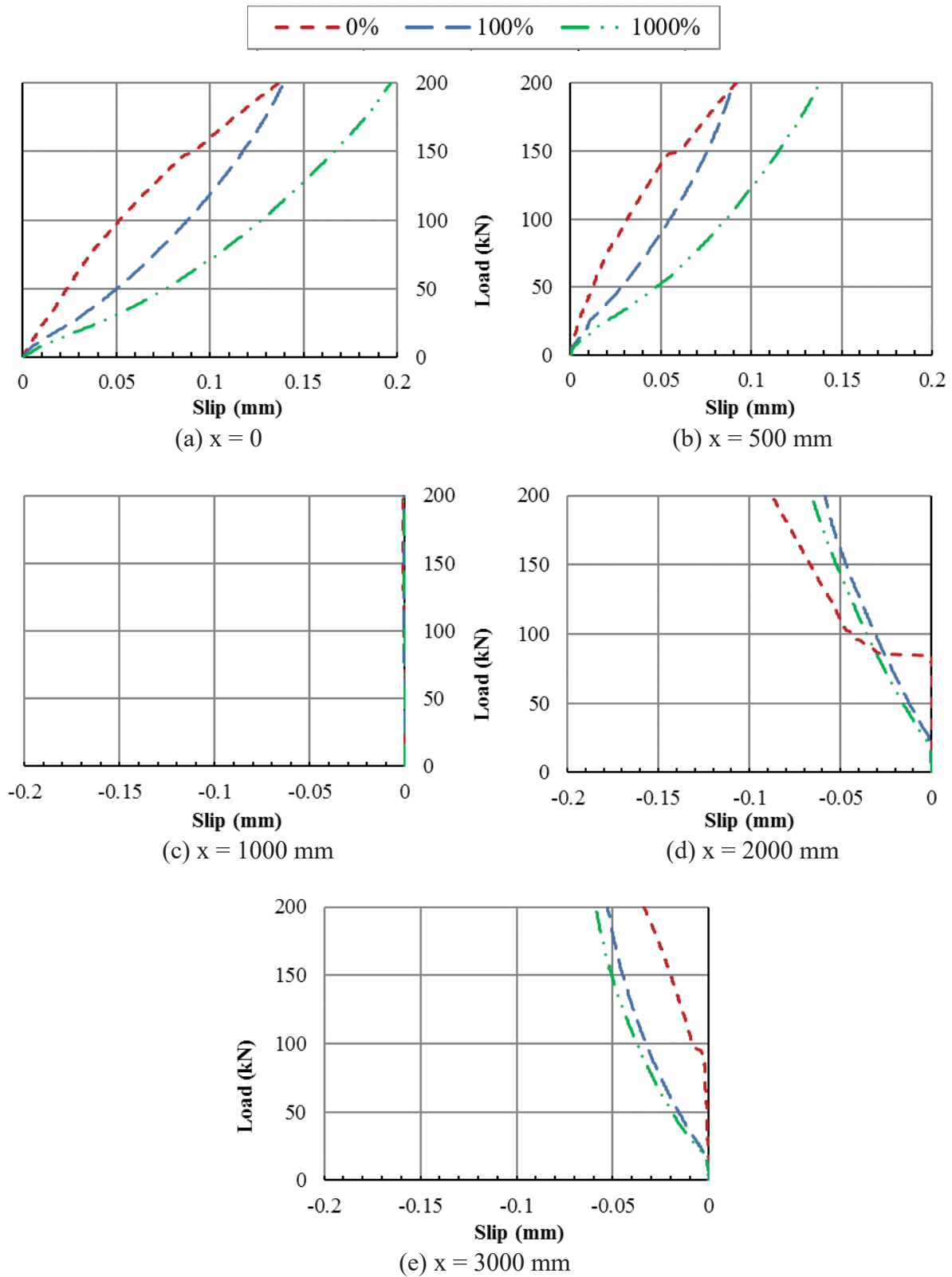
Figure 4-5: Load-slip plots for (a) Slip 1 through (e) Slip 5 for Specimen P140. Note: positive when the slab slips to the west, and negative when the slab slips to the east, relative to the steel flange.
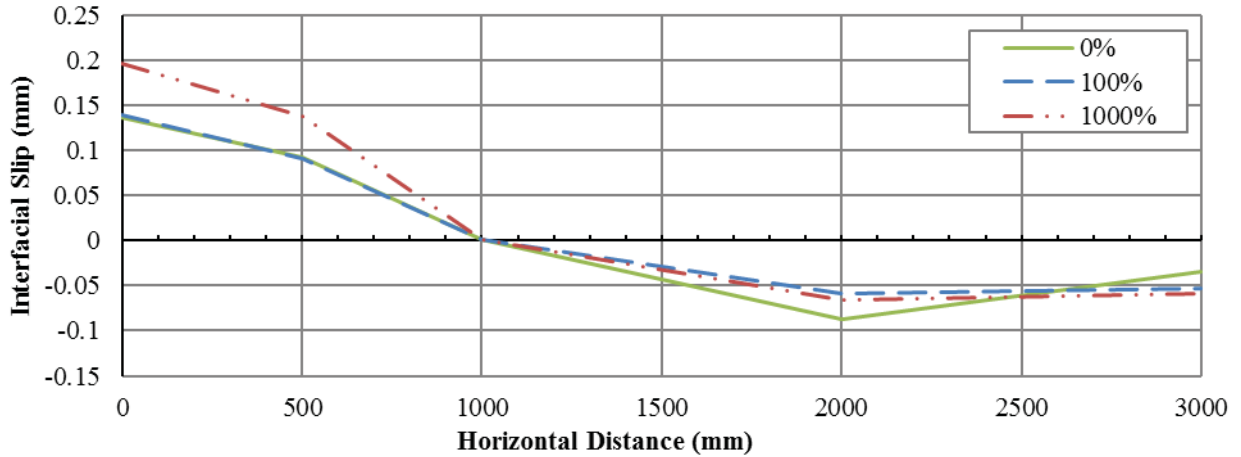
Figure 4-6: Interfacial slip profile for Specimen P140 at an applied load of P = 200 kN. Note: positive when the slab slips to the west, and negative when the slab slips to the east, relative to the steel flange.

Table 4-4: West End Slip 1 Results (P = 200 kN).

Specimen	0% (mm)	100% (mm)	100% Change relative to 0%	1000% (mm)	1000% Change relative to 0%
C067	0.153	0.163	7%	-	-
P067	0.155	0.133	-14%	-	-
C100	0.167	0.172	3%	0.250	50%
P100	0.153	0.141	-8%	0.194	26%
C120	0.072	0.096	33%	0.158	119%
P120	0.131	0.141	8%	0.220	68%
C140	0.158	0.183	16%	0.262	66%
P140	0.137	0.140	2%	0.197	44%
C200	0.108	0.181	67%	0.296	173%
P200	0.126	0.157	24%	0.289	129%
C300	0.158	0.289	83%	0.452	186%
P300	0.110	0.204	85%	0.744	575%
CIP Average	0.136				
Precast Average	0.135				

When comparing the slip data at the 1000% fatigue life, the precast specimens P100, P120, P140, and P200 all showed a smaller increase in slip (relative to the slip at 0%) compared to their CIP equivalents. The increase in slip is associated with the decrease in shear interaction (i.e., longitudinal shear rigidity) due to fatigue cracking. This suggests that the studs in the precast specimens experienced less fatigue damage from the cyclic loading compared to the studs in the CIP specimens, resulting in longer fatigue lives. Additional slip can be present due to damage of

73

the concrete around the studs, particularly around the weld collar. At the weld collar, the stud behaves most rigid and demonstrates little deformation in comparison to the rest of the shank when resisting the longitudinal shear forces. Due to this rigidity, more force is attracted to the area that may result in strain-softened concrete when cycled.

A hypothesis regarding why the precast specimens demonstrated less slip and fatigue damage compared to the CIP specimens is due to concrete shrinkage. The concrete shrinkage effectively shifts the stress histories applied to the studs into cyclic compression, or cyclic tension, depending on the direction of the resisted longitudinal shear force from the applied load and concrete shrinkage. Fatigue cracking will occur on both sides of the stud if cyclic tensile stresses are present on each side as well. This will decrease the longitudinal stiffness of a stud more rapidly compared to a stud whose fatigue cracking propagates from one side alone. A more in-depth analysis and discussion on this effect is presented in Section 5.3.3.

4.1.3 Strain Profiles & Slab Force

Strain profiles are an excellent tool to understand how a composite cross-section performs under loading. Two objectives were explored using the strain profiles. The first was to observe any changes in the measured strains as the composite action degraded due to the fatigue damage. The second goal was to use the strain data to determine the actual axial slab forces being transferred by the studs. Determining the slab force in this manner allows the shear stud stress to be calculated, and provides an alternative method to determine the stress ordinate in the fatigue life (S-N plots), rather than using the theoretically calculated values. The purpose of this is to represent the S-N data as accurately as possible. Typically, bridges are constructed with a full shear connection and assumed to exhibit zero slip at the interface (i.e., full shear interaction). Since the specimens have been constructed with partial shear connection, and henceforth partial shear interaction, the actual stress values experienced by the shear connectors will inherently be lower.

In the early stages of the laboratory testing program, strain profiles were measured at Profiles E and B, corresponding to the horizontal distances 250 mm and 1000 mm from the west support. Each of these profiles included seven strain measurements: top of concrete slab, top longitudinal reinforcing bar, bottom longitudinal reinforcing bar, bottom of concrete slab, bottom of the top

steel flange, mid-height of web, and underside of the bottom steel flange. Preliminary analysis of the data showed that the strains obtained from the concrete slab and longitudinal reinforcement provided accurate results compared to the hypothesized behaviour. However, these data were easily rendered inaccurate and found to be unreliable once the concrete began to crack and the reinforcing gauges became damaged during or damaged prior to the fatigue loading. Starting with the testing of the fourth specimen (P200), Profiles A, Y, and Z were introduced at the 500 mm, 2000 mm, and 2500 mm distances from the west support. Each of these profiles adopted an approach that included only two strain gauges; one on the bottom of the top flange, and the other on the underside of the bottom flange. It was found that the gauges on the steel section were more reliable and provided an efficient means of determining the axial slab force compared to the concrete strain gauges. All of the modifications applied to the profile instrumentation are discussed in greater detail in Section 3.3.1 and Appendix B.

The strain profiles and slab force diagrams are provided in Appendix E3 for an applied load of 200 kN. In this section of the thesis, sample strain profiles and a summary of the calculated slab forces are presented. Note that the negative strain values in the diagrams correspond to tensile strain, while positive strain values denote compressive strains. Figure 4-7 illustrates the strain profiles of the C200 specimen at locations E and B. For comparison purposes, the static test data are overlaid on top of the theoretical strain profile that assumes full interaction at the interface (i.e., no interfacial slip). An outline of the composite section geometry is also overlaid on each of the plots for visual aid.

The fully composite neutral axis is located 243 mm from the bottom of the composite cross section, and is illustrated in the figure where the theoretical strain profile, represented by the black dashed line, intersects the zero strain ordinate. This intersection occurs within the top flange of the steel section. The strain profile shown in Profile E (left in Figure 4-7) demonstrates a discontinuity in strain at the steel-concrete interface. This strain discontinuity is expected since the number of shear studs used in the specimens are not sufficient for full composite action (i.e., partial shear interaction is expected).
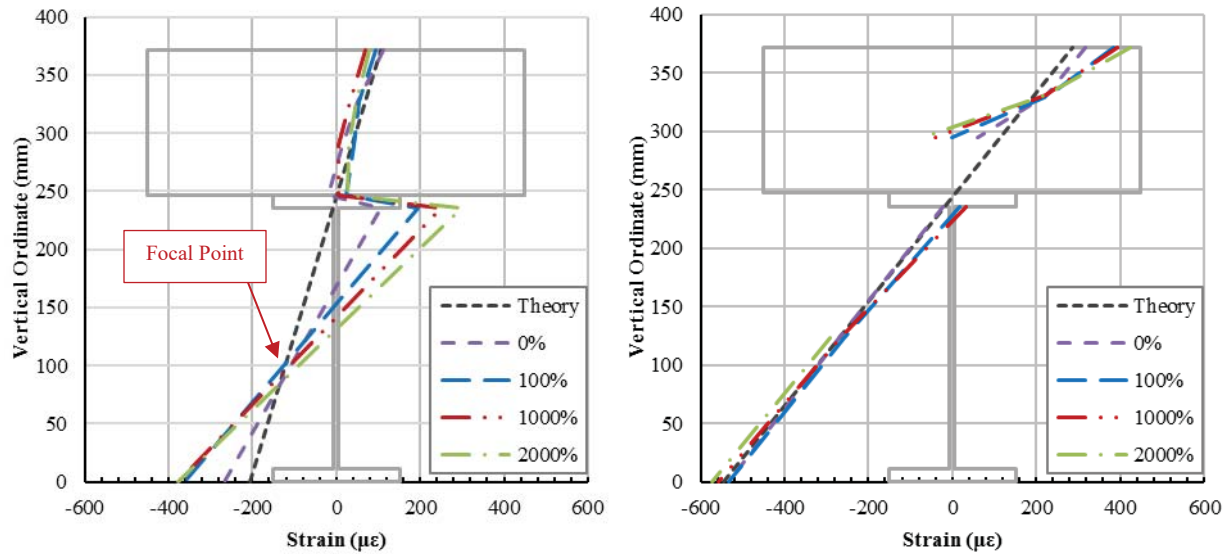
(a) x = 250 mm   (b) x = 1000 mm

Figure 4-7: Strain profiles at (a) E and (b) B for Specimen C200 at P = 200 kN.

The magnitude of the strain discontinuity between the concrete slab and steel section, also known as slip strain, is related to the amount of interfacial slip present at that location. The amount of interfacial slip at a given location can be determined by integrating the slip strain along the longitudinal axis. As the fatigue damage experienced by the connectors increases, the slip and strain discontinuity also increased. As previously discussed in Section 4.1.2., additional slip can be present due to damage of the concrete around the studs around the weld collar. The trend of increasing slip strain with fatigue damage is clear in almost all of the strain profiles provided in Appendix E3. Another general trend observed for the specimens was as fatigue damage accumulated, the slope of the strain profiles increased (corresponding to an increase in section curvature), and the location of the neutral axis migrated towards the middle of the steel section. This was the anticipated behaviour of the specimens over the course of their fatigue lives. As the longitudinal shear stiffness and composite action decreased, an increase in curvature and strains was expected. Once a strain profile intersected the y-ordinate at 124 mm (neutral axis of the steel beam alone), the degree of interaction and net compression force in the slab due to composite behaviour was equal to 0.

Considering that most of the slip occurs near the west support, Profiles E and A demonstrated the largest magnitude of strain discontinuity and lowest neutral axis, compared to the other profiles.

76

Profile B is located at the point of maximum moment, and as discussed previously, had a slip value of zero (initially). Therefore, the strain profile at B (right-hand plot in Figure 4-7) closely matched the strains predicted by theory. Additionally, Profiles Y and Z deviated by only a small amount from the theoretical profiles, suggesting behavior close to full composite. This behavior is evident in the strain profile results for Specimen P300 as illustrated in Figure 4-8. The figure includes the strains located at Profile A, B, Y, and Z.

An interesting observation in the strain profile data was that as the strain profiles increased in slope (i.e., curvature increased) over the course of fatigue loading, the profiles for a given section pivoted about a specific location, and providing a focal point in which all of the profiles intersected. This phenomenon was most prominent at Profiles E, A, and B, especially for the specimens subjected to higher load levels. This focal point was found to range between 50 mm to 100 mm from the bottom of the section in all of the specimens, as emphasized in Figure 4-7 and 4-8 with a red arrow and labelled as "Focal Point." Further investigation into the literature suggests that for composite beams with partial interaction, the strain profiles intercept at two points; one in the concrete and one in the steel. These intercepts have been referred to as partial interaction focal points, and have been proven mathematically to remain stationary for any degree of interaction for given cross-sectional properties (D. J. Oehlers & Seracino, 2002). Due to the locations of these focal points, the strain gauge installed on the underside of the top flange demonstrated a greater change compared to the gauge installed on the underside of the bottom flange.

The concrete strain gauges located on the top and bottom of the slab in Profile E, A, and B were used in the first attempt to determine the actual axial forces being transferred into the studs from composite action. Due to concrete cracking, the concrete strain data were frequently rendered unusable, leading to unreliable force predictions. As a result, strain data from the steel was utilized to back calculate the force in the slab using static equilibrium and this approach was found to provide more consistent results. Profile E was removed from the instrumentation program after the fourth specimen because it was located within the D-region of the support where the assumption of a linear strain profile may not be valid.
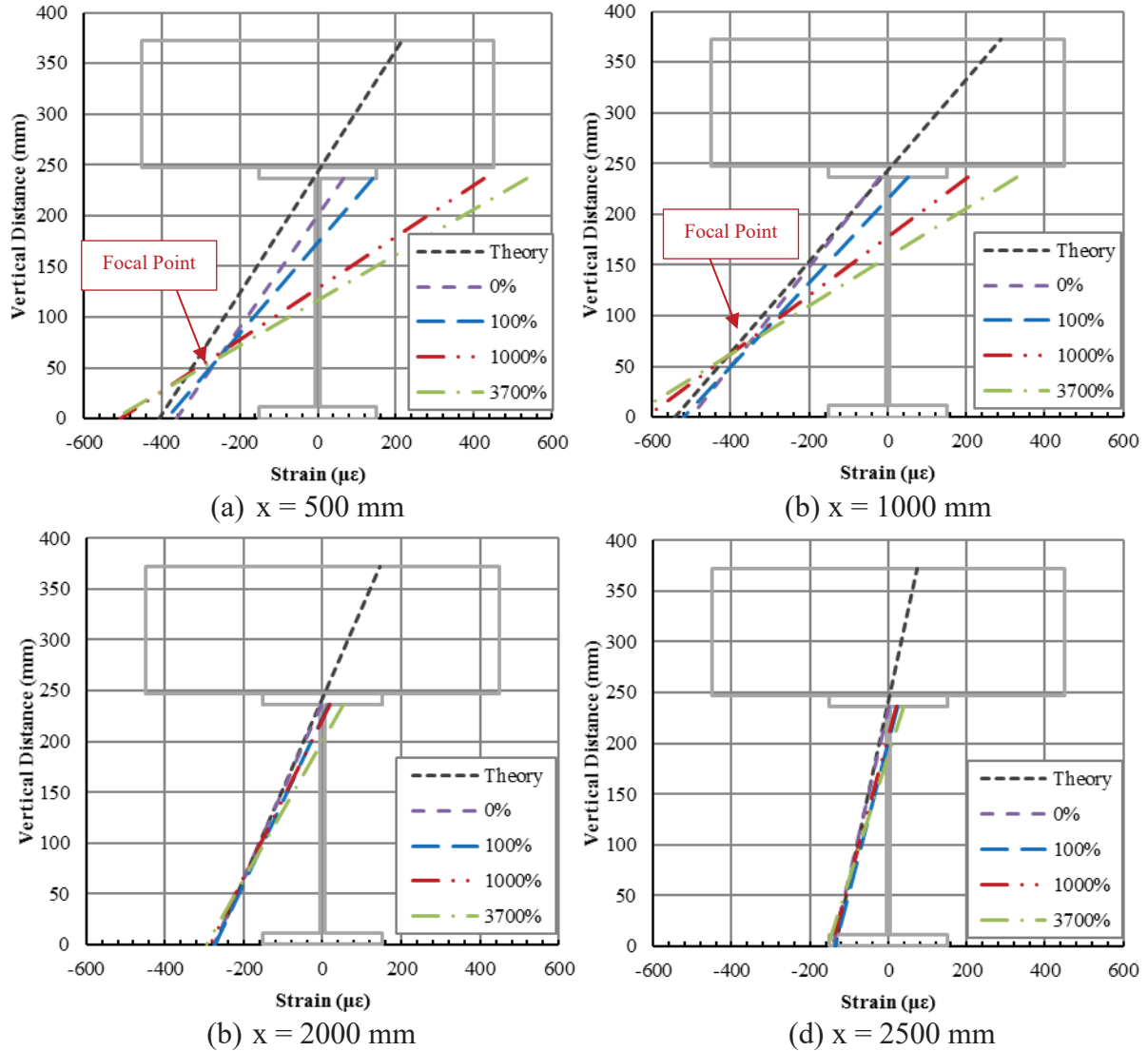
Figure 4-8: Strain profiles at (a) A, (b) B, (c) Y, and (d) Z for Specimen P300 at P = 200 kN.

The net compressive force in the concrete slab was calculated based on the steel strain profile using the equilibrium of forces at a given cross section. As described by Oehlers & Seracino (2002), the internal resultant moment at a cross section is comprised of three components: the force couples in the concrete, steel, and an additional composite couple consequential from the shear interaction, denoted by M_c (red), M_s (blue), and M_{comp} (green force couple), respectively. A schematic of these resistive moments and forces are provided in Figure 4-9.
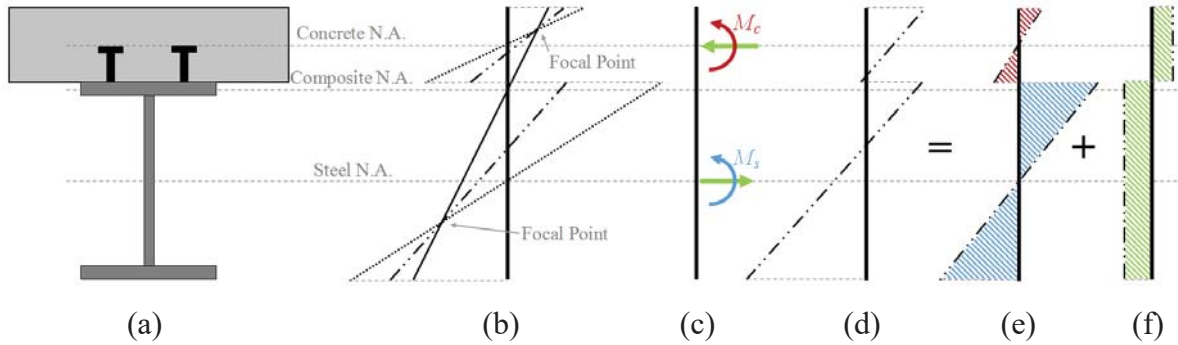
Figure 4-9: Diagram showing the force couples acting on the cross section (note that negative strain corresponds to tension, similar to the results). (a) Composite beam cross section. (b) Variation of strain profile given degree of shear interaction. (c) Internal resistive forces. (d) Stress profile. (e) Super position of stress profile into internal moments M_c and M_s. (f) Super position of the force couple that generates M_{comp}.

The net tension resultant in the cross section of the steel is equivalent to the net compression resultant in the concrete and is illustrated by the uniform green stress profiles. This force is transferred between the concrete slab and steel cross-section at the interface by the shear connectors and interfacial friction. Although this friction was present in the testing, it was assumed that the connectors transferred all of the load without any contribution from friction. Another assumption made in order to complete this calculation was that plane sections remained plane, such that the stress distribution throughout the cross-section of the steel was completely linear. The resisting couple moment, M_{comp}, produced by the shear connection in a composite beam is reduced when the degree of shear interaction is also reduced. In order for a composite beam to provide an adequate amount of moment resistance in the case of a reduction in shear interaction, M_s and M_c must increase and make up for the difference by increasing in curvature. This behaviour was observed in all of the specimens as the shear interaction was decreased due to fatigue damage.

The net compressive slab forces were determined for each of the specimens, and are summarized into a table and plotted in Appendix E3. Results are provided for the 0%, 100%, and 1000% static tests, as well as the percentage decrease, compared to each of the initial, 0% tests. The results for Specimen P300 are provided in Figure 4-10 as an example of the results included in Appendix E3. This figure shows the calculated axial slab force for Profile A (500 mm), B (1000 mm), Y (2000 mm) and Z (2500 mm) assuming full composite action along with the results based on the measured steel strain profiles at 0%, 100%, 1000%, and 3700% of its expected fatigue life, and

represented by the green, purple, blue, and orange square markers, respectively. The theoretical axial slab force was calculated assuming full interaction and is denoted by the red square marker.

Figure 4-10 demonstrates a large decrease in axial slab force at Profiles A and B as the studs were damaged by the fatigue loading, eventually decreasing the force at Profile A to zero. This behaviour is expected as the applied fatigue loading had an equivalent stress of 300 MPa on Stud Pairs 1 and 2, making this the largest stress level tested. Similar behaviour was seen in the CIP equivalent, C300.
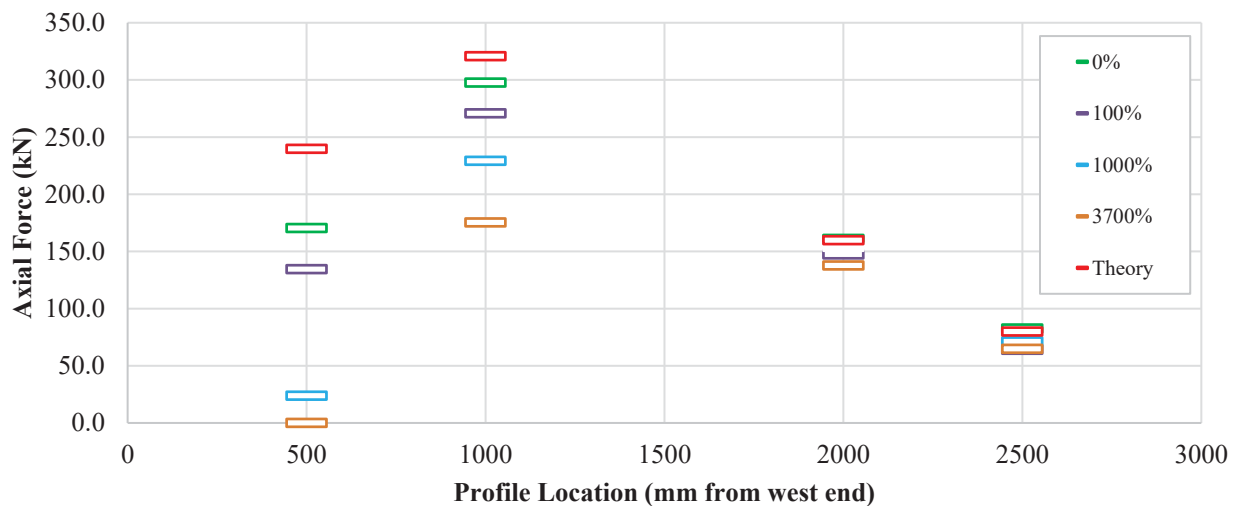
Figure 4-10: Concrete slab axial force diagram for Specimen P300 at an applied load of 200 kN.

The calculated slab forces are summarized in Table 4-5 where the average results for the 0% static tests are listed for the CIP and precast specimens. The first row of data represents the theoretical result assuming full interaction. The difference between the theoretical slab force and the respective averages determined from the laboratory testing are also shown in the table. A statistical Student's t-test was performed on the CIP and precast data set to determine whether the two are likely to have come from the same two underlying populations containing the same mean. Specifically, the test provides the likelihood that there is no difference between the initial CIP and precast net axial force behaviour in the slab. The calculation was completed assuming a two-tailed distribution and homoscedasticity. The bracketed numbers beside each of the profile letters in Table 4-5 correspond to the total number of specimens for which the data were averaged. That is, Profile E was only measured for the first four specimens: C140, P140, C200, and P200 and was

subsequently discontinued due to concerns over the strain profile being located in the D-region of the west support. Thus, a Student's t-test was not performed on Profile E because there were too few data points to represent each of the data sets to hold any statistical significance. The resulting values are 2%, 8%, 79%, and 1% similarity between the CIP and Precast initial net slab forces for Profiles A, B, Y, and Z, respectively. Figure 4-11 plots the results in Table 4-5 in the form of a comparative bar graph.

Table 4-5: Average Axial Slab Force Results for the 0% Static Test at P = 200 kN.

Profile	E (4)*		A (9)		B (12)		Y (9)		Z (9)	
x (mm)	250		500		100		2000		2500	
	Slab Force (kN)	Change rel. to Theory	Slab Force (kN)	Change rel. to Theory	Slab Force (kN)	Change rel. to Theory	Slab Force (kN)	Change rel. to Theory	Slab Force (kN)	Change rel. to Theory
Theory	120		240		321		160		80	
CIP	67	-44%	225	-6%	323	1%	159	0%	60	-24%
Precast	95	-21%	185	-23%	308	-4%	161	1%	82	3%
t-test			2%		8%		79%		1%	

*Note: The numbers in the parentheses correspond to the total number of specimens that included the profile.

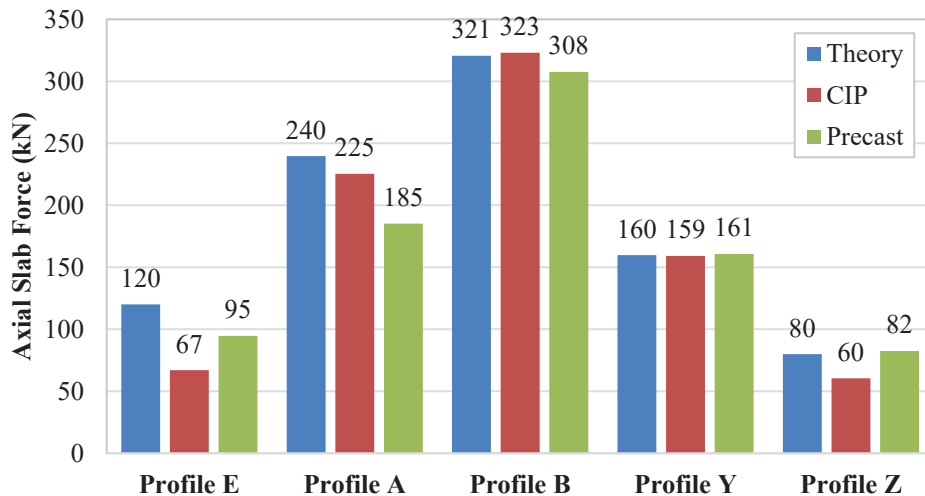**Figure 4-11:** Average compressive force in the slab for each of the specimen types at P = 200 kN.

The CIP slab forces were found to be lower than the precast near the ends of the beams (results from Profile E and Profile Z) and has been hypothesized to be a result of higher frictional forces at the interface. The friction in the precast specimens has been assumed to be less than the CIP

81

because the concrete slab was placed on top of the steel and then the shear pockets grouted without a haunch along the length of the beam. Thus the only locations where the slab was in full bonded contact with the top surface of the steel beam were at the pockets, compared to the CIP specimens where slab was in full bonded contact with the entire length of the top flange of the steel beam. The slab force values at Profile B (location of max moment) and Profile Y for both the CIP and precast specimens corresponded well with what theory predicted. After completing a Student's t-test, it is apparent that the CIP and precast slab forces are dissimilar statistically speaking. The possible cause for this difference in behaviour could be attributed due to the friction at the steel-concrete interface as previously discussed. In order to experimentally determine if this is true, a set of precast specimens must be grouted with a small haunch to simulate the same friction characteristics as the CIP specimens. The axial slab force data will be used in the subsequent S-N analyses for determining the actual stresses acting on the studs compared to the stud stress calculated by theory (see Section 6.1).

4.2   Fatigue Testing Results

This section presents the experimental results gathered throughout the fatigue testing phase, including beam deflection, interfacial slip, and local distortion gauge data recorded for each cycle over the course of the testing. The analysis of these data provides a means of accurately determining when a stud or a pair of studs has failed. It is hypothesized that the increase or change in the deflection, interfacial slip, and local distortion gauge trends will provide an accurate method to distinguish the number of cycles to failure, and provide insight on the progressive failure of adjacent studs once a stud failure has already occurred.

Fatigue loading was applied on each of the specimens utilizing a variable amplitude load history as previously discussed in Section 3.2.1. As a reminder, the numerical value assigned in each of the specimen names corresponds to the target equivalent stress range, as well as a C or P to distinguish a CIP or Precast constructed member. Also recall, that the largest stress range in the variable amplitude load history is 2.00 times larger than the equivalent stress range, and occurs once every 1,024 cycles. Although the digital controller used in the experimental setup was programmed to attain the target equivalent stresses in the studs, the equivalent stress ranges recorded for each of the specimens was found to deviate slightly from the target. Table 4-6

provides a summary of the sequence in which each specimen was tested, the equivalent stress ranges, theoretical life based on the equivalent stress range according to CAN/CSA S6 (2014), and the number of total cycles experienced until the test was stopped.

Table 4-6: Fatigue Test Summary.

Test	Specimen	Stud Equivalent Stress Range (MPa)	Theoretical Fatigue Life	No. of Cycles to End of Test
1	C140	140.8	258,166	2,555,926
2	P140	140.6	259,573	2,719,172
3	C200	202.3	87,127	2,489,438
4	P200	201.9	87,569	3,296,102
5	C300	302.1	26,162	2,053,420
6	P300	301.9	26,194	1,168,548
7	C100	98.8	747,459	9,503,532
8	P100	98.6	721,001	7,178,574
9	C120	119.5	423,034	5,205,441
10	P120	119.9	418,366	2,288,865
11	C067	63.5	2,815,880	10,428,252
12	P067	62.7	2,925,046	12,897,344

The tests were stopped when the local distortion strain data trends plateaued after displaying a peak in Studs Pairs 1 or 2 (primary studs) and the specimens reached their 1000% fatigue life cycle mark. Specimens C067 and P067 were stopped around their 500% fatigue lives due to time restrictions. The data acquisition setup utilized a peak-detect algorithm that collected the channel readings when a peak in the load history was detected. Thus the system recorded the strain and LVDT values at each of the peaks and valleys in the data. Since the specimens experienced anywhere from 0.6 million to 10 million applied loading cycles, a MATLAB program was developed in order to process, compile, and manipulate the large data sets. The program subtracts the values collected at the peak load from the previous valley load, resulting in the change in behaviour (i.e., load, displacement, strain) for each load cycle. Initially, the values corresponding to the largest stress range were chosen when plotting the results. Upon inspection, global trends in the data were apparent, however, the data demonstrated a noisy and variable behaviour. Upon further analysis, it was found that the second largest stress range provided more distinct results with trends that demonstrated far less variability. Therefore, the data presented throughout the subsequent section correspond to the values determined at the second largest stress range or load

range. The second largest stress range was determined to be 1.86 times larger than the equivalent stress range for each of the specimens, and occurs every 23 times every 1,024 cycles. A reduction in this data set was completed due to the congestion of data on a single plot. Therefore, every 100 to 300 data points were skipped incrementally depending on how many cycles were included in each fatigue test, effectively thinning out the data. Table 4-7 summarizes the second largest load ranges applied to each of the specimens corresponding to their respective equivalent stress ranges.

Table 4-7: The load ranges at which the data is presented

Equivalent Stress Range (MPa)	2nd Largest Load Range (kN)
67	86.1
100	128.5
120	154.2
140	179.9
200	257.0
300	385.4

The fatigue data are provided in Appendix F and are broken down into Sub-Appendices F1, F2, and F3 corresponding to the deflection, interfacial slip, and local distortion data. During the fatigue testing, the data acquisition software failed to record periods of data for Specimens C067, C100, and P200. As a result, each of the three specimens encompass data gaps that vary in length. Judgment and interpolation of the data was necessary when estimating if an event, such as a stud failure, occurred during this period.

4.2.1 Variation of Beam Deflection During Fatigue Loading

The beam deflection data were obtained utilizing an LVDT positioned 1300 mm from the west support. The LVDT was mounted to an isolated stand and the core was positioned on the underside of the bottom flange. The results plotted in Appendix F1 compare a CIP and precast specimen at each of their respective equivalent stress range categories. In each of the plots, the black circles represent the CIP specimen and the red circles represent the precast specimen. The theoretical deflection value is also overlaid onto each plot and includes bending and shear deformation, assuming a 33% shear connection. These theoretical deflection values were calculated using the same methodology as described for the static tests in Section 4.1.1.

The C300 and P300 specimens demonstrated the most significant changes in deflection data, as illustrated in Figure 4-12. The C300 deflection trend started initially at 6.03 mm and experienced a significant increase to 6.49 mm at the 60,700 cycle mark. The trend then became gradual increasing to 6.86 mm at 622,000 cycles. Specimen P300 exhibited a constant deflection of approximately 5.88 mm until 106,000 cycles. From this point, a significant increase in deflection to 6.83 mm took place at 151,000 cycles, followed by a steady and gradual increase in deflection. From inspection, it appears that the slope of the deflection trend is larger in P300 compared to C300. This correlates to a similar behaviour seen in the P200 and C200 specimens, with the precast also demonstrating an increased slope in comparison to the CIP equivalent. The theoretical deflection calculated for this data set is 4.61 mm.
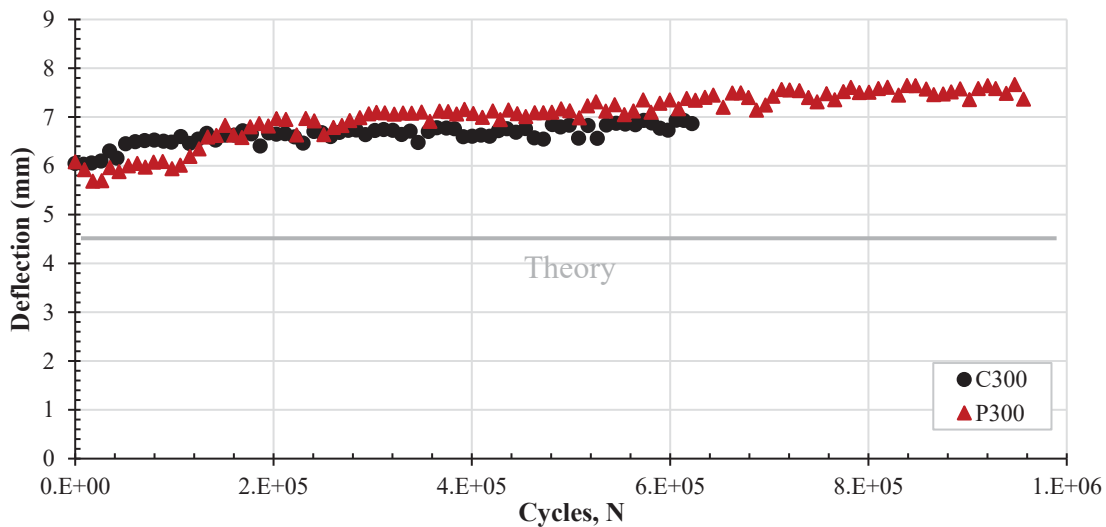

Figure 4-12: Deflection versus cycles for Specimens C300 and P300.

The deflection trends for Specimens C067, P067, C100, and P100 did not display a gradual loss of stiffness. This was expected, as the equivalent stress ranges are the lowest tested in the investigation, and only applied to Stud Pair 1 and 2 (17% of the shear connection). The rest of the studs (83% of the shear connection) experienced an equivalent stress range that was 66% lower than the target studs. Rather than displaying a gradual loss of stiffness, the trends were quite variable and demonstrated random occurrences of stiffening and softening. The C067 and P067 specimens both demonstrated similar deflection values averaging approximately 1.58 mm over the duration of their respective fatigue lives. The C100 and P100 specimens both demonstrated

deflection values averaging 2.45 mm over the duration of their respective fatigue testing. The average values of 1.58 mm and 2.45 mm were found to be larger than that determined by theory, being 1.03 mm and 1.53 mm, respectively.

The deflection data for the specimen pairs at the 120 and 140 stress levels displayed a slight increase over the duration of fatigue testing compared to the initial values. C120 and P120 were found to have an average deflection of 2.49 mm and 2.90 mm, respectively, over the duration of the test, which was larger than 1.84 mm determined by theory. C140 and P140 both shared a similar average deflection at approximately 2.44 mm over the duration of the test compared to the theoretical deflection of 2.14 mm.

Specimens C200 and P200 both displayed a gradual increase in deflection from their initial values over the course of fatigue testing. Since the values changed gradually with time (unlike the deflection trends for the other specimens), taking the average values of the data sets for comparison would be inappropriate. Instead, the initial and the 1000% of the fatigue life values will be examined. Initially, the C200 and P200 deflection values were 3.44 mm and 4.01 mm, respectively. At the 1000% of their theoretical fatigue lives (901,250 cycles), the deflection values were 3.53 mm and 4.49 mm for the C200 and P200 specimens, corresponding to a 2.6% and 12% increase, respectively. The theoretical deflection for the specimens was calculated to be 3.06 mm.

4.2.2   Variation of Interfacial Slip During Fatigue Loading

As described in Section 4.1.2, the interfacial slip was recorded at five locations along the longitudinal axis of the beams. They are labelled as Slip 1 through 5 and are located at x = 0, 500, 1000, 2000, and 3000 mm from the west support. The fatigue results however, do not present data for the Slip 3, the slip at the max moment, since it was recorded only for the first seven specimens. Also, it was established that Slip 3 demonstrated insignificant amounts of slip in comparison to the others based on the first seven specimens tested. The variation of interfacial slip (absolute values) over the duration of fatigue loading is presented in Appendix F2 for each of the specimens. The black circles, red diamonds, cyan squares, and white triangles represent Slip 1, Slip 2, Slip 4, and Slip 5 respectively. The following discussion regarding the trends in interfacial slip will primarily compare each of the CIP specimens to their respective precast equivalent, and note any

significant events or findings. The Slip 1 values are also compared considering that they were the most affected by the fatigue loading.

Specimen C067 demonstrated an increase in interfacial slip at Slip 1 and Slip 2, while Slip 4 and Slip 5 remained constant. The increased slip initiated at approximately 6.4 million cycles, and the increase in Slip 1 from its initial value to the end of the fatigue test was approximately 0.02 mm. Specimen P067 did not demonstrate any change in interfacial slip over the course of fatigue testing.

Slips 1, 2, 4 and 5 all demonstrated an increase in slip compared to the initial responses for Specimen C100. Slip 1 displayed a tri-linear behaviour with the first linear portion displaying no slope until approximately 0.6 million cycles. The second linear segment demonstrated the largest slope, transitioning to the third linear portion at approximately the 3 million cycle mark. For Specimen P100 however, Slips 1 and 2 were the only locations that experienced an increase compared to their initial values, regressing into a linear trend. The change in Slip 1 was larger for C100 compared to P100, increasing from the initial value by 0.07 mm and 0.04 mm, respectively, at the 7.2 million cycle mark (1000% of the theoretical fatigue life).

Specimen C120 demonstrated a clear increase in Slip 1, Slip 2, Slip 4, and Slip 5. Slip 1 displayed a sudden increase in slip at 0.25 million cycles that transitioned into a smooth non-linear trend that decreased in slope as the number of cycles increased. Slip 2 and Slip 4 remained fairly constant until the 3 million cycle mark, where it appears an event (such as a stud failure) occurred, providing an increase in Slip 4 and a discontinuity in Slip 2. This slip event is due to a change in longitudinal shear stiffness, and may signify a stud failure. Lastly, Slip 5 followed a linear trend that initially started with a larger slip value than Slip 1. The interfacial slip data for Specimen P120 at locations 1 and 2 demonstrated an increase until 0.5 million cycles. The slip then decreases until 1.2 million cycles, followed by a linear increase in slip until the data plateaus at approximately 3 million cycles. The increase in slip at the 1000% fatigue life was 0.07 mm and 0.08 mm for C120 and P120, respectively.

Specimens C140 and P140 both demonstrated increases in interfacial slip at locations 1 and 2. Slips 4 and 5 did not increase noticeably and remained essentially constant over the duration of

fatigue loading. At 1000% of the specimen fatigue life, Slip 1 increased by 0.10 mm and 0.08 mm for C140 and P140, respectively.

Slips 1, 2, 4, and 5 all experienced significant increases due to fatigue for Specimens C200 and P200. The slip trends in C200 were fairly linear with no discontinuities suggesting a constant increase in fatigue damage and decrease in longitudinal shear stiffness. The increase in Slip 1 values at the 1000% fatigue life was 0.11 mm and 0.19 mm for specimens C200 and P200, respectively.

Specimens C300 and P300 displayed discontinuous and non-linear slip trends as shown in Figure 4-13. Note that the absolute values of the interfacial slip are plotted over the fatigue life of the specimens. For Specimen C300, significant increases in Slip 1 occurred at approximately 26,000 and 142,000 cycles, followed by continued increasing slip. Specimen P300 experienced significant slip events in Slip 1 and 2 at 30,000 and 106,000 cycles, but the slip values remained essentially constant during further fatigue loading. The increase in Slip 1 values at the 1000% fatigue life was 0.45 and 0.89 mm for specimens C300 and P300, respectively.
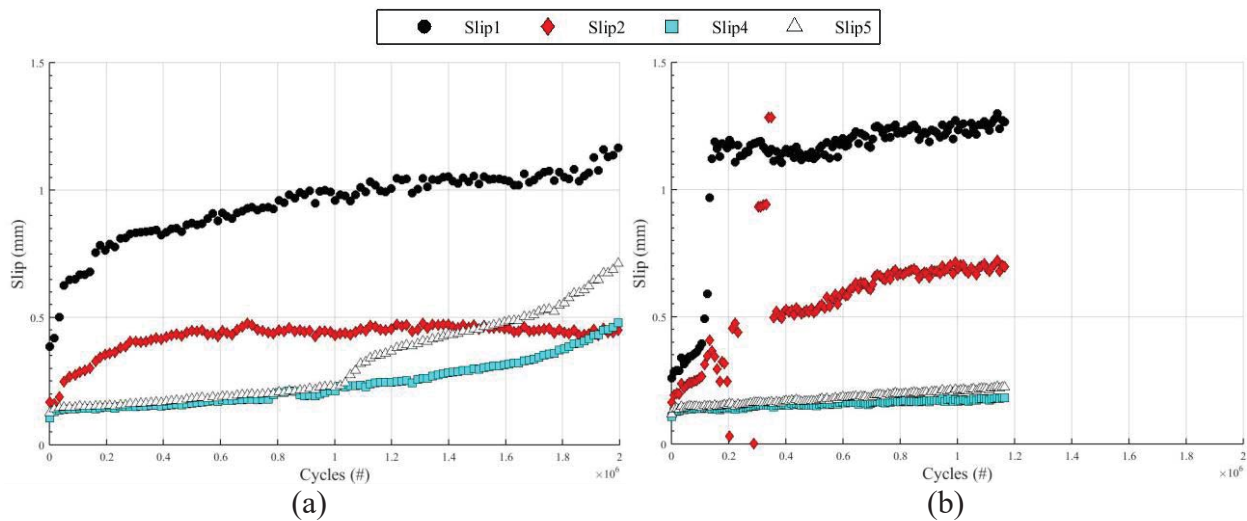

Figure 4-13: Slip versus cycles for (a) C300 and (b) P300.

The change in Slip 1 occurring from 0% to the 1000% fatigue life is summarized in Table 4-8 for each of the specimens. Initially, the CIP specimens all demonstrated larger or equivalent Slip 1 values compared to the Precast equivalents, with the exception of P120. The precast specimens

88

demonstrated a lower percentage increase in Slip 1 compared to their CIP equivalents at the 67, 100, and 120 MPa stress ranges. Based on these results, it suggests that the precast specimens performed greater than their CIP equivalents when subject to lower fatigue stresses in the range of 67 to 120 MPa. As discussed briefly in Section 4.1.2, the stress histories acting on the studs are shifted due to the concrete shrinkage in the CIP specimens. This concrete shrinkage may shift the west and east sides of the stud into cyclic compression or cyclic tension given its location along the span. A more in depth analysis on this effect has been completed in Section 5.3.3.

Table 4-8: Slip 1 Fatigue Summary

Specimen	Fatigue life	Initial Slip (mm)	Slip at Fatigue Life (mm)	Change in Slip 1 (mm)	Increase from Initial
C067	500%	0.06	0.08	0.02	38%
P067	500%	0.06	0.06	0	0%
C100	1000%	0.12	0.19	0.07	57%
P100	1000%	0.08	0.12	0.04	56%
C120	1000%	0.06	0.13	0.07	117%
P120	1000%	0.10	0.18	0.08	80%
C140	1000%	0.15	0.25	0.10	71%
P140	1000%	0.11	0.19	0.08	73%
C200	1000%	0.19	0.29	0.11	58%
P200	1000%	0.17	0.36	0.19	111%
C300	1000%	0.39	0.83	0.45	116%
P300	1000%	0.26	1.15	0.89	345%

4.2.3 Variation of Local Distortion Strains During Fatigue Loading

The local distortion strain data were collected using gauges installed on the underside of the top flange of the steel beam directly underneath the welded shear stud locations. The gauges at this location captured the strains in the top flange due to global (beam) bending, as well as the strains induced by the local bending effects of the shear stud connection. The resistive forces produced by the stud result in localized bending stresses in the top flange and are sensitive to changes in the stiffness/condition of the connector. The top flange may have been in either tension or compression depending on where the neutral axis was located in the steel section throughout the testing. Typically, the bending strain would have to be subtracted from the total strain value to isolate the actual local distortion strain. The positioning of the gauges also affected the magnitude of the local

distortion strains. However, it was determined that the general trend of the strain data, rather than the magnitude of the strain, was important in detecting stud failures using the strain data. As mentioned in previous sections, this type of strain data has been confirmed to deliver a reliable means of capturing changes in the load-carrying behaviour of individual studs over time (King et al., 1965). The local distortion strain data for each of the specimens is provided in Appendix F3.

In most of the specimens, a typical trend in the data was observed. Therefore, rather than going through each of the specimens individually and providing a discussion on each of the trends, a general discussion regarding the results is provided for brevity. The strain increased to some maximum value and then decreased, shaping a distinctive peak. It has been previously explained that once the fatigue crack forms and begins to propagate, the connection becomes sufficiently less stiff, and the strains caused by the local distortions decrease in magnitude.

Stud Pairs 1 and 2 (the primary studs located at the west end) exhibited peaks in the data prior to the others. This was expected due to the offset loading, which applied a stress range three times greater to these studs in comparison to Stud Pairs 3 through 12. Additionally, it was hypothesized that Stud Pairs 3 and 4 would experience an increase in stress due to redistribution once Stud Pairs 1 and 2 were severely damaged due to fatigue. As a result, Stud Pairs 5 through 12 were expected to demonstrate a longer life than Stud Pairs 3 and 4, regardless of the fact that they initially experienced the same theoretical stress ranges. Upon observation of the strain data, this hypothesis did not consistently hold true and failed in the following cases:

- C100: Both S10 and S12 demonstrated a peaking behaviour prior to Stud Pairs 3 and 4 (i.e., N3, S3, N4, and S4).
- C120: Studs S10, S11, and S12 reached a peak during the fatigue testing while Stud Pairs 3 and 4 were still rising.
- P200: Studs N9 and N12 peaked prior to Stud Pairs 3 and 4. S9, N10, and S10 peaked soon after S3 and N4 reached a maximum (Figure 4-14).
- C300: N11 climaxed at a similar time as Stud Pairs 3 and 4.
- P300: It appears S3 experienced a peak early on, while N3 N4 and S4 reach a maximum at a similar point in time as S11 and N12.

Figure 4-14 depicts the local distortion strain data for Specimen P200. Included are four plots that display the strain data for Stud Pairs 1 and 2 (a), 3 and 4 (b), 9 and 10 (c), and 11 and 12 (d). In this figure, the typical trends discussed previously are observed. The local distortion strain increases to a maximum value and then decreases, shaping a distinctive peak.
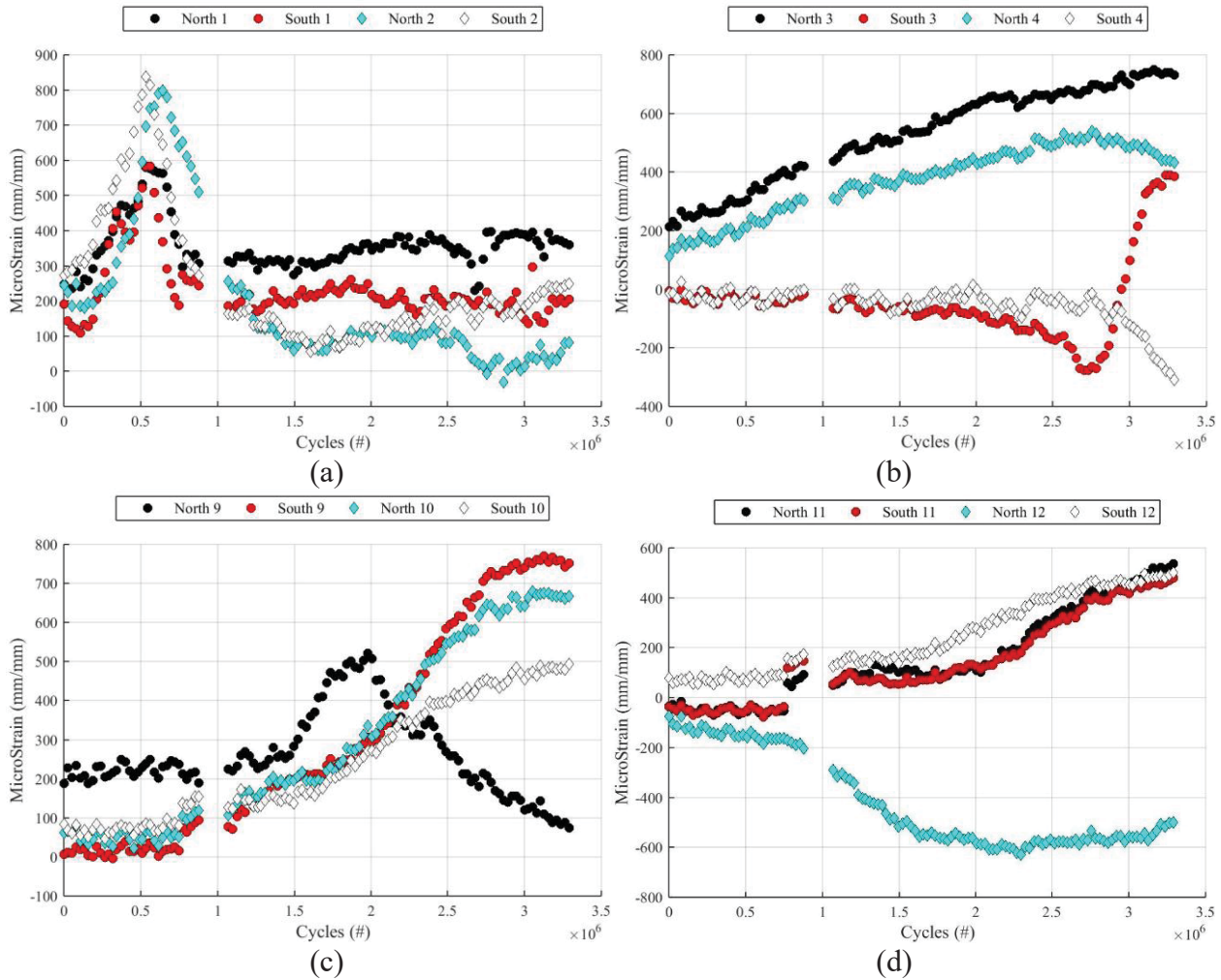

Figure 4-14: Local distortion strain data versus cycles for Specimen P200. (a) Stud Pairs 1 and 2, (b) 3 and 4, (c) 9 and 10, (d) and 11 and 12.

In order to further summarize the results obtained from the local distortion data, Table 4-9 includes the cycle number corresponding to an observed peak in Studs N1, N2, S1, and S2 for each of the specimens. Also included in Table 4-9 is the equivalent stress range that the studs actually experienced, as well as the estimated fatigue life according to the provisions in CAN/CSA S6 (2014). When a stud was not instrumented, it was denoted with an N.I., and when the stud

91

demonstrated a run-out (i.e., no fatigue failure), it was represented with an R.O. The dashed lines in N1 and S1 for C300 signify a lack of definitive peak evidence.

Table 4-9: Number of cycles to a peak in the local distortion data.

Specimen	Actual Equivalent Stress Range (MPa)	Estimated Fatigue Life	N1	S1	N2	S2
C067	63.3	2,842,655	6,731,000	6,731,000	R.O.	R.O.
P067	62.8	2,911,095	5,000,000	R.O.	R.O.	R.O.
C100	98.8	747,592	1,000,000	**711,000**	2,200,000	2,200,000
P100	98.6	752,150	3,140,000	4,133,000	4,290,000	5,710,000
C120	119.5	422,505	**305,600**	2,224,000	677,400	R.O.
P120	119.9	418,290	1,515,000	1,225,000	1,174,000	2,078,000
C140	140.8	258,302	650,000	300,000	N.I.	N.I.
P140	140.6	259,406	1,091,000	1,692,000	1,640,000	R.O.
C200	202.3	87,086	161,500	407,700	705,000	705,000
P200	201.9	87,604	568,000	400,000	614,000	543,000
C300	302.1	26,151	-	-	86,220	62,850
P300	301.9	26,203	83,380	138,000	92,590	146,600

It was hypothesized that the specimens would demonstrate peaks in the local distortion data (i.e., demonstrate longer fatigue lives) later than estimated by the bridge code (CSA S6, 2014). As discussed in Section 2.3.2, the bridge code provisions were established utilizing the mean log-log regression of push test data. Push tests in comparison to beam tests have been proven to provide conservative results and this trend can be observed in the data collected in Table 4-9. The hypothesis was found to hold true, with the exception of Specimens C100 and C120, which demonstrated a peaking behaviour prior to the fatigue life estimated by the bridge code (CSA S6, 2014). These values are highlighted by the red and bolded font. The peaks in the local distortion data were found to align with the increase in variation of Slip 1 for the specimens. For Specimen C100 and C120 demonstrated increases in Slip 1 at approximately 600,000 and 250,000 cycles, respectively. These increases in Slip 1 were found to occur prior to when a peak in the local distortion data was observed by approximately 19% for Specimen C100 and 22% for Specimen C120.

Further analysis of the data in Table 4-9 suggests that the precast specimens demonstrated a longer fatigue life compared to their CIP equivalents, with the exception of P067. A more in-depth analysis on why the precast specimens may demonstrate a greater fatigue performance compared to the CIP specimens has been completed in Section 5.3.3.

4.3   Specimen Autopsy

Once the fatigue testing was completed, autopsies were conducted on the specimens to quantify the fatigue damage incurred by the studs and to help establish a failure criterion. This section will first detail the procedural steps taken in all of the specimen autopsies. Secondly, the results collected from the investigations will be presented and discussed. Lastly, a failure criterion is established by correlating the autopsy findings to the collected fatigue data presented in Section 4.2.

4.3.1   Autopsy Procedure

The methodology for the specimen autopsies was to remove the concrete or grout encasing the studs without causing any damage to the studs, and then to inspect the studs. The stud locations autopsied were ones that demonstrated peaks in the local distortion strain data. This typically included the studs at the ends of the beams (Stud Pairs 1, 2, 12), as it has been shown in previous research studies (King et al., 1965) that these are the studs to first fail. Additionally, all studs were investigated that displayed a post peaking behaviour, several that were rising, and several that had no response. This was completed in order to confirm and establish if the local distortion data trends could provide an effective means of establishing a failure criterion.

Once the studs of interest were located and identified, the concrete slab surrounding the areas were cut with a concrete saw at a safe distance from the studs. A sledgehammer was utilized to break apart large portions of concrete while preserving the stud condition. A pneumatic hand jack hammer was then used to chisel away any remaining concrete, and the stud was cleaned utilizing compressed air and a steel-wire brush. Once the concrete was removed from the surrounding area of the studs, a visual inspection was conducted to identify if the studs displayed any signs of visual cracking in the shank or weld collar due to fatigue.

The next step was to complete a bend test on the studs. This was completed by attempting to bend the studs over with blows from a sledgehammer. A stud passes the bend test when it becomes fully bent over, with its head touching the top flange of the beam and does not fracture. This is adapted from CSA W59 (2013), where the bend test requires a bent angle of 30 degrees. The bend test is a

sign of residual ductility and strength, and is a standard procedure for any stud welder to perform during the welding process. Performing the bend test after fatigue loading does not carry the same meaning as the initial welding bend test, as some studs that are cracked can still pass the bend test due to flexibility, but it was found to be a useful classification tool. The stud would either behave in a ductile manner like a normal bend test, would expose a crack while maintaining ductility, or fail by damaging any remaining area in contact.

Once the bend test was completed, cross sections of the studs were cut out longitudinally to investigate the fatigue damage further. These longitudinal cross sections were completed on studs which typically passed the bend test whether or not they displayed visual cracking. Another factor in selecting the stud cross section for sectioning was if they displayed a post-peaking behaviour but did not display visual cracking. Additionally, several studs were cut that displayed either a rising trend or a no response trend to help confirm the state of the studs. The objective of cutting out cross-sections was to observe how large the cracks were when a visual crack was present, and to observe any other cracks that were not observed initially.

If a stud was removed or a cross sectional cut was completed, the size of the cracks (if one was present) was measured. The total length and depth of the crack was measured using a pair of calipers and noted. Sometimes a crack was present on both the east and west sides.

4.3.2   Autopsy Results

This section presents the results gathered from the specimen autopsy investigations in the order of increasing equivalent stress, alternating between the CIP and precast pairs. The full set of autopsy reports is provided in Appendix G using forms containing all of the information gathered from the investigations. The forms detail each of the studs and state the local strain behaviour at the time the fatigue testing was stopped. The next row details whether or not any cracking was apparent visually, or once a crack could be visually seen when a cross-section was taken. The following row notes if the studs passed or failed the bend test. A non-instrumented or not investigated stud is delineated with a N.I. in the autopsy forms. The following three rows on the form describe the cracking quantitatively. If the stud failed the bend test, the remaining area is provided as a percentage of the original un-cracked area of a stud. The crack lengths propagating from the west

94

and east faces, respectively and depths are also noted for each of the studs where applicable. A bolded box around a stud category signifies that a cross-sectional cut was made and investigated. Additionally, where applicable, figures containing the stud cross sections and figures of the failed studs are included.

The autopsy on Specimen C067 was completed in order to investigate N1, S1, N12, and S12. Both N1 and S1 exhibited post peaking behaviour and N12 and S12 displayed no response in the local distortion data. Upon visual inspection, both N1 and S1 presented cases of visual cracking on the west side of the weld collar. A cross-sectional cut was completed on S1 and revealed a 10 mm long crack propagating from the west face of the weld collar, and down 5 mm into the top of the flange. N12 was also cut, however, no cracking was revealed. An autopsy was not completed on Specimen P067.

Stud Pairs 1, 2, 10, 11, and 12 were investigated on C100 and visual cracking was apparent on Stud Pairs 1, 2, and 12. Studs N1, S1 and N12 failed the bend tests effortlessly, detaching themselves after 1 blow from the sledgehammer. Studs N1 and S1 both exhibited cracks which grew from the west side through the heat affected zone (HAZ). Stud N12 displayed cracks propagating from both the east and west faces, however, the west side was more prominent. Cross-sectional cuts were completed on Studs N2, S2, N10, S10, and S11. Stud N2 (Figure 4-15) and S2 displayed dominant cracking on the west face, initiating at the weld collar toe and propagating down into the top flange. Stud N10 did not exhibit a local distortion response although the cut revealed a 3 mm crack in the shank, initiating at the top of the weld collar (Figure 4-16). Stud S10 did display a peaked response, however, no cracking was observed throughout the cross section. Lastly, Stud S11 was in a post peaking state and a crack 9 mm in length from the east face was measured.
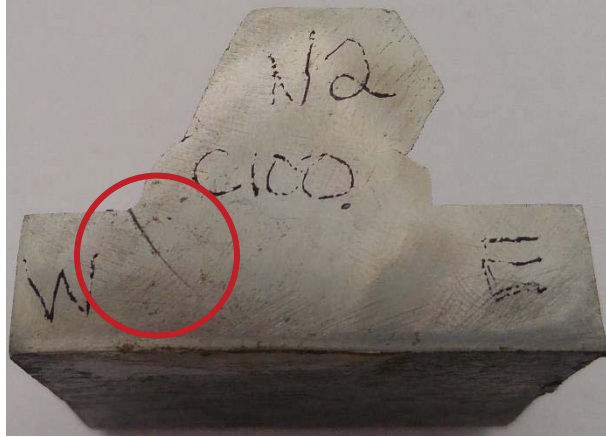
Figure 4-15: Cross-sectional cut made longitudinally through Stud N2 in Specimen C100.
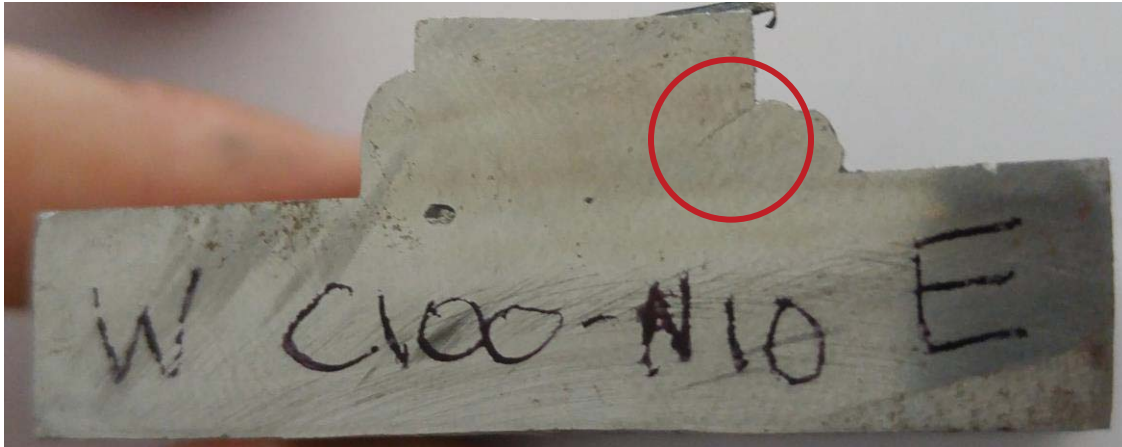

Figure 4-16: Cross-sectional cut made longitudinally through Stud N10 in Specimen C100.

The investigation on Specimen P100 was limited to Pocket 1, which included Studs N1, S1, N2, and S2. These studs displayed a post peaking behaviour when the fatigue testing was stopped. Visual cracking was observed on all four of these studs and each one passed the bend test. No cross-sectional cuts were made on this specimen.

The autopsy on Specimen C120 investigated Stud Pairs 1, 2, 3, 4, 9, 10, 11, and 12. Visual cracking was seen on Studs N1, S1, N2, S2, S11, N12, and S12. Studs N1, S1, S11 and S12 failed the bend test revealing a 10%, 10%, 50%, and 30% area remaining of the original uncracked area, respectively. For Studs N1 and S1, only one crack was present that initiated at the west weld collar toe. Studs S11 and S12 also had only one crack, however, the cracking initiated at the east weld

collar toe. Cross-sectional cuts were completed on Studs S10 and N11, which revealed small 3 mm and 2 mm cracks, respectively, originating on the east side of the stud and penetrating down into the HAZ.

The Specimen P120 autopsy inspected Stud Pairs 1, 2, 11, and 12 (Pockets 1 and 6). Visual cracking was observed on all the studs in the first pocket, however, no cracks were seen in Pocket 6. Studs N1, N2, and S2 failed the bend test, with cracks originating at both the west and east sides of the studs. The cracks propagated down into the flange along the HAZ, and were close to intercepting one another at equal distances. Stud S1 passed the bend test and a cross-sectional cut was completed to provide further information on its state. The cross-section revealed cracks which initiated at the west and east collar toe, measuring at 3 mm and 10 mm in length. It was found the east crack almost penetrated through the entire top flange depth, with a depth of 9.5 mm. The cross-section of S1 is provided in Figure 4-17.
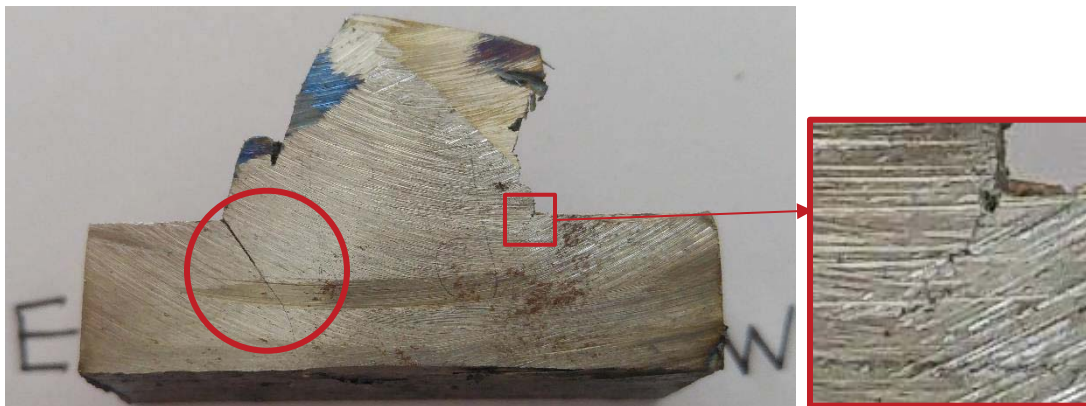
Figure 4-17: Cross-sectional cut made longitudinally through Stud S1 in Specimen P120.

Stud Pairs 1 and 2 were examined in the autopsy of Specimen C140. Visual cracking and bend test failure was observed on Studs N1 and S1, revealing a remaining contact area of 10% for both N1 and S1. Both Studs N1 and S1 demonstrated cracking on the west and east sides of the weld collar, however, the west side was more dominant as shown in Figure 4-18.
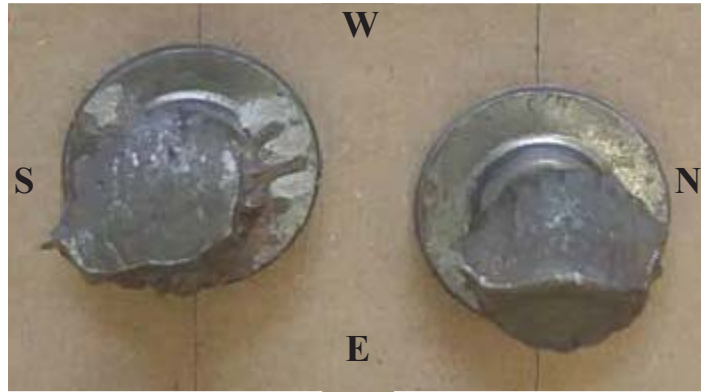
Figure 4-18: The bottom of N1 (right) and S1 (left) from Specimen C140 depicting the fatigue crack propagation.

The first pocket in Specimen P140 was investigated. Each of the studs displayed post peaking behaviour when the fatigue testing was completed and displayed visual signs of fatigue cracking. Studs N1, S1, N2 and S2 all failed the bend test with 10%, 20%, 50% and 50% area remaining, respectively. The area remaining for each of the studs can be observed in Figure 4-19. The fatigue cracking in Studs N1 and S1 was found to penetrate into the flange and originate from both the west and east sides of the weld collar. However, Studs N2 and S2 demonstrated a dominant crack on the east side, and penetrated the top flange by approximately half the amount as the first stud pair.
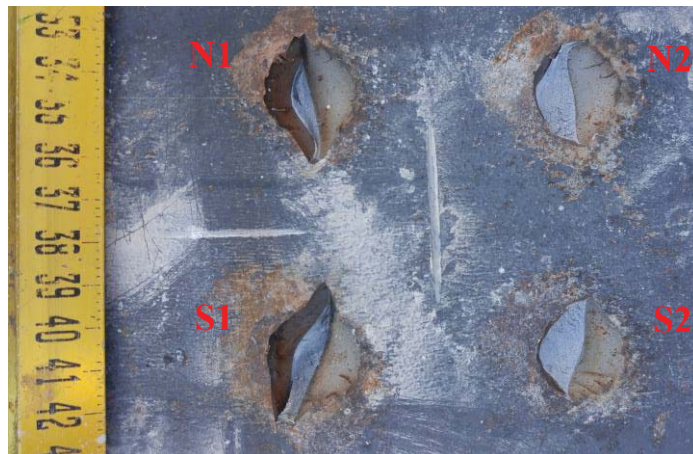
Figure 4-19: Fatigue cracking into the top flange of Specimen P140.

98

The entire concrete slab was removed for Specimen C200 and visual cracking was observed on most studs with the exception of Studs S3, N4, S4, N5, S5, N6, S6. All of the studs with visual cracking also failed the bend test, with the exception of Stud N3. Studs N1 and S1 were removed by hand prior to the bend test because no area was remaining and the stud was completely severed. Upon removal, the crack surface was found to be polished due to the mechanical action and friction throughout the fatigue cycling. Stud S9 and Stud Pairs 10, 11 and 12 also displayed a small amount of area remaining, which was approximated at 0%. Once the bend tests were completed, 16 failed and an average area remaining of 8% was found with values ranging from 0% to 30%. Additionally, a crack propagating transversely through the top flange at Stud S2 was observed as depicted in Figure 4-20.

Figure 4-20: Fatigue crack propagating transversely though top flange at S2 in Specimen P200.

Once the slab was completely removed for Specimen P200, visual cracking was apparent on all studs with the exception of Stud Pairs 5 and 6. The entire first pocket was removed by hand and the surfaces along the crack front were polished due to mechanical action. After completing the bend test, 14 of the studs that failed averaged an area remaining of 23%, ranging between 0% and 70%. It was assumed that Stud S11 would likely fail the bend test, similar to its neighbouring studs, so a cross-sectional cut was made to investigate the state prior to any blows from a sledgehammer. Fatigue cracking was observed and the cross-section is illustrated in Figure 4-21.
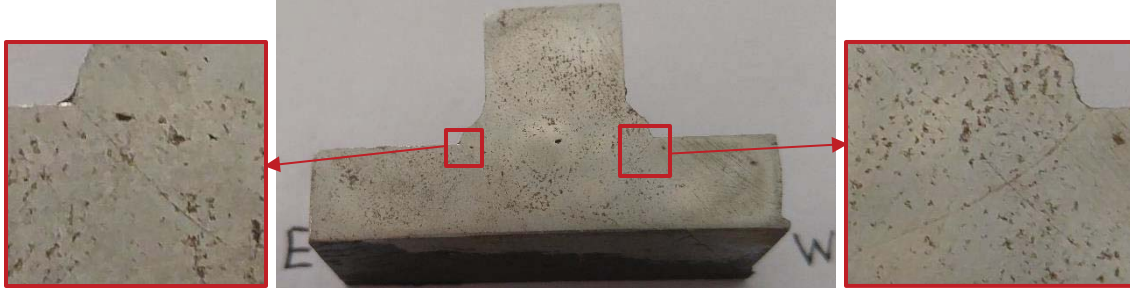
Figure 4-21: Cross-sectional cut made longitudinally through Stud S11 in Specimen P200.

The autopsy on Specimen C300 required the removal of the entire slab to expose all of the studs. It appeared that Stud Pairs 1 and 2 were completely severed along the bottom of the shank and the surfaces were polished due to post failure mechanical interaction. All studs demonstrated signs of visual cracking with the exception of Studs N5 and S5. All of the studs were found to fail the bend test and have 0% area remaining with the exception of Stud Pairs 4, 5 and 6. Stud Pairs 4 and 5 passed the bend test, while Studs N6 and S6 failed, with a 40% and 50% area remaining, respectively. Cross-sectional cuts were completed on Studs S4 and S5 to determine possible reasons for not failing. The cross-section of Stud S4 revealed a crack formed completely though the top flange on the west side (Figure 4-22) and Stud S5 revealed a small 1.1 mm crack on the west toe of the weld collar.

Figure 4-22: Cross-sectional cut made longitudinally through Stud S4 in Specimen C300.

The concrete slab and grout pockets were removed in their entirety for the autopsy investigation on Specimen P300. The first pocket containing Stud Pairs 1 and 2 lifted off by hand, revealing failures that occurred close to the bottom of the shank. Post-failure mechanical action polished the surfaces, rendering it difficult to make notes pertaining to the failure surface. Visual cracking was observed on all studs except for Studs N5, S5, N6, S6, N7, and N8, which also all passed the bend

100

test. However, the bend test exposed visual signs of fatigue cracking on Studs N7 and N8. No cross-sectional cuts were completed on Specimen P300. Stud Pairs 1, 2, 3, and 4 had 0% area remaining when the fatigue testing was completed. The studs on the east end ranged between 10% and 80% area remaining. More in-depth details pertaining to the autopsy results are provided in Appendix G.

Included below each summary autopsy form in Appendix G are three beam illustrations of the stud layout to assist conceptualize the data visually. The first, second, and third illustrations summarize the bend test, local distortion strain, and crack direction results, respectively. The test results are detailed by the different circle indicators which are defined in each of the respective legends. Provided below are two samples of what is found in Appendix G. Figures 4-23 and 4-24 illustrate the results for Specimens P200 and C300, respectively. The studs that have a red outline symbolize that the stud had visual cracking upon removal of the slab.
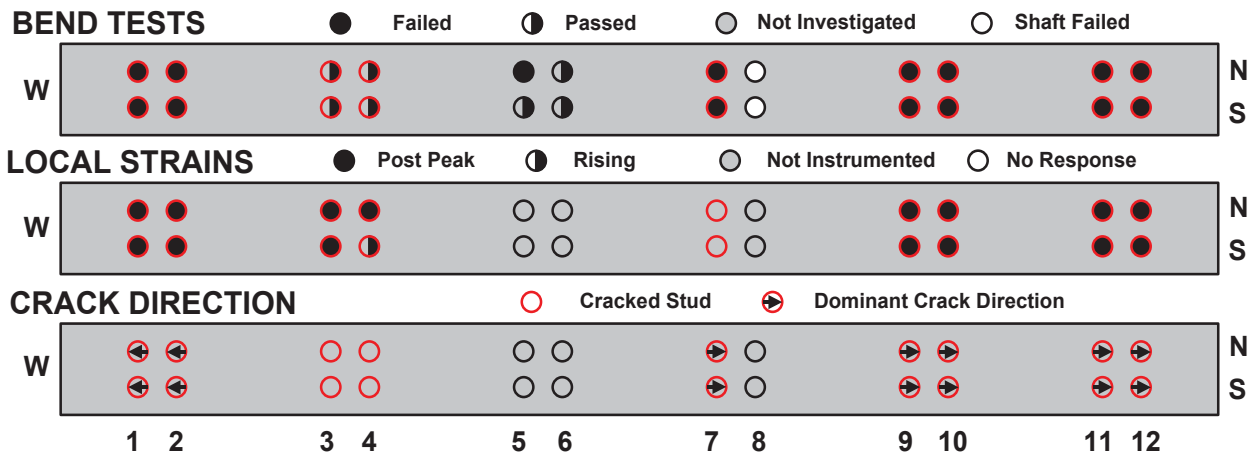
Figure 4-23: Bend test, local distortion strain, and crack direction results for Specimen P200.
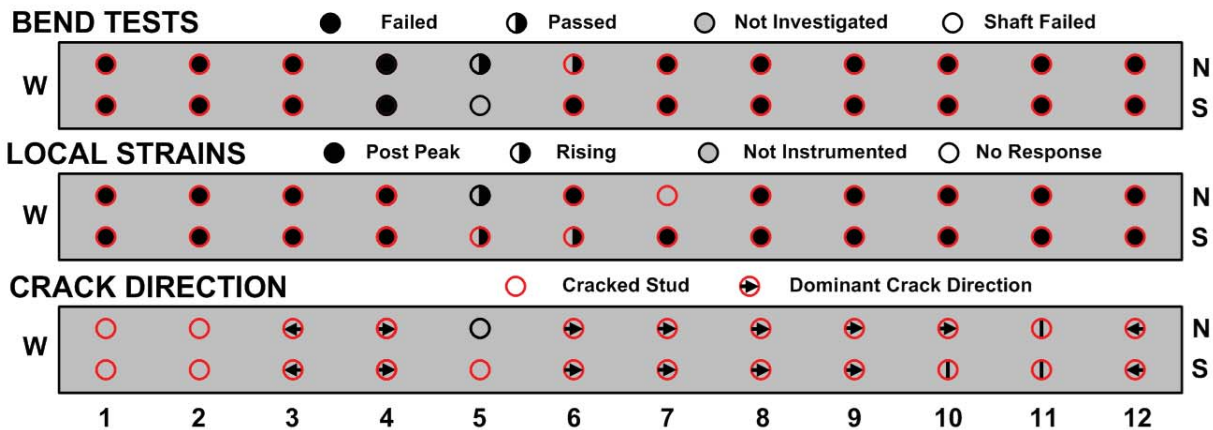
Figure 4-24: Bend test, local distortion strain, and crack direction results for Specimen C300.

An interesting observation identified throughout the specimen autopsies was the direction and lengths at which the fatigue cracks were more dominant. For the CIP specimens, it was typical that Stud Pairs 1 and 12 were dominated by cracks growing from the outer (beam end) faces and propagating towards the middle of the beam. Taking a step inwards, Stud Pairs 2 and 11 did not show signs of dominant crack directions, having both the east and west cracks of equal lengths. Stud Pairs 3 to 10 began to show cracks with dominant directions initiating on the side of applied shear force (Stud Pairs 3 and 4 on the east face, Stud Pairs 5 to 10 on the west face). A different behaviour was observed for the precast specimens. Typically, it was observed that the dominant crack initiated on the face that experienced the applied shear force. Thus, Stud Pairs 1 to 4 experienced dominant cracking initiating at the east face and propagating towards the west, and Studs Pairs 5 to 12 experienced the exact opposite. A more in depth analysis on this effect has been completed in Section 5.3.3 and explains how concrete shrinkage affects the stud's initial stress state in a CIP specimen in comparison to a precast specimen, ultimately resulting in the different observed fatigue crack patterns.

4.3.3   Fatigue Failure Criterion for Shear Studs

One of the objectives of this thesis is to establish and confirm an instrumentation technique that accurately detects and classifies stud failure. However, in order to do so, the definition of failure for a single stud must first be established. The criterion for failure can be selected at one of three distinctive milestones during the fatigue life of a stud:

1. The initiation of a fatigue crack. It is difficult to pinpoint the exact moment when a fatigue crack is initiated. In fracture mechanics, it is always assumed that a small crack or imperfection with a given radius is present. For the sake of defining a failure criterion, crack initiation will be defined by a crack that reaches 1 to 2 mm in length. This is based on the observed results and will be discussed further in this section.

2. The onset of a reduction in the stiffness of the stud. This defines when the stud truly begins to experience the negative effects of the fatigue cracking and will be defined by the first peak and subsequent decrease in the local strain distortion data.

3. The complete severance of the stud from the top flange with no capacity remaining.

Failure Criterion 1 is the most conservative, however, there is no practical method of determining when the fatigue crack has initiated to 1 to 2 mm in length without conducting cross-sectional autopsies. Early on in the research study, it was hypothesized that the peaking behaviour in the local distortion data denoted a point in time where the fatigue crack initiated to a small length. This was, however, proven to be false, as cracks were discovered on studs that did not have a peaking response and on studs that demonstrated only a rising behaviour. Failure Criterion 2 defines a physical state when the fatigue cracks are substantial enough to negatively affect the stud performance. It is defined by the first definitive peak in the local distortion data and is the point when the stud begins to resist less shear force due to force redistribution. Failure Criterion 3 is the least conservative and defines when the fatigue cracks have propagated to a point which completely severs the stud from the top flange or has very little area in contact remaining. Studs falling into this failure criterion could either be removed by hand or with a single blow from a hammer.

An important step in selecting and validating a definition of failure was investigating various studs demonstrating a no response, rising, and post peaking local distortion behaviour. The bend test was also performed on many of the studs to confirm its validity in terms of determining the residual strength of a stud after incurring fatigue damage. Table 4-10 provides a collection of data utilized

for establishing the failure criterion. The table contains the data from the studs where cross-sections were taken, as well as several studs which were visually inspected during the autopsies. The results have been categorized by the local distortion states at the time the fatigue testing was terminated.

Table 4-10: Autopsy and cross-section results used to establish a failure criterion.

Local Distortion State	Specimen	Stud	Cross-Section	Findings	Bend Test
No Response	C100	N10	Yes	3 mm (E) crack in shank	Not tested
No Response	C120	N11	Yes	2 mm (E)	Pass
No Response	C067	N12	Yes	No cracking	Pass
Post Peak	C100	N2	Yes	12 mm (W)	Pass
Post Peak	C067	S1	Yes	10 mm (W)	Pass
Post Peak	P120	S1	Yes	3 mm (W) & 10 mm (E)	Pass
Post Peak	C100	S10	Yes	No cracking	Not tested
Post Peak	C120	S10	Yes	3 mm (E)	Pass
Post Peak	C100	S11	Yes	9 mm (E)	Pass
Post Peak	P200	S11	Yes	11 mm (W) & 7.5 mm (E)	Not tested
Post Peak	C100	S2	Yes	Visual cracking (not measured)	Pass
Post Peak	C300	S4	Yes	11 mm (W) & 3 mm (E)	Pass
Rising	C300	S5	Yes	1 mm (W)	Pass
Rising	C120	N10	No	No visual cracking	Pass
Rising	C120	N2	No	Visual cracking	Pass
Rising	C120	N3	No	No visual cracking	Pass
Rising	C120	N4	No	No visual cracking	Pass
Rising	C200	N4	No	No visual cracking	Pass
Rising	C300	N5	No	No visual cracking	Pass
Rising	P300	N6	No	No visual cracking	Pass
Rising	P300	N8	No	Visual cracking	Pass
Rising	C120	S2	No	Visual cracking	Pass
Rising	C120	S3	No	No visual cracking	Pass
Rising	C120	S4	No	No visual cracking	Pass
Rising	C200	S4	No	No visual cracking	Pass
Rising	P200	S4	No	Visual cracking	Pass
Rising	P300	S5	No	No visual cracking	Pass
Rising	P300	S6	No	No visual cracking	Pass
Rising	P300	S8	No	6.6 mm (W)	Fail

The first three rows detail the cross-sectional findings from studs demonstrating no response. Two of these three studs were found to contain small cracks of 3 mm and 2 mm. This possibly suggests that the strain gauge was not installed in the correct location to detect the local strain changes, or that the small cracks will not result in a measureable change in stiffness. Studs N12 and N11 on Specimens C067 and C120 passed the bend test, while N10 on C100 was not investigated. It is assumed that this stud would likely pass the bend test, despite its 3 mm fatigue crack.

The following nine rows detail the cross-sectional findings from studs stopped after demonstrating a peaking behaviour. Out of the nine studs, only Stud S10 from C100 was did not display signs of fatigue cracking (all others were cracked). Additionally, all studs that were investigated passed the bend test. Although a bend test was not performed on S11 in P200, it was assumed that it would have failed the bend test, similar to its neighbouring studs. This was completed in order to preserve the stud's condition and have it intact with the flange for the cross-sectional cut. Typically, 9 to 11 mm fatigue crack lengths were measured in these cross sections.

The remaining rows of data summarize the autopsy findings for studs demonstrating a rising local strain behaviour when the fatigue test was terminated. Stud S5 on Specimen C300 was the only cross-section taken for a stud exhibiting a rising behaviour and a crack size of 1 mm was observed. For the other studs inspected during the autopsies, 5 of 16 (31%) displayed visual cracking while the other 11 of 16 (69%) displayed no visual signs of fatigue cracking. Stud S8 from Specimen P300 was the only stud to fail the bend test, which subsequently exposed a 6.6 mm fatigue crack.

These findings ascertain that the peak in the local distortion data does not define the initiation of a crack, but rather indicates the point at which the fatigue cracks are sufficient enough to reduce the stiffness of the stud thereby attracting less shear force. It is difficult to pinpoint the exact moment when a fatigue crack is initiated as two of the no response studs exhibited a 2 and 3 mm fatigue crack. These crack lengths were also found to not reduce the stiffness of the stud by an amount large enough to be observed in the local distortion trends. Bend tests did not always provide an accurate means of determining failure as they were highly dependent on the crack growth. Bend tests enforce pivoting about the flange and if the crack is more vertical than horizontal, the stud

typically passed the test. Additionally, it was found that studs failed the bend test when approximately 50% or less of the original area was remaining.

After consolidating these findings, Failure Criterion 2 was selected as the definition of failure for a single stud. This fundamental definition of failure is further extended and applied later in Section 5.2 of this thesis. Section 5.2 completes multiple S-N analyses by varying the stress and number of cycles to failure, depending on how the stress was calculated and how the failure of the beam is defined. Failure for the beam or studs will be defined utilizing two approaches. The first approach defines a beam failure when the first stud displays a peaking behavior in the local strain data. The second approach defines a failure point for each stud demonstrating a peaking behaviour. The first approach is considered to be most conservative since the results collected from the static and fatigue data provided evidence that the specimens did not display a significant decrease in performance once the studs peaked. The large number of shear connectors present in a composite beam provide the structural system with a high degree of redundancy and capacity for force redistribution. This failure criterion is important, but can also be hard to utilize in field applications, as the peaking behaviour cannot be identified without onsite instrumentation.

5 Finite Element Analysis of Beam Behaviour

This chapter of this thesis presents a non-linear finite element analysis (FEA) study of the test specimens utilizing the software ABAQUS. The details of the FEA model material inputs and steps taken to verify the model are described. The FEA model is then compared to the experimental results, and an investigation into the effects of concrete shrinkage on the cast-in-place (CIP) models was explored.

5.1 Finite Element Analysis Model Types: Cast-In-Place and Precast

Two three-dimensional (3D) models were developed utilizing ABAQUS to model both a CIP and precast composite beam test specimen. First, the behaviour of the FEA models were verified by comparing the simulation results to the experimental data. The load-deflection behaviour, interfacial slip profile, strain profile, axial slab force, predicted by the models by comparing the model results to the experimental data obtained in the laboratory, and to investigate the effects of concrete shrinkage on the stress range in the shear connectors in the CIP model.

5.2 Geometry and Material Properties

The CIP and precast composite beam models were developed to replicate the test specimens as closely as possible. Details of test specimens were presented previously in Section 3.1. The primary difference between the actual specimen design and the ABAQUS model was in the modelling of the pockets in the precast concrete deck panels, in that the tapered pockets were replaced with 150 mm by 150 mm rectangular pockets that extruded vertically through the slab. To increase the analysis efficiency, planar symmetry was applied along the longitudinal centerline of the beam, effectively reducing the number of elements by a factor of two.

To accurately model the non-linear behaviour of the concrete slab and grout pockets, the concrete damaged plasticity function was utilized. This model function requires the following parameters: the uniaxial compressive strength (f'_c) and behaviour, uniaxial tensile strength (f'_t) and behaviour, Poisson's ratio ($v = 0.20$), dilation angle ($\psi = 40°$), shape factor ($K_c = 0.667$), stress ratio ($\sigma_{b0}/\sigma_{c0} = 1.16$), eccentricity ($\varepsilon = 0.1$), and viscoplastic regularization ($\mu = 0.00001$) parameters. The

properties for the concrete and grout were differentiated from one another by only adjusting the uniaxial compressive and tensile behaviour appropriately. The values for the remaining parameters were obtained from the extensive recent parametric FEA investigations conducted by Stoner (Stoner, 2015) and Genikomsou (Genikomsou & Polak, 2015) at the University of Waterloo.

The stress-strain equations used in defining the uniaxial compressive behaviour of the concrete and grout pockets are presented in Equations 5-1, 5-2, and 5-3 represent the linear elastic, nonlinear, and post-peak strain-softening behaviour of concrete in compression, respectively. The first region behaves linearly elastic until it reaches 40% of its maximum compressive strength, f'_c. Beyond this point, the material behaves non-linearly as it ascends up to f'_c. Following the peak, the material begins to descend until no strength remains at ε'_{cmax}. Equation 5-4 is a common relationship that determines the strain at the compressive peak, ε'_c, given f'_c and E_{co}, the initial stiffness of the concrete (Equation 5-5), typically called the tangential modulus of elasticity. The secant modulus of elasticity, E_{sec}, is defined by Equation 5-6.

$$\sigma_c = E_{co}\varepsilon_c \quad when, \quad \sigma_c \leq 0.4 f'_c \tag{5-1}$$

$$\sigma_c = f'_c \left[2\left(\frac{\varepsilon_c}{\varepsilon'_c}\right) - \left(\frac{\varepsilon_c}{\varepsilon'_c}\right)^2 \right] \quad when, \quad \frac{\varepsilon_c}{\varepsilon'_c} \leq 1.0 \tag{5-2}$$

$$\sigma_c = f'_c \left[1 - \frac{\left(\varepsilon_c - \varepsilon'_c\right)^2}{\left(\varepsilon'_{cmax} - \varepsilon'_c\right)^2} \right] \quad when, \quad \frac{\varepsilon_c}{\varepsilon'_c} > 1.0 \tag{5-3}$$

$$\varepsilon'_c = \frac{2 f'_c}{E_{co}} \tag{5-4}$$

$$E_{co} = 5500\sqrt{f'_c} \ (MPa) \tag{5-5}$$

$$E_{sec} = 5000\sqrt{f'_c} \ (MPa) \tag{5-6}$$
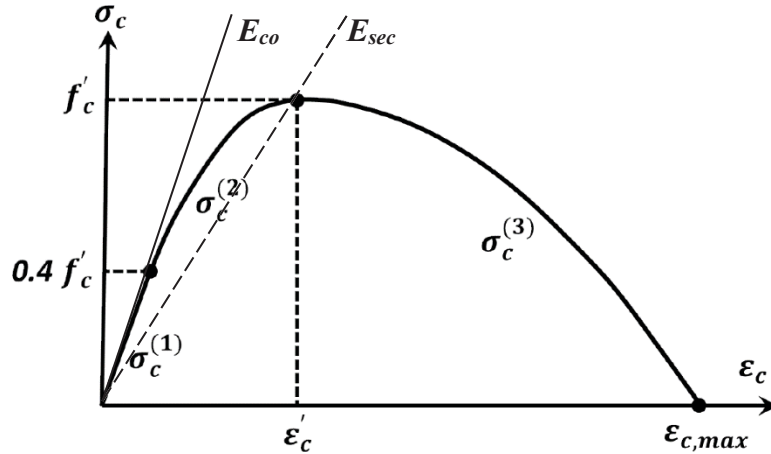
Figure 5-1: The stress-strain relationship defining the uniaxial compressive behaviour (Stoner, 2015).

When simulating the uniaxial tensile strength of concrete in ABAQUS, it is often characterized by a stress-crack opening displacement response rather than a stress-strain relationship. Researchers employing the stress-strain approach in the past have often come across significant convergence difficulties. Stoner (2015) experienced numerical issues when utilizing a stress-strain approach, and found that it introduced unreasonable amounts of mesh sensitivity into the results (i.e., results varied largely based on assigned element sizes). It has been suggested that the sharp discontinuity change in curvature at the tensile peak is solely responsible for this problem (Wang and Hsu, 2001).

The stress-crack opening displacement method utilized in the model is based on the fracture energy approach. The fracture energy of concrete is dependent on several factors, including the water to cement ratio, aggregate size, curing conditions, and age of the concrete. The most influential factor on fracture energy in concrete however, is the compressive strength (International Federation for Structural Concrete, 2013). The Model Code 1990 has estimated the fracture energy, G_f, for concrete utilizing the following empirically derived equations:

$$G_f = G_{fo} \left(\frac{f_{cm}}{f_{cmo}} \right)^{0.7} \tag{5-7}$$

$$f_{cm} = f_{ck} + 8MPa \tag{5-8}$$

$$f_{ck} = f'_c - 1.6MPa \tag{5-9}$$

109

where:

G_{fo} = the base fracture energy value [N/mm],

f_{cm} = the mean value of the concrete compressive strength [MPa],

f_{cmo} = defined as 10 MPa, and

f_{ck} = the characteristic compressive strength [MPa].

The stress-crack opening displacement approach in ABAQUS requires the input of a stress-displacement curve, defined by the post cracking tensile stress as a function of the crack opening displacement, w. This function is typically modeled in three different ways: linearly, bi-linearly, or exponentially. In Stoner's (2013) research, he determined that the linear model produced responses that demonstrated additional strength during post-cracking compared to the others. The bi-linear and exponential functions both demonstrated accurate and identical results compared to one another. Thus, for the purpose of this thesis, a bi-linear stress-crack opening displacement response was selected due to its simpler form and is illustrated in Figure 5-2a. This bi-linear curve is defined by the Equations 5-10 to 5-15.
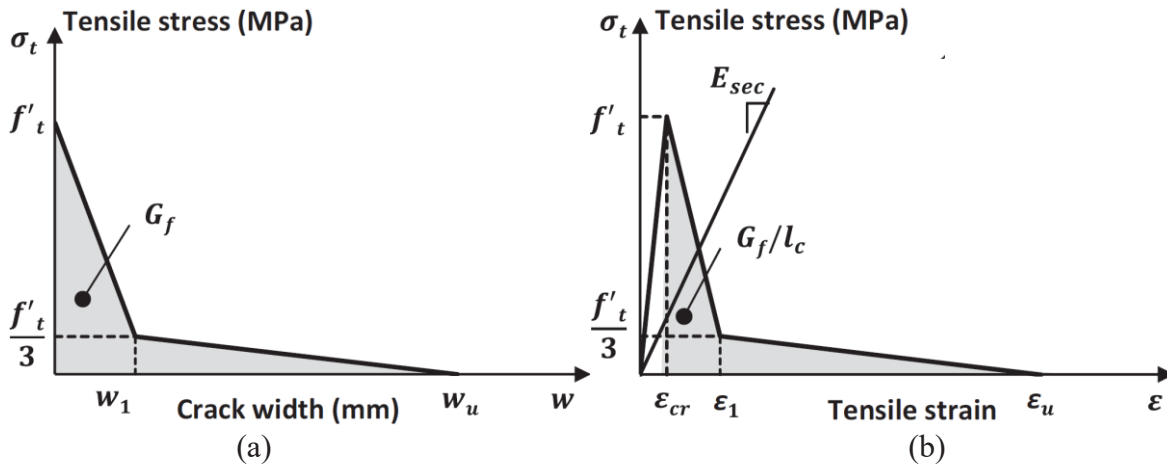
Figure 5-2: (a) Uniaxial tensile stress-crack opening displacement and (b) stress-strain relationship for concrete (Genikomsou & Polak, 2015).

$$w_1 = 0.8\left(\frac{G_f}{f'_t}\right) \tag{5-10}$$

$$w_u = 3.6\left(\frac{G_f}{f'_t}\right) \tag{5-11}$$

$$f'_t = 0.33\sqrt{f'_c} = E_{co}\varepsilon_{cr} \tag{5-12}$$

$$l_c = \sqrt[3]{V} \tag{5-13}$$

$$\varepsilon_1 = \varepsilon_{cr} + \frac{w_1}{l_c} \tag{5-14}$$

$$\varepsilon_u = \varepsilon_{cr} + \frac{w_u}{l_c} \tag{5-15}$$

Translating stress-crack opening displacement behaviour into a stress-strain curve is completed by dividing the crack width (w) by the characteristic length of the element (l_c) and adding the cracking strain (ε_{cr}). In 3D elements, the characteristic length can be defined by the cubic root of its volume (V) (Genikomsou & Polak, 2015).

The parameters defining the concrete and grout compressive and tensile behaviour were calculated assuming a compressive strength of 45 MPa and 60 MPa, respectively. The maximum compressive strain values were selected at 0.008 mm/mm for both materials. The base fracture energy values suggested by the Model Code (1990) are tabulated as a function of the maximum aggregate size in the concrete or grout matrix. The maximum aggregate sizes for the concrete and grout were 16 mm and 10 mm, respectively, resulting in G_{fo} values of 0.030 N/mm and 0.026 N/mm, respectively. Furthermore, the fracture energy values for the concrete and grout were calculated to be 94.4 N/m and 97.8 N/m. The compressive and tensile stress-strain responses for the concrete and grout are plotted in Figure 5-3.

The reinforcing bars, steel section, and studs were modeled by applying a bi-linear stress-strain relationship as depicted in Figure 5-4. The relationship assumes an elastic, perfectly-plastic response. The steel components were assumed to have an elastic modulus of 200,000 MPa, with yield strengths of 400 MPa for the reinforcing bars, and 350 MPa for the steel section and shear studs.
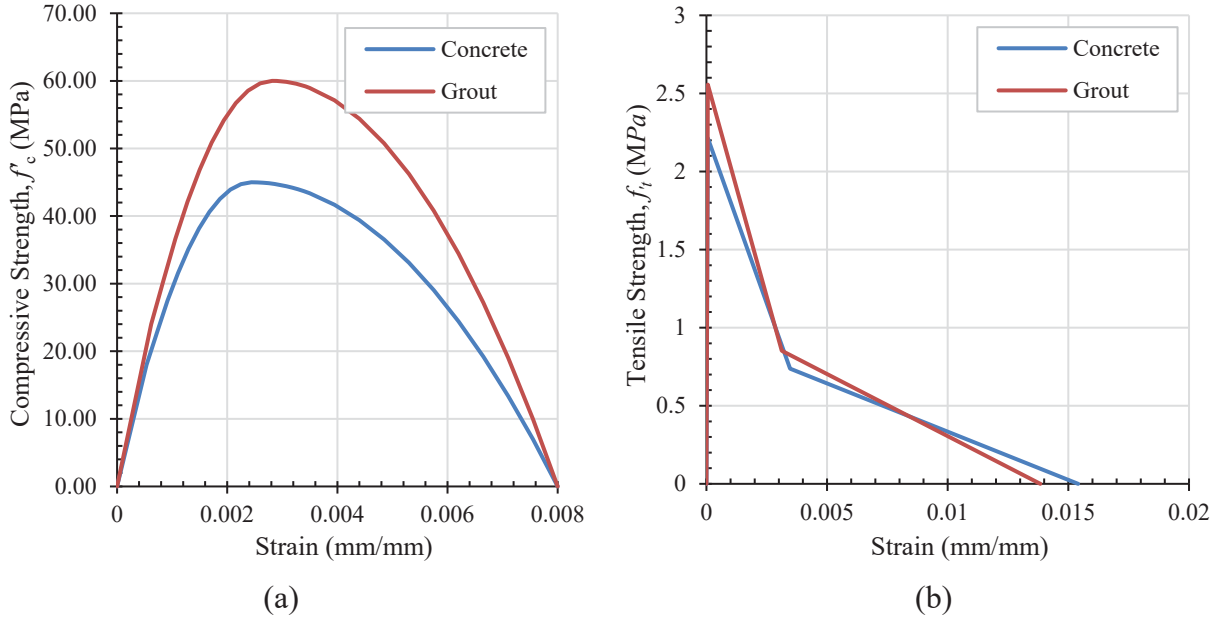
Figure 5-3: (a) Compressive strength and (b) tensile strength for the concrete and grout.
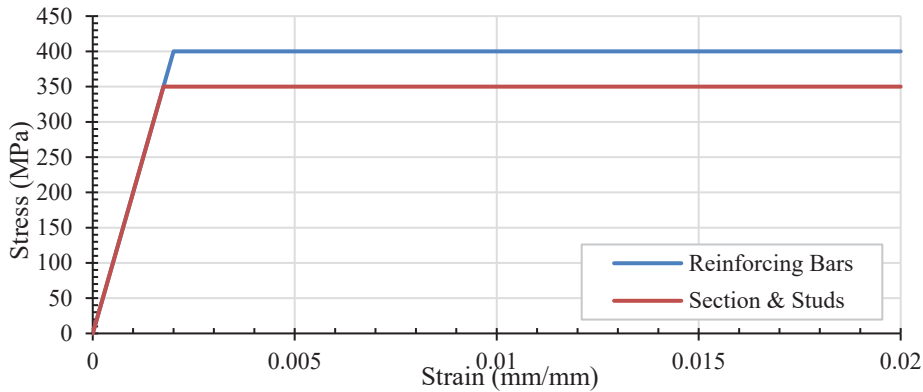
Figure 5-4: Stress-strain behaviour for the reinforcing bars, steel section, and studs.

The concrete slabs, steel sections, and shear studs for both the CIP and precast models were simulated utilizing 8-noded brick elements with reduced integration (C3D8R). The grout pockets in the precast model were also simulated using C3D8R elements and the 10M reinforcing bars were replicated utilizing 2-node linear 3D truss elements. The concrete slab and grout pocket mesh was seeded and fashioned from elements 10 mm in size. The studs, steel section, and reinforcing bars, utilized element sizes of 5mm, 15 mm, and 25 mm, respectively. Table 5-1 provides a summary of components used in the model. It includes the element types, elements sizes, plasticity models, failure stresses, and failure strains. Figure 5-5 provides illustrative examples of the mesh density utilized for the concrete, grout, steel, and shear studs. A mesh refinement study was not

112

completed to determine the effects of mesh size on the simulation results. It was assumed, however, that the mesh sizes and element types selected for the various components would provide accurate results, based on previous and similar simulations completed by Liu, Bradford, Chen, and Ban (2016).

Table 5-1: Component summary.

Component	Element Type	Element Size (mm)	Plasticity Model	fy, f'c (MPa)	εy, ε'c
Concrete	C3D8R	10	Concrete Damaged Plasticity	45	0.00244
Grout	C3D8R	10	Concrete Damaged Plasticity	60	0.00282
Studs	C3D8R	5	Plastic	350	0.00175
Steel Section	C3D8R	15	Plastic	350	0.00175
Reinforcing Bars	T2D2	25	Plastic	400	0.00200
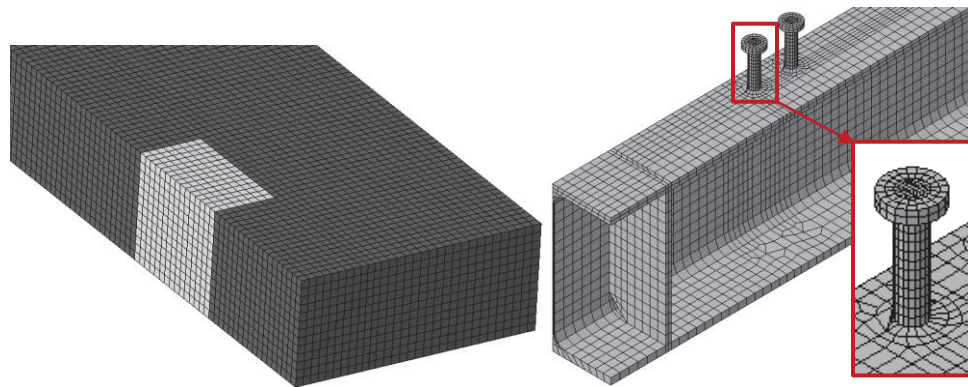
Figure 5-5: Mesh density for the concrete slab, grout pocket, steel beam, and shear studs.

The longitudinal and transverse reinforcing bars in the concrete slab were modeled by utilizing the embedment constraint. The embedment technique is used to specify a group of elements (reinforcement) that lie embedded in a group of host elements (concrete). It was noted that the embedment constraint assumes perfect bond between the embedded and host materials. The same constraint was applied when modelling the longitudinal shear connection. The studs were either embedded into the concrete slab or grout pockets for the CIP or precast models, respectively. The studs were selected as the group of elements hosted inside the concrete medium. Figure 5-6 demonstrates the embedment constraints for the reinforcement and studs in the precast model. The reinforcement and studs are highlighted in red, denoting the embedded material. The concrete and pockets are highlighted in magenta to denote the host material.
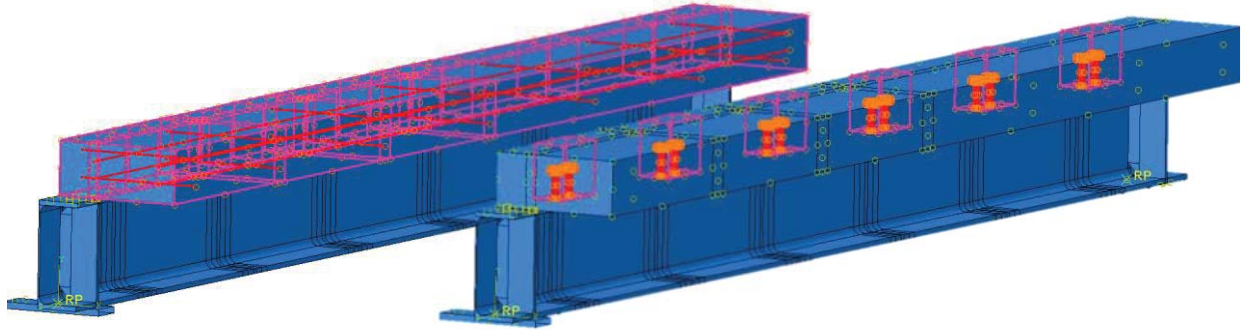
Figure 5-6: Reinforcement and stud embedment constraints.

A hard contact condition was implemented between the underside of the slab and the top of the steel beam flange. For the tangential behaviour, friction was assigned using the penalty formulation option. For both the CIP and precast models, a friction coefficient of 0.83 was applied. This friction coefficient was determined from the past experimental work by Chen (2013) when investigating the interfacial friction between concrete slabs and steel flanges. A surface to surface discretization method was selected assuming finite sliding.

The beams were modeled assuming a pin support at the west end, and a roller at the east end. The supports were modeled utilizing 3D rigid bodies that were tied to the underside of the beam. The width of the rigid plates was 75 mm and represented the actual widths of the pins and rollers used in the testing. At the bottom the rigid body, a reference point was established in which the behaviour of a roller or pin could be assigned (Figure 5-7). The pin at the west support was allowed to rotate about the x-axis. The roller located at the east support was free to translate along the z-axis and rotate about the x-axis. A symmetry boundary condition was assigned to the model face representing the longitudinal centerline of the beam since the symmetrical specimen geometry was accounted for to improve model efficiency. This boundary condition restrains translations in the x-direction and restricts rotations about the y- and z-axes.
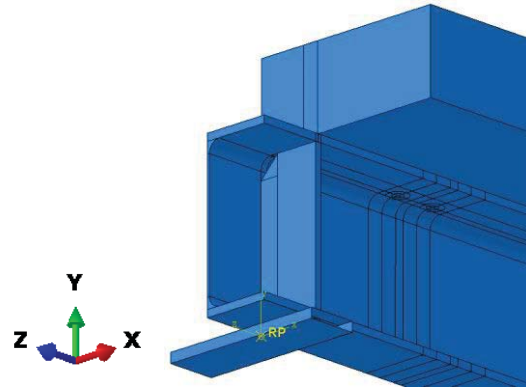
Figure 5-7: West pin support applied to the FEA model consisting of a rigid plate and a reference point.

The loading on the composite beam was applied to the specimen as a pressure at the two loading points located at 500 mm and 1000 mm from the west support. The pressure was applied using the total force option, and was selected over a 50 mm x 100 mm area for each of the two points. The load applied to the half model is exactly half of the load required to achieve the same moment in a full model. A total load of 500 kN was applied to the half model (reflecting a 1000 kN load on a full model) in order to explore the beams non-linear response at the ultimate limit state. To compare the results of the FEA to the experimental results measured during the static load cycles, a 100 kN load (200 kN full model) was also applied. Figure 5-8 illustrates the boundary condition and pressure load configurations on the model; the highlighted area on the vertical face depicts the selection for the symmetry boundary condition, and the horizontal highlighted area on top of the slab locates where the loading is applied.
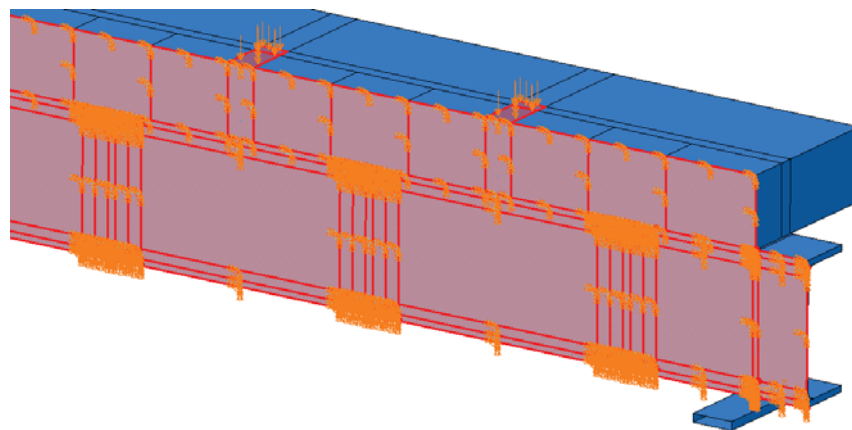
Figure 5-8: Symmetry boundary condition and the two loading points applied to the FEA model.

115

The FEA simulation was conducted by applying ABAQUS/Standard, which utilizes solution techniques that are ideal for static and low-speed dynamic solutions. The alternative choice is ABAQUS/Explicit, which is best suited for transient and highly nonlinear simulations. Although the explicit package is more powerful, the standard package is more user friendly and is the more ideal selection for the simulation since the problem is static in nature. The solution was first attempted by solving the loading step with the general solver, however, it experienced difficulties when iterating for adequate solutions when the material began to behave nonlinearly. The RIKS solver was then employed since it is excellent at solving problems that experience significant changes in the model stiffness due to nonlinear material behaviour, buckling, or collapse.

5.3 Finite Element Analysis Results

The first analyses were conducted to a total load of 1000 kN to verify the non-linear response of the models. It was estimated from hand calculations that the ultimate capacity of the beams assuming full-shear connection was 861 kN for the given configuration. Considering that the beams in the experimental program had a 33% partial shear connection for a 1000 mm shear span, it was assumed that the beams would display plastic behaviour and possibly experience failure prior to the calculated ultimate capacity of 861 kN for full composite behaviour. Following the load-deflection behaviour, the CIP and precast models were utilized to determine the nominal stress behaviour of the stud with respect to the applied loading of the beam. This was completed to ascertain the adequacy of assuming a linear relationship and being able to scale the applied loads on the beam to the nominal shear stress in the studs, which is completed in Section 6.1. In addition to the non-linear response checks, both the CIP and precast FEA models are compared to the static test data collected at an applied load of 200 kN load.

5.3.1 Non-Linear Response of The CIP and Precast Model

The non-linear load-displacement response of the CIP and precast models are presented in Figure 5-9. For reference, the theoretical load-displacement responses for a full-interaction composite beam, beam with 33% partial shear connection, and a steel beam alone (no slab) are overlaid on the plot. Additionally, the ULS for the full-interaction composite beam and steel beam alone are illustrated on the plot as grey horizontal dashed lines, representing an applied load of 861 kN and 444 kN, respectively. Upon inspection of both the models, it was determined that Studs Pair 1

(closest to west support) began to experience localized yielding at an applied load of 282 kN for the CIP and 343 kN for the precast. Stud Pair 2 began to yield at an applied load of 350 kN for the CIP and 334 kN for the precast. The estimated applied load at which the studs begin to yield assuming full interaction is 241 kN for both stud pairs. The 41 kN to 109 kN difference can be attributed to the fact that as the degree of shear connection and interaction decreases, the resistive moment provided by composite action, M_{comp}, also decreases. This results in a reduction of the resistive force transferred along the steel-concrete interface by the shear connectors for a given applied load. The beams curvature increases as a result, and the resistive moments provided in the steel and concrete, M_s and M_c, increase to make up for the loss in M_{comp} (see Section 4.1.3). Thus, the studs in a beam with partial shear connection/interaction will resist a lower longitudinal shear force than a beam with full interaction subject to the same applied load. Additionally, The FEA model incorporated friction at the steel-concrete interface, reducing the stud forces even further.

The web was next to yield in shear near the west support for the CIP and precast models at an applied load of 500 kN. Lastly, the bottom flange of the steel section started to yield at the location of maximum moment at a load of 722 kN and 747 kN respectively. The estimated applied load at which the bottom flange yields assuming full interaction and Euler-beam theory is 643 kN. It was not expected that the theoretical load yielding the bottom flange in bending would be lower than what was estimated by the FEA model. When assuming full interaction (theory), the stress at the bottom flange due to bending should be smaller in comparison to a partially connected beam (FEA) because the curvature is less in the full interaction case given the same applied load. There is a possibility that due to the web yielding near the west support, significant force redistribution and changes in bending behaviour have taken place in the FEA model, resulting in lower stresses compared to a beam in pure theoretical bending. The Von-Mises stress contour plots of the three yielding events for the CIP model are presented in Figures 5-10 to 5-12, and are denoted by the three white circles in Figure 5-9.

The initial response of the CIP and precast models were found to be less stiff than the full-interaction case, but was more stiff than the 33% partial shear connection case. The CIP and precast models demonstrated identical bending stiffnesses up to an applied load of 722 kN. At this applied load level, the bottom flange of the CIP model begins to yield resulting in a deviation from the

precast response. Once the bottom flanges in both models yield due to bending, they begin to demonstrate similar non-linear responses that reduce in stiffness as the applied load is increased. It is hypothesized that the bottom flange yields in the precast model after the CIP due to the increased strength and modulus of elasticity of the grout. At higher loads, the localized concrete crushing around the studs in reduced, subsequently reducing the interfacial slip at the interface, and ultimately reducing the bending stress at the lower flange.
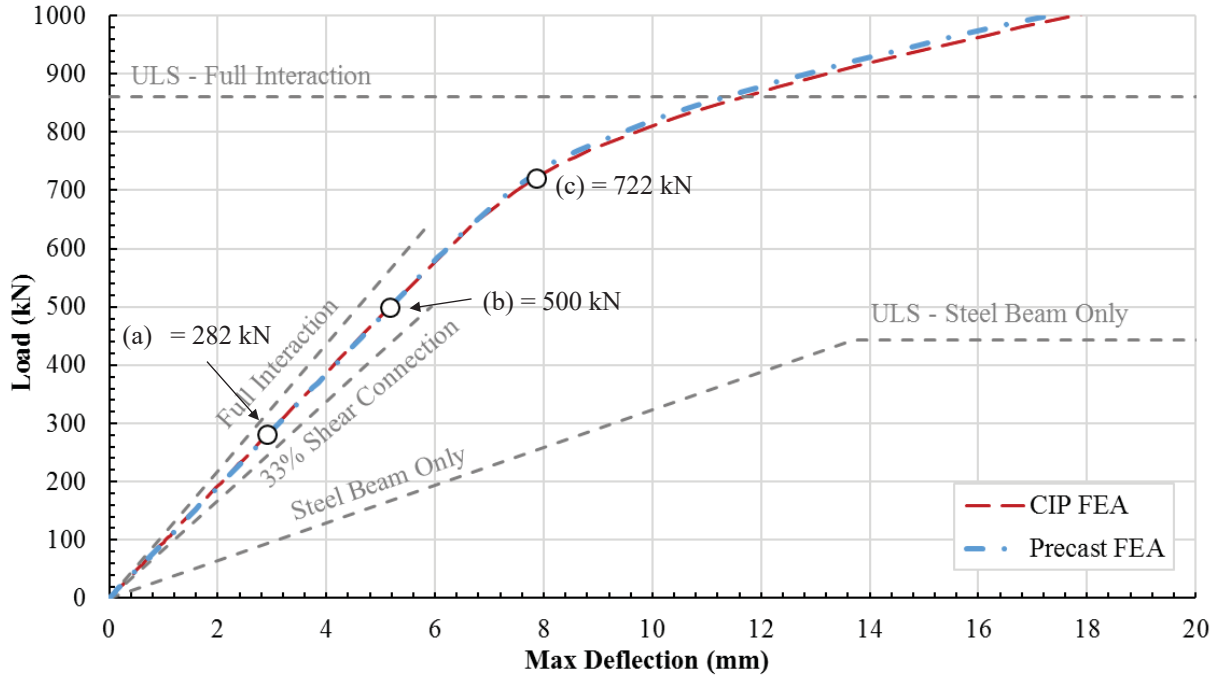
Figure 5-9: Non-linear load-displacement response of the CIP and Precast FEA model. (a) Stud Pair 1 demonstrating localized yielding in CIP, (b) web near west support yields in CIP, and (c) bottom flange at max moment yields in CIP.
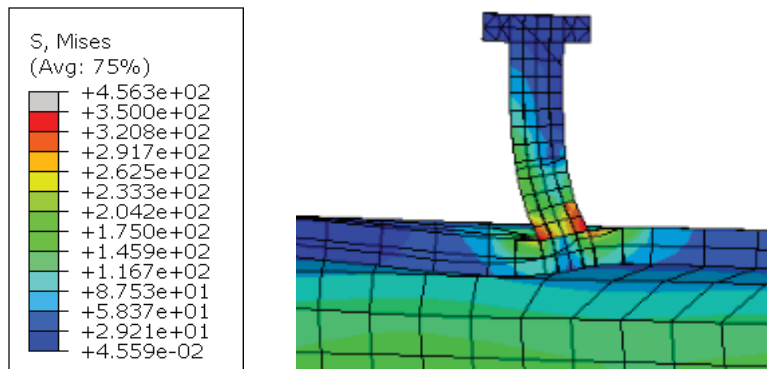
Figure 5-10: Von Mises stress contour plot demonstrating yielding in Stud Pair 1 at an applied load of 282 kN for the CIP model.

118

Figure 5-11: Von Mises stress contour plot demonstrating yielding of the web located at the west support at an applied load of 500 kN for the CIP model.
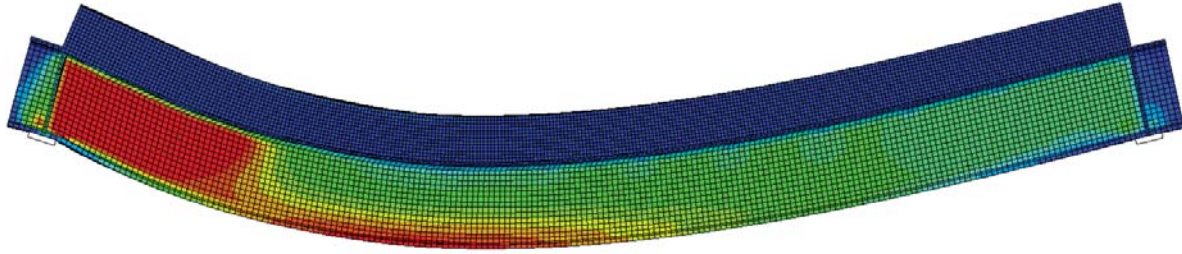
Figure 5-12: Von Mises stress contour plot demonstrating yielding of the bottom of the flange located at max moment at an applied load of 722 kN for the CIP model.

The behaviour of the stud stress with respect to the applied loading on the beam was also explored in both of the FEA models. According to theory, the nominal shear stress acting on the studs is a linear function with respect to the applied loading. This assumes Bernoulli's beam theory, with plane sections remaining plane, and no slip or friction at the steel-concrete interface. Both the CIP and precast models incorporate slip, friction, and utilize non-linear material properties, enforcing the shear stress to decrease by an unknown magnitude. Since the studs in the CIP and precast models are encased in concrete with a compressive strength of 45 MPa and 60 MPa, respectively, it was hypothesized that localized crushing of concrete at the base of the stud would occur at different load levels, ultimately changing the behaviour of the stud as the load is increased. The free body function was utilized in determining the resistive forces acting on Stud Pairs 1 and 2. This function finds the resulting static forces and moments for the selected set of elements. The resulting shear force resisted by the stud was then divided by its nominal area to determine its nominal shear stress. The nominal shear stress in Stud Pairs 1 and 2 as a function of the applied load for both the CIP and precast models is presented in Figure 5-13.
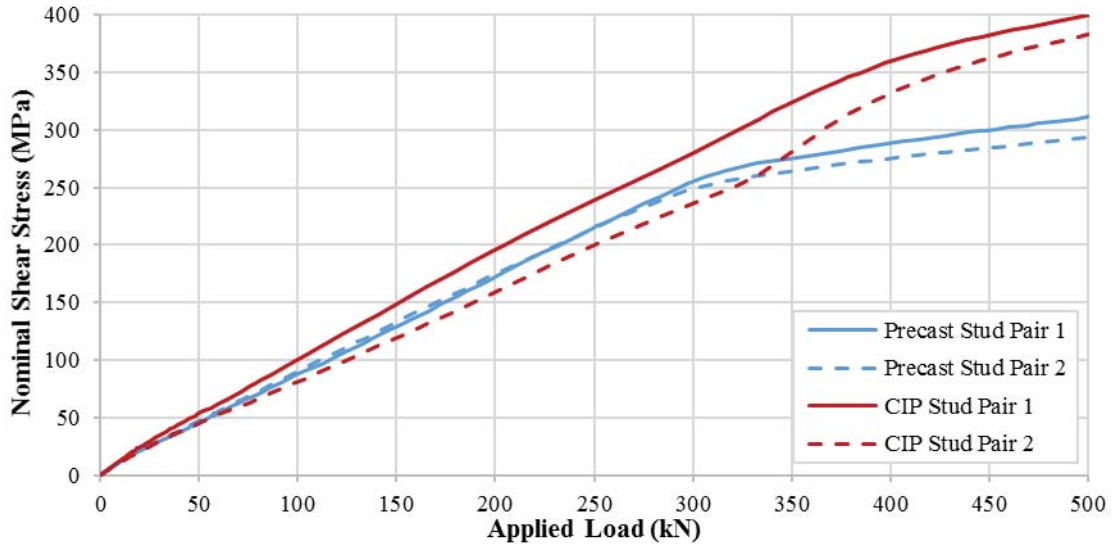
Figure 5-13: Nominal shear stress as a function of the applied load for Stud Pairs 1 and 2 in the CIP and Precast models.

The relationships plotted in Figure 5-13 demonstrate a linear response for Stud Pairs 1 and 2 in both the CIP and precast models for an applied load up to approximately 300 kN. According to theory, this corresponds to a theoretical stud stress of 447 MPa. The only test where the applied load was greater than 300 kN was for Specimens C300 and P300. Due to the overloads in the variable amplitude loading history being two times greater than the equivalent stress, a load of 402 kN was applied to achieve a theoretical stress of 600 MPa (effectively yielding the connection). The rest of the tests stayed well under the 300 kN load, with C200 and P200 peaking at an applied load of 268 kN resulting in a theoretical shear stress of 400 MPa. From these findings, it can be concluded that the shear stress in Stud Pairs 3 to 12 also behave linearly with respect to the applied load level being that they experience a theoretical shear stress three times lower than Stud Pairs 1 and 2. Additionally, this behaviour ascertains the adequacy of assuming a linear relationship and being able to scale the applied loads on the beam to the nominal shear stresses in the studs when the applied load is less than 300 kN. The application of this is further explained in Section 6.1.

5.3.2   Comparison of FEA Results to Experimental Results at 200 kN

The predicted responses from the CIP and precast FEA models were compared to the initial (0%) static test results for Specimen C100 and P300 at the 200 kN load level. The comparison included the load-deflections (Figure 5-14), slip profiles (Figure 5-15), strain profiles at A and B (Figures

5-16 and 5-17), and slab axial forces (Figure 5-18). The FEA load-deflection results (Figure 5-14) for both the CIP and precast models were identical to one another demonstrating a deflection of 2.06 mm at the location of maximum moment for a 200 kN load. The load-deflection behaviour was linear in nature, and the initial static results for C100 and P300 demonstrated deflections of 2.59 mm and 2.48 mm, respectively. A stiffer deflection response was demonstrated by both the FEA models compared to both the specimens and what theory, assuming a 33% shear connection, would estimate. This difference in stiffness could be due to an increased degree of shear interaction at the steel-concrete interface consequently decreasing the curvature and deflection of the beam. Thus, the shear connection stiffness may have been overly estimated by utilizing the embedment constraint with friction at the interface.
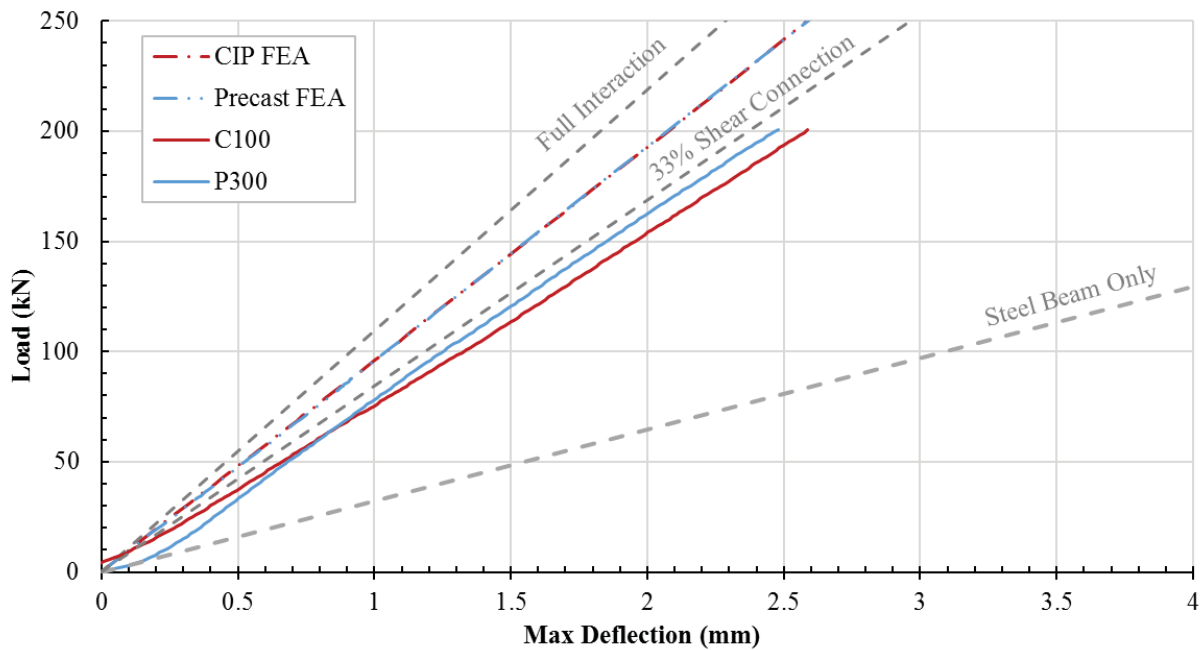
Figure 5-14: Comparison of experimental and FEA load-deflection results up to an applied load of 200 kN.

The FEA slip profile results are shown in Figure 5-15 and have an excellent correlation to the experimental results. Unlike the deflection results, these data suggest the interfacial shear stiffness was accurately modeled and estimated in the FEA models. Figure 5-15 contains the interfacial slip values along the longitudinal axis (U3) of the composite beam determined at a load of 200 kN. The FEA interfacial slip was determined by subtracting the U3 nodal translations of the bottom of

121

the concrete slab relative to the translations at the top of the beam flange, resulting in the change in position relative to one another. A positive and negative value for this plot represents that the slab is slipping to the left and right, respectively, relative to the top flange of the beam. The experimental results were collected at 0, 500, 1000, 2000, and 3000 mm from the west support. The FEA results were collected at 60 mm intervals (totaling 51 data points) along the beam axis. When sampling at this interval, the behaviour of the slip in between stud pockets or individual stud rows becomes apparent. The interfacial slip decreases in magnitude at the locations of the stud rows, while the slip in between stud rows increases in magnitude, resulting in an undulating trend.
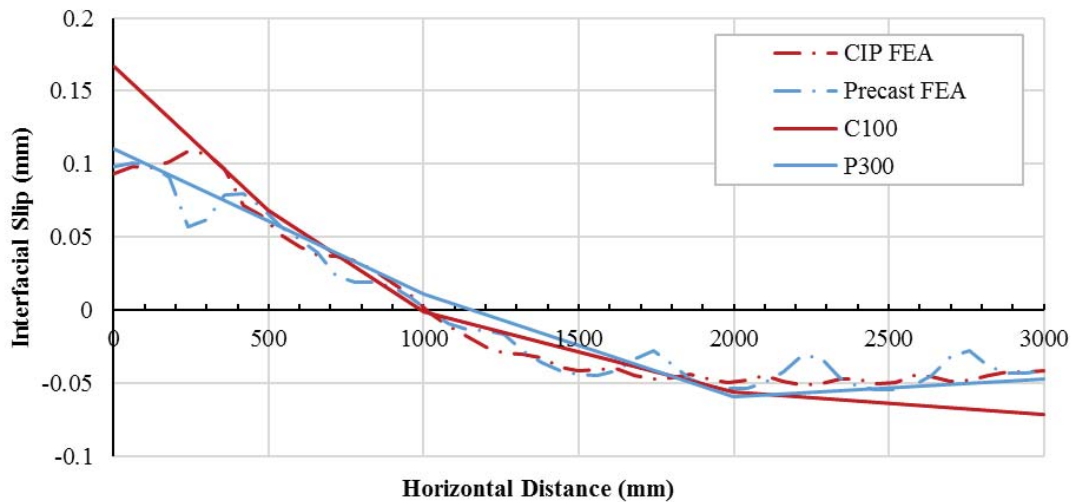
Figure 5-15: Comparison of experimental and FEA slip profile results at an applied load of 200 kN.

The FEA strain results (E33 or strain along the longitudinal axis of the beam) are plotted for Profile A and B in Figures 5-16 and 5-17, respectively. The black dashed line represents the theoretical strain profile assuming full composite interaction with no slip at the interface. For both profiles, the CIP and precast strain results were nearly identical through the concrete slab and steel beam. The slip-strain at the steel-concrete interface for Profile A and B was found to be 198 $\mu\varepsilon$ and 148 $\mu\varepsilon$, respectively. This was determined by taking the difference in strain values at the top of the steel section and bottom of the concrete slab at the interface of the profiles. The slip at a given location is equal to the integration of slip-strain along the interface from the location of zero moment to the end of the slab. The location of the neutral axis in the steel beam at Profile A was lower in the experimental results than the FEA models, suggesting reduced composite interaction. At Profile B, the neutral axis in the steel was found to be similar for the CIP and precast FEA

models, and Specimens C100 and P300. The FEA results displayed lower magnitude strains at the bottom of the steel section in comparison to the experimental specimens. It also appears that the FEA models display a lower degree of curvature compared to the experimental models, suggesting that the stiffness of the longitudinal shear connectors in the FEA model are higher than in the experimental specimens.
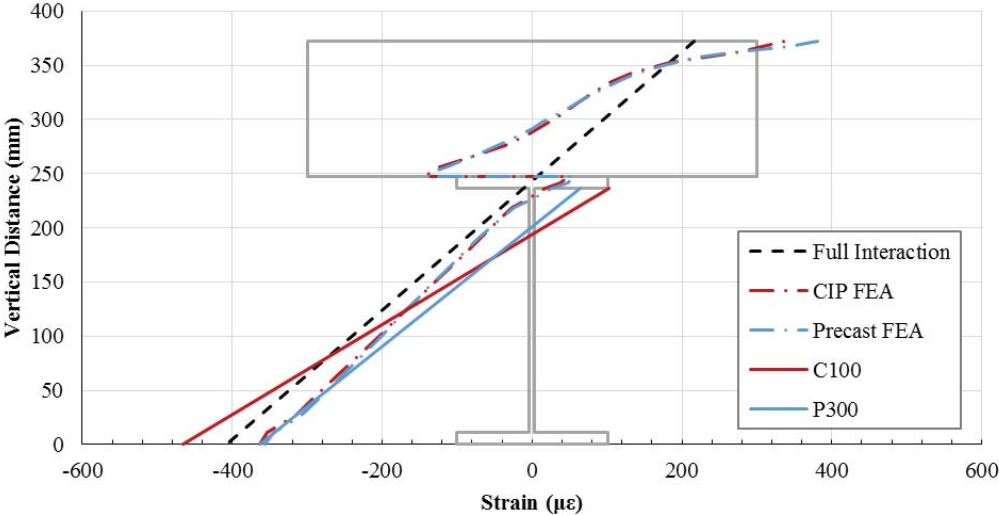
Figure 5-16: Comparison of experimental and FEA strain results at Profile A for an applied load of 200 kN.
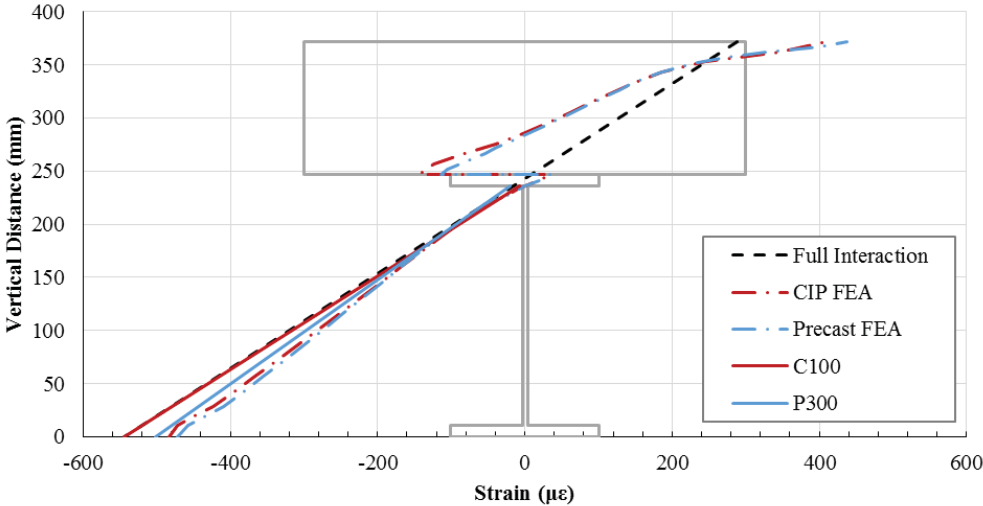
Figure 5-17: Comparison of experimental and FEA strain results at Profile B for an applied load of 200 kN.

The slab axial forces predicted by the FEA were obtained by summing the nodal forces across the slab cross section at a 200 kN load level. The slab axial force was determined at 60 mm intervals along the longitudinal axis and plotted as shown in Figure 5-18. The theoretical value and initial (0% fatigue life) experimental values for C100 and P300 are also plotted for comparison at locations A, B, Y, and Z (500, 1000, 2000, 2500 mm). At the stud locations, a significant drop in slab axial force is observed in the FEA results, and is due to the studs transferring the longitudinal slab forces at the slab-beam interface. In between the stud locations, two types of behaviour can be seen depending on the longitudinal location. At the locations where the beam is loaded (500 mm and 1000 mm) and at the supports (0 and 3000 mm), the axial force in the slab demonstrates a gradual decrease due to friction at the interface. Friction can only take effect at a location where a normal force is present and is evident at the locations of load application. However, the fiction near the supports of the beams is due to the slab bearing into the top flange of the steel section. At locations 1500 mm to 2750 mm, plateau like behaviour is observed between studs, suggesting friction has little to no effect on the amount of force transferred into the studs in this region. In real life application, the self-weight of the slab creates a normal force along the entire length of the interface, effectively reducing the forces resisted by the shear connectors. In terms of design, the fact that the frictional forces and slip at the interface are neglected result in shear flow calculations that are larger in magnitude. Thus the shear connectors are experiencing lower than calculated shear ranges in beam tests over push-out tests, and suggest that the fatigue life of shear connectors in composite sections perform longer.
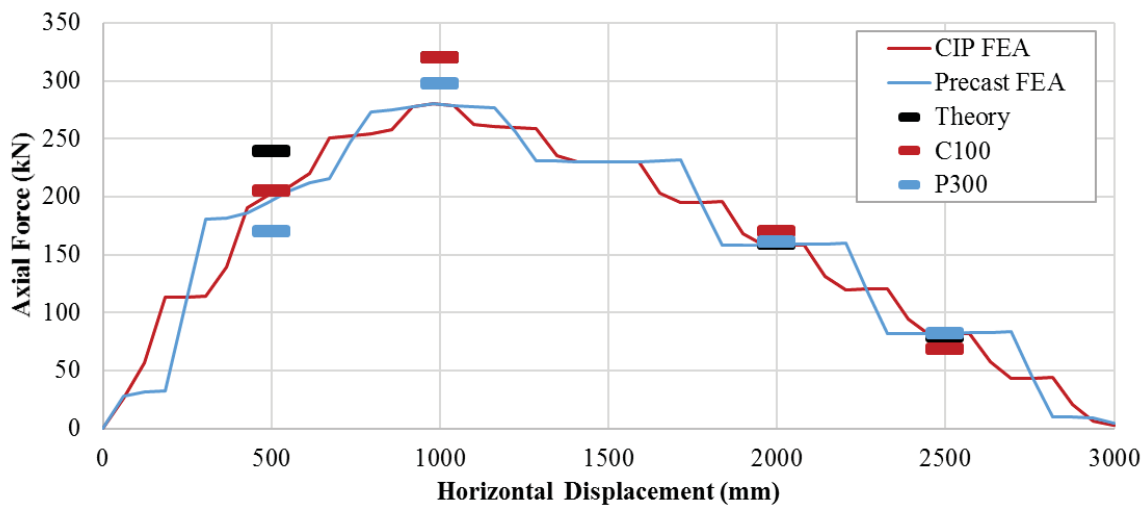
Figure 5-18: Comparison of experimental and FEA axial slab force results at an applied load of 200 kN.

In general, there is good agreement between the experimental results and the results predicted by the FEA. Although a parametric analysis was not completed to investigate the effects of varying the coefficient of friction across the steel-concrete interface, this should be considered in future research to achieve a more thorough understanding of the specimen behaviour and its effect on the shear connectors.

5.3.3 Effect of Concrete Shrinkage in Cast-In-Place Model

The FEA model was also used to investigate the effects of concrete shrinkage on the behaviour of the CIP composite beams. As demonstrated in the autopsy program (Section 4.3), the fatigue cracking behaviour in the CIP specimens was different than what was observed in the precast specimens. The construction process for the two specimen types differs in that the precast deck panels are not made composite to the steel beam until sometime after initial fabrication and concrete curing. As a result, the precast concrete will have experienced some portion of its early age shrinkage before installation on the steel beam. In contrast, the CIP deck is restrained by the steel beam during its entire period of concrete shrinkage. Thus, it was hypothesized that the effect of concrete shrinkage could be responsible for altering the stress state of the shear connectors between the two specimen types. This was investigated by estimating the concrete shrinkage and applying the unrestrained shrinkage as a loading type in the CIP FEA model to determine the resulting conditions. Prior to the FEA investigation, two calculation methods presented by ACI 209R-92 and CSA S6 (2014) for calculating shrinkage strain will be compared.

Concrete shrinkage is a phenomenon that occurs over time due to the curing process. It is defined as the decrease in volume of a hardened concrete matrix resulting from the loss of water by evaporation of water from the capillary pores of the mortar fraction of the hardened concrete, and due to the ongoing hydration of cement after hardening of the concrete. This contraction can result in unwanted cracks and stresses, and ultimately must be considered by engineers when designing concrete elements. Shrinkage strains start to develop immediately after exposing the concrete to a drying environment. Typically, models for shrinkage in cementitious concrete are used to express shrinkage strain development over time, as well as final or ultimate shrinkage strain. The common feature of the models is the ability to estimate shrinkage strain in concrete structures based on simple variables available early in the design stage.

The ACI 209R-92 addresses concrete shrinkage for normal density and normal strength concrete. The Cement Association of Canada (CAC) has adopted the ACI 209R-92 formulation for shrinkage strain in Section 1.2.3 of the CAC Handbook (2004) shown in Equation 5-16:

$$\varepsilon_{sh} = \frac{t}{C_s + t} \varepsilon_{shu} P_{sh}$$ (5-16)

where:

ε_{sh}	=	the shrinkage strain at a given time [mm/mm],
t	=	time in days starting immediately after the initial wet curing [days],
C_s	=	35 if moist cured for 7 days, 55 if steam cured for 1-3 days [unitless],
ε_{shu}	=	the ultimate shrinkage strain, 0.00078 in lieu of a more accurate analysis [mm/mm], and
P_{sh}	=	a correction factor for conditions that are other than standard [unitless],

The modification factor, P_{sh}, is calibrated to adjust the shrinkage strain for the effects of relative humidity and concrete mixture composition. P_{sh} is equal to the product of six modification factors defined by ACI 209R-92. These include factors for relative humidity, ratio of fine to total aggregate, volume to surface area ratio for the concrete element in question, slump, air entrainment, and cement content. It is mentioned by CAC Handbook (2004) that the procedure is meant for unreinforced and unrestrained concrete. In reinforced concrete members, the time-dependent deformations are restrained by the reinforcement. Thus, it is recommended for the use in lightly reinforced members, and that its application for most reinforced members is questionable. As such, it is recommended to account and adjust for the restraining effects of the reinforcement appropriately. Typically, the prescribed method produces unrestrained shrinkage strain values on the magnitude of 0.0002-0.0008 mm/mm dependent on the relative humidity and concrete mix design. In reinforced members with commonly used percentages of reinforcement, the values of 0.0002-0.0003 mm/mm are utilized CAC Handbook (2004).

The CSA S6 (2014) Canadian Highway Bridge Design Code (CHBDC) provides an alternate method for calculating the shrinkage strain in normal density and normal strength concrete. These provisions have been adopted from the 1990 CEB-FIP Model Code and adjusted to follow

Canadian standards. Shrinkage strains can be determined on the basis of test data or the provisions found in Clause 8.4.1.5.2, which presents the following design equations:

$$\varepsilon_{sh} = \varepsilon_{sh0}\left[\beta_s(t)\right]$$ (5-17)

$$\varepsilon_{sh0} = \beta_{RH}\left[160 + 50\left(9 - \frac{f'_c + a}{10}\right)\right] \times 10^{-6}$$ (5-18)

$$\beta_{RH} = -1.55\left[1 - \left(\frac{RH}{100}\right)^3\right]$$ (5-19)

$$\beta_s(t) = \sqrt{\frac{t}{350\left(\frac{2r_v}{100}\right)^2 + t}}$$ (5-20)

where:

ε_{sh0}	=	the notional shrinkage coefficient [mm/mm],
$\beta_s(t)$	=	describes the development of shrinkage with time,
β_{RH}	=	the coefficient describing the effect of relative humidity on shrinkage in concrete,
a	=	the difference between mean concrete strength and specified strength at 28 days [MPa],
RH	=	the annual mean relative humidity [%], and
r_v	=	the volume per unit length of a concrete section divided by the corresponding surface area in contact with freely moving air [mm].

Equations 5-17 through 5-20 reflect current practice in the design and construction of segmental bridges. These design equations have been derived empirically from experimental tests and the main factors dictating the shrinkage strain are the relative humidity, concrete strength, and volume to surface area ratio. In comparison, the ACI 209R-92 Equation 5-16 for shrinkage is sensitive to relative humidity, concrete mix composition, and volume to surface area ratio.

A comparative analysis was completed to assess each of the proposed shrinkage calculation methods. For the purpose of this comparison, several assumptions were made pertaining to the dimensions, mix design, composition, relative humidity, and etc., in order to simulate the

127

conditions in the laboratory conditions as accurately as possible. For the ACI 290R-92 and CSA S6 (2014) methods, Tables 5-2 and 5-3 summarize the variables and modification factors, respectively.

Table 5-2: Assumed shrinkage strain variables for ACI 209R-92.

Attribute		Variable	Value
Curing type	Moist cured	C_s	35
Ultimate shrinkage strain		ε_{shu}	0.00078
Cement Content	410 kg/m^3	P_c	1
Humidity	75% RH*	P_h	0.65
Ratio of fine aggregate	0.5**	P_f	1
Ratio of volume to surface area	51.7 m^3/m^2	P_r	0.94
Slump	70 mm	P_s	1
Air entrainment	8%	P_v	1.01
Calculated correction factor		P_{sh}	0.617

*Interpreted from Figure 1.6 in the CAC Handbook (2004).
**Assumed value.

Table 5-3: Assumed shrinkage strain variables for CSA S6 (2014).

Variable	Value	Units
f'_c	45	MPa
a	0	MPa
RH	75	%
r_v	51.7	mm
β_{RH}	0.896	
ε_{sh0}	0.00032	mm/mm

The variation of shrinkage strain with time for the two proposed methods is compared in Figure 5-19. It can be seen when comparing the two trends that the ACI 209R-92 method for calculating shrinkage provides strains approximately 40% larger at the ultimate value. The ultimate shrinkage strain for the ACI 209R-92 and CSA S6 (2014) methods were calculated as 0.00048 mm/mm and 0.00032 mm/mm respectively.
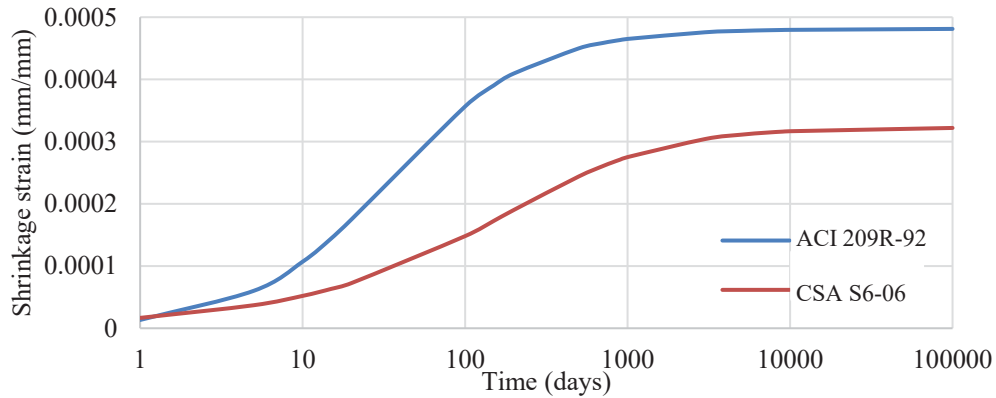
Figure 5-19: Comparison of predicted variation of shrinkage strain with time.

Considering that the ACI 209R-92 method is to be utilized in cases where the concrete is unrestrained, larger shrinkage strains were expected and calculated in comparison to the CSA S6 (2014) method. The CAC Handbook (2004) also suggests that values for shrinkage strains of normally reinforced members are in the range of 0.0002 to 0.0003 mm/mm, aligning with the values the CSA S6 (2014) method predicts. Since the CSA S6 (2014) method was based on the empirical findings of restrained concrete experiments, the prediction accounts for the reduction due to the counteracting effects of creep and restraining effects due to reinforcement. Since the FEA will be incorporating the restraining effects of the reinforcement and shear connectors, the method prescribed in ACI 209R-92 is considered more applicable, and a value of 0.00048 mm/mm will be applied. This value represents the ultimate long-term shrinkage strain value and is utilized in the subsequent analyses. The approximate unrestrained shrinkage strain at the time of experimental testing ranges between 0.00039 mm/mm and 0.00045 mm/mm depending on when the testing of each specimen commenced.

The FEA model utilized in the concrete shrinkage analysis was identical to the half CIP model described in the previous sections. However, rather than applying vertical loading to the top of the slab to simulate flexure, a change in temperature was applied to the concrete slab to simulate shrinkage strains. The CIP slab was given a coefficient of thermal expansion of 10×10^{-6} mm/mm/°C, and a uniform change in temperature of $\Delta T = -48$°C was applied over the slab to produce an unrestrained shrinkage strain of 0.00048 mm/mm if no reinforcement or shear connection was present. The goals of this analysis were to determine the resulting ultimate

129

shrinkage strain accounting for the effects of restraint, and to determine the magnitude and sense of the restraining forces developed in the shear connectors.

The FEA analysis estimated the resulting shrinkage strain at the top of the slab, bottom of the slab, and the average over the slab depth to be 0.000460 mm/mm, 0.000290 mm/mm, and 0.000395 mm/mm, respectively. These values were collected at midspan of the beam (1500 mm from the west support), illustrated by the black dashed line in Figure 5-20. This figure illustrates the deformed shape that has been emphasized by a scale factor of 100. Upon inspection of the deformed shape, it is evident that there are significant forces acting on the studs towards the midspan of the beam. Additionally, slab uplift is apparent since gaps along the steel-concrete interface are evident, particularly at Stud 1 and at the end of the beam.
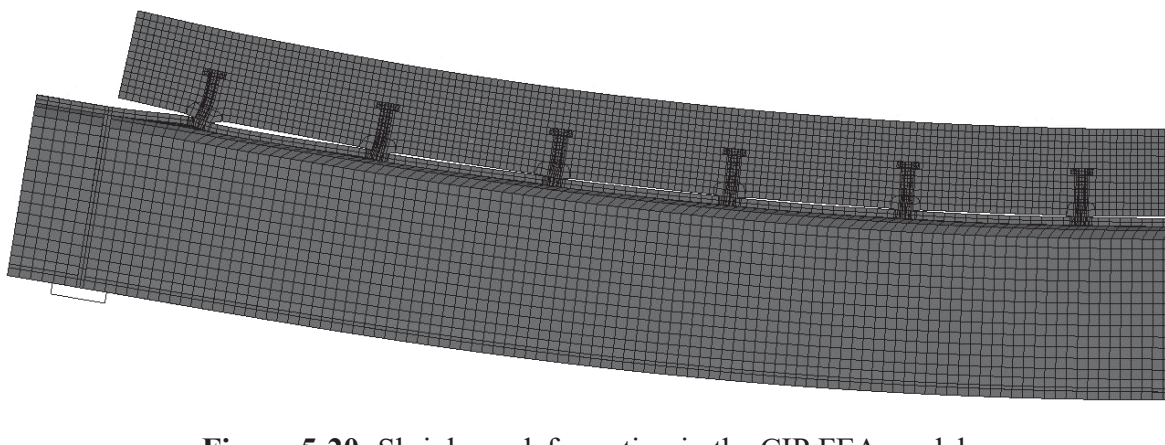
Figure 5-20: Shrinkage deformation in the CIP FEA model.

The free body function was utilized in determining the resistive forces acting on the shear connectors. This function finds the resulting static forces and moments for the selected set of elements. Due to symmetry about the beam centerline, Studs 1 and 12, 2 and 11, and etc. were found to experience the same force. Studs 1 and 12 experienced a force (towards the centerline of the beam) of 34.6 kN, resulting in a longitudinal shear stress of 172.1 MPa in the stud. Studs 2 and 11 experienced a stress of 80.1 MPa. The resulting longitudinal shear stresses for each of the studs are plotted in Figure 5-21. The change in shear stud stress moving from the end of the beam towards the beam midspan was consistently 51% to 54% lower than the previous stud, or approximately half of the previous stress. This trend takes the form of an exponentially decaying function or a geometric series with each successive term being obtained by dividing the previous

term by approximately two. Although out of the scope of this research project, further parametric studies must be completed before a function estimating the forces in the studs due to shrinkage is concluded. This behaviour is a function of many variables, including, but not limited to, the geometry of the beam, material properties, number of studs, and the reinforcement ratio in the slab.
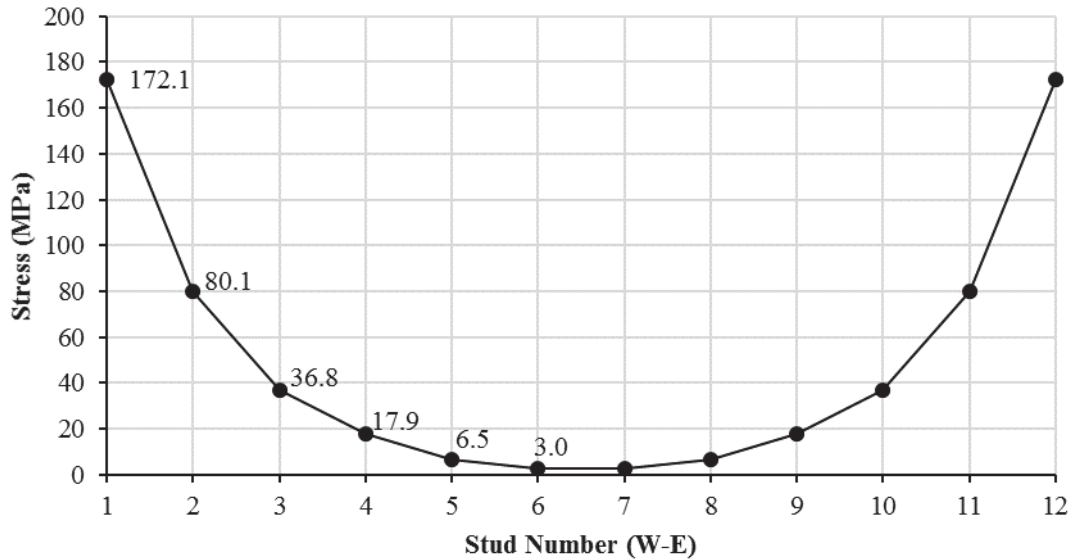
Figure 5-21: Longitudinal shear stresses acting on the studs (positive is towards the centerline of the beam).

The stress in the longitudinal axis (S33) of the model is illustrated in Figure 5-22. The coloured contour scale is provided on the left hand side and ranges from red denoting 350 MPa in tension, to blue representing 350 MPa in compression. The results for Stud 1 are magnified in the inset figure on the right. From this S33 contour, the effects of concrete shrinkage are shown clearly; due to the inward force developed due to the concrete shrinkage, the outer face (denoted with the "O") of the stud is placed under a significant tensile stress prior to application of fatigue loading on the beam. On the inside face (denoted with the "I") of the stud, an equal compressive stress is developed by the shrinkage restraining effects. Based on the simulation results, a stress (S33) concentration of approximately 250 MPa was observed. It is suggested that the mesh is to be refined around the base of the studs at the weld collar to achieve a more accurate estimate of the stress concentrations.

131
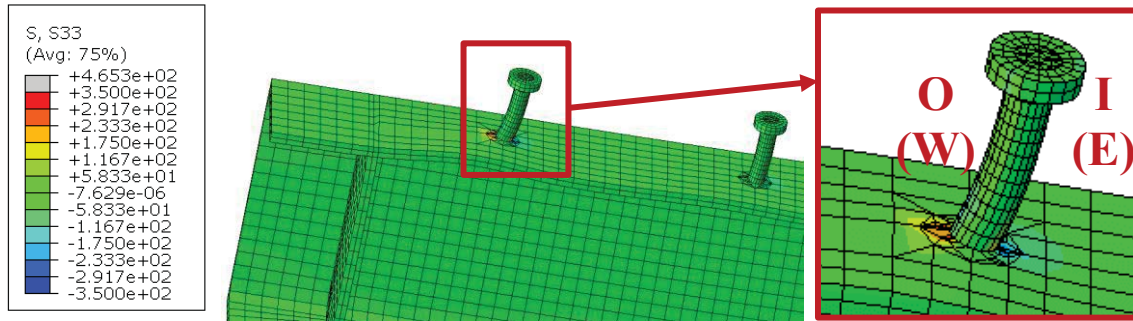
Figure 5-22: Stress along the longitudinal axis of the beam for Stud 1 due to concrete shrinkage.

The effects of concrete shrinkage on the shear stud stress history patterns were investigated more in depth. First, the different stress components were characterized. Stresses due to concrete shrinkage and cyclic loading have been discussed thus far. In addition to these stresses, tensile residual stresses due to arc-welding of the stud are present. According to Hildebrand and Soltanzadeh (2014), the residual stresses approach the yield stress of the material due to the high temperatures and low yield strengths of the materials. Although the residual stresses may be upwards of 350 MPa, for the purpose of the following analysis, it was assumed that these tensile stresses were 100 MPa at the weld toe. The stresses from concrete shrinkage and welding effectively shift the fluctuating stress ranges caused by the applied fatigue loading. This may shift fluctuating tensile stresses into the compression range, reducing fatigue damage, or increase fluctuating compressive stresses into the tension range, increasing fatigue damage. Examples of this are provided for Stud Pairs 1 through 4 in Figure 5-23 assuming 100 MPa of tensile residual stress at the weld toes on both faces. The loading history segment used in this example contains the first 25 cycles within a fatigue loading history utilized for a 100 MPa equivalent stress. The red line represents the outer face of the studs (west side) and the blue line represents the inner face of the studs (east side).
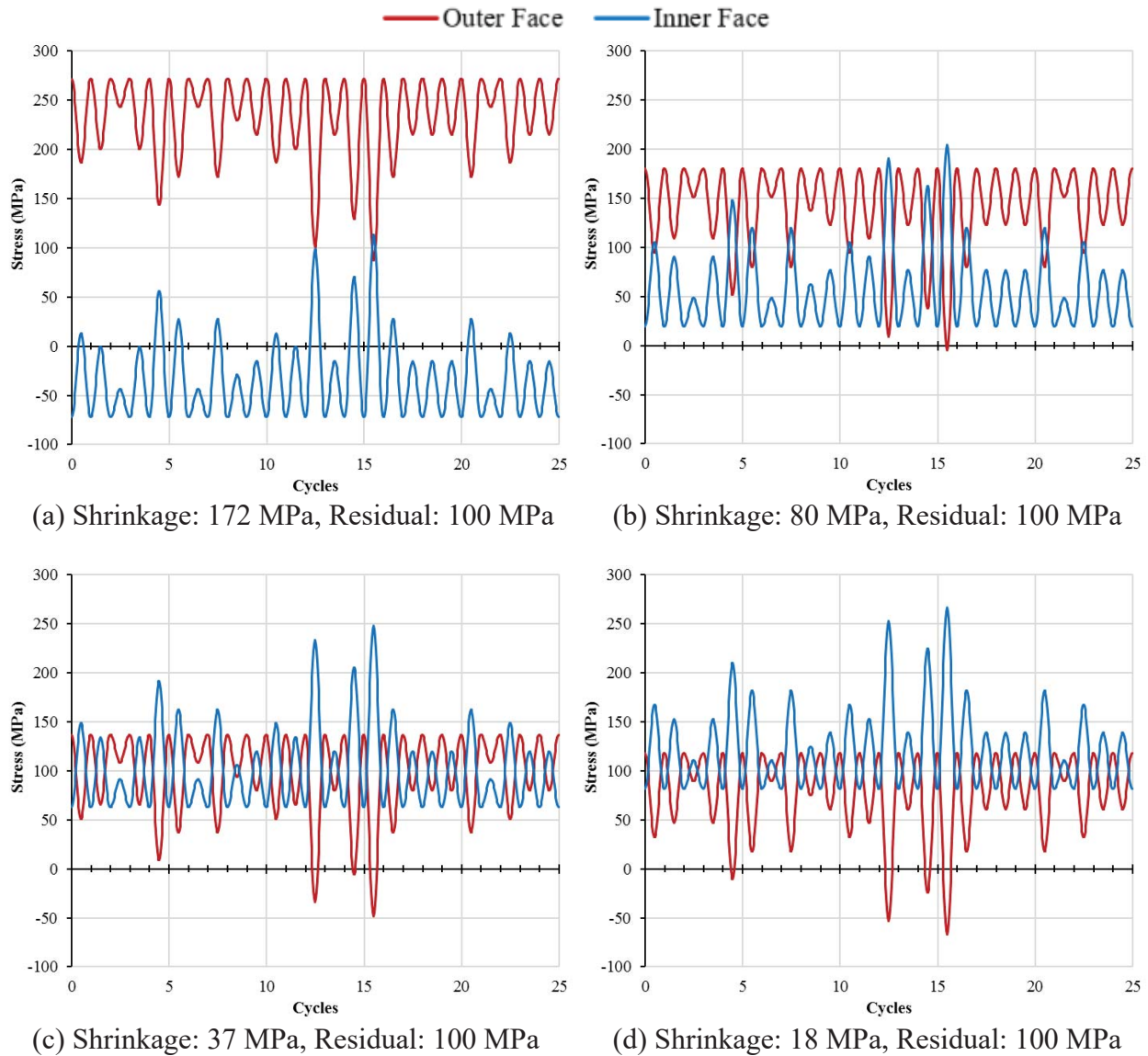
Figure 5-23: Example stress histories (equivalent stress of 100 MPa) after bring shifted due to concrete shrinkage and welding effects. (a) Stud Pair 1, (b) Stud Pair 2, (c) Stud Pair 3, (d) Stud Pair 4. Note: Tensile stress is positive.

From the example stress histories provided in Figure 5-23, the effect of concrete shrinkage and tensile residual stresses from welding are apparent. The effect of concrete shrinkage separates the inside and outside face stress histories from one another, while the residual stress from welding effectively shifts the datum of the histories in the same direction along the vertical axis. When analyzing Stud Pair 1 (Figure 5-23a), the outside face history remains in the tensile zone, or in the positive stress region. The outside stress history is shifted upwards by 172 MPa due to shrinkage

133

and 100 MPa from welding, resulting in a +272 MPa shift. The inner face history remains mostly in the compression zone because the shrinkage shifts the history downwards by 172 MPa and the tensile welding stresses shift the history upward by 100 MPa. This results in a net shift of -72 MPa. The applied fatigue loading then exerts compressive and tensile stress ranges onto the outer face and inner face, respectively. This suggests that the outer face will experience more fatigue crack propagation than the inside face because only some of the larger stress range peaks on the inside face enter the tensile region to contribute to the fatigue damage. The outside and inside faces of Stud Pair 2 (Figure 5-23b) experience shifts of +180 MPa and +20 MPa, respectively. It is apparent from the plot that all of the cyclic stress ranges are in the positive stress zone suggesting that cracks will propagate equally from both sides. Stud Pairs 3 and 4 (Figures 5-23c and 5-23d) demonstrate purely tensile stress ranges on the inside faces of the studs. Some of the larger stress ranges on the outer faces of the studs, however, enter into the compressive zone, limiting the amount of damage incurred. This trend proposes that the inner face would demonstrate more fatigue crack propagation, particularly as the effects due to concrete shrinkage decrease.

A direct correlation can be made between the analyzed behaviour and the fatigue cracking observed from the CIP specimen autopsies. Figure 5-24 illustrates each of the dominant crack directions of the studs for Specimen C300. The arrows represent the direction of the dominant fatigue cracks. Stud Pairs 1 and 2 experienced an equivalent fatigue stress range of 300 MPa, and Stud Pairs 3 to 12 experienced an equivalent fatigue stress range of 100 MPa. Therefore, the stress history provided in Figure 5-23a, b, c, and d correspond to the histories experienced by Stud Pairs 12, 11, 10, and 9, respectively. The fatigue cracking on Stud Pair 12 was dominated by cracks propagating from the outer face towards the middle of the beam. According to Figure 5-23a, this behaviour can be expected due to the stress history applied on the inner face being mostly in a zone of cyclic compression, and the outer face in cyclic tension. Stud Pair 11 was dominated by cracks of equal length on both the inside and outside faces. This was represented by a vertical line in Figure 5-24, symbolizing that the cracks on both faces propagated and intersected along the centerline of the stud. According to Figure 5-23b, this behaviour was as anticipated since both the stress histories for the inside and outside faces were in cyclic tension. Moving further towards the center of the beam, Stud N10 demonstrated fatigue cracking behaviour dominated by the inside face, and Stud S10 demonstrated cracks of equal length. This behaviour agrees to what Figure 5-

23c depicts. The larger magnitude stress cycles on the outside face begin to enter the compression zone, reducing the amount of damage these cycles would normally induce. This is emphasized even further for Stud Pairs 9. The effect of concrete shrinkage decreases to a point where the inside face incurs more fatigue damage than the outside face.
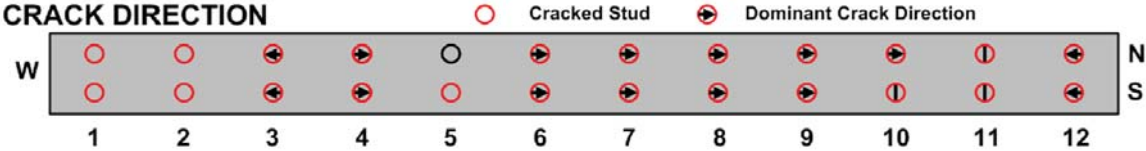
Figure 5-24: Dominant crack directions for Specimen C300.

The FEA of the effect of concrete shrinkage on the shear stud stresses in the precast specimens showed that concrete shrinkage has a minimal effect on their initial stress state. Although concrete shrinkage still plays an effect after the precast slab has been installed and the shear connection is established, the amount is largely reduced in comparison to a CIP composite beam. As an extreme case, Figure 5-25 provides an example stress history on a stud if the stress due to concrete shrinkage was ignored and only the tensile residual effects from welding are considered. Figures 5-25a and 5-25b are segments taken from stress histories with an equivalent stress due to fatigue loading of 100 MPa and 200 MPa, respectively. Both assume a tensile residual stress of 100 MPa from welding. As the applied loading is increased, the outer face (red) stress history increasingly enters into the compression zone, and fatigue crack propagation would be dominated by the inner face (blue). Figure 5-26 provides information regarding the dominant crack directions for Specimen P300. Stud Pairs 3 to 12 on Specimen P300 experienced an equivalent stress range of 100 MPa, and the stress histories pertaining to these studs are represented by Figure 5-25a. Since the larger magnitude stress cycles applied to the outer faces enter into compression, the fatigue damage on the outer face of the stud is reduced, facilitating dominant crack growth on the inside face. This trend agrees strongly with what was observed in Specimen P300 as the studs were all dominated by cracks propagating from the inside face towards the ends of the beam.

(a) Shrinkage: 0 MPa, Residual: 100 MPa, σ_{eq} = 100 MPa

(b) Shrinkage: 0 MPa, Residual: 100 MPa, σ_{eq} = 200 MPa
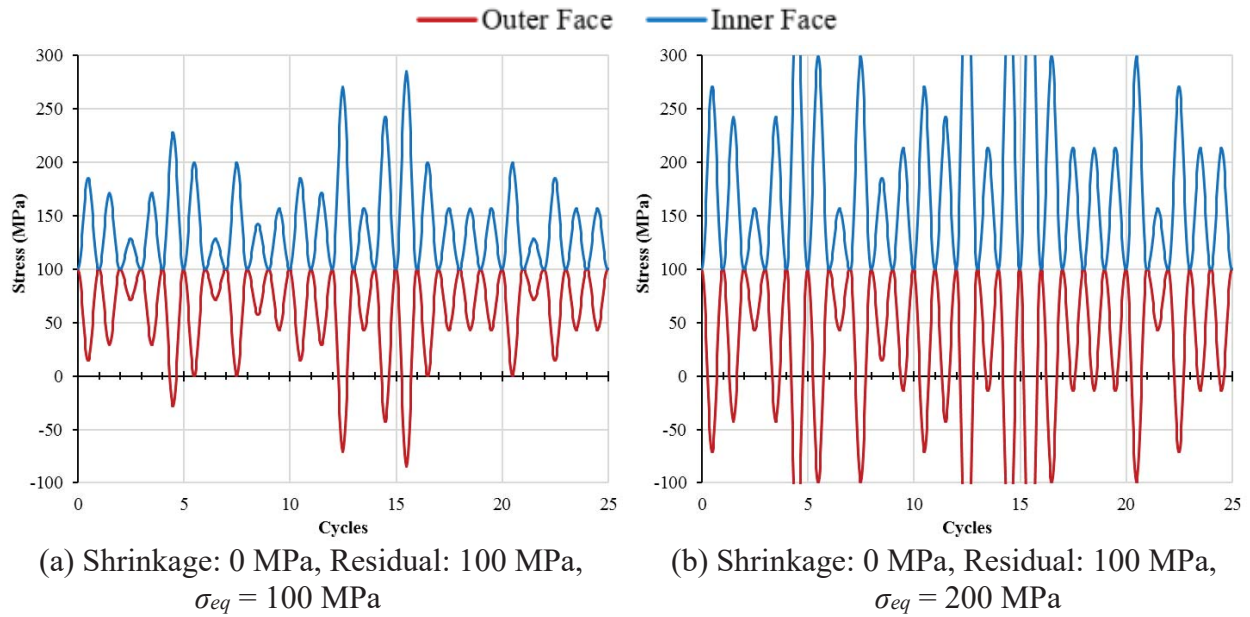
Figure 5-25: Stress history for precast specimens assuming no concrete shrinkage at (a) 100 MPa and (b) 200 MPa equivalent stress ranges. Note: Tensile stress is positive.
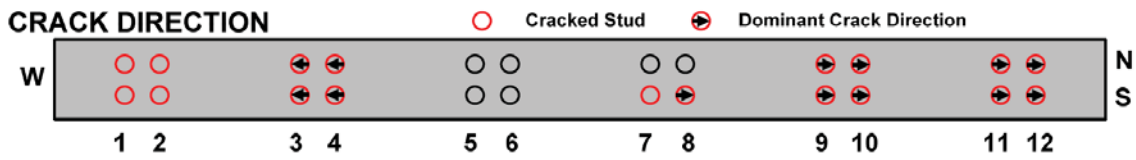
Figure 5-26: Dominant crack directions for Specimen P300.

6 Fatigue Life (S-N) Analysis of Experimental Data

The fatigue experiments in this study were completed to establish a fatigue resistance curve for the welded component and structural detail. This fatigue resistance curve is also known as an S-N curve, where S is the range of fluctuating tensile nominal stress along the ordinate and N is the endurance in cycles along the abscissa. In the S-N analysis described in this chapter, three different approaches for determining the stress range, or S, are explored. Secondly, the methodology for completing the log-log linear regressions is described. Lastly, the results obtained from the regression analysis are plotted and discussed.

6.1 Methods for Determining the Stress Range

Three alternative methods for determining the nominal stress ranges acting on the studs were explored in this investigation:

1. Theory: The theoretical stress is determined using an elastic transformed section analysis and assuming full composite interaction (i.e., no slip at the interface).
2. Measured: The measured stress is determined from the experimental strain profile data (Section 4.1.3).
3. FEA: The FEA stress is determined from the ABAQUS simulation results (Section 5.3.2).

When determining the theoretical stress, the classic shear flow equation, similar to Equation 2-17, but without the *0.52* and C_L calibration factors, was utilized. The 0.52 and C_L calibration factors were introduced into the CHBDC (CSA S6, 2014) to account for the variability in typical truck traffic data when designing with the CL-625 design code truck. The shear flow formula assumes plane sections remain plane, meaning that there is no slip at the concrete-steel interface. With no slip at the interface, the studs are assumed to be infinitely stiff, resulting in larger stud stresses than what is typically found in actual behaviour. The theoretical approach is normally the method that engineers use when determining the stress in studs for analysis and design purposes, and is how the stresses were determined in the previous analyses conducted in Chapters 4 and 5.

The stress in the shear studs cannot be measured directly in the experiments. However, the shear stress can be calculated based on the measured strain profile in the steel beam (see Section 4.1.3).

The methodology for determining the shear stud stresses in the studs based on the measured strain profile is more involved and requires several assumptions. First, the strain profile data collected at the initial static test for each specimen was used to determine the axial force in the slab at Profiles A, B, Y, and Z at the 200 kN applied load level. This procedure was described previously in Section 4.1.3. The average initial slab forces were then determined at each profile location for each specimen type. The change in the slab force between strain profiles is equal to the total resistive force carried by friction and the studs in that sectional length. The total force was averaged over the total number of studs in that section, making the assumption that each carried an equal amount of shear force. In actuality, this force is lower than what was calculated due to the contribution from friction, effectively lowering the resistive force required by the studs. Since the measured stresses were determined based on measured strain profiles obtained at the 200 kN applied load level during the static tests, it was assumed that the nominal shear stress applied to the studs is a linear function with respect to the applied load level. This assumption was proven to be valid in Section 5.3.1 after determining that the stud stress behaved as a linear function with respect to the applied load (up to 300 kN). In doing so, it was possible to estimate the measured stresses at all load levels. Although the behaviour of the studs may not be entirely linear elastic throughout fatigue testing, in practice, the assumption of linear elastic behaviour is typical when confirming the fatigue limit states for nominal stresses less than yield. Several factors that may render the linear elastic behaviour include, but are not limited to, concrete cracking, localized concrete crushing, and fatigue cracking at the base of the studs. These factors effectively reduce the stiffness of the stud resulting in lower resistive forces than estimated.

The last method utilized for determining the stress acting on the studs was based on the FEA simulation results. At a 200 kN load, the free body toolset in ABAQUS was applied to determine the longitudinal force acting on each of the individual studs. The shear stud stresses were then linearly scaled to match the equivalent applied load for a tested specimen. Again, this assumes that the stress applied to the studs is linearly proportional to the applied load level and was proven to be valid in Section 5.3.1.

Figure 6-1 compares the theoretical, measured, and FEA stud stresses at a 200 kN applied load. The data points are summarized in Table 6-1 and include the stud stresses for each of the three

methods. The percentages provided in the brackets correspond to the scale factor used to linearly scale the stresses in the subsequent analysis.

The FEA stress results in Stud Pairs 1 and 2 were found to be considerably lower than the theoretical and measured stress methods. It was hypothesized that the FEA stresses would be less than theory because the theoretical calculation assumes full interaction at the steel-concrete interface (i.e., no slip), resulting in a larger couple moment, M_{comp}, as previously discussed in Section 4.1.3. The effect of interfacial friction has the greatest influence where the normal force at the interface is largest. Since the beam is loaded at x = 500 mm (between Stud Pairs 2 and 3) and 1000 mm (between Stud Pairs 4 and 5) from the west support, the effect of friction is the greatest near these locations. The interfacial friction aids the studs by providing a resistive force that decreases the contributing force the stud must provide. This effect is most pronounced between Stud Pairs 1-6 as observed in the FEA results. The differences compared to theory can also be attributed due to the change in the transverse shear profile. In reality, the shear profile for a beam subject to bending is not entirely discontinuous at the loading points, and rather follows a continuous profile at the transitions.

The measured stresses in Stud Pairs 3 and 4 were larger than what both the theory and FEA methods predicted. The measured stresses were determined by subtracting the compressive slab force at Profile B (x = 1000 mm from the west support, and location of maximum moment) from Profile A (x = 500 mm from the west support) and dividing by the total nominal shear area of the studs at the location. Since Profile A yielded lower than expected results, the difference between Profile A and B was larger, subsequently resulting in a larger force. The measured stud stress was determined from the strain profiles and represents the entire force transferred at the interface. Therefore, it includes the resistive forces at the interface due to both friction and the studs. If the frictional forces were isolated and removed from the measured stress, it would compare directly to the FEA stud stresses. It was hypothesized that Profile A resulted with a lower compressive slab force due to being located within a D-region between the support and the first loading point. The D-region may have resulted in a portion of the load to be passed directly through the web of the beam and into the support, rather than being completely carried through bending action.
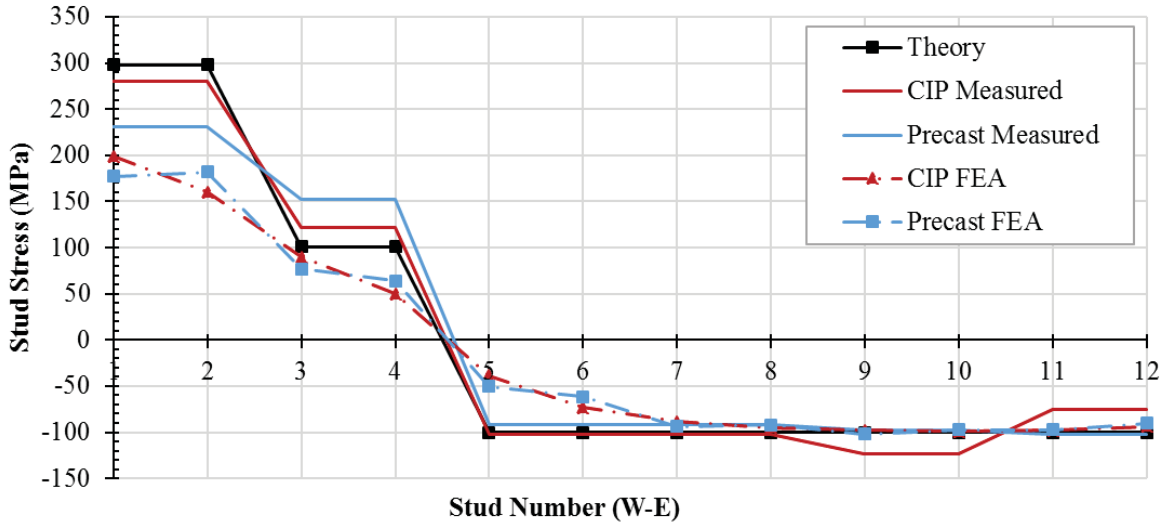
Figure 6-1: Theoretical, measured, and FEA stud stresses at P = 200 kN.

Table 6-1: Theoretical, measured, and FEA stud stresses at P = 200 kN including scale factors.

Stud Pair	Theory (MPa)	CIP Measured (MPa)		Precast Measured (MPa)		CIP FEA (MPa)		Precast FEA (MPa)	
1	298	280	(94%)	230	(77%)	199	(67%)	177	(59%)
2	298	280	(94%)	230	(77%)	160	(54%)	182	(61%)
3	100	121	(121%)	152	(152%)	90	(90%)	77	(77%)
4	100	121	(121%)	152	(152%)	50	(50%)	64	(64%)
5	-100	-102	(102%)	-91	(91%)	-39	(39%)	-51	(51%)
6	-100	-102	(102%)	-91	(91%)	-73	(73%)	-62	(61%)
7	-100	-102	(102%)	-91	(91%)	-89	(89%)	-94	(94%)
8	-100	-102	(102%)	-91	(91%)	-95	(95%)	-92	(92%)
9	-100	-123	(123%)	-97	(97%)	-98	(98%)	-102	(102%)
10	-100	-123	(123%)	-97	(97%)	-99	(99%)	-97	(97%)
11	-100	-75	(75%)	-103	(103%)	-98	(98%)	-97	(97%)
12	-100	-75	(75%)	-103	(103%)	-94	(94%)	-90	(90%)

Note: The bracketed percentages refer to the factor required to linearly scale the theoretical equivalent stress to the measured and FEA stress methods.

The theoretical, measured, and FEA methods for estimating the stud stress magnitudes provide three different levels of conservatism when establishing a fatigue resistance curve for design. For the purpose of the study, a method is more conservative relative to another when a lower stress for

140

a given fatigue life is predicted. Thus, the theoretical method is considered the least conservative due to the larger predicted stress and the FEA is considered the most conservative due to the lower predicted stress for the same fatigue life. In addition to plotting the stress utilizing the three methods, the S-N regression will also be completed utilizing two sets of data. The first data set represents the first stud failure on each beam. This results in 6 CIP and 6 precast data points. The second data set was obtained by considering the subsequent stud failures (after the first stud failure was detected) collected during the fatigue testing, resulting in 43 CIP and 35 precast data points. The second data set is assumed to be more conservative in comparison to the first data set, since it is likely that once the first studs begin to fail, there will be significant increases in stress on neighbouring studs. Thus, the initial stress used for plotting purposes will likely be lower than the actual effective stress experienced by the studs once other studs have failed.

6.2   S-N Regression Analysis

A log-log linear regression analysis is presented in this section to determine the mean regression values denoted by $a = logC$ and $b = m$ in Equation 6-1 for each of the data sets. Further statistical analysis incorporating confidence intervals and reliability indices are outside the scope of this thesis and will be included in future research publications.

The log-log linear regression analysis was completed by taking the logarithm of the number of cycles to failure, $log(N)$, as the dependent variable and the logarithm of the equivalent cyclic stress range, $log(\Delta\tau)$ as the independent variable. The dependent variable, x, and independent variable, y, have been arranged in such a way that constants a, the y-intercept, and b, the slope, can be determined by minimizing the square difference of y:

$$\underset{x}{\log N} = \underset{a}{\log C} - \underset{b}{m} \cdot \underset{y}{\underbrace{\log \Delta \tau}} \tag{6-1}$$

The regression analysis was completed on 24 different sets of data, 12 each for the CIP and precast specimens. A regression analysis was then conducted twice for each of the specimen types, first without constraining the slope of the regression line, and the second with the slope of the regression line set equal to 3. Selecting a slope of 3 is of standard practice for determining the fatigue resistance curves for steel details according to the CHBDC (CSA S6, 2014). Table 6-2 presents

141

the data utilized for all of the first stud failure regression analyses, including the theoretical, measured, and FEA equivalent stress ranges for the first failed studs in each beam specimen.

The theoretical equivalent stress ranges listed in the table slightly differ from the whole values previously listed in the test matrix (Table 3-3). This is the result of the hydraulic actuator producing a slightly different loading history than what was programed into the controller. The additional data utilized for all the stud failures is included in Appendix H.

Table 6-2: The equivalent stress ranges utilized for the first stud failures.

Specimen Type	Theory Stress (MPa)	Measured Stress (MPa)	FEA Stress (MPa)	N Failure	Failed Stud
CIP	63	60	42	6,783,000	N1
CIP	99	93	66	711,000	S1
CIP	120	112	80	305,600	N1
CIP	141	132	94	300,000	S1
CIP	202	190	136	161,500	N1
CIP	302	284	163	62,850	S2
Precast	63	48	37	5,000,000	N1
Precast	99	76	58	3,140,000	N1
Precast	120	92	73	1,174,000	N2
Precast	141	108	83	1,091,000	N1
Precast	202	156	119	400,000	S1
Precast	302	232	178	83,380	N1

Table 6-3 contains a summary of the results collected from the regression analysis when the regression slope was not fixed. The table summarizes the calculated slope (m) and y-intercept ($logC$) for each data set. Table 6-4 summarizes the regression analysis results when the slope was fixed at a value of 3 by listing the calculated y-intercept ($logC$) for each data set. For reference, a Category D (refer to Figure 2-17) fatigue detail in the CHBDC (CSA S6, 2014) is defined by a slope of $m = 3$, and a y-intercept of $logC = 11.858$. A Category C (refer to Figure 2-17) fatigue detail is defined by a slope of $m = 3$ and a y-intercept of $logC = 12.158$.

Table 6-3: Regression analysis results with variable slope, *m*.

		CIP		Precast	
Stress	**Stud Failure**	**m**	**log(C)**	**m**	**log(C)**
Theory	1st	2.78	11.53	2.63	11.58
	All	1.74	9.44	1.87	9.89
Measured	1st	2.78	11.46	2.63	11.28
	All	1.61	9.19	2.33	10.74
FEA	1st	3.15	11.73	2.64	11.00
	All	2.11	9.92	2.45	10.74

Table 6-4: Regression analysis results for fixed slope (*m* = 3).

			CIP	Precast	
Stress	**Stud Failure**	**m**	**log(C)**	**log(C)**	
Theory	1st	3	12.013	12.373	
	All	3	11.903	12.239	Red = ↓ Cat D
Measured	1st	3	11.932	12.033	Green = ↑ Cat D
	All	3	11.888	12.103	Blue = ↑ Cat C
FEA	1st	3	11.444	11.693	
	All	3	11.557	11.792	

The results of the regression analysis with variable slope (Table 6-3) suggest that all of the slopes were less than 3, with the exception of the first stud failures in the CIP specimens utilizing the FEA stress where the slope was 3.15. Additionally, the slope values when all stud failures were considered were consistently lower in comparison to slopes for the first stud failures. When the slope magnitude is lower in Equation 6-1, the line becomes more vertical. This suggests that the initial stress ranges utilized for secondary stud failures is lower than the actual effective stress experienced by the studs during testing due to force redistribution after the first stud failure(s). This can be accounted for by determining the effective stud stresses over time, rather than just utilizing the initial value. Lastly, note that the *logC* values in Table 6-3 are greatly influenced by the slopes of the regression lines, and thus it is not meaningful to compare the *logC* values in this analysis.

Since the regression results summarized in Table 6-4 were determined utilizing a fixed slope of 3, the *logC* values can be compared to one another and to the current CHBDC (CSA S6, 2014) provisions. Larger *logC* values correspond to fatigue details that have greater resistance to fatigue.

The legend provided to the right of Table 6-4 describes the colour coding assignment for each of the *logC* values in the table. When the value is red in colour, it is lower than a Category D fatigue detail. If the value is green, it is larger than a Category D fatigue detail. Lastly, if the number is blue, it was found that it is larger than a Category C fatigue detail. Utilizing the theoretical equivalent stresses, the CIP was found to perform greater than a Category D, and the precast outperformed a Category C. When utilizing the measured equivalent stresses, both the CIP and precast outperformed the Category D fatigue detail. Lastly, when utilizing the FEA stresses, the fatigue performance of the CIP and precast was found to be inferior to a Category D. From these initial observations, it is evident that the beams with precast deck slabs consistently outperformed those with CIP decks as indicated by larger *logC* values in every case, no matter how the stud stress was determined.

It is believed that the most accurate set of data defining the fatigue resistance of the connectors is defined by the first stud failures when plotted against the measured equivalent stress ranges. After the first stud begins to fail and force redistribution occurs, the equivalent stress ranges on the other studs increase, effectively rendering the effective stress ranges inaccurate. Additionally, utilizing the measured stresses would be most accurate compared to the theory, which assumes full interaction, and FEA, which can only serve as an approximation of actual behaviour.

The regression results are illustrated in the S-N plots found in Figures 6-2 though Figure 6-7. Figures 6-2, 6-3, and 6-4 are the S-N plots representing first stud failures with equivalent stress ranges determined from theory, measured, and FEA, respectively. Figures 6-5, 6-6, and 6-7 contain the S-N plots representing all stud failures with equivalent stress ranges also determined from theory, measured, and FEA, respectively. For reference, each of the S-N plots are accompanied by the Category D fatigue detail (grey dashed line), and a cloud of data points collected from the literature. The CIP and precast data utilized in the regressions are denoted by the red diamond and blue circle markers, respectively. The CIP regression lines are also red, with the dashed representing the when the slope was not fixed, and solid denoting a fixed slope of 3. The precast regression lines are similar to the CIP, however, are colored blue to match the data markers.
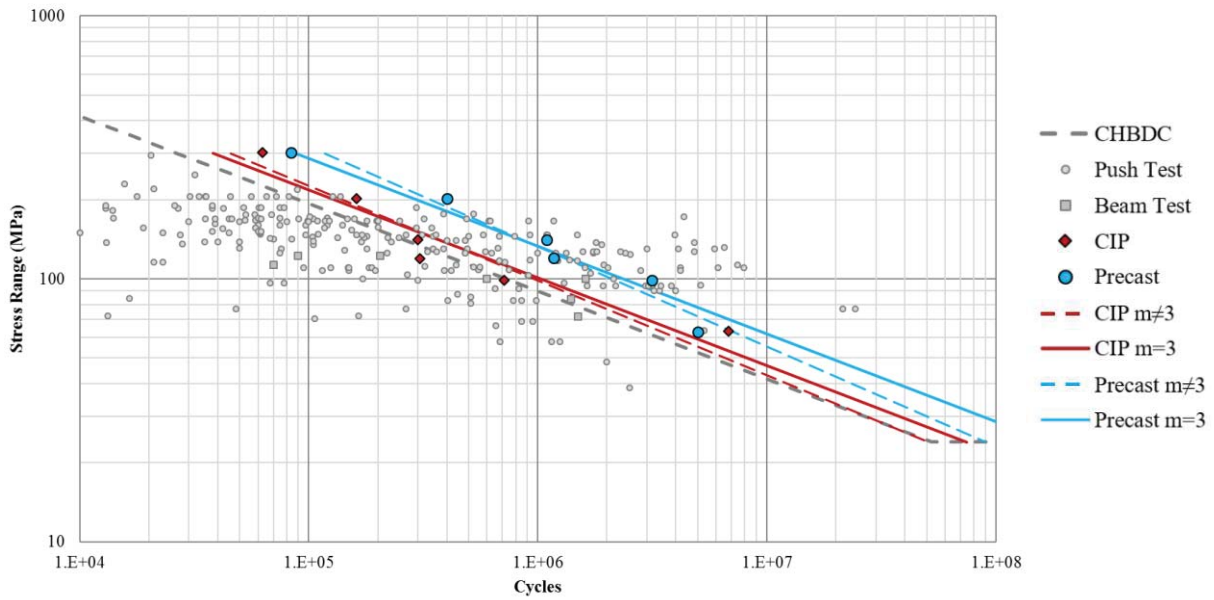
Figure 6-2: S-N plot for first stud failure and theoretical equivalent stress range.
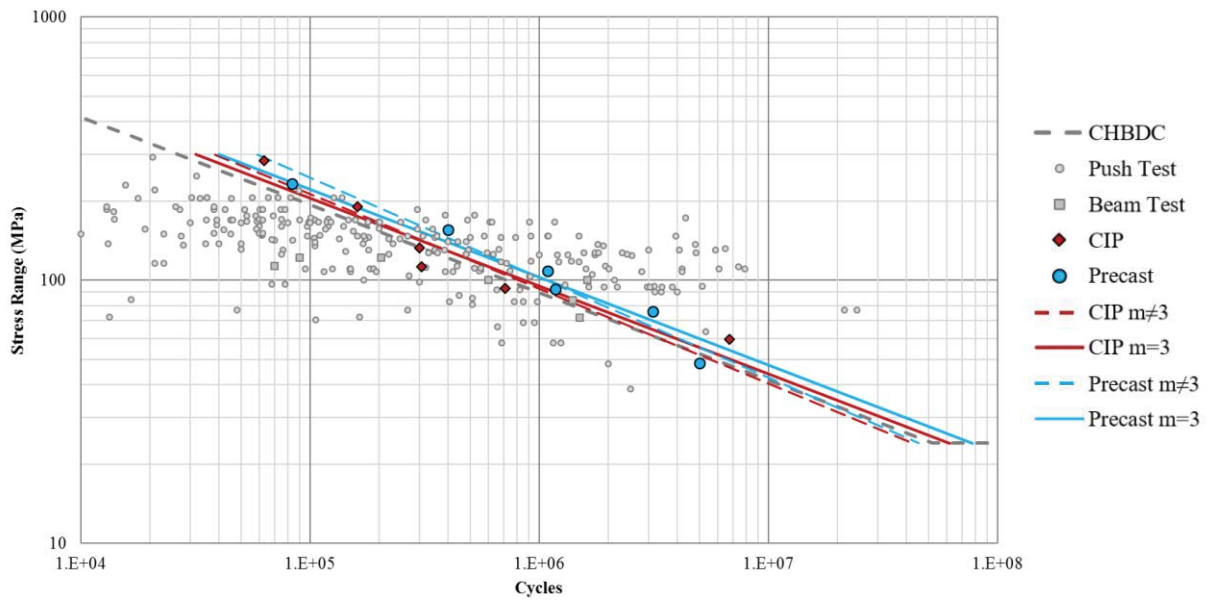
Figure 6-3: S-N plot for first stud failure and measured equivalent stress range.

145
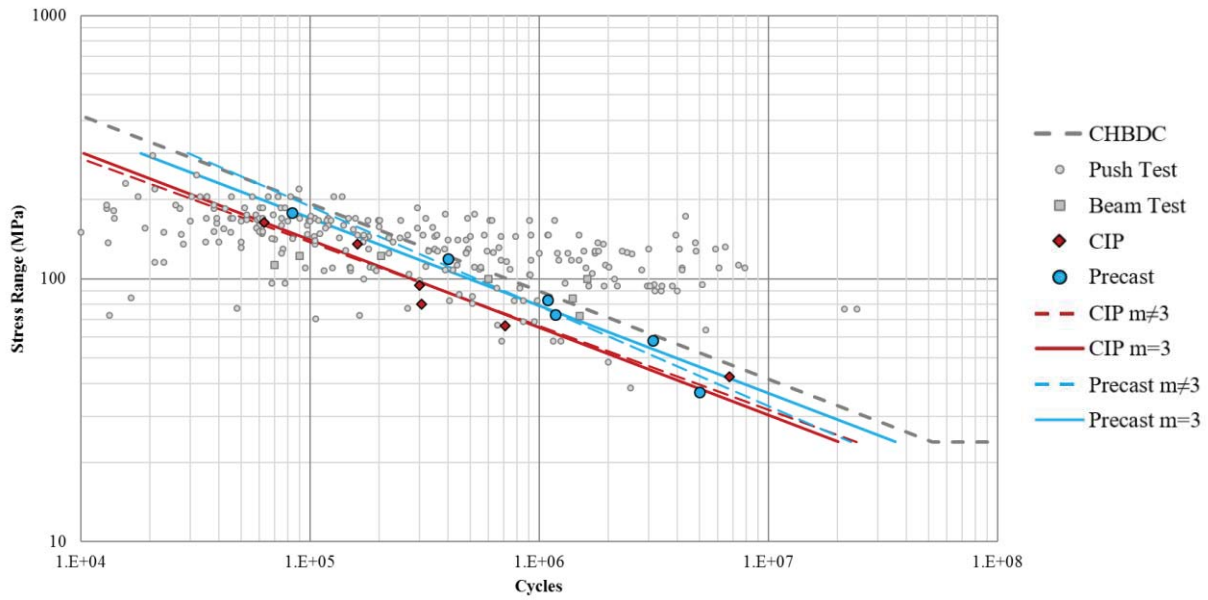
Figure 6-4: S-N plot for first stud failure and FEA equivalent stress range.
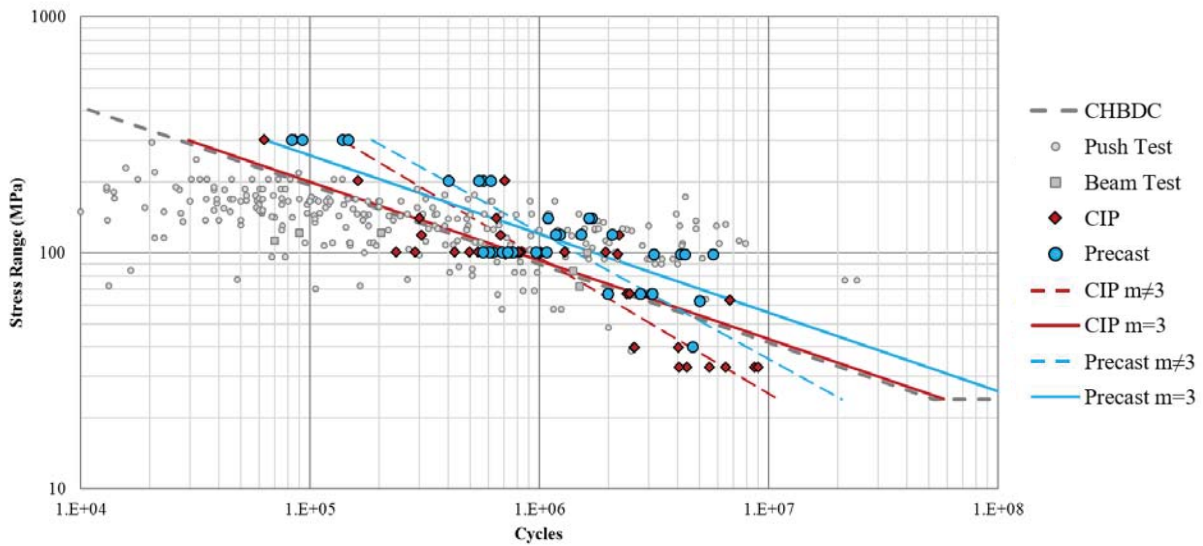
Figure 6-5: S-N plot for all stud failures and theoretical equivalent stress range.

146
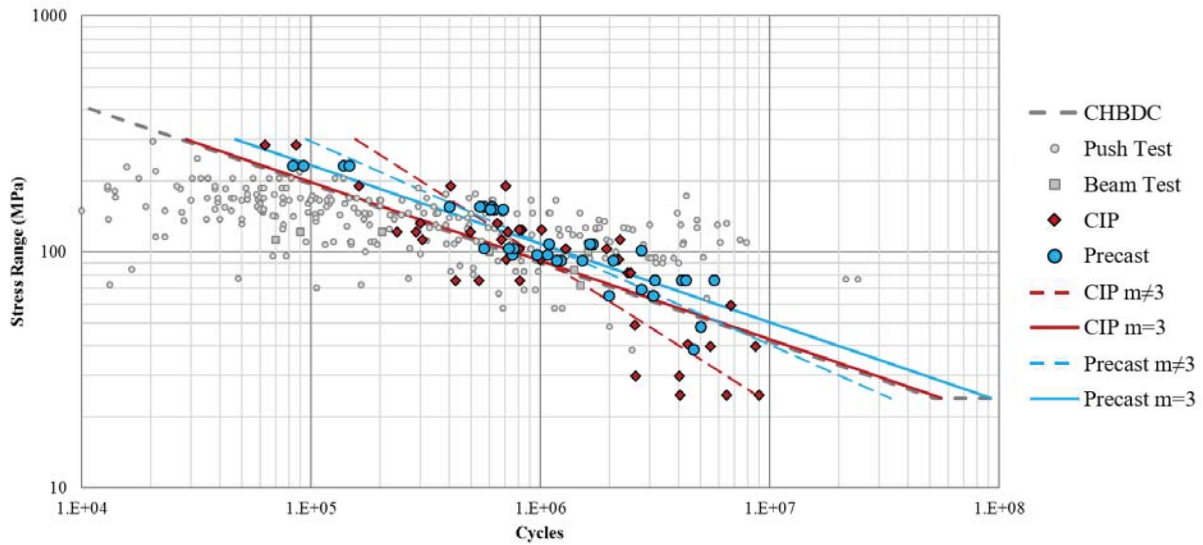
Figure 6-6: S-N plot for all stud failures and measured equivalent stress range.
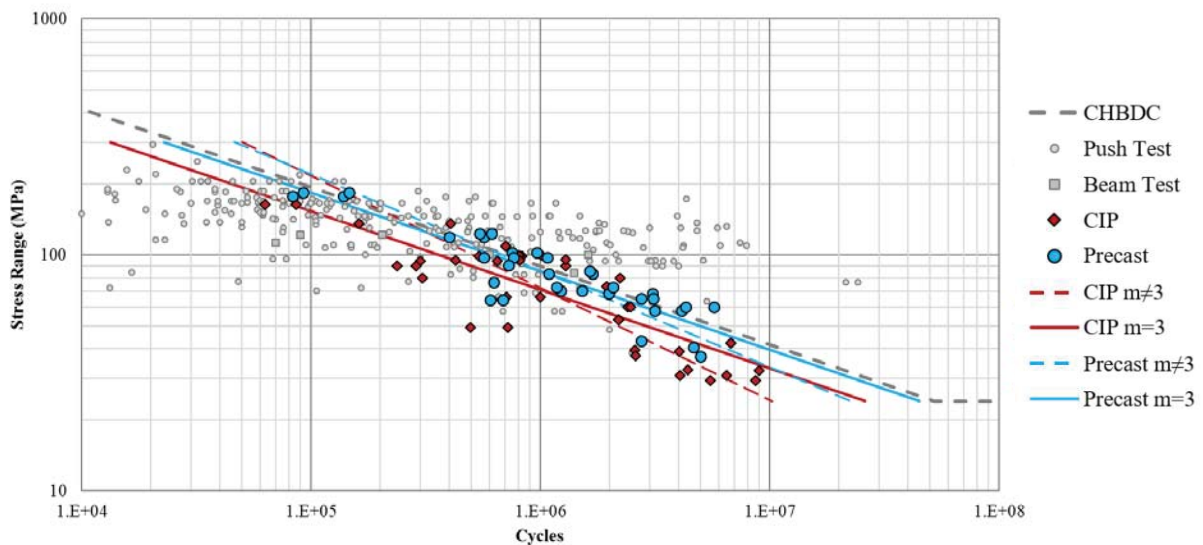
Figure 6-7: S-N plot for all stud failures and FEA equivalent stress range.

Statistical t-test analyses were performed in order to further analyze the fatigue performance results and to ascertain a difference between the fatigue lives of the CIP and precast specimens. A two sided t-distribution was utilized to compare data and to determine if the means of two data sets are significantly different. In other words, the tests were performed on the data sets and provide the

probabilities whether the two are likely to have come from the same two underlying populations containing the same mean. The calculations were completed on the *logC* values in each data set when the slopes were equal to 3, and assuming a two-tailed distribution and homoscedasticity. A summary of the analyses are provided in Table 6-5.

Table 6-5: Statistical t-test results.

Stress	Stud Failure	CIP vs. Precast	CIP vs. Category D	CIP vs. Category C	Precast vs. Category D	Precast vs. Category C
Theory	1st	1.0%	14.4%	16.5%	0.1%	2.2%
	All	6.8%	48.8%	0.0%	2.3%	81.5%
Measured	1st	38.7%	44.4%	5.3%	4.4%	11.2%
	All	25.6%	68.1%	0.1%	12.8%	41.7%
FEA	1st	3.3%	0.3%	0.0%	5.0%	0.1%
	All	13.3%	0.0%	0.0%	31.2%	0.1%

The CIP and precast specimen data sets were compared to one another as presented in the third column of Table 6-5. Relatively low probabilities of similarity were determined when considering the theoretical and FEA equivalent stress ranges, suggesting that the two data sets do not come from the same mean, and should not be combined into the same fatigue detail category. Larger probabilities were found, however, when considering the measured equivalent stress range data sets. For the first and all stud failures, a 38.7% and 25.6% similarity were found, respectively. Although these percentages are larger than the other methods, it does not provide enough supporting evidence that they should be grouped into the same fatigue detail category.

The CIP data set was then compared to the Category D and Category C fatigue details. The Category D similarity results are provided in the fourth column, and the Category C similarity results are provided in the fifth column of Table 6-5. In almost all cases, the CIP had greater similarity with Category D over Category C. This suggests that the CIP specimens have a greater conformity with a fatigue resistance curve defined by a Category D detail, as already suggested by the current CHBDC (CSA S6, 2014).

The precast data set was also compared to the Category D and Category C fatigue details. The Category D similarity results are provided in the sixth column, and the Category C similarity

results are provided in the seventh column of Table 6-5. In almost all cases, the precast had greater similarity with Category C over Category D. This suggests that the precast specimens have a greater conformity with a fatigue resistance curve defined by a Category C detail rather than a Category D as suggested currently by the CHBDC (CSA S6, 2014).

Based on the comprehensive analysis and results presented in this section, it was found that the studs in the precast specimens outperformed the studs in the CIP specimens in terms of fatigue performance. After completing a concrete shrinkage simulation and analyzing how the phenomenon alters the initial stress state of the studs in the CIP specimens in Section 5.3.3, it was found that for the particular case, the studs at the end of the beam were placed under an initial nominal stress of 182 MPa towards the center of the beam. This effect combined with the tensile residual stress from the welding process effectively shifts the stress histories acting on each side of the stud. In the CIP case, more fatigue damage is incurred due to this effect compared to the precast, which was assumed to have negligible effects from concrete shrinkage.

The regression analyses in this section determined the mean regression curve corresponding to a 50% survival probability. In the past, the mean regression curve has been used as the design curve and deemed adequate, recognizing the level of conservatism employed when utilizing push-out tests to evaluate the fatigue resistance. This was discussed previously in Section 2.1.3, highlighting that beam tests capture all the complexities associated with true flexural behaviour experienced in composite girders. This suggests that for beam test results, the design curve should be established and calibrated to consider the consequence of failure with an appropriate reliability index, rather than assume a 50% survival probability. Additionally, it was determined by Oehlers and Foley (1985) that the effect on the fatigue life of varying the maximum load, which may be the peak load or an overload, is much more important in beam tests due to friction. These overloads (i.e., heavy trucks or convoys) are significant as they may induce localized areas of tensile or compressive plastic deformation at the root of the weld due to significant stress concentrations, effectively altering the fatigue properties. Therefore, is suggested that as a continuation of this research, the effects of fatigued studs on the performance of full scale steel-concrete composite bridges are to be studied and analyzed. Thus, it is suggested that the design provisions governing the fatigue

performance of shear connectors remains unchanged until a more intensive probabilistic approach is completed.

The findings from this research imply that modification to the current CHBDC provisions regarding the fatigue design of shear studs are to be made. Although a more probabilistic approach with a calibrated reliability index is suggested prior to any modifications, it is anticipated that these revisions will directly impact and decrease the material and labour costs associated with steel-precast composite girder bridge construction. A decreased number of studs will require welding, and the precast deck pockets will be reduced in size, ultimately reducing the volume of grouting and providing more flexibility to engineers for slab reinforcing layouts. The cost benefits of utilizing precast over conventional CIP decks are already widely acknowledged in the bridge industry, and if the number of required shear connectors is lower in comparison to CIP construction, it will provide even more incentive to engineers to adapt the accelerated bridge construction alternative.

7 Conclusions and Recommendations

This research has explored the fatigue performance of headed shear stud connectors in steel-CIP and steel-precast composite girder applications. In Section 7.1, the significant findings are reported and conclusions are drawn. Section 7.2 identifies the recommendations for future work arising from this research thesis.

7.1 Conclusions

A total of six steel-CIP and six steel-precast composite beams were fabricated and tested under both static and variable amplitude fatigue loading. The laboratory test specimens were then autopsied once stud failures were observed to further investigate and quantify the damage. The lab results were then utilized to verify the CIP and precast finite element models assembled in ABAQUS. Lastly, a variety of S-N regression analyses were completed to establish fatigue resistance curves for the studs in CIP and precast application. The conclusions drawn for each of the research milestones are provided in the subsequent subsections.

7.1.1 Static Testing

Based on the static testing of the CIP and precast composite laboratory specimens, the following conclusions are drawn:

- The load-deflection behaviour of the specimens loaded with 67, 100, 120, and 140 MPa equivalent stress range histories experienced insignificant changes over the course of their fatigue lives. The specimens loaded with a 200 and 300 MPa equivalent stress range demonstrated dramatic increases in deflection over the progression of their fatiguing due to the rate at which studs failed.

- The average of the initial deflections for the CIP and precast specimens were both found to equal 2.66 mm at a load of 200 kN. After completing a statistical t-test, a 94% possibility was determined that both deflection data sets are likely to have come from the same population. The data suggest that initially, the CIP and precast specimens demonstrated identical load-deflection behaviour.

- The average initial slip values at the west support (Slip 1) for the CIP and precast specimens were 0.136 mm and 0.135 mm, respectively, at a load of 200 kN. A statistical t-test was performed on the CIP and precast initial slip data, resulting in a 97% probability that the data sets come from the same population. This proposes that initially, the CIP and precast specimens demonstrated identical slip behaviour.

- When comparing the Slip 1 data recorded during a static load cycle at the 1000% predicted fatigue life, Specimens P100, P120, P140, and P200 all demonstrated a lower percent increase in Slip 1 values compared to their CIP equivalents. The slip data imply that the precast specimens experienced less fatigue damage due to the cyclic loading compared to the CIP specimens. It was later found that the precast received less fatigue damage compared to the CIP due to the effects of concrete shrinkage and its effect on altering the studs initial stress state.

- The axial slab forces and measured stud stresses were accurately determined utilizing the steel's strain profiles installed along the length of the beam.

7.1.2 Fatigue Testing

The following conclusions are drawn based on the fatigue testing data of the CIP and precast composite beam specimens:

- The maximum deflection did not increase over the fatigue life of the specimen for loading at the 67 and 100 MPa equivalent stress range tests. In contrast, the 120 and 140 MPa tests displayed gradual deflection increases, while the 200 MPa and 300 MPa tests demonstrated significant increases ranging from 2.6% to 14% for the CIP and 12% to 16% for the precast. The deflection was found to increase over the course of fatigue loading due to the studs cracking from fatigue and becoming less stiff. Subsequently, the degree of shear interaction decreases, which effectively increases the beams curvature.

- The local distortion strain trends for Studs N1 and S1 for Specimens C120 and C100, respectively, indicated that the studs experienced a fatigue failure prior to the estimated fatigue life based on CSA S6-14. The observed fatigue lives for Stud Pairs 1 and 2 in all other specimens were found to exceed the Code estimated fatigue lives.

- It was hypothesized that Stud Pairs 3 and 4 would experience an increase in stress due to redistribution once Stud Pairs 1 and 2 were severely damaged due to fatigue. As a result, Stud Pairs 5 through 12 were expected to demonstrate a longer life than Stud Pairs 3 and 4, regardless of the fact that they initially experienced the same theoretical stress ranges. There were 6 cases in the CIP specimens, and 4 cases in the precast specimens in which the hypothesis was found to fail. This behaviour suggests that the stresses in Stud Pairs 3 and 4 were lower than the Stud Pairs at the end of the beam and is a result of friction having a greater effect near the loading points. The effect of interfacial friction has the greatest influence where the normal force at the interface is largest. Considering that the beam was loaded at two locations on either side of Stud Pairs 3 and 4, the effect of friction is expected to be greatest at this location. The interfacial friction aids the studs by providing a resistive force that decreases the contributing force the stud must provide.

7.1.3 Autopsy Results

The following conclusions have been established based on the autopsy results of the CIP and precast specimens:

- For the CIP specimens, it was typical that Stud Pairs 1 and 12 were dominated by cracks growing from the outer faces and propagating towards the middle of the beam. Taking a step inwards, Stud Pairs 2 and 11 did not show signs of dominant crack directions, having both the east and west cracks being of equal lengths. Stud Pairs 3 to 10 began to show cracks with dominant directions initiating on the side of the applied shear force (Stud Pairs 3 and 4 on the east face, Stud Pairs 5 to 10 on the west face).

- A different behaviour was observed for the precast specimens. Typically, it was observed that the dominant crack initiated on the face which experienced the applied shear force. Thus, Stud Pairs 1 to 4 experienced dominant cracking initiating at the east face and propagating towards the west, and Studs Pairs 5 to 12 experienced the exact opposite.

- The autopsy findings ascertain that the peak in the local distortion data does not define the initiation of a crack, and rather the point in which the stud's fatigue cracks are sufficient enough to reduce the stud's stiffness and attract less interface shear force.

- Striking the studs laterally with a hammer did not always provide an accurate means of determining failure as they were highly dependent on the crack propagation geometry. The

studs failed the bend test when approximately 50% or less of the original area was remaining.

7.1.4 Finite Element Analysis

The conclusions drawn from the finite element simulations of the CIP and precast models are as follows:

- The CIP and precast simulation results were almost identical to one another and aligned well with the static testing results. The load-deflection behaviour of both models were identical, however, demonstrated a stiffer flexural response than observed in the laboratory. This may have been due to modelling inaccuracies of the shear connection or friction characteristics.

- Stud stresses in the CIP model due to concrete shrinkage were found to be as large as 172 MPa in Stud Pairs 1 and 12. Stud Pairs 2 and 11 were found to be approximately 80 MPa and Stud Pairs 3 and 10 equaling 37 MPa.

- The stresses from the concrete shrinkage and arc-welding effectively shifts the fluctuating stress ranges caused by the applied loading. Depending on the magnitudes of each, they can shift fluctuating tensile stresses into the compression zone, reducing fatigue damage, or increase fluctuating compressive stresses into tension zones. A direct correlation between the effects of the shifted stress histories to the crack propagation findings was observed for both the CIP and precast specimens.

7.1.5 S-N Regression

Based on the S-N regression analyses, the following conclusions regarding the fatigue behaviour of the test specimens have been made:

- The theoretical, measured, and FEA methods for estimating the stud stress magnitudes provide three different levels of conservatism when establishing a fatigue resistance curve for design. A method is more conservative relative to another when a lower stress for a given fatigue life is predicted. Thus, the theoretical method is considered the least conservative due to the larger predicted stress and the FEA is considered the most conservative due to the lower predicted stress for the same fatigue life.

154

- The regression analyses in this section determined the mean regression curve corresponding to a 50% survival probability.

- The regression analysis slope values, m, when considering all stud failures were consistently lower in comparison to the first stud failure regression lines. When the slope magnitude is lower, the resistance line becomes more vertical. This outcome suggests that the initial stress utilized for secondary stud failures is lower than the actual effective stress experienced due to force redistribution.

- When the slope was set to $m = 3$, it was evident that the beams with precast deck slabs consistently outperformed those with CIP decks as indicated by larger $logC$ values in all cases, no matter how the stud stress was determined:

    - When utilizing the theoretical equivalent stresses, the CIP was found to perform greater than a Category D, and the precast outperformed a Category C.

    - When utilizing the measured equivalent stresses, both the CIP and precast outperformed the Category D fatigue detail.

    - When utilizing the FEA stresses, the fatigue performance of the CIP and precast was found to be inferior to a Category D.

    - In almost all cases, the CIP had greater similarity with Category D over Category C. This suggests that the CIP specimens have a greater conformity with a fatigue resistance curve defined by a Category D detail.

    - In almost all cases, the precast had greater similarity with Category C over Category D. This proposes that the precast specimens have a greater conformity with a fatigue resistance curve defined by a Category C detail.

- The findings from this research imply that modification to the current CHBDC provisions regarding the fatigue design of shear studs are to be made. Although a more probabilistic approach with a calibrated reliability index is suggested prior to any modifications, it is anticipated that these revisions will directly impact and decrease the material and labour costs associated with steel-precast composite girder bridge construction.

7.2   Recommendations for Future Work

The following recommendations are made to further advance the research and development of the design of headed shear connectors in steel-CIP and steel-precast composite girders:

- The S-N regression analyses determined the mean regression curve corresponding to a 50% survival probability. In the past, the mean regression curve has been used as the design curve and deemed adequate, recognizing the level conservatism employed when utilizing push-out tests to evaluate the fatigue resistance. For beam test results, however, the design curve should be established to accommodate a 95% survival probability, or calibrated to consider the consequence of failure with an appropriate reliability index. Thus, it is suggested that the design provisions governing the fatigue performance of shear connectors remains the same until a more intensive probabilistic approach is taken.

- An investigation into correcting the actual stud stress over time and accounting for force redistribution on secondary stud failures is suggested. This can be completed by utilizing the fatigue strain profile data collected over the specimens' entire life rather than determining the averages of the initial static strain profile data.

- A great level of conformity between the experimental results and the results gathered from the FEA models can be observed. Although a parametric analysis was not completed to investigate the effects of varying the coefficient of friction across the steel-concrete interface, it is suggested that one is completed to achieve a more thorough understanding of the specimen behaviour. Additionally, if the models are calibrated appropriately, the properties can then be extended onto larger scale bridge models for a more intensive and more applicable investigation.

References

American Association of State Highway and Transportation Officials. (2014). AASHTO LRFD Bridge Design Specifications. *Washington, DC, USA.*

American Society of Civil Engineers. (2013). Report Card for America's Infrastructure.

ABAQUS (2007). *Version 6.7, Dassault Systèmes, USA.*

ACI Committee 209 (1992). ACI-209-R92. Prediction of creep, shrinkage, and temperature effects in concrete structures. *American Concrete Institute: Farmington Hills, MI, USA.*

Badie, S. S., Girgis, A. F., Tadros, M. K., & Nguyen, N. T. (2010). Relaxing the stud spacing limit for full-depth precast concrete deck panels supported on steel girders. *Journal of Bridge Engineering*, *15*(October), 482–492. http://doi.org/10.1061/(ASCE)BE.1943-5592.0000082

Bowser, M. G. (2010). Development of a shear connection for a portable composite bridge.

British Standards Institution. (1980). BS 5400-10:1980. Steel, concrete, and composite bridges. Code of practice for fatigue. *London, England.*

Canadian Infrastructure Report Card: *Informing the Future*. (2016).

Canadian Standards Association (2004). CAN/CSA-A23.3-04, Design of Concrete Structures, *Canadian Standards Association: Mississauga, ON, Canada.*

Canadian Standards Association. (2006). CAN/CSA-S6-06 Canadian Highway Bridge Design Code. *Canadian Standards Association: Mississauga, ON, Canada.*

Canadian Standards Association (2013). CAN/CSA-G40.21-13. Structural Steel Quality. *Canadian Standards Association: Mississauga, ON, Canada.*

Canadian Standards Association (2013). CAN/CSA-W59-13. Welded Steel Construction (Metal Arc Welding). *Canadian Standards Association: Mississauga, ON, Canada.*

Canadian Standards Association. (2014). CAN/CSA-S6-14 Canadian Highway Bridge Design Code. *Canadian Standards Association: Mississauga, ON, Canada.*

Canadian Standards Association. (2014). CAN/CSA-S6.1-14 Canadian Highway Bridge Design Code Commentary. *Canadian Standards Association: Mississauga, ON, Canada.*

Chen, W. F. (1982). Plasticity in Reinforced Concrete. *McGraw Hill, New York, USA.*

CISC (2014). Handbook of Steel Construction, Ninth Edition. CISC Commentary on CAN/CSA-S-16-14 Canadian Institute of Steel Construction. *Canadian Standards Association: Mississauga, ON, Canada.*

Comité Européen de Normalisation. (2005) CEN 1994-2 Eurocode 4. Design of composite steel and concrete structures - Part 2: General rules for bridges. *Brussels, Belgium.*

Dassault Systemes Simulia (DSS) (2012). ABAQUS 6.12. *Providence, RI, USA.*

Genikomsou, A. S., & Polak, M. A. (2015). Finite element analysis of punching shear of concrete slabs using damaged plasticity model in ABAQUS. *Engineering Structures*, *98*, 38–48. http://doi.org/10.1016/j.engstruct.2015.04.016

Hildebrand, J., & Soltanzadeh, H. (2014). A review on assessment of fatigue strength in welded studs. *International Journal of Steel Structures*, *14*(2), 421–438. http://doi.org/10.1007/s13296-014-2020-2

Huh, B., Lam, C., & Thermabala, B. (2010). Effect of shear stud clusters in composite girder design. *Proceedings of the 8th International Conference on Short and Medium Span Bridges*, (i), 1–11.

Issa, M. A., Anderson, R., Domagalski, T., Asfour, S., & Islam, M. S. (2008). Full-Scale Testing of Prefabricated Full-Depth Precast Concrete Bridge Deck Panel System, (104).

Japan Society of Civil Engineers. (2009). JSCE-09. Standard Specifications for Steel and Composite Structures.

Johnson, R. P. (2000). Resistance of stud shear connectors to fatigue. *Journal of Constructional Steel Research*, *56*(2), 101–116. http://doi.org/10.1016/S0143-974X(99)00082-6

Kwon, G. U., Engelhardt, M. D., & Klingner, R. E. (2010). Behavior of post-installed shear connectors under static and fatigue loading. *Journal of Constructional Steel Research*, *66*(1), 532–541. http://doi.org/10.1016/j.jcsr.2009.09.012

Liu, X., Bradford, M. A., Chen, Q.-J., & Ban, H. (2016). Finite element modelling of steel–concrete composite beams with high-strength friction-grip bolt shear connectors. *Finite Elements in Analysis and Design*, *108*, 54–65. http://doi.org/10.1016/j.finel.2015.09.004

Nussbaumer, A., Helmerich, R., Herion, S., Kolstein, M. H., Walbridge, S., Androic, B., … Dimova, S. (2008). Assessment of Existing Steel Structures : Recommendations for Estimation of Remaining Fatigue Life, *3*(February).

Oehlers, D., & Foley, L. (1985a). the Fatigue Strength of Stud Shear Connections in Composite

Beams. *ICE Proceedings*, *79*, 349–364. http://doi.org/10.1680/iicep.1985.995

Oehlers, D., & Foley, L. (1985b). the Fatigue Strength of Stud Shear Connections in Composite Beams. *ICE Proceedings*, *79*(August), 349–364. http://doi.org/10.1680/iicep.1985.995

Oehlers, D. J., & Seracino, R. (2002). A tiered approach to the fatigue assessment of composite steel and concrete bridge beams, (3), 249–257.

Shariati, M., Sulong, N. H. R., Arabnejad, M. M. K. H., & Mahoutian, M. (2011). Shear resistance of channel shear connectors in plain, reinforced and lightweight concrete, *6*(4), 977–983. http://doi.org/10.5897/SRE10.1120

Slutter, R. G., & Fisher, J. W. (1966). Fatigue Strength of Shear Connectors. *45th Annual Meeting of the Highway Research Board*, *315*(147). Retrieved from http://trid.trb.org/view.aspx?id=1306976

Slutter, R. G., King, D. C., & Driscoll, G. C. J. (1965). Fatigue strength of 1/2 inch diameter stud shear connectors. *Highway Research Record*, (103).

Stoner, J. G. (2015). Finite Element Modelling of GFRP Reinforced.

Tadros, M. K., Badie, S. S., Girgis, A. F., & Sriboonma, K. (2011). Full-scale testing for composite slab/beam systems made with extended stud spacing. *Journal of Bridge Engineering*, (October), 653–661. http://doi.org/10.1061/(ASCE)BE.1943-5592.0000215.

Toprac, A. A. (n.d.). Fatigue Strength of 3/4 Inch Studs in Lightweight Concrete (Push-out Tests), (May 1965).

Yu-Hang, W., Jian-Guo, N., & Jian-Jun, L. (2014). Study on fatigue property of steel–concrete composite beams and studs. *Journal of Constructional Steel Research*, *94*, 1–10. http://doi.org/10.1016/j.jcsr.2013.11.004

Yura, J. A., Methvin, E. R., & Engelhardt, M. D. (2008). Design of Composite Steel Beams for Bridges (FHWA/TX-08/0-4811-1), *7*.

Appendix A: Fabrication Drawings

PRECAST (DWG 100)

CIP (DWG 200)
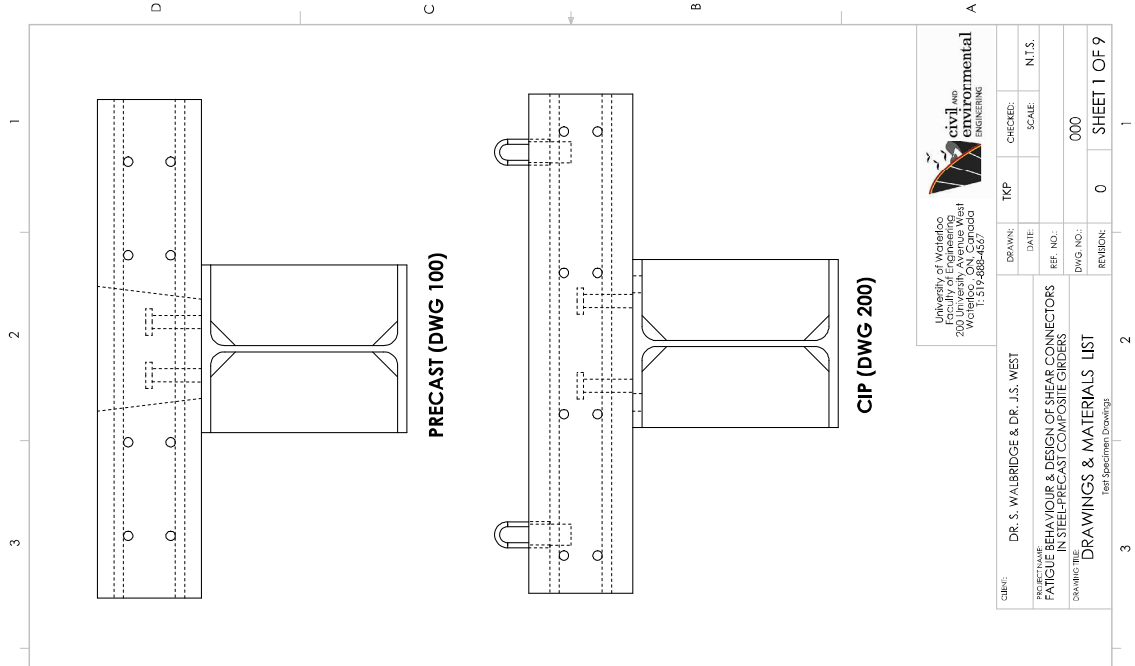
DISCRIPTION	DWG NO.	DISCRIPTION	DWG NO.
DRAWING & MATERIALS LIST	000		
PRECAST SPECIMEN ASSEMBLY	100		
PRECAST SLAB	110		
BEAM WELDMENT	120		
STIFFENERS	121		
SHEAR STUDS	122		
CIP SPECIMEN ASSEMBLY	200		
SLAB	210		
BEAM WELDMENT	220		

MATERIALS	PART NO.	QTY.	
W250X49 - 3200mm			
STIFFENERS - 10mm PL			
HEADED SHEAR STUDS - 16mm D TYPE B			
REBAR - 10M X 3000mm			
REBAR - 10M X 600mm			
40MPA READY MIX CONCRETE			
60MPA NON-SHRINK GROUT			

CLIENT:

PROJECT NAME:
FATIGUE BEHAVIOUR & DESIGN OF SHEAR CONNECTORS
IN STEEL-PRECAST COMPOSITE GIRDERS

DR. S. WALBRIDGE & DR. J.S. WEST

DRAWING TITLE:
DRAWINGS & MATERIALS LIST
Test Specimen Drawings

DRAWN: TKP	CHECKED:
DATE:	SCALE: N.T.S.
REF. NO:	
DWG. NO.:	000
REVISION: 0	SHEET 1 OF 9

DO NOT SCALE DRAWING

163

TOP VIEW

SIDE VIEW

FRONT VIEW

FILL WITH NON-SHIRNK GROUT
TO ESTABLISH SHEAR CONNECTION

3200
3000
125
600
247
202

DO NOT SCALE DRAWING

ITEM	DESCRIPTION	DWG. NO.	QTY.

University of Waterloo
Faculty of Engineering
200 University Avenue West
Waterloo, ON, Canada
T: 519-888-4567

civil AND
environmental
ENGINEERING

CLIENT:

PROJECT NAME:
FATIGUE BEHAVIOUR & DESIGN OF SHEAR CONNECTORS
IN STEEL-PRECAST COMPOSITE GIRDERS

DRAWING TITLE:
PRECAST ASSEMBLY
Test Specimen Drawings

DRAWN: TKP
DATE:

CHECKED:
SCALE: N.T.S.

REF. NO.:
DWG. NO.:
REVISION: 0

DR. S. WALBRIDGE & DR. J.S. WEST

100

SHEET 2 OF 9

TOP VIEW

150
119.30
150
3000
600

REINFORCING CAGES ASSEMBLED
FROM 10M BARS

SIDE VIEW

14°

500
500
400
250
73.70
25.65
100

FRONT VIEW

36.95
51.10
112.50
75

ITEM	DESCRIPTION	DWG. NO.	QTY.

DO NOT SCALE DRAWING

University of Waterloo
Faculty of Engineering
200 University Avenue West
Waterloo , ON Canada
T: 519-888-4567

civil AND
environmental
ENGINEERING

CLIENT:

PROJECT NAME:
FATIGUE BEHAVIOUR & DESIGN OF SHEAR CONNECTORS
IN STEEL-PRECAST COMPOSITE GIRDERS

DRAWING TITLE:
PRECAST SLAB DETAIL
Test Specimen Drawings

DRAWN: TKP
DATE:
REF. NO.:
DWG. NO.: 110
REVISION: 0

CHECKED:
SCALE: N.T.S.

SHEET 3 OF 9

DR. S. WALBRIDGE & DR. J.S. WEST

165

TOP VIEW

SIDE VIEW

FRONT VIEW

3000

850

350

100

64

64

202

24 TYP. WITH STUD GUN

8 TYP.

6 6

DRAWN: TKP	DATE:
CHECKED:	SCALE: N.T.S.
REF. NO:	
DWG. NO.:	
REVISION: 0	120	SHEET 4 OF 9

CLIENT:
PROJECT NAME: DR. S. WALBRIDGE & DR. J.S. WEST
FATIGUE BEHAVIOUR & DESIGN OF SHEAR CONNECTORS IN STEEL-PRECAST COMPOSITE GIRDERS
DRAWING TITLE: PRECAST BEAM WELDMENT
Test Specimen Drawings

ITEM	DESCRIPTION	DWG. NO.	QTY.
1	W250X49		
2	STIFFENER		
3	SHEAR STUD		

DO NOT SCALE DRAWING

166

167

SIDE VIEW

10

TOP VIEW

FRONT VIEW

225

97

30

30

TOP VIEW

SIDE VIEW

$\varnothing 31.75$

67

$\varnothing 16$

CLIENT:

PROJECT NAME:
FATIGUE BEHAVIOUR & DESIGN OF SHEAR CONNECTORS
IN STEEL-PRECAST COMPOSITE GIRDERS

DR. S. WALBRIDGE & DR. J.S. WEST

DRAWING TITLE:
HEADED SHEAR STUDS
Test Specimen Drawings

DRAWN: TKP

DATE:

REF. NO.:

DWG. NO.:
122

REVISION:
0

CHECKED:

SCALE: N.T.S.

SHEET 6 OF 9

DO NOT SCALE DRAWING

TOP VIEW

SIDE VIEW

FRONT VIEW

3200
3000
125
600
247
202

CLIENT:		DRAWN:	TKP	CHECKED:	
		DATE:		SCALE:	N.T.S.
PROJECT NAME: DR. S. WALBRIDGE & DR. J.S. WEST		REF. NO.:			
FATIGUE BEHAVIOUR & DESIGN OF SHEAR CONNECTORS IN STEEL-PRECAST COMPOSITE GIRDERS		DWG. NO.:			200
DRAWING TITLE: CIP ASSEMBLY		REVISION:	0		SHEET 7 OF 9
Test Specimen Drawings					

ITEM	DESCRIPTION	DWG. NO.	QTY.

DO NOT SCALE DRAWING

REINFORCING CAGES ASSEMBLED
FROM 10M BARS

TOP VIEW

SIDE VIEW

FRONT VIEW

3000

500

400

100

31

63

125

70

LIFTING HOOKS EMBEDED
DURING CAST

42.30

40.40

170

45

125

170

DO NOT SCALE DRAWING

ITEM	DESCRIPTION	DWG. NO.	QTY.

CLIENT:

DR. S. WALBRIDGE & DR. J.S. WEST

PROJECT NAME:

FATIGUE BEHAVIOUR & DESIGN OF SHEAR CONNECTORS
IN STEEL-PRECAST COMPOSITE GIRDERS

DRAWING TITLE:

CIP SLAB DETAIL

Test Specimen Drawings

DRAWN: TKP
DATE:

CHECKED:
SCALE: N.T.S.

REF. NO.:

DWG. NO.:   210

REVISION: 0

SHEET 8 OF 9

TOP VIEW

475
225
202
102

FRONT VIEW

6 6 / 8 TYP.

100

SIDE VIEW

3200

24 TYP. WITH
STUD GUN

DRAWN: TKP
CHECKED:

DATE:
SCALE: N.T.S.

REF. NO:

CLIENT:

PROJECT NAME:
FATIGUE BEHAVIOUR & DESIGN OF SHEAR CONNECTORS
IN STEEL-PRECAST COMPOSITE GIRDERS
DR. S. WALBRIDGE & DR. J.S. WEST

DRAWING TITLE:
CIP BEAM WELDMENT
Test Specimen Drawings

DWG. NO.: 220

REVISION: 0

SHEET 9 OF 9

ITEM	DESCRIPTION	DWG. NO.	QTY.

DO NOT SCALE DRAWING

171

Appendix B: Instrumentation

	Test No.		1	2	3	4	5	6	7	8	9	10	11	12
	Type		CIP	Precast	CIP	Precast	CIP	Precast	CIP	Precast	CIP	Precast	CIP	Precast
	Eq. Stress (MPa)		140	140	200	200	300	300	100	100	120	120	67	67
LVDTs	Max Deflection	75 mm stroke	x	x	x	x	x	x	x	x	x	x	x	x
	Slip 1 (West End)	10 mm stroke	x	x	x	x	x	x	x	x	x	x	x	x
	Slip 2 (Profile A)	10 mm stroke	x	x	x	x	x	x	x	x	x	x	x	x
	Slip 3 (Profile B)	10 mm stroke	x	x	x	x	x	x						
	Slip 4 (Profile Y)	10 mm stroke	x	x	x	x	x	x	x	x	x	x	x	x
	Slip 5 (East End)	10 mm stroke	x	x	x	x	x	x	x	x	x	x	x	x
Local Distortion Gauges Under Studs	N1	10 mm	x	x	x	x	x	x	x	x	x	x	x	x
	S1	10 mm	x	x	x	x	x	x	x	x	x	x	x	x
	N2	10 mm		x	x	x	x	x	x	x	x	x	x	x
	S2	10 mm		x	x	x	x	x	x	x	x	x	x	x
	N3	10 mm		x	x	x	x	x	x	x	x	x	x	x
	S3	10 mm		x	x	x	x	x	x	x	x	x	x	x
	N4	10 mm		x	x	x	x	x	x	x	x	x	x	x
	S4	10 mm		x	x	x	x	x	x	x	x	x	x	x
	N5	10 mm						x	x	x				
	S5	10 mm						x	x	x				
	N6	10 mm						x	x	x				
	S6	10 mm						x	x	x				
	N7	10 mm												
	S7	10 mm						x	x	x				
	N8	10 mm						x	x	x				
	S8	10 mm						x	x	x				
	N9	10 mm					x	x	x	x	x	x		
	S9	10 mm					x	x	x	x	x	x		
	N10	10 mm					x	x	x	x	x	x		
	S10	10 mm					x	x	x	x	x	x		
	N11	10 mm					x	x	x	x	x	x	x	x
	S11	10 mm					x	x	x	x	x	x	x	x
	N12	10 mm					x	x	x	x	x	x	x	x
	S12	10 mm					x	x	x	x	x	x	x	x
Profile Gauges	E (Top Conc)	60 mm	x	x	x	x								
	E (Top Rebar)	10 mm	x	x	x									
	E (Bot Rebar)	10 mm	x	x	x									
	E (Bot Conc)	60 mm	x	x	x									
	E (Top Steel)	10 mm	x	x	x	x								
	E (Mid Steel)	10 mm	x	x										
	E (Bot Steel)	10 mm	x	x	x	x								
	A (Top Conc)	60 mm		x	x									
	A (Bot Conc)	60 mm		x	x									
	A (Top Steel)	10 mm				x	x	x	x	x	x	x	x	x
	A (Bot Steel)	10 mm				x	x	x	x	x	x	x	x	x
	B (Top Conc)	60 mm	x	x	x	x								
	B (Top Rebar)	10 mm	x	x	x	x								
	B (Bot Rebar)	10 mm	x	x	x	x								
	B (Bot Conc)	60 mm	x	x	x									
	B (Top Steel)	10 mm	x	x	x	x	x	x	x	x	x	x	x	x
	B (Mid Steel)	10 mm	x	x	x	x								
	B (Bot Steel)	10 mm	x	x	x	x	x	x	x	x	x	x	x	x
	Y (Top Steel)	10 mm				x	x	x	x	x	x	x	x	x
	Y (Bot Steel)	10 mm				x	x	x	x	x	x	x	x	x
	Z (Top Steel)	10 mm				x	x	x	x	x	x	x	x	x
	Z (Bot Steel)	10 mm				x	x	x	x	x	x	x	x	x
	Temperature	10 mm			x	x	x	x	x	x	x	x	x	x

Appendix C: Concrete & Grout Cylinder Testing

Table C-1: Concrete Cylinder Test Results.

	Pour 1		Pour 2		HP-S10 Grout (Avg)	
Date:	15-Apr-15		4-May-15		2-Jul-15	
Slump:	130 mm		180 mm		N.A	
	Day	**Strength (MPa)**	**Day**	**Strength (MPa)**	**Day**	**Strength (MPa)**
	0	0	0	0	0	0
	7	26.2	7	25.1	4	44.9
	15	34.6	28	35.5	28	56.9
	28	42.9	190	50.1	131	59.4
	169	44.7	213	49.7	214	76.3
	209	48.3	300	49.6	280	64.2
	273	46.4				
	280	45.9				
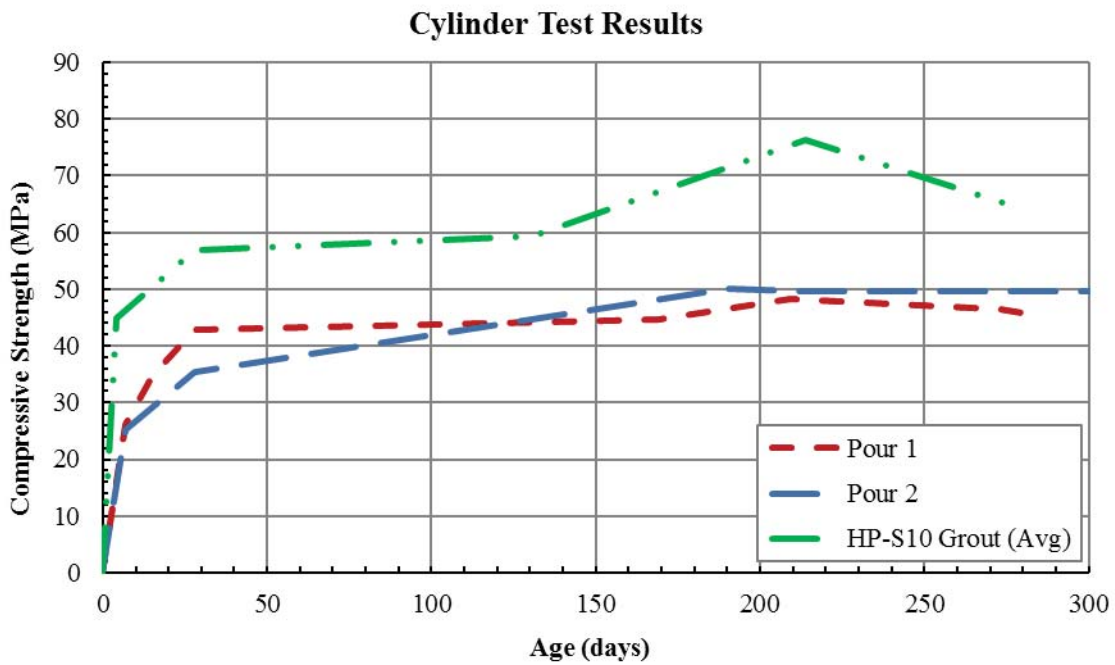
Figure C-1: Compressive strengths of the concrete and grout cylinders.

Appendix D: Experimental Design Spreadsheet

Geometry	Symbol	Value	Units
Steel Geometry			
Span	L	3000	mm
Steel Section		W250x49	
Area	A	6250	mm2
MOI (x)	Ix	7.06E+07	mm4
Depth	d	247	mm
Flange Width	b	202	mm
Flange Thickness	tt	11	mm
Web Width	w	7.4	mm
Dead Load	DL	0.481	kN/m
Slab Geometry			
Slab Thickness	tc	125	mm
Effective Width	be	600	mm
Top Cover	ct	25	mm
Bottom Cover	cb	25	mm
Top Bar Type		10M	
No. Top Bars	ntb	4	bars
Top Area	Atr	400	mm2
Bottom Bar Type		10M	
No. Bottom Bars	nbb	4	bars
Bottom Area	Abr	400	mm2
Shear Connectors			
Diameter	dsc	16	mm
Area	Asc	201	mm2
Amount	nsc	4	

Material Properties	Symbol	Value	Units
Steel Section			
Yield Strength	fy	350	MPa
Ultimate Strength	fu	450	MPa
Elastic Modulus	Es	200000	MPa
Concrete			
Comp. Strength	f'c	40	MPa
Density	gamma	2300	kg/m3
Stress Block Factor	alpha1	0.79	
Stress Block Factor	beta1	0.87	
Elastic Modulus	Ec	27771	MPa
Rebar			
Yield Strength	fyr	400	MPa
Shear Connectors			
Yield Strength	fysc	350	MPa
Ultimate Strength	fusc	450	MPa
Resistance Factors			
Steel Section	φs	1	
Concrete	φc	1	
Rebar	φr	1	
Shear Connectors	φsc	1	

Attribute	Symbol	Value	Units
Elastic Transformed Section Analysis			
Modular ratio	n	7.20	
E.N.A in:		STEEL	
Centroid	ybar	129.1	mm
MOI Transformed	It	2.23E+08	mm4
Moment of Area	Q	6.93E+05	mm3
S Transformed	St	9.19E+05	mm3
Ultimate Limit State (ULS)			
Shear Res. Conc	qr	106.0	kN
Shear Res. Stud	qr	90.5	kN
Governing	qr	90.5	kN
Force Slab @ Ult	P	2870	kN
Force steel @ Ult	P	2187.5	kN
Governing	P	2187.5	kN
Shear span @ 1500	Nstuds	12	
% Shear Connection		50%	
Shear span @ 1000	Nstuds	8	
% Shear Connection		33%	

Appendix E: Static Test Data

Appendix E1: Load-Deflection Results
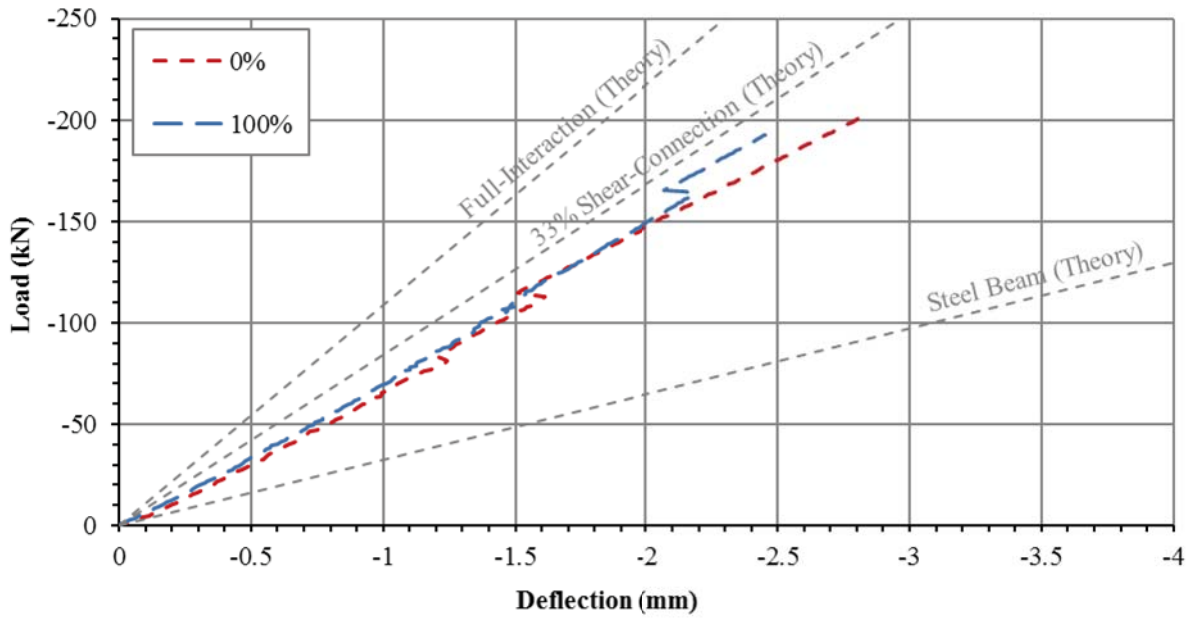
Figure E1-1: C067 – Load Deflection Data
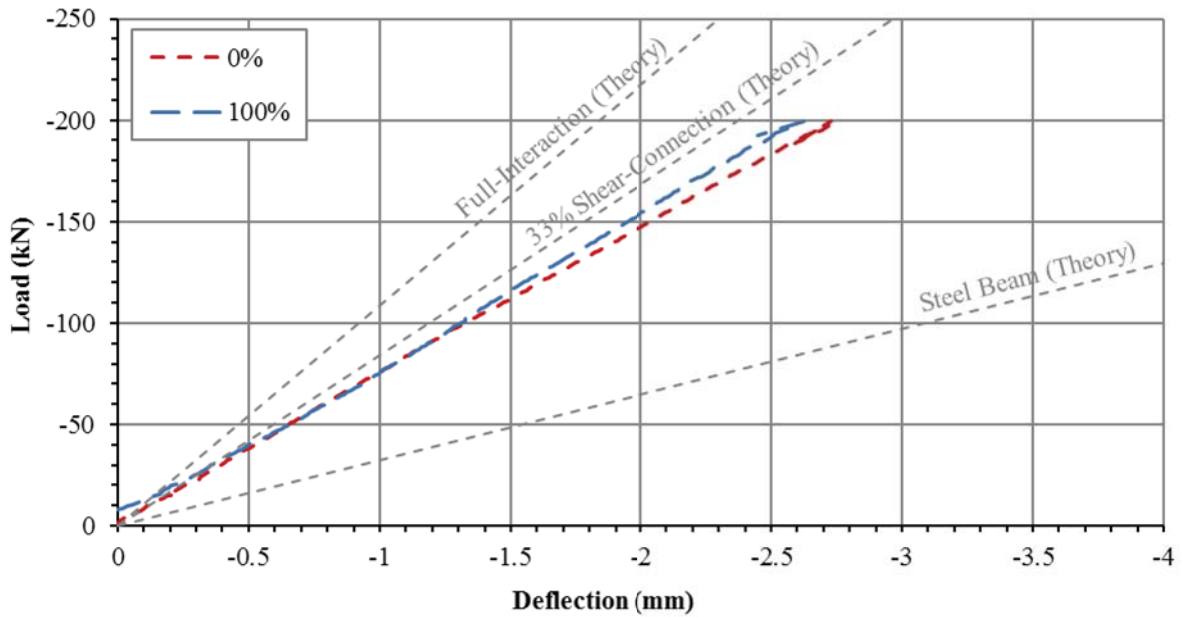
Figure E1-2: P067 – Load Deflection Data
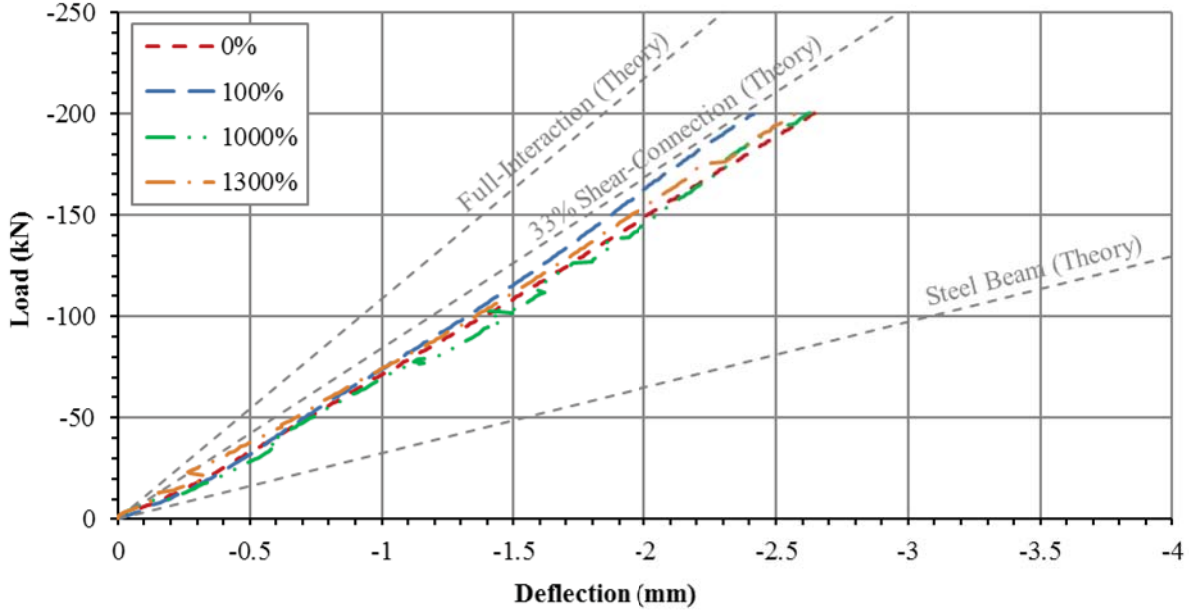
Figure E1-3: C100 – Load Deflection Data
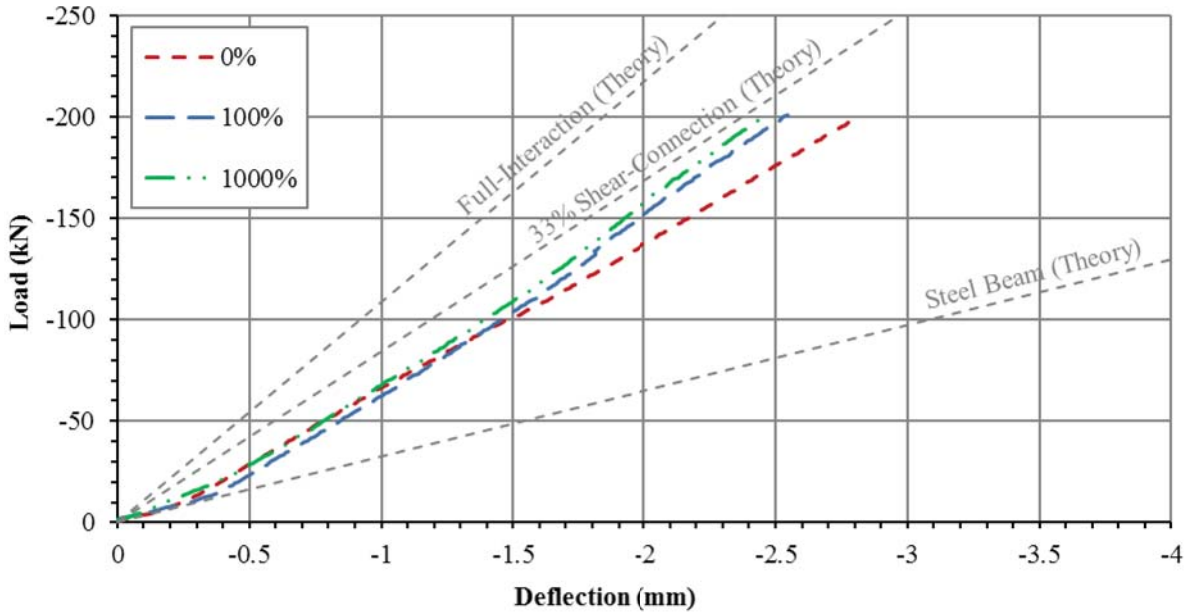
Figure E1-4: P100 – Load Deflection Data

177
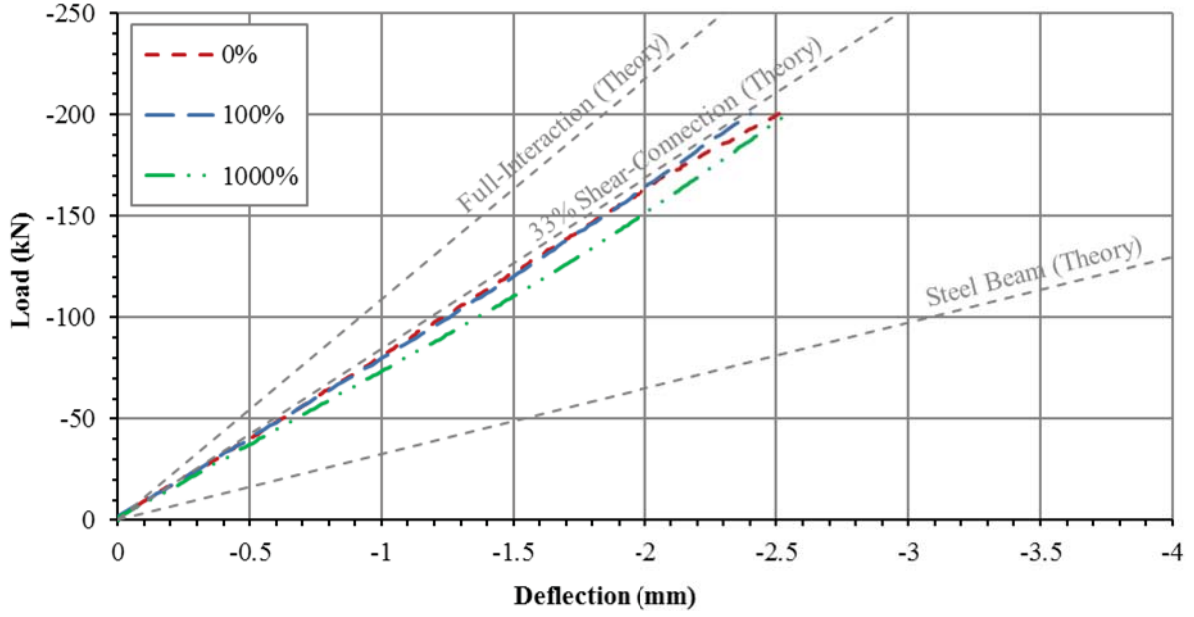
Figure E1-5: C120 – Load Deflection Data
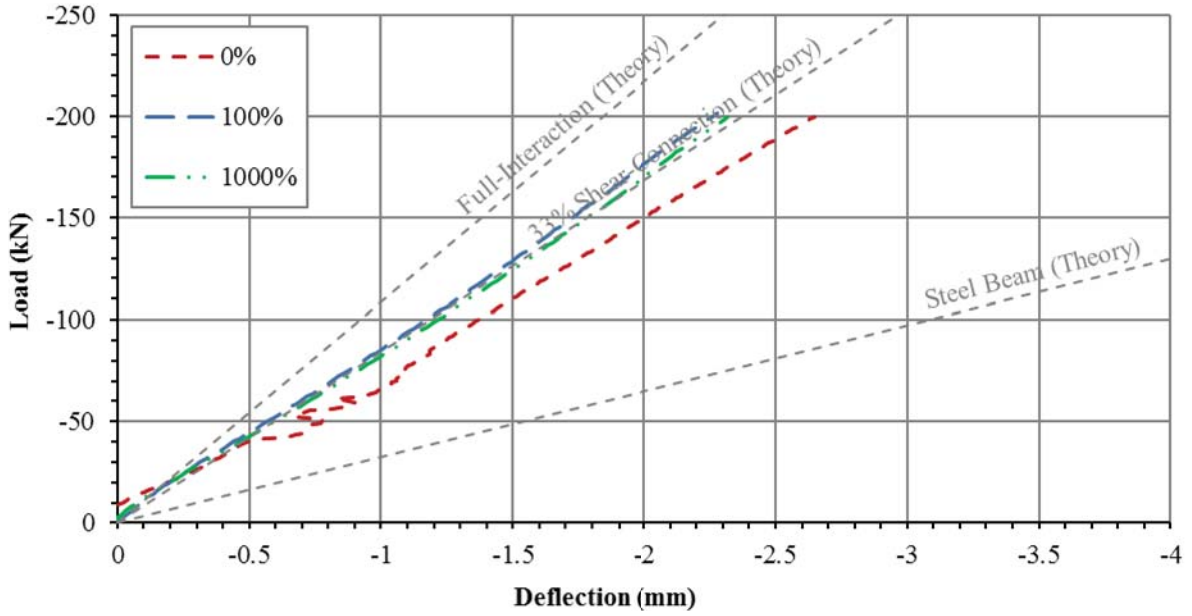
Figure E1-6: P120 – Load Deflection Data
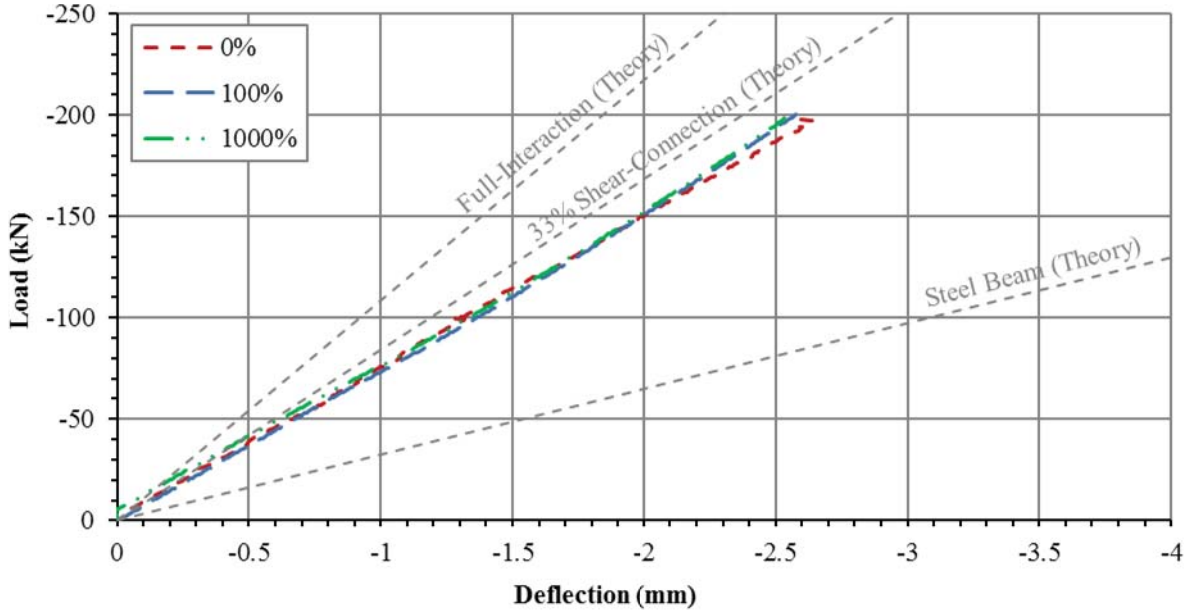
Figure E1-7: C140 – Load Deflection Data
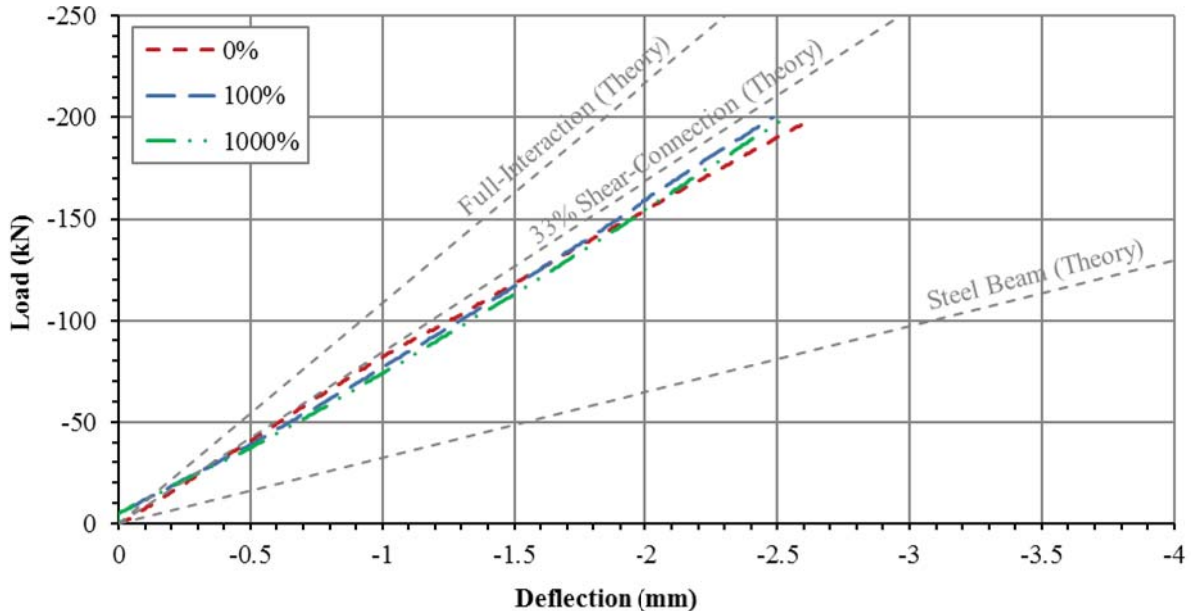
Figure E1-8: P140 – Load Deflection Data
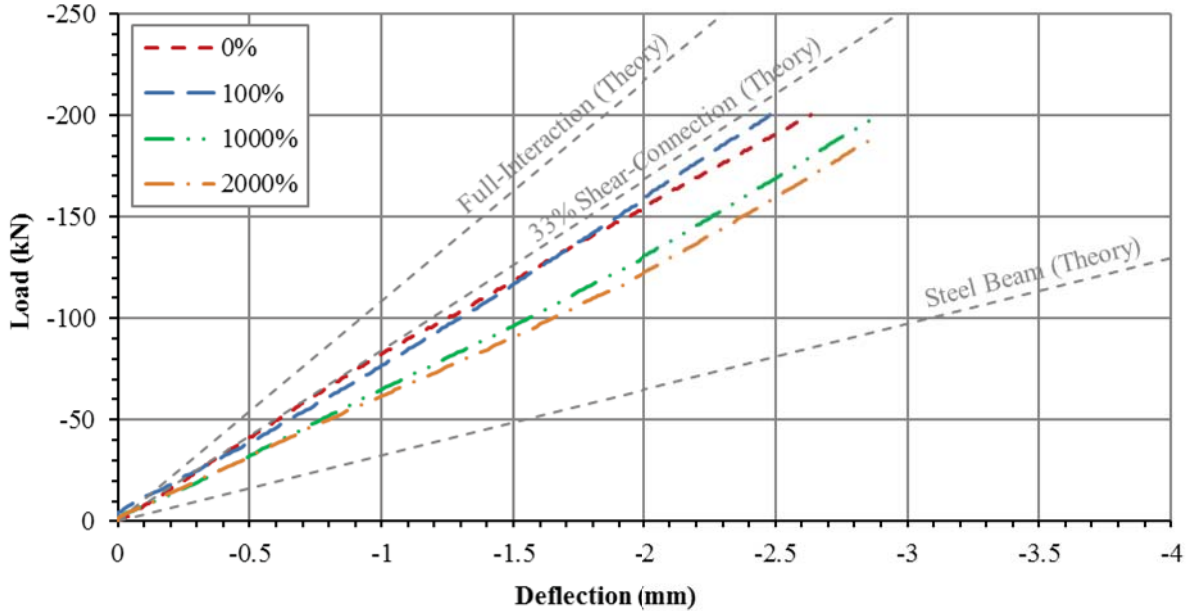
Figure E1-9: C200 – Load Deflection Data
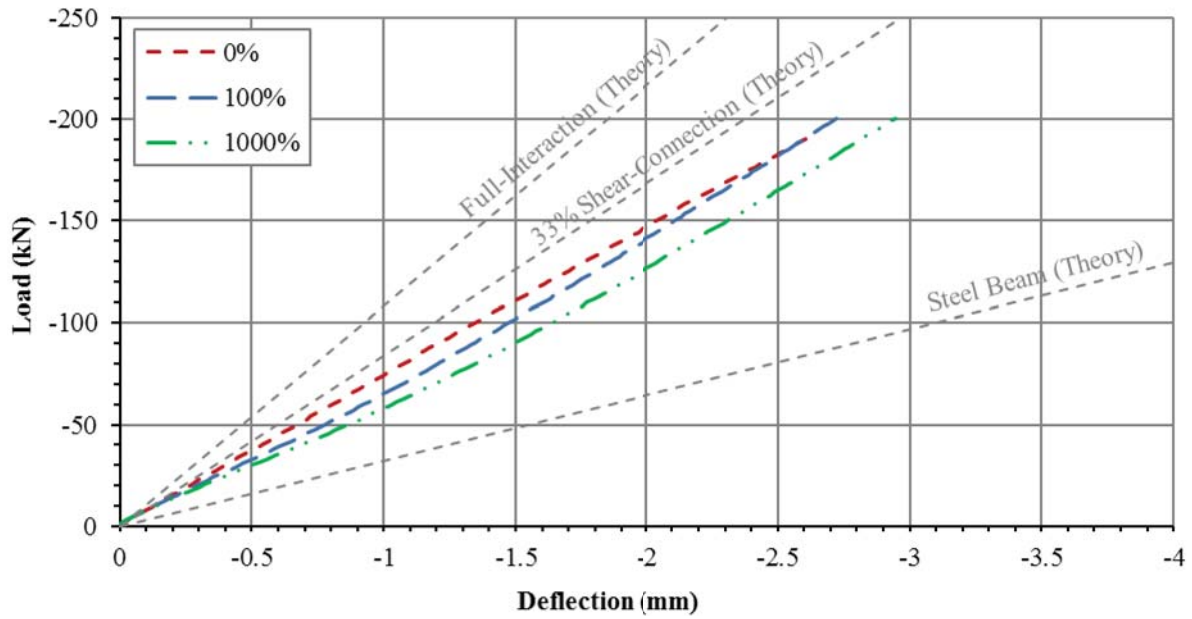
Figure E1-10: P200 – Load Deflection Data
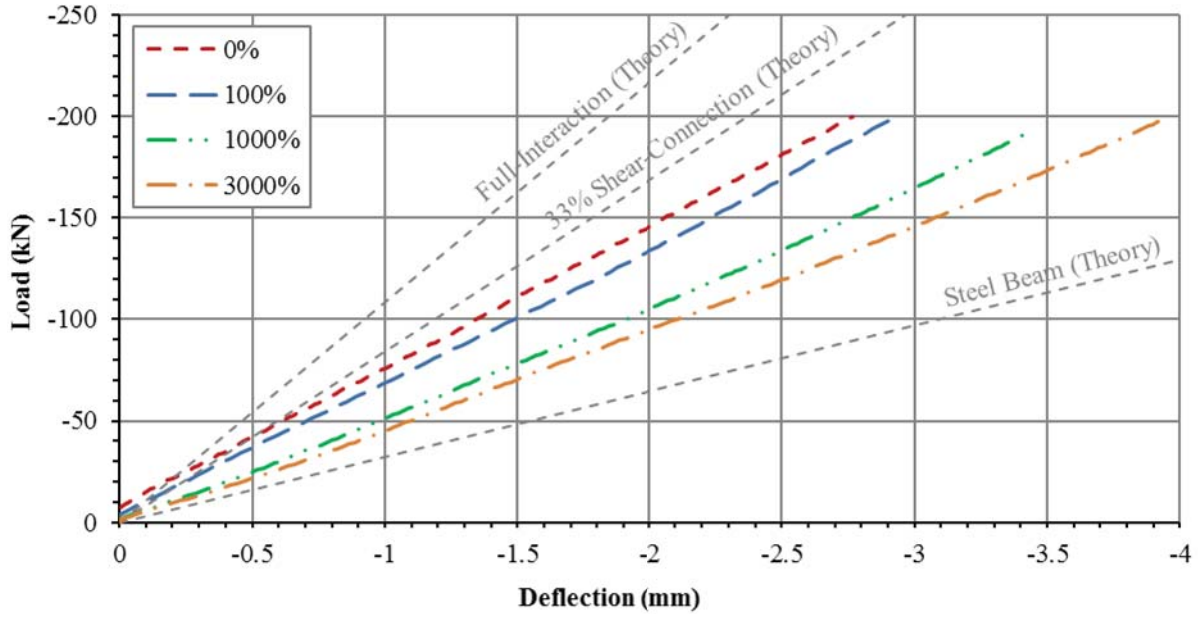
Figure E1-11: C300 – Load Deflection Data
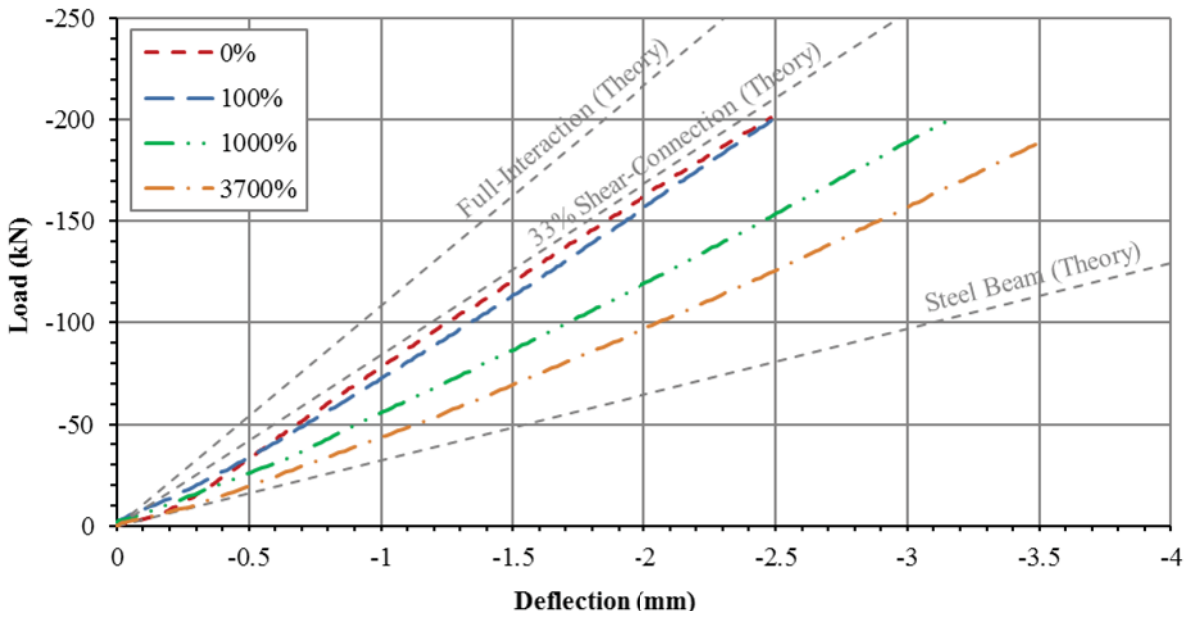
Figure E1-12: P300 – Load Deflection Data

Appendix E2: Interfacial Slip Results
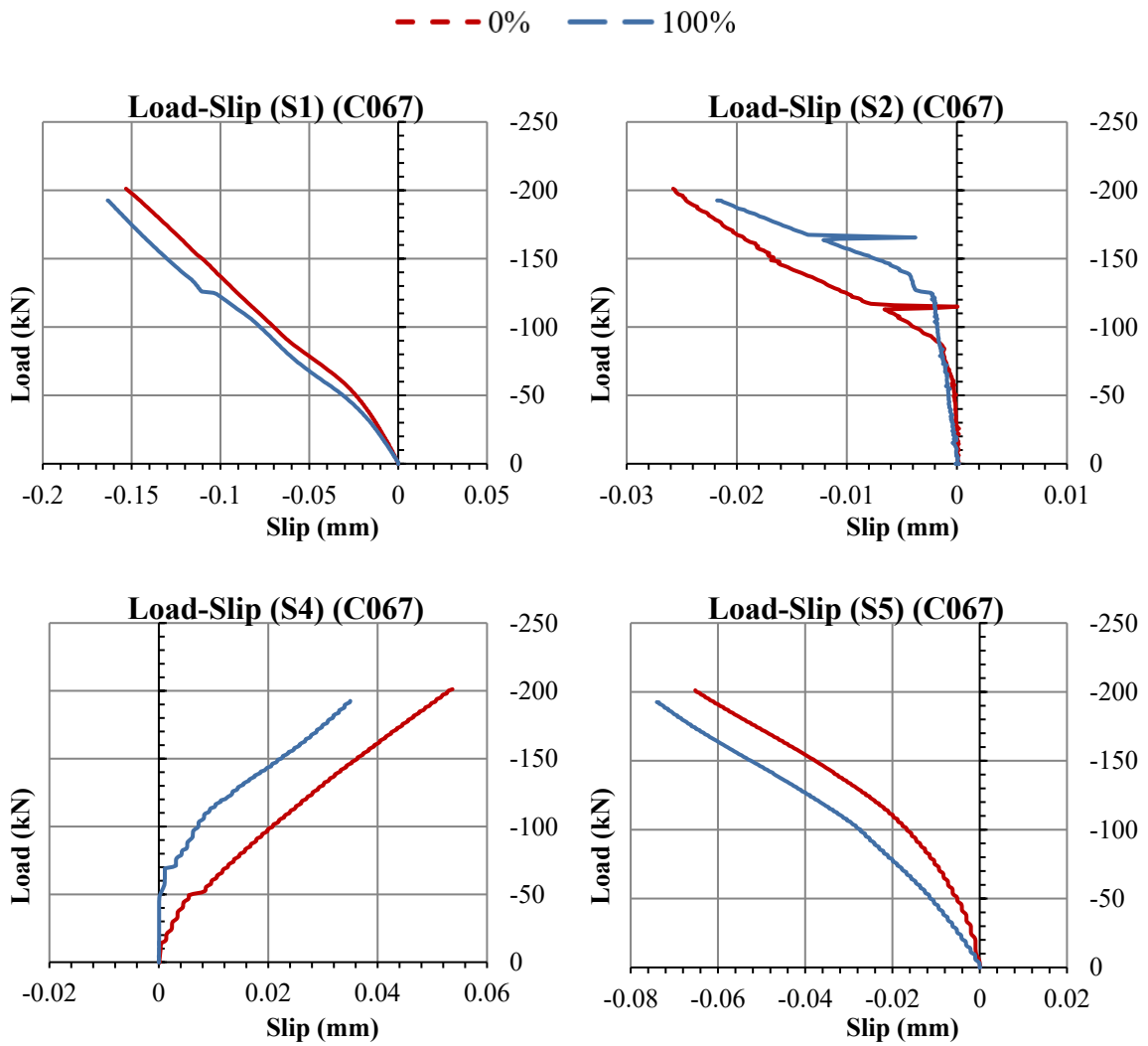
Figure E2-1: C067 – Load Slip Data
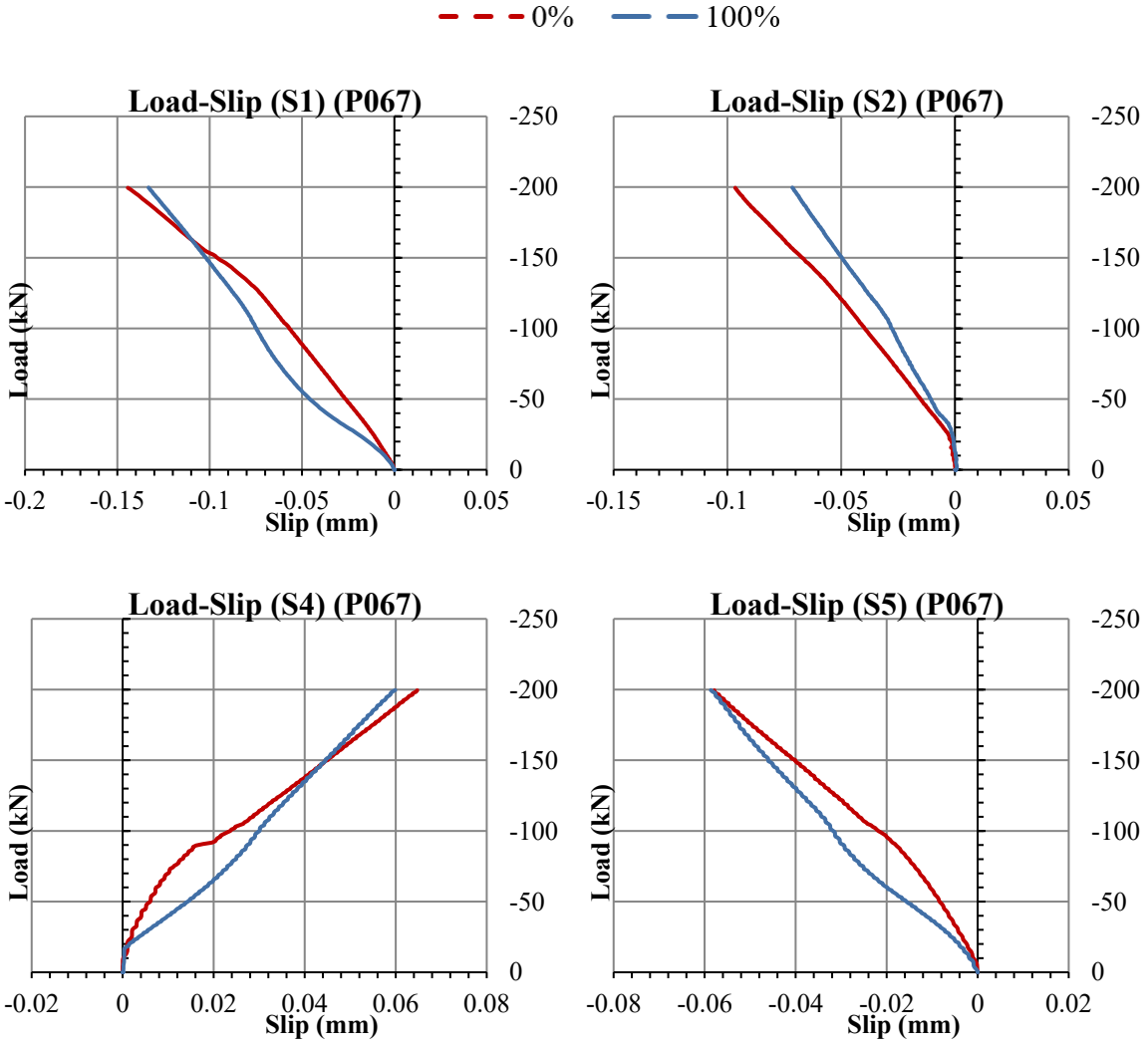
Figure E2-2: P067 – Load Slip Data
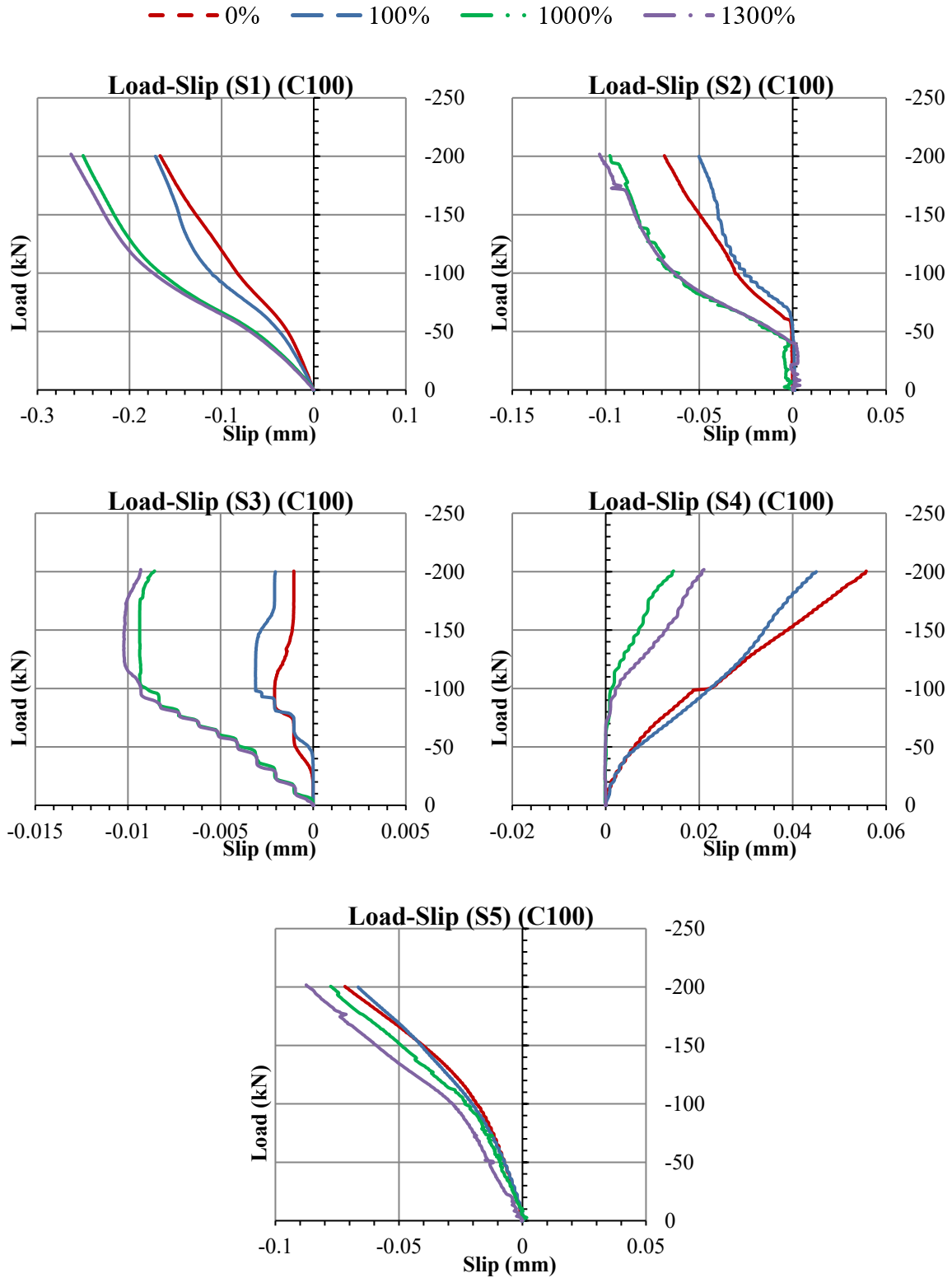
Figure E2-3: C100 – Load Slip Data
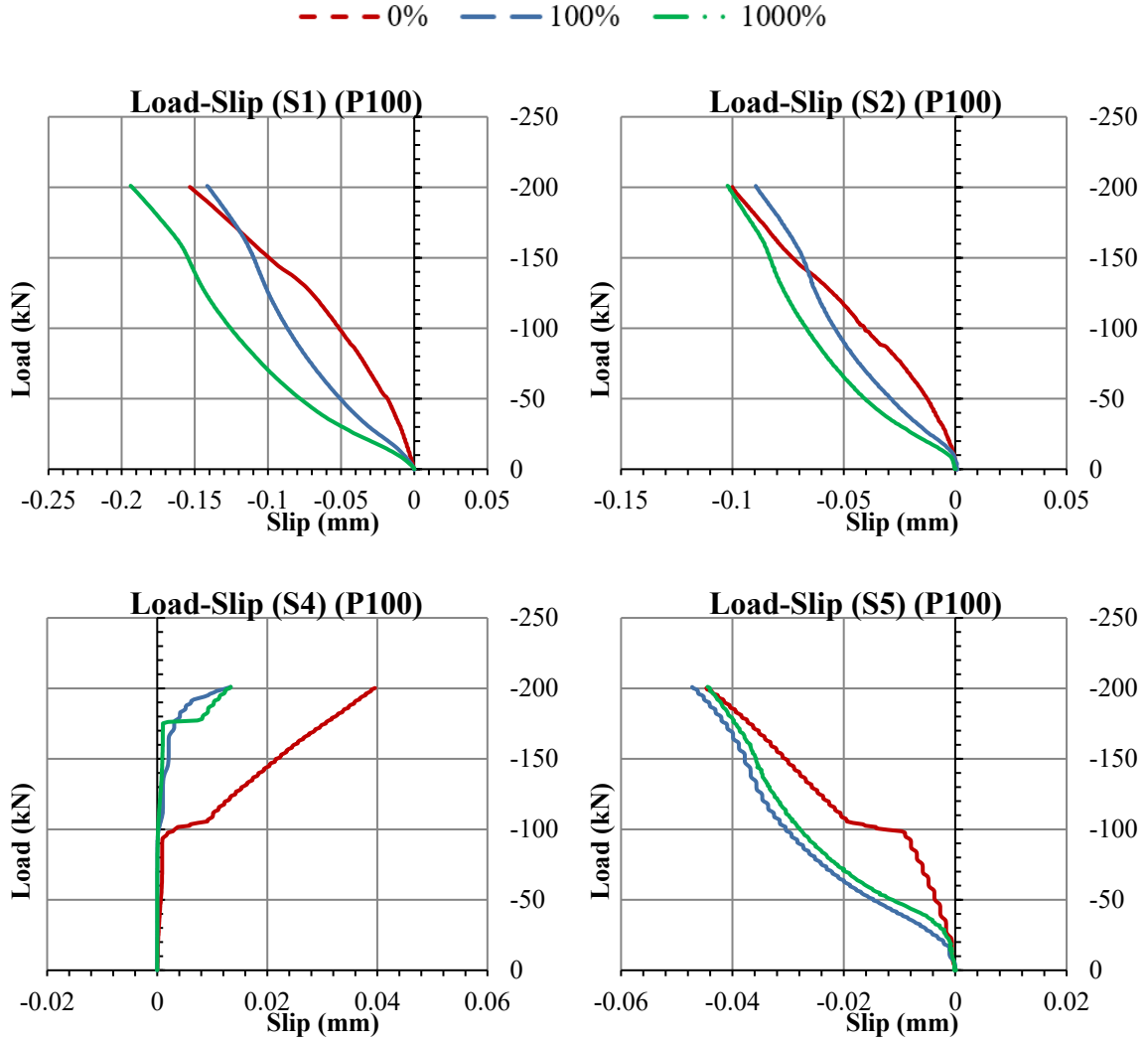
Figure E2-4: P100 – Load Slip Data

185
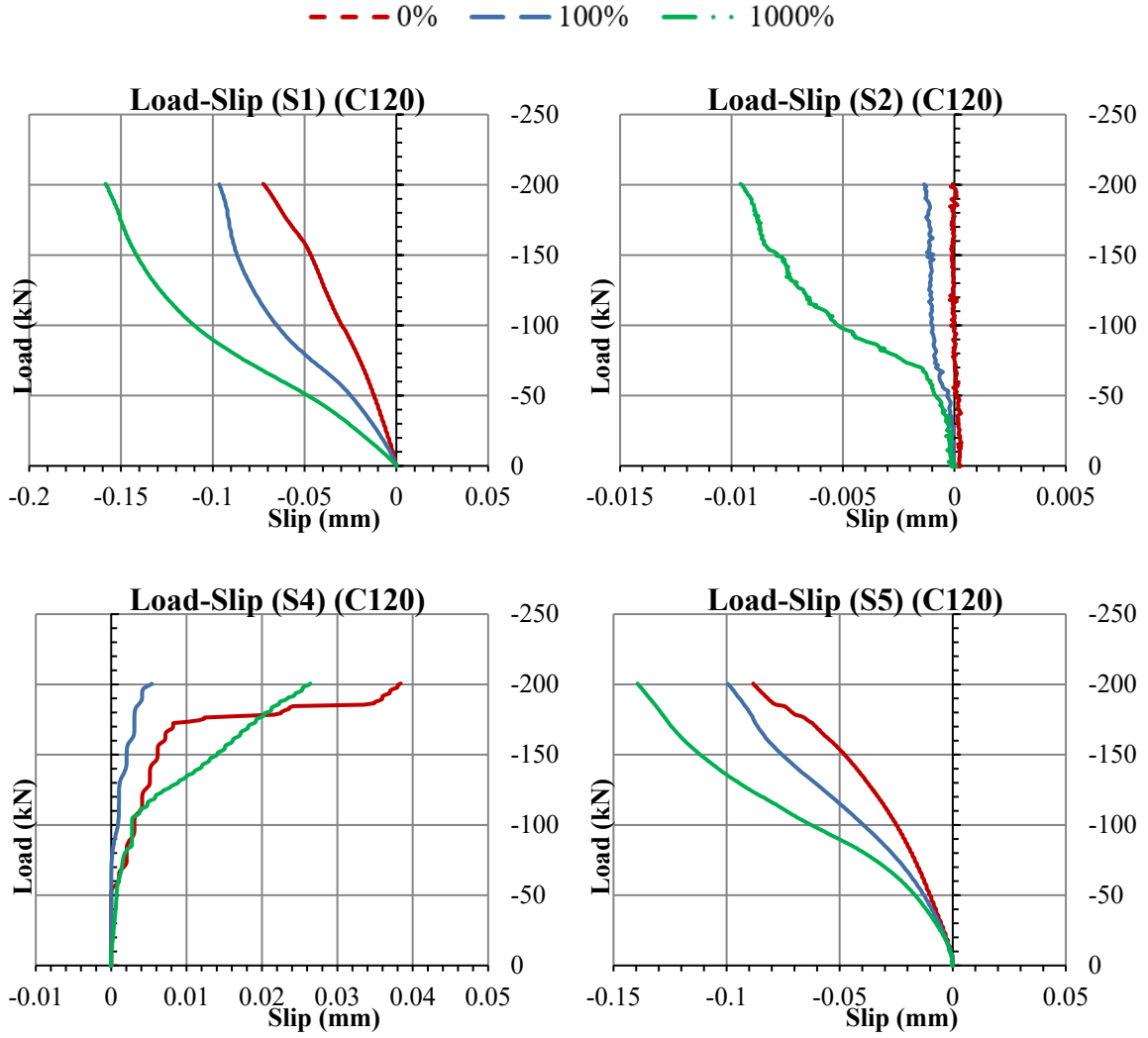
Figure E2-5: C120 – Load Slip Data
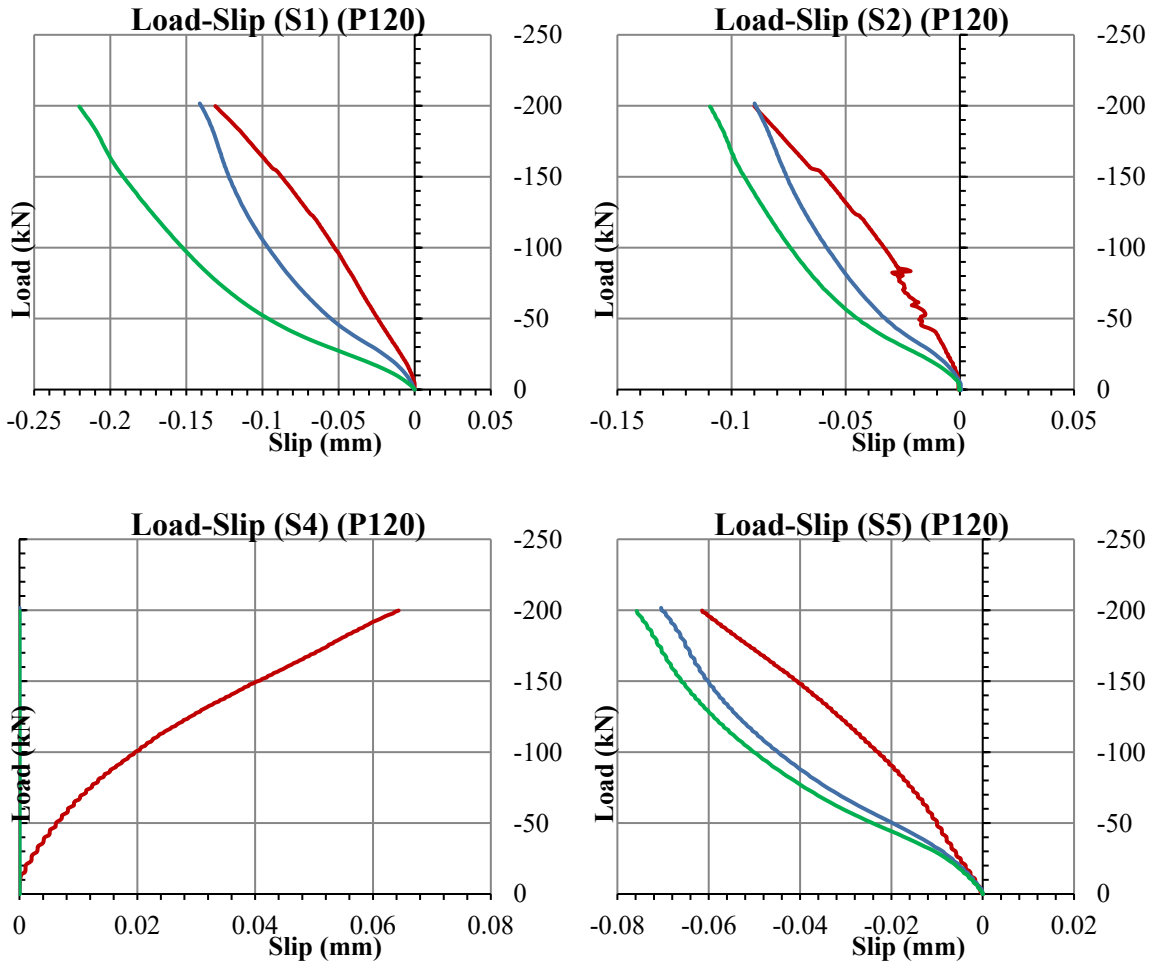
Figure E2-6: P120 – Load Slip Data
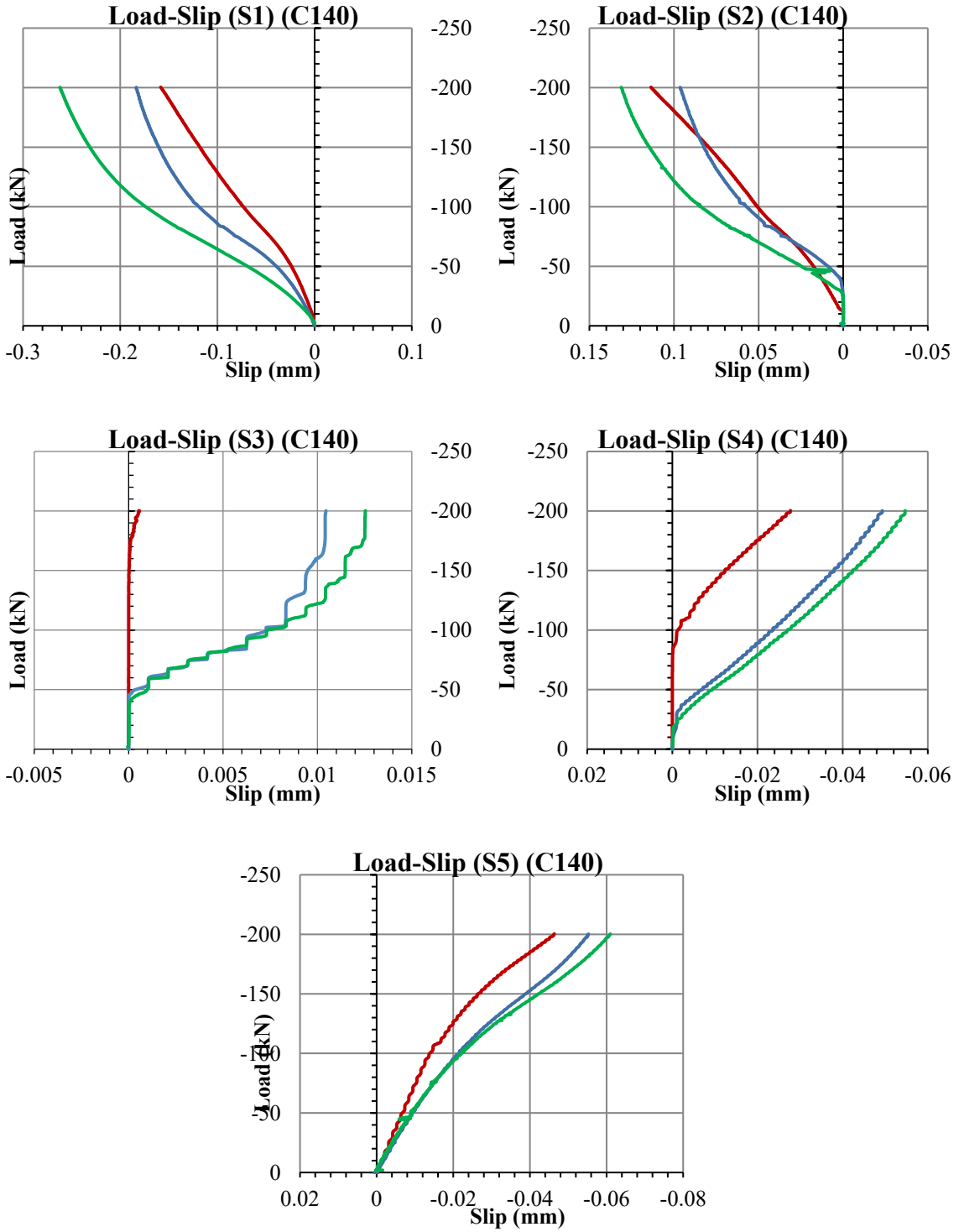
Figure E2-7: C140 – Load Slip Data
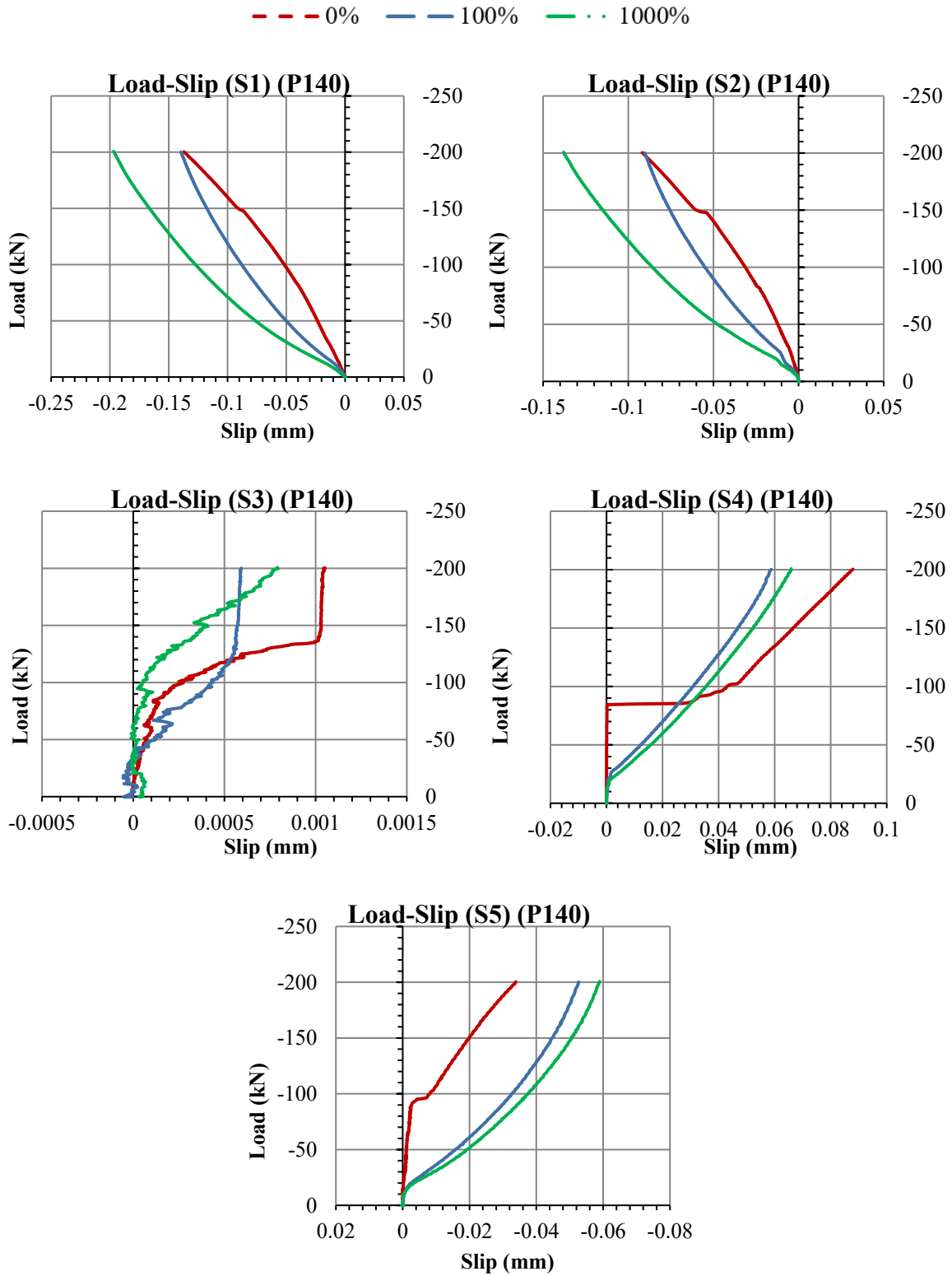
Figure E2-8: P140 – Load Slip Data

189
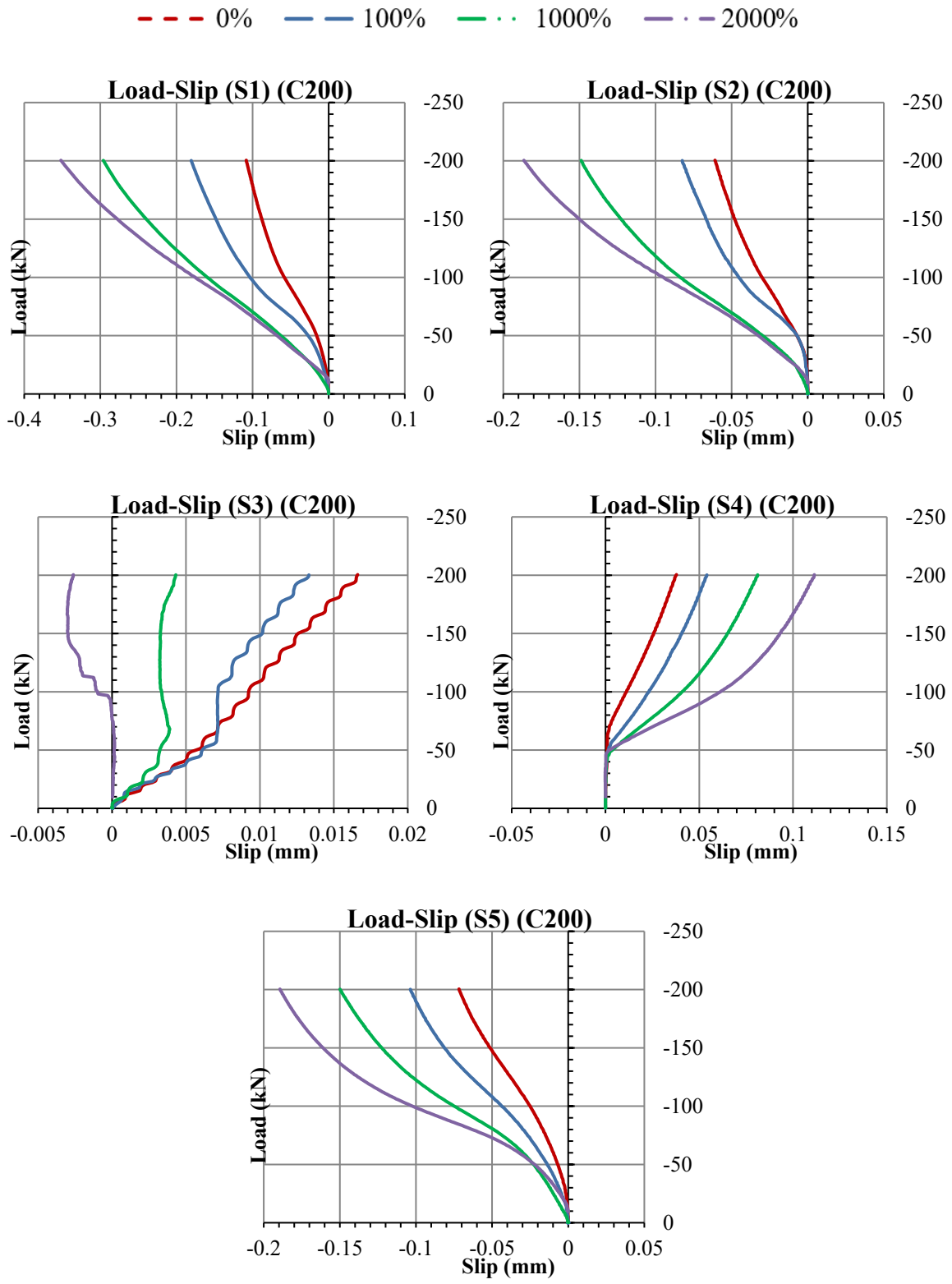
Figure E2-9: C200 – Load Slip Data
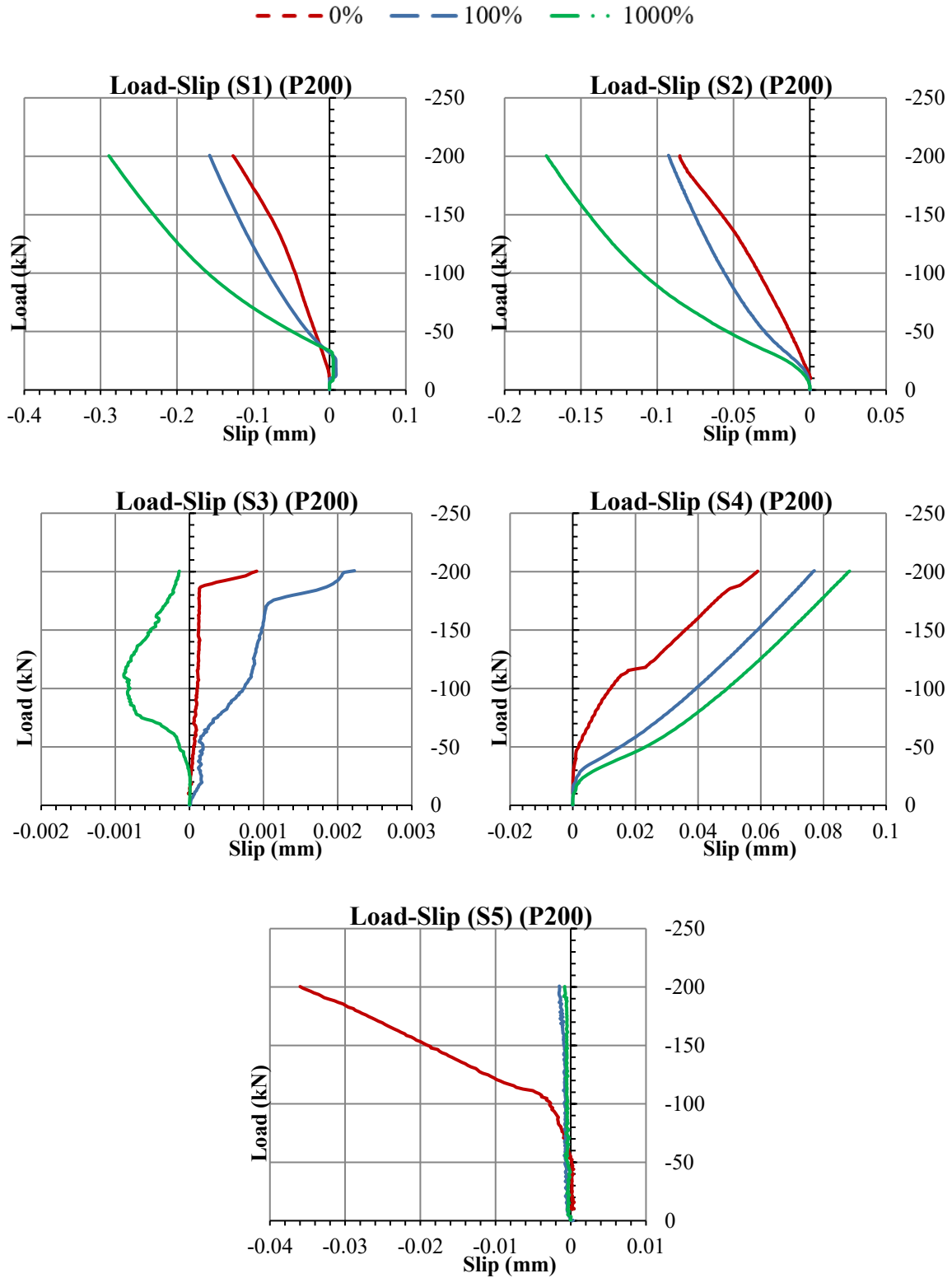
Figure E2-10: P200 – Load Slip Data
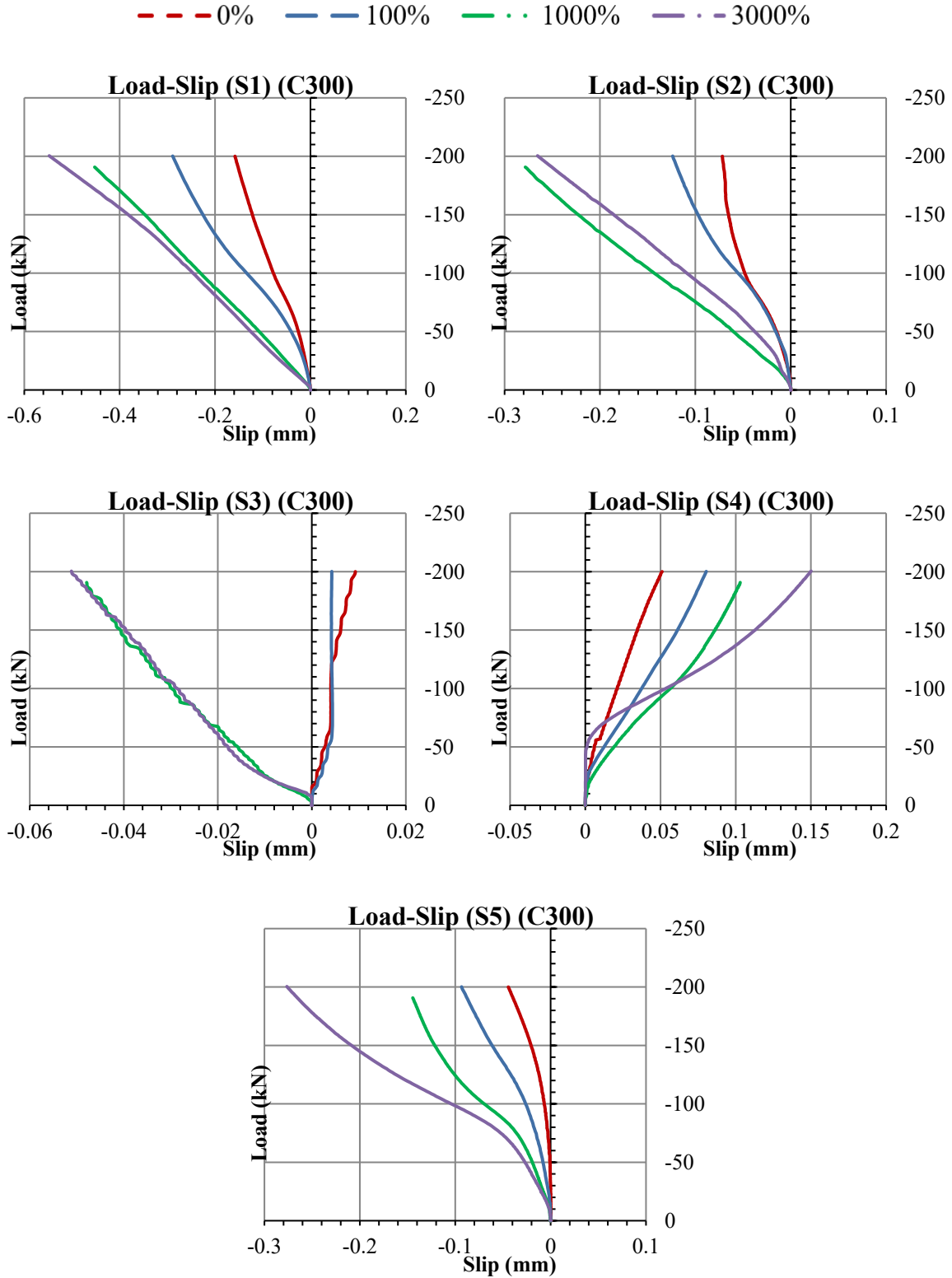
Figure E2-11: C300 – Load Slip Data

192
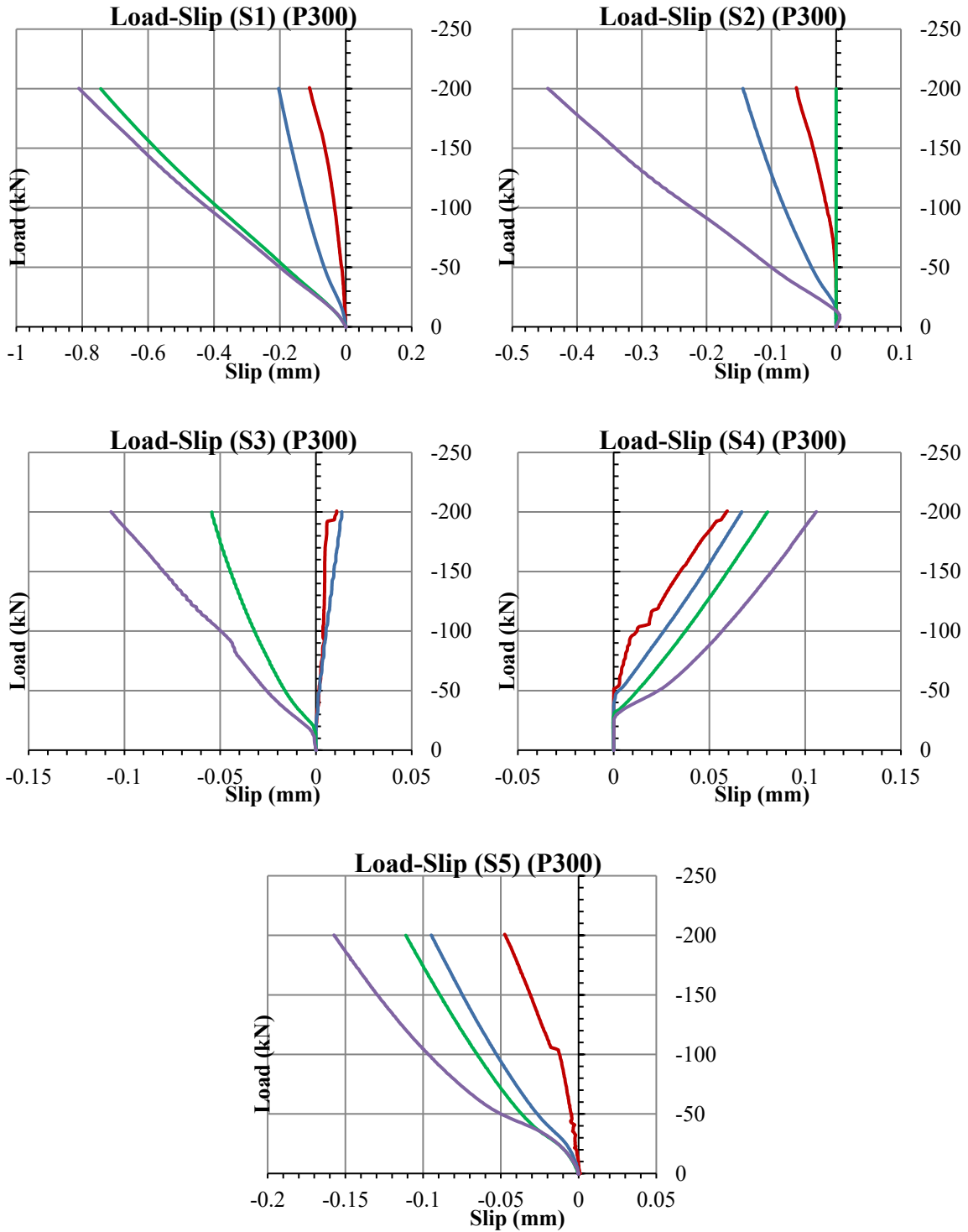
Figure E2-12: P300 – Load Slip Data
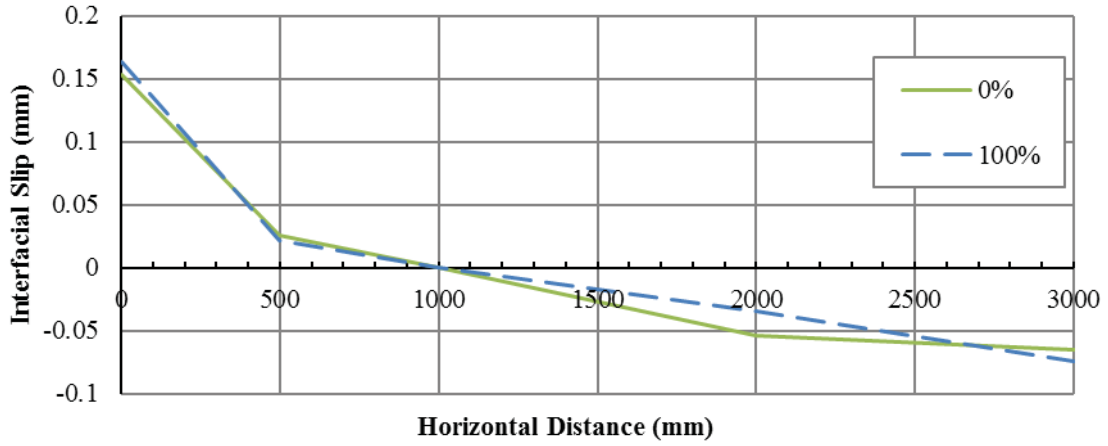
Figure E2-13: C067 – Slip Profile
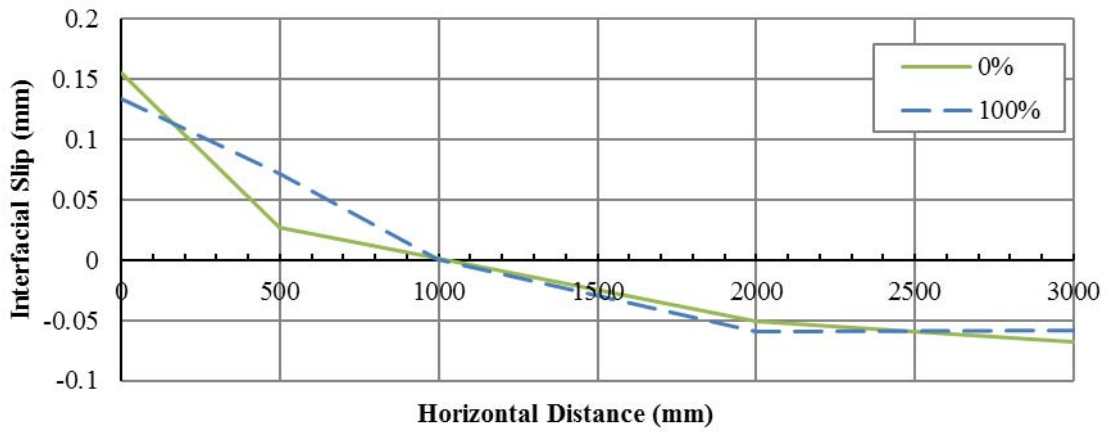
Figure E2-14: P067 – Slip Profile
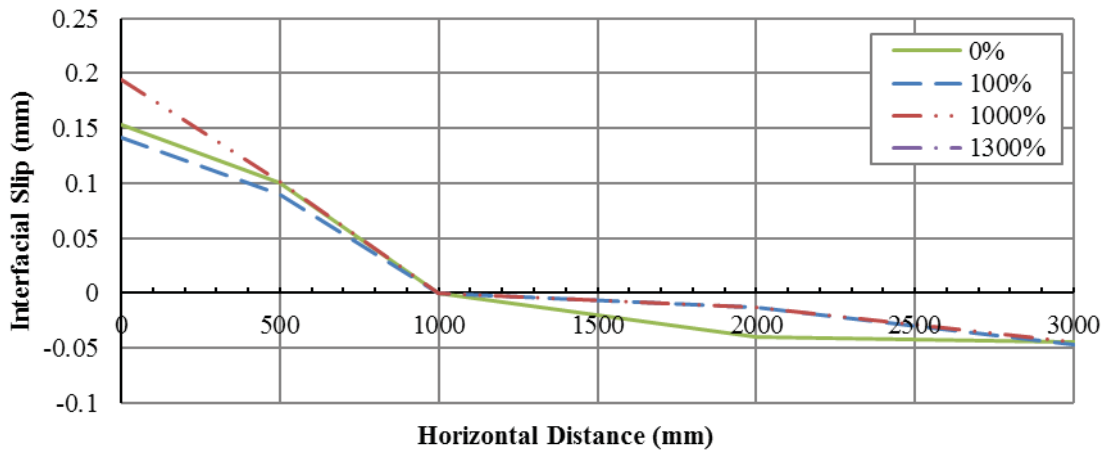
Figure E2-15: C100 – Slip Profile

194
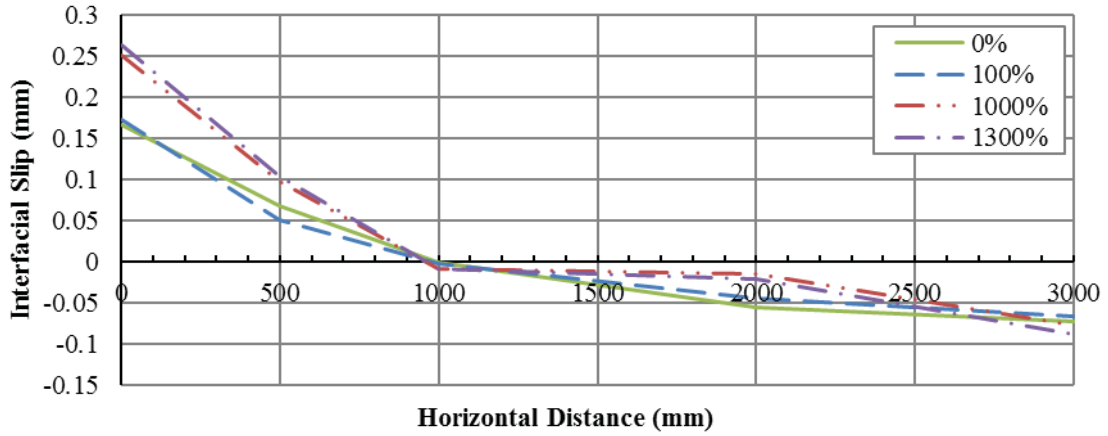
Figure E2-16: P100 – Slip Profile
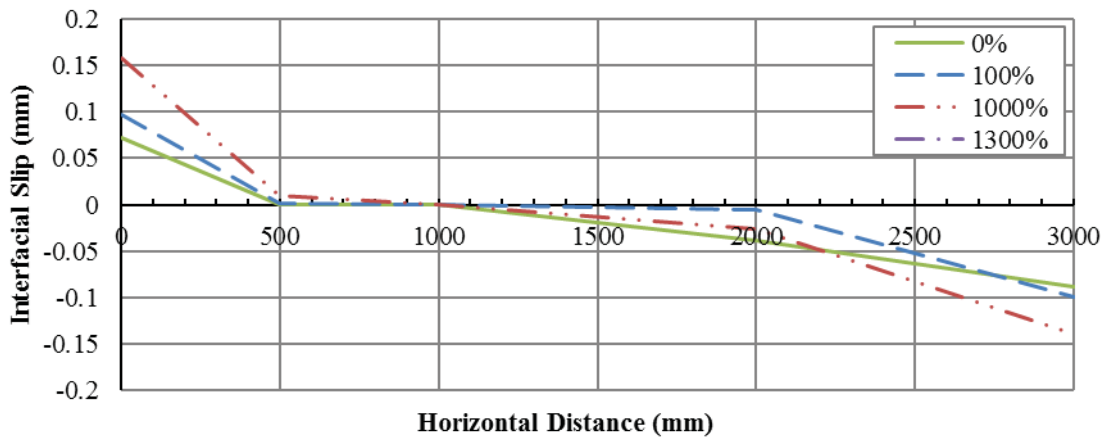
Figure E2-17: C120 – Slip Profile
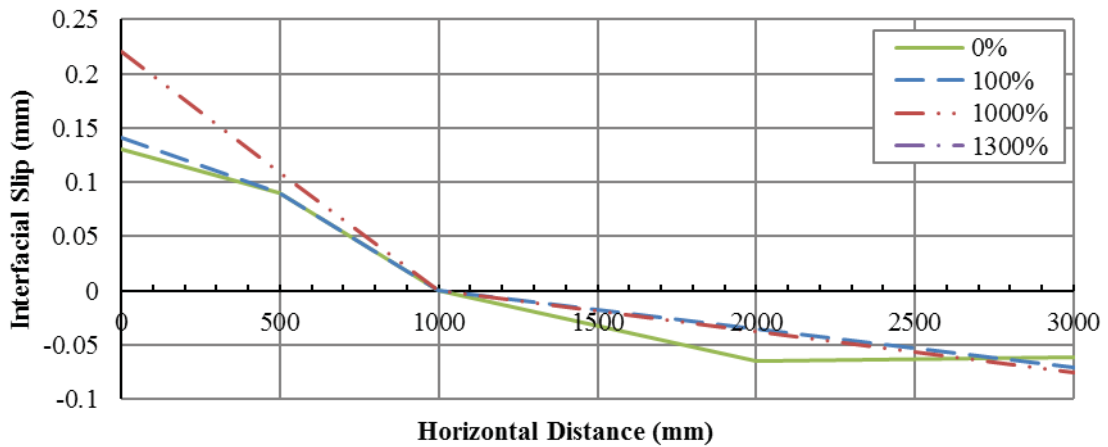
Figure E2-18: P120 – Slip Profile

195
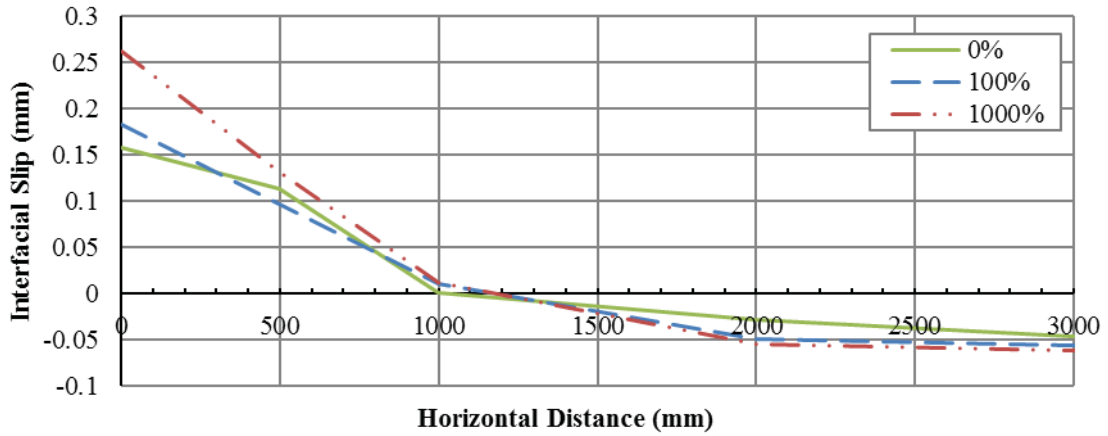
Figure E2-19: C140 – Slip Profile
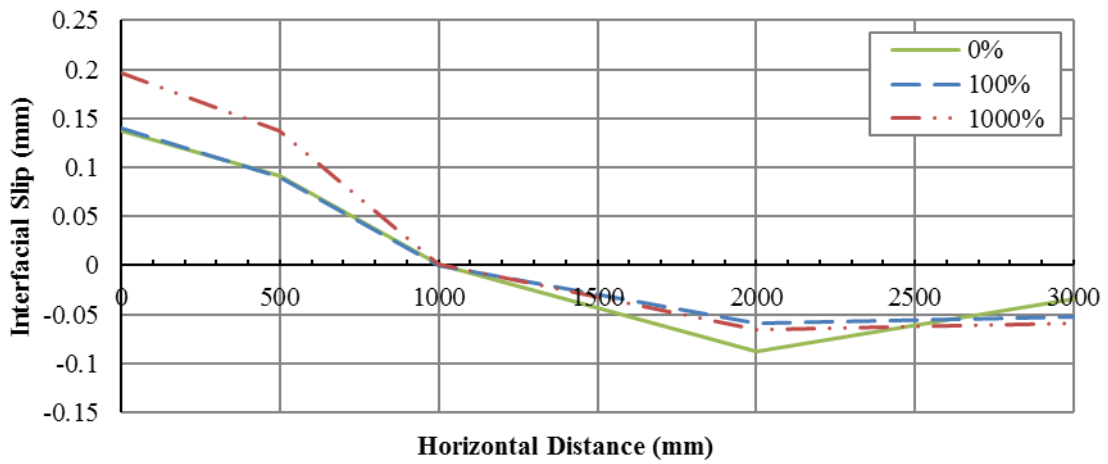
Figure E2-20: P140 – Slip Profile
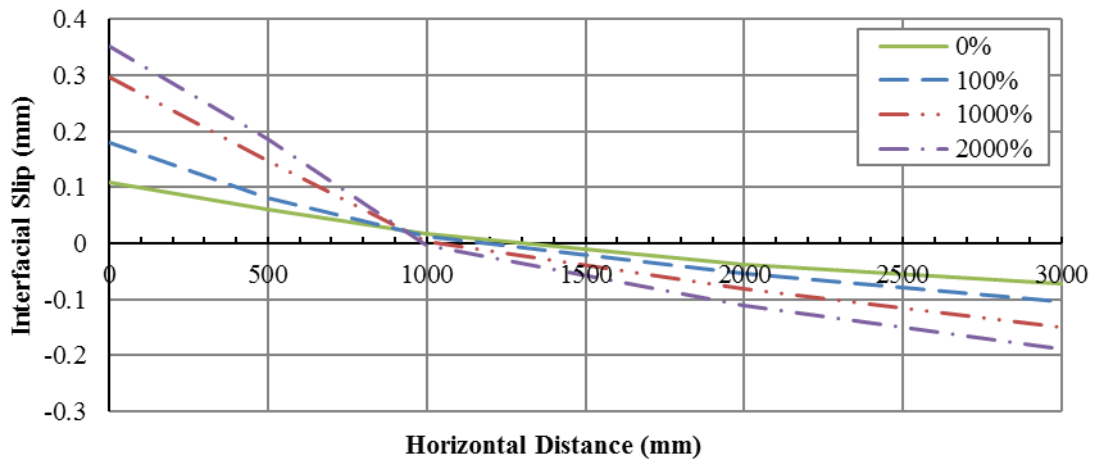
Figure E2-21: C200 – Slip Profile

196
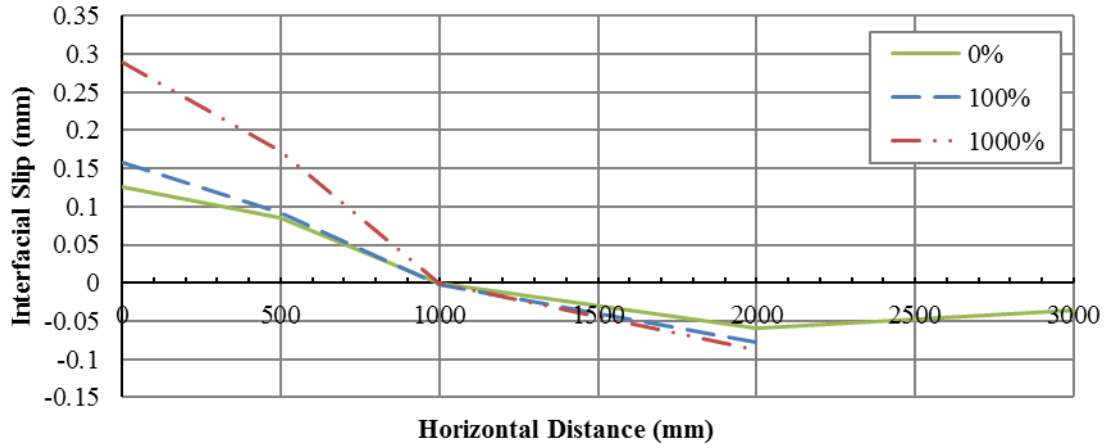
Figure E2-22: P200 – Slip Profile
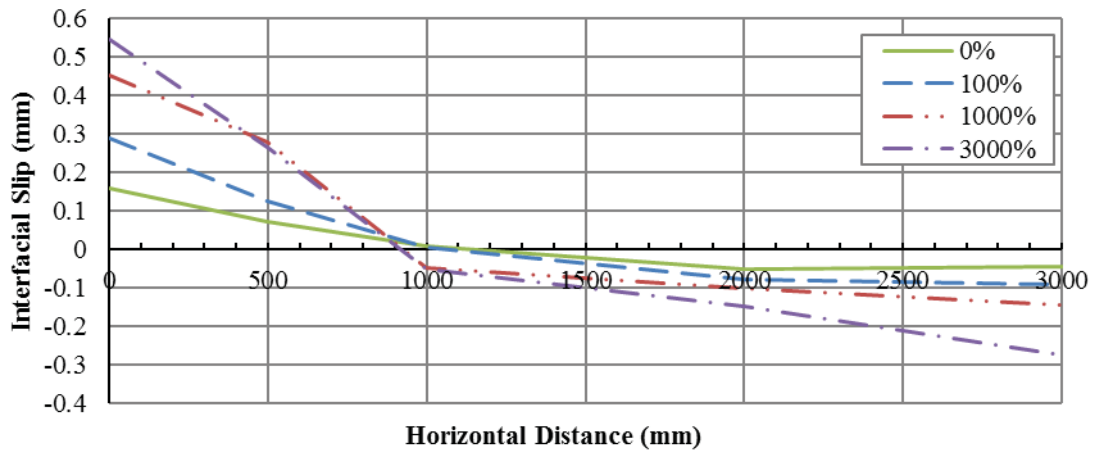
Figure E2-23: C300 – Slip Profile
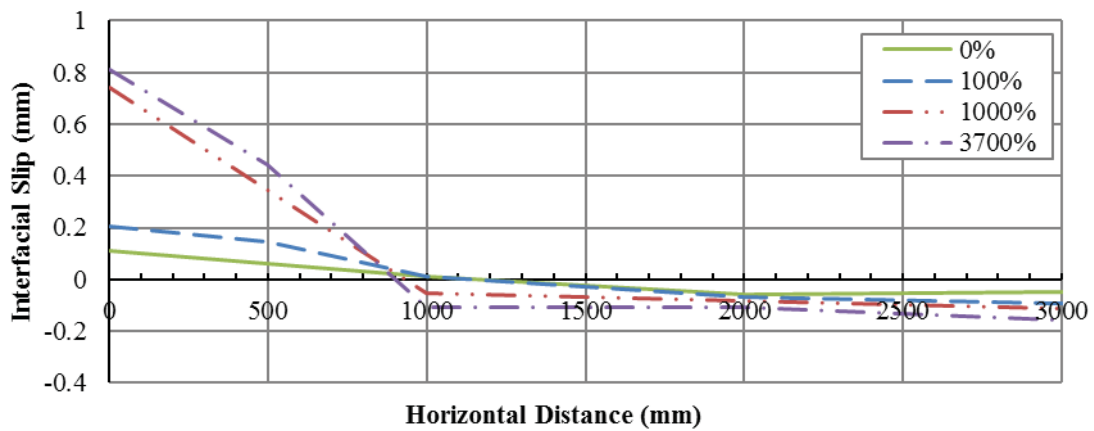
Figure E2-24: P300 – Slip Profile

197

Appendix E3: Strain Profile & Axial Force Results
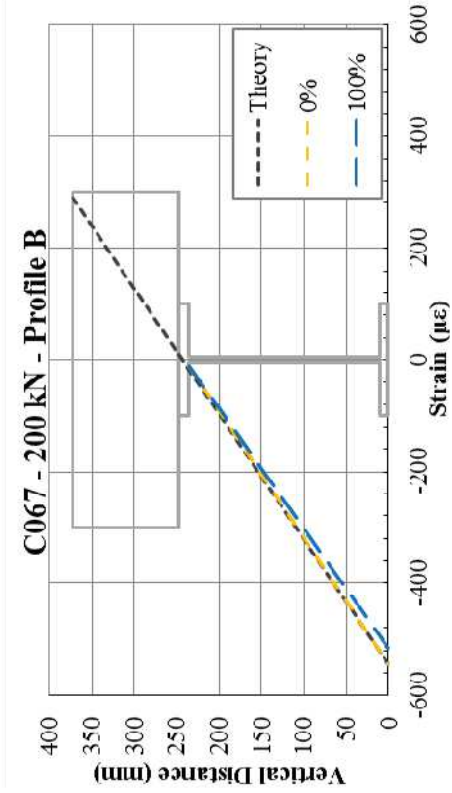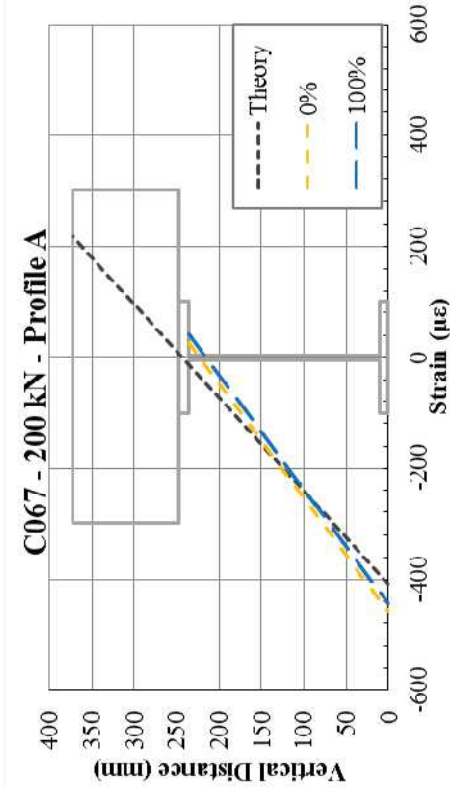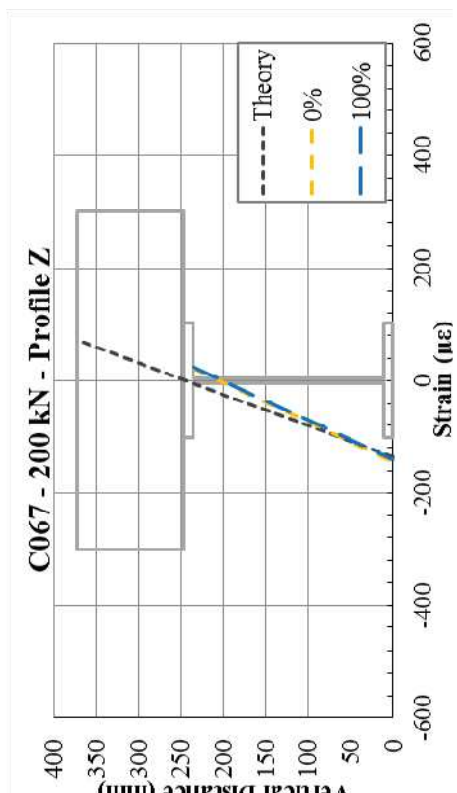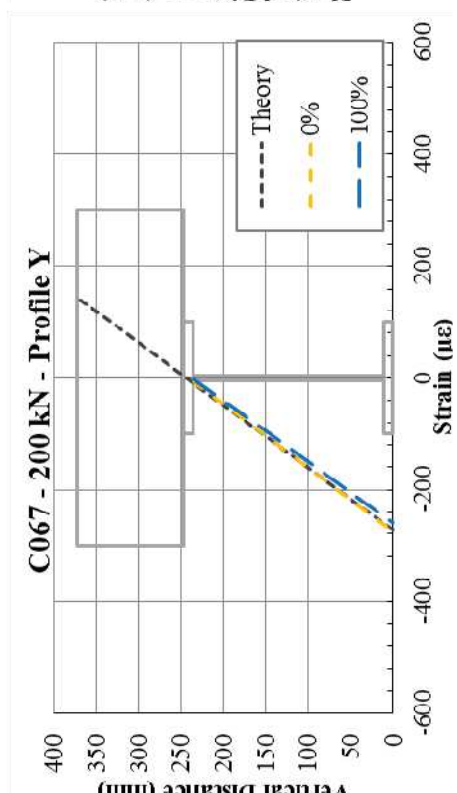
Figure E3-1: C067 – Strain Profiles (P = 200 kN)

199
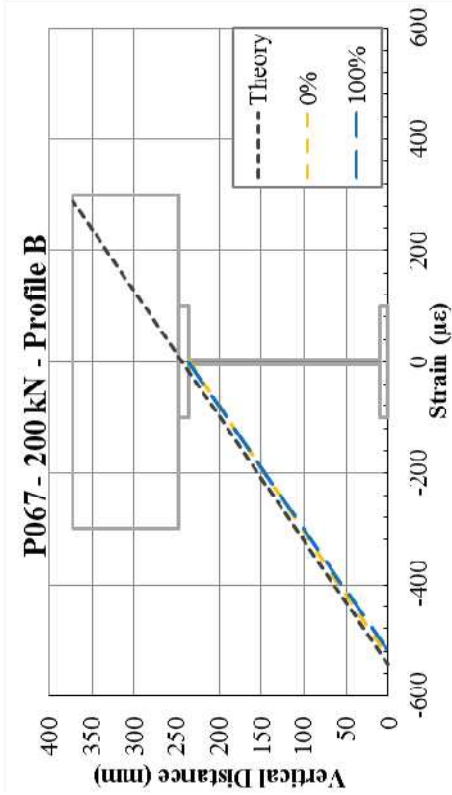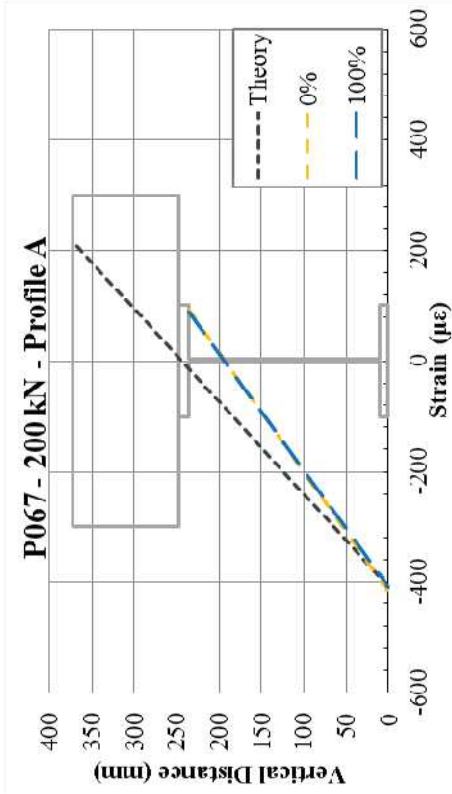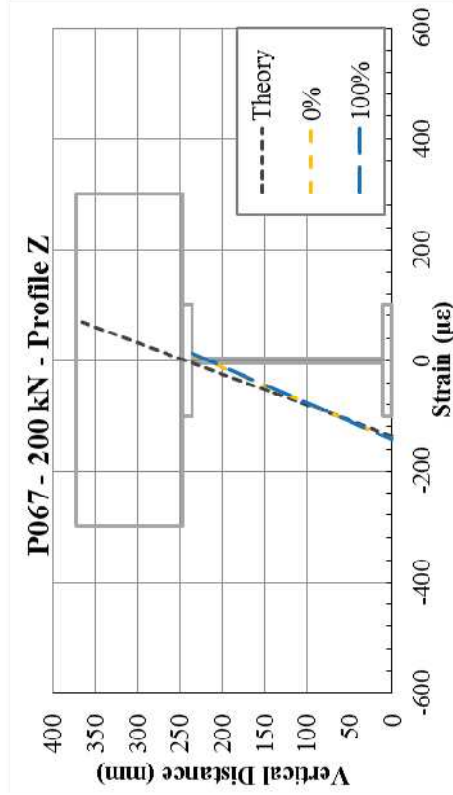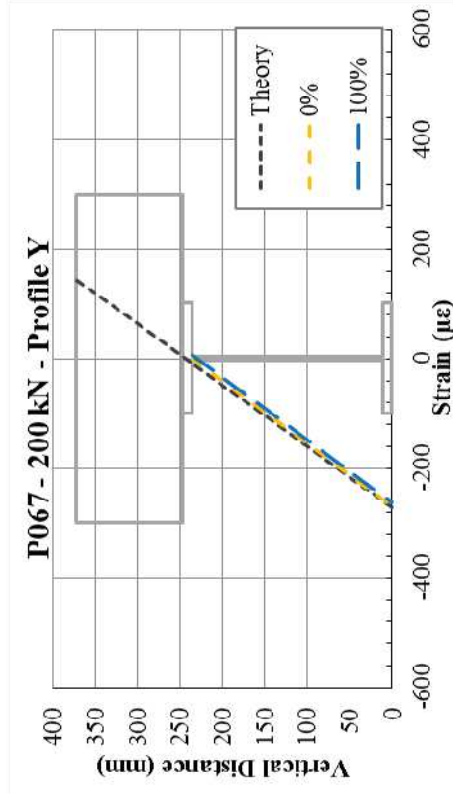
Figure E3-2: P067 – Strain Profiles (P = 200 kN)

200
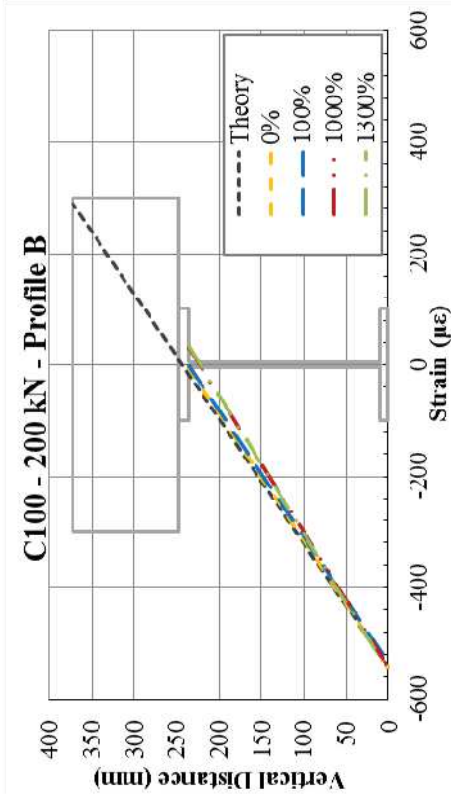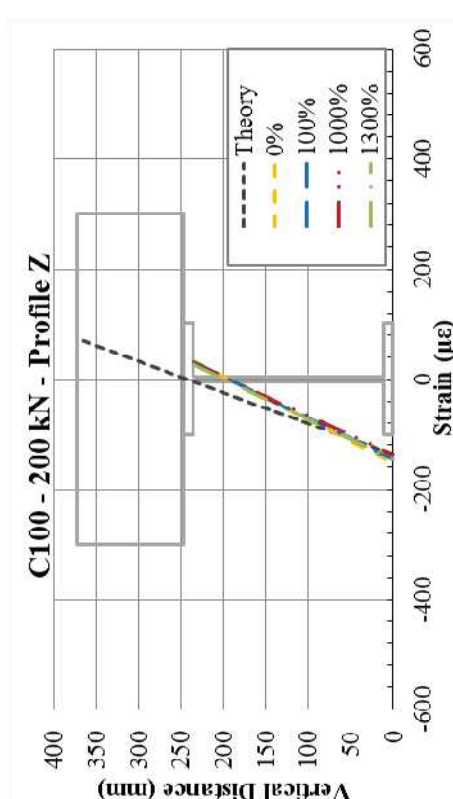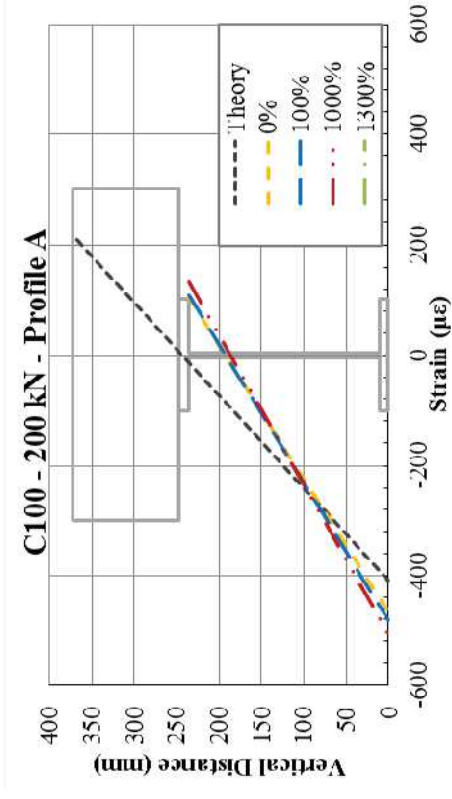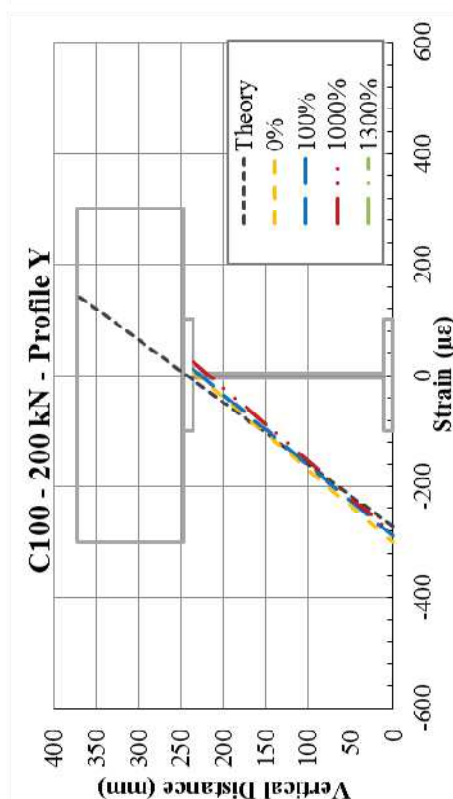
Figure E3-3: C100 – Strain Profiles (P = 200 kN)

201
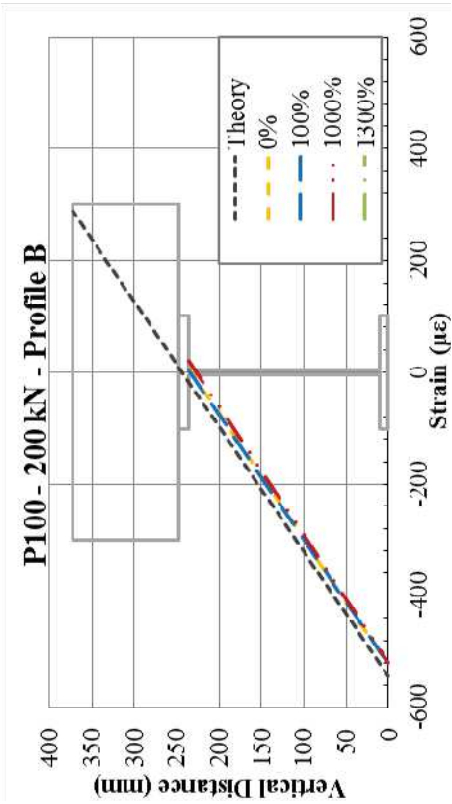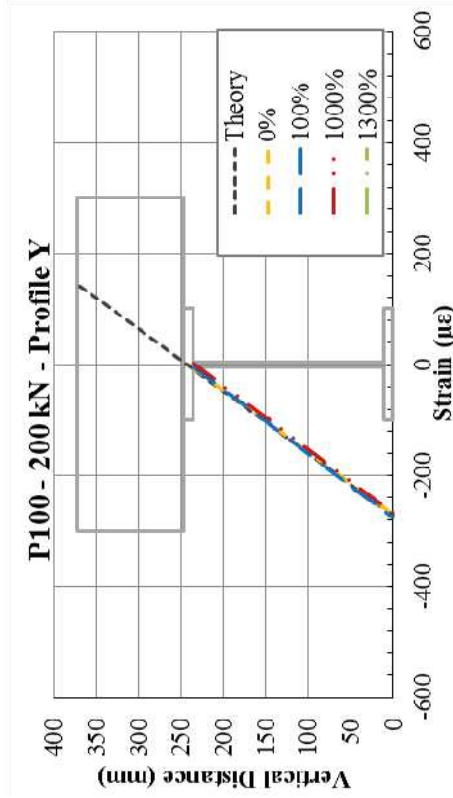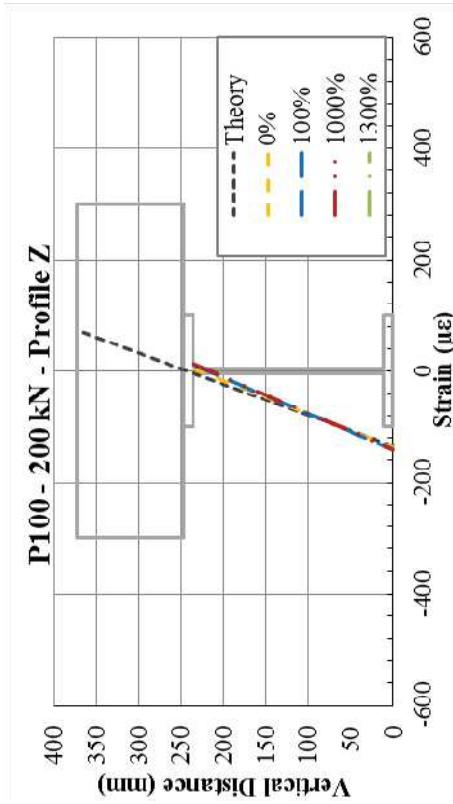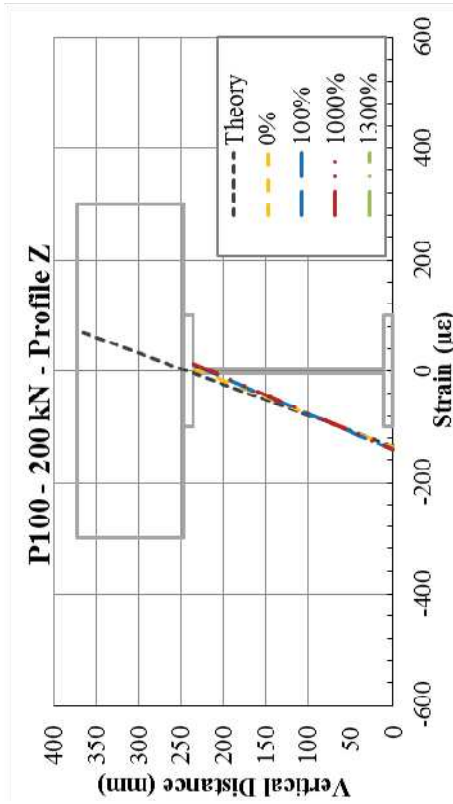
Figure E3-4: P100 – Strain Profiles (P = 200 kN)
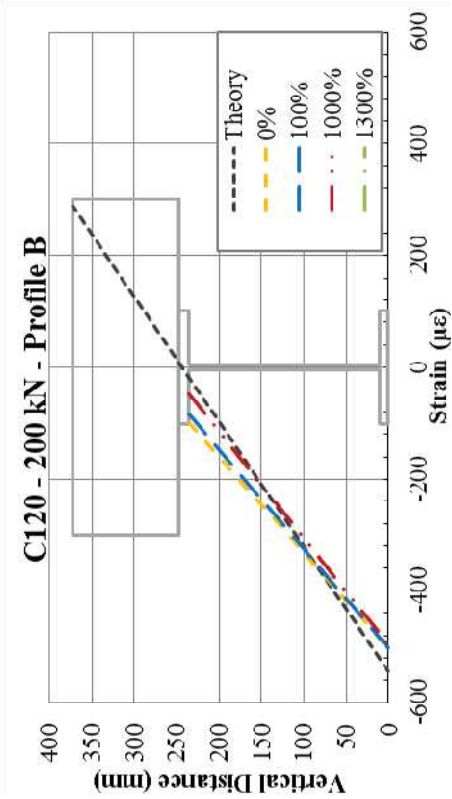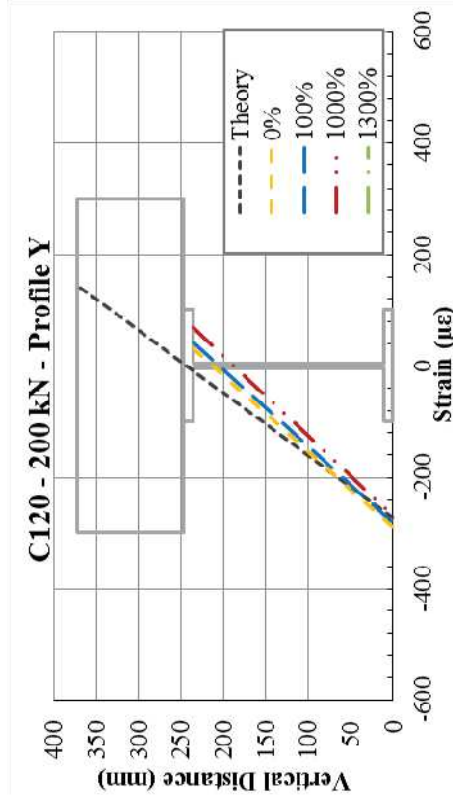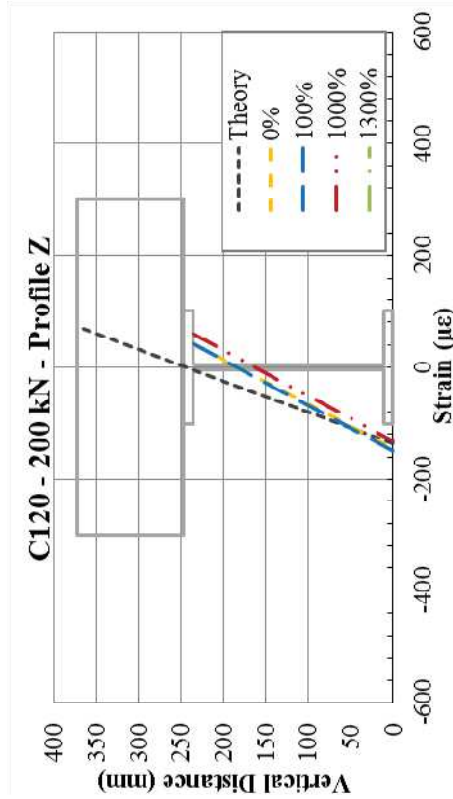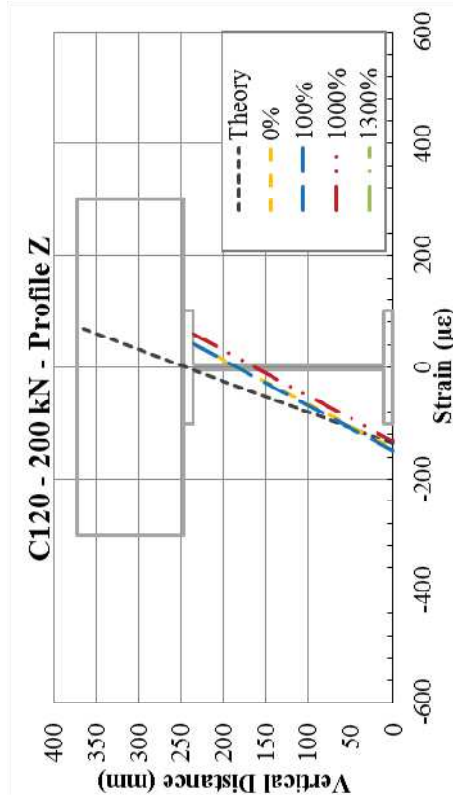
Figure E3-5: C120 – Strain Profiles (P = 200 kN)

203
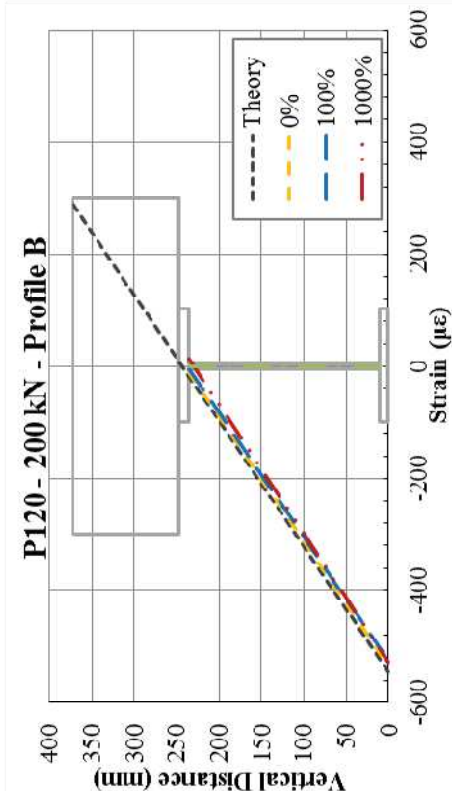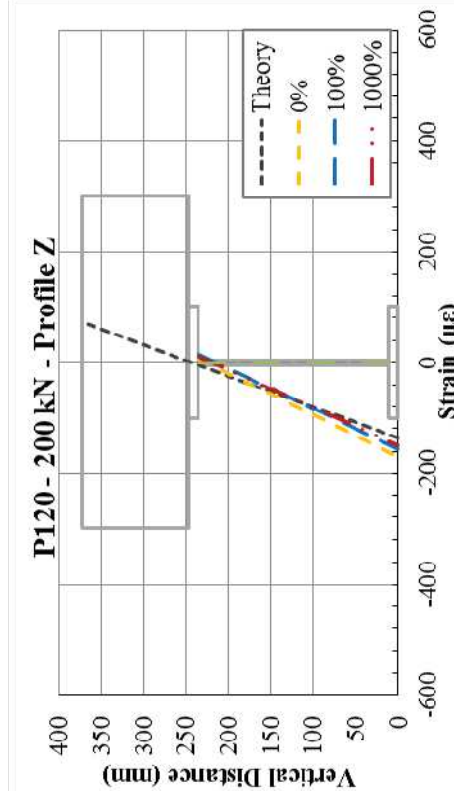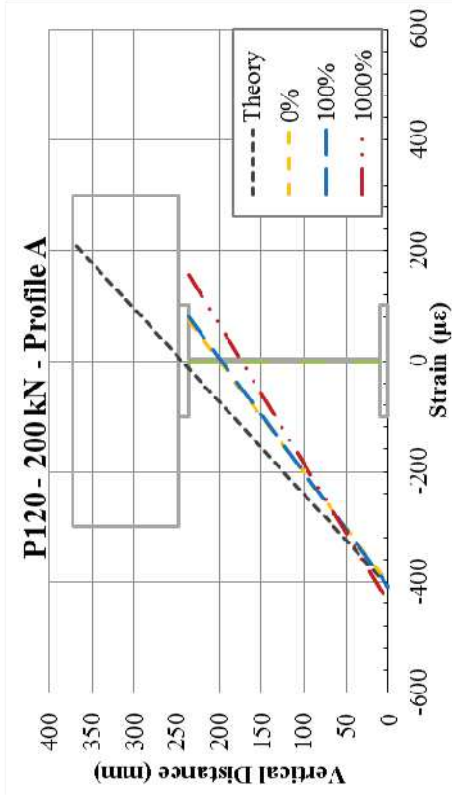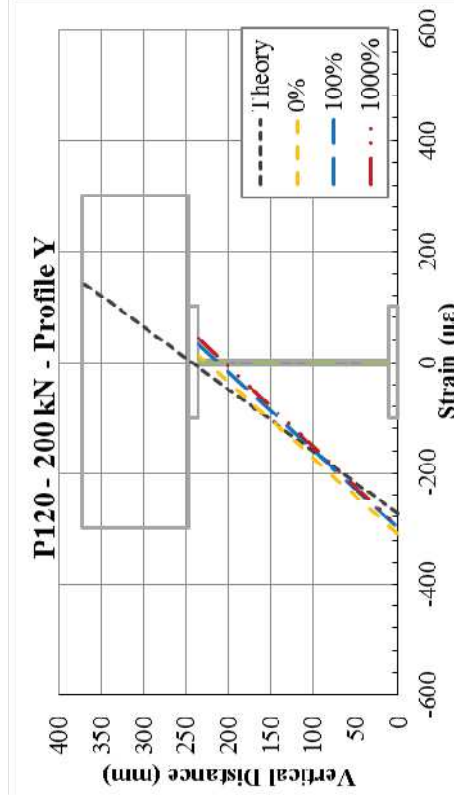
Figure E3-6: P120 – Strain Profiles (P = 200 kN)

204
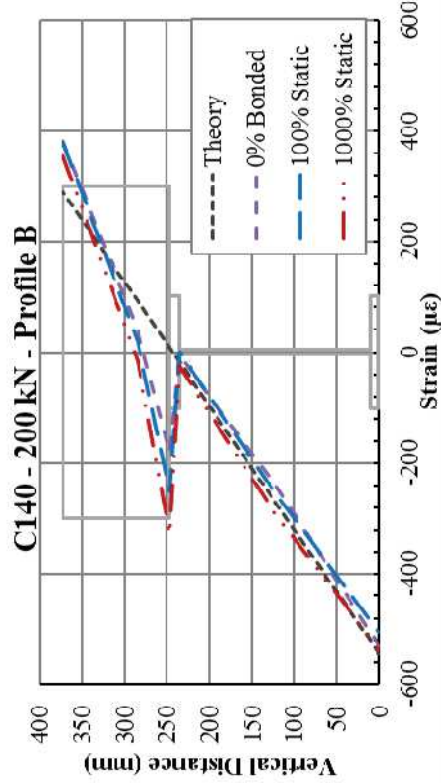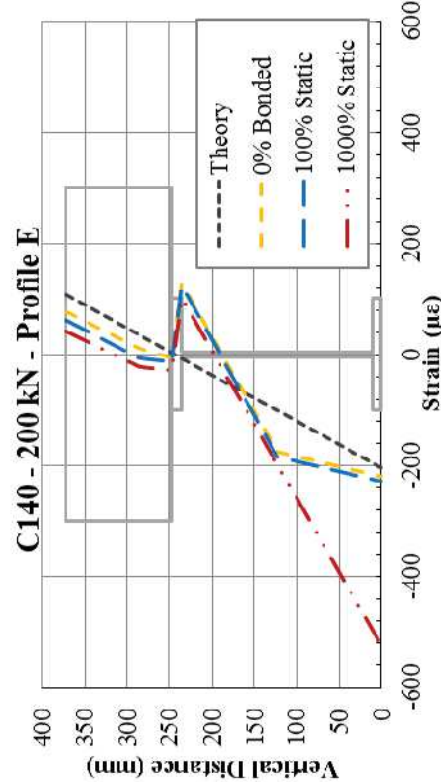
Figure E3-7: P140 – Strain Profiles (P = 200 kN)
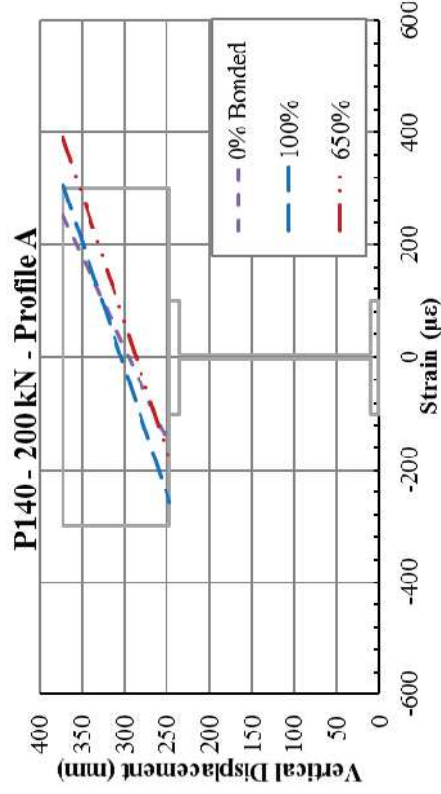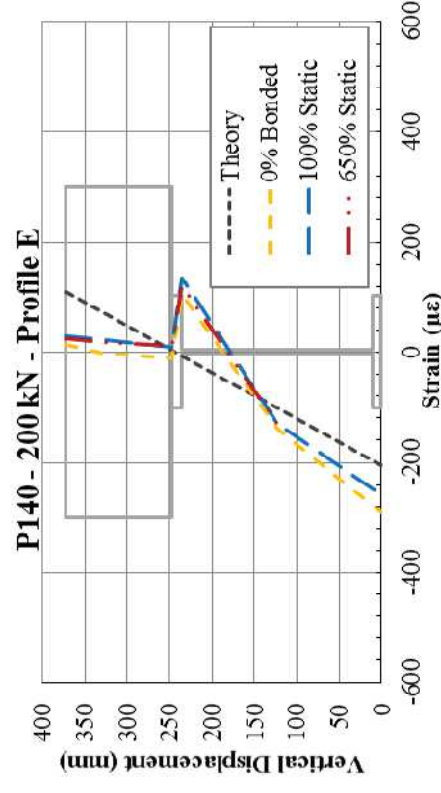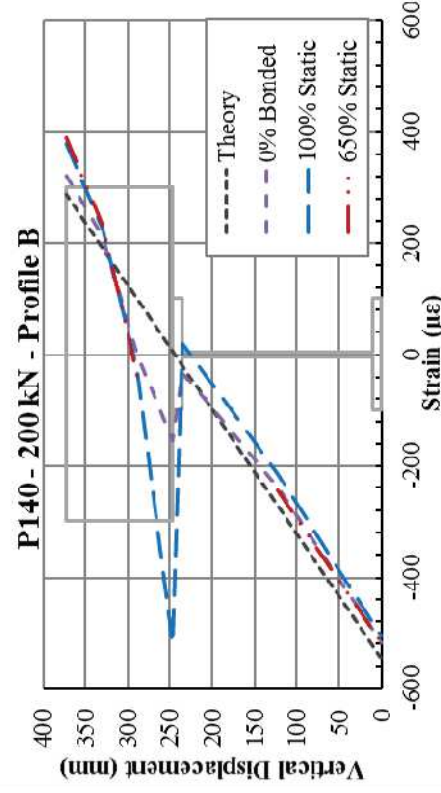
Figure E3-8: P140 – Strain Profiles (P = 200 kN)

206
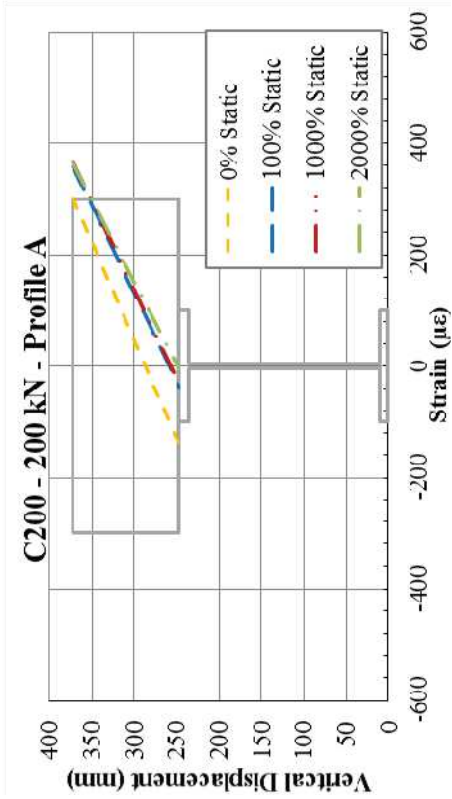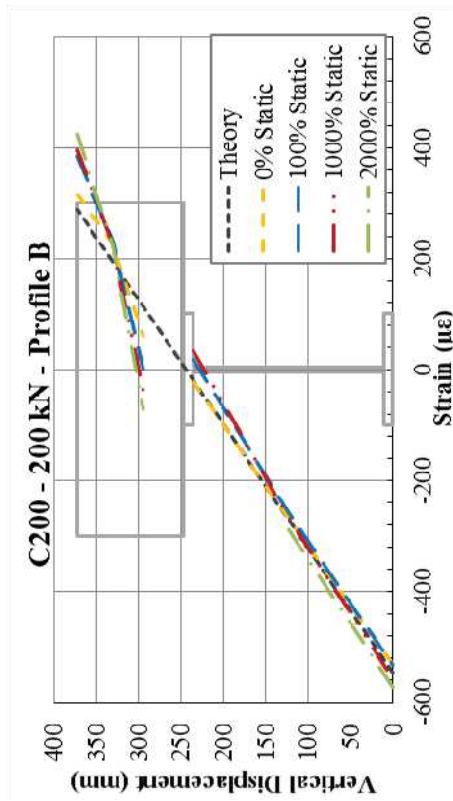
Figure E3-9: C200 – Strain Profiles (P = 200 kN)

207

(a)

(b)
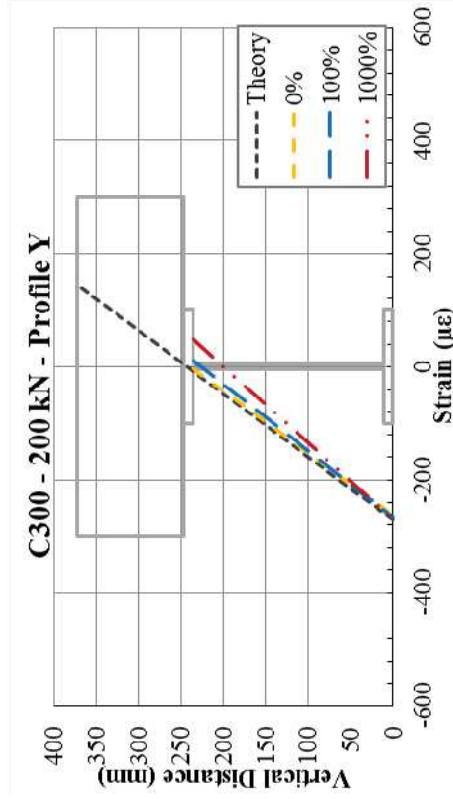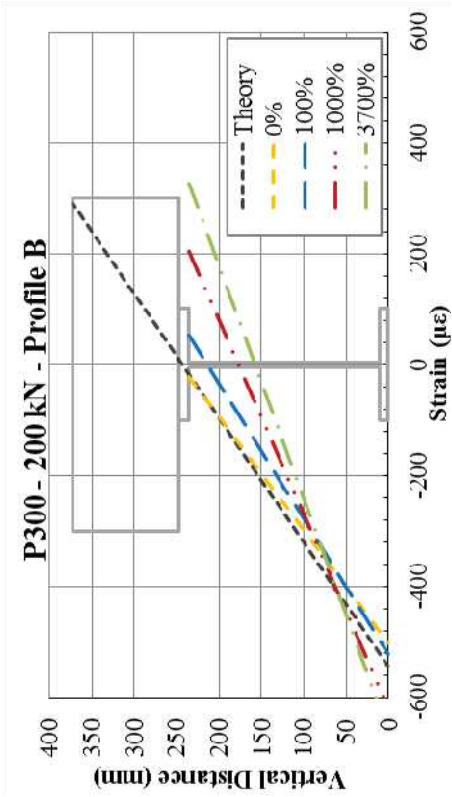
(c)

208
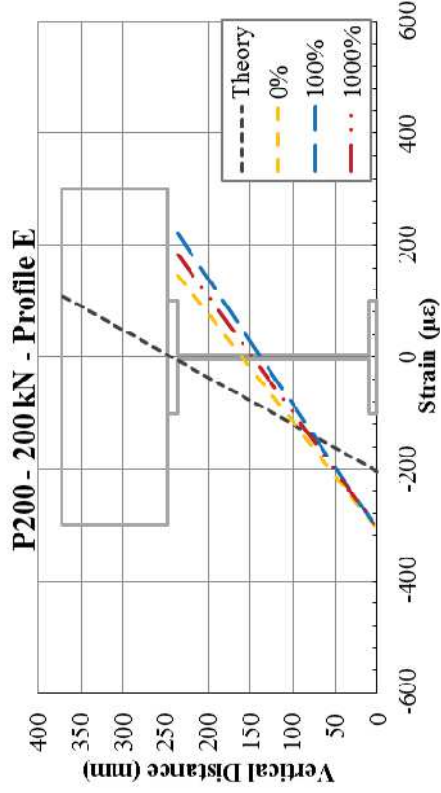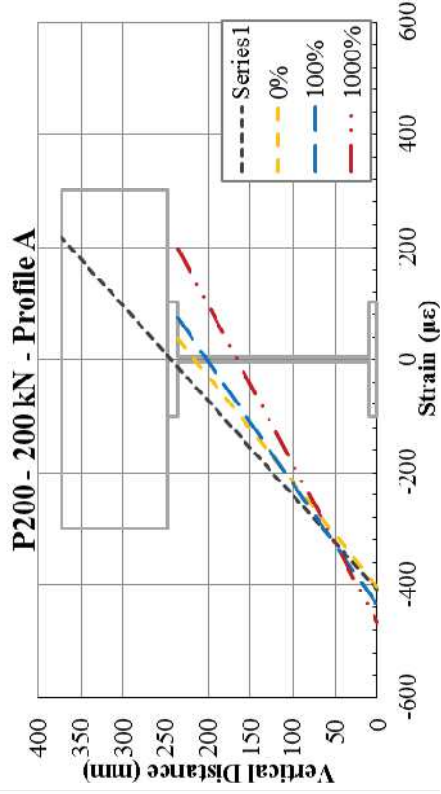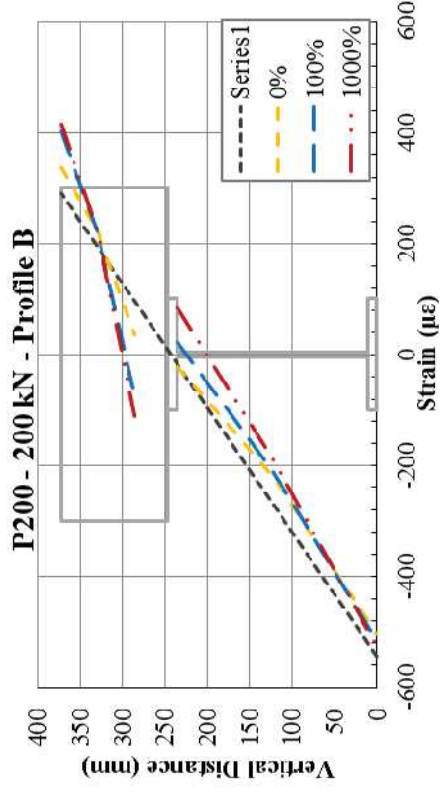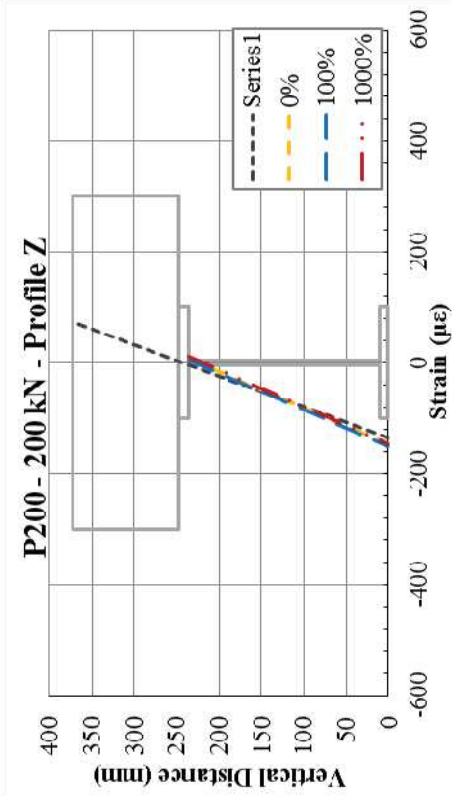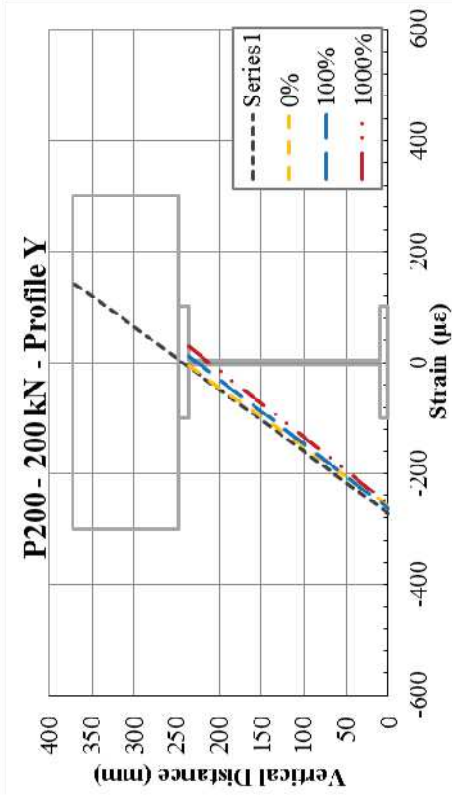
Figure E3-10: P200 – Strain Profiles (P = 200 kN)

209
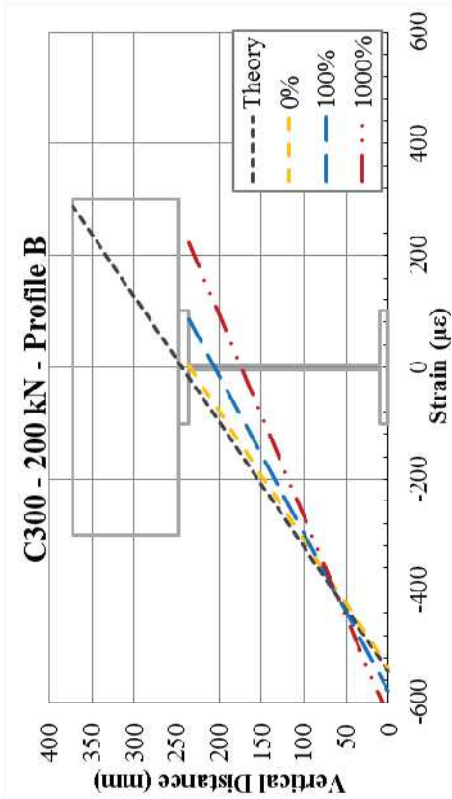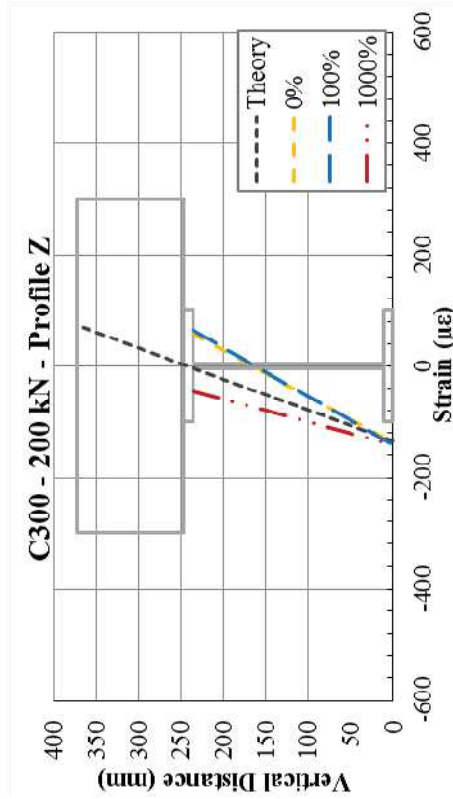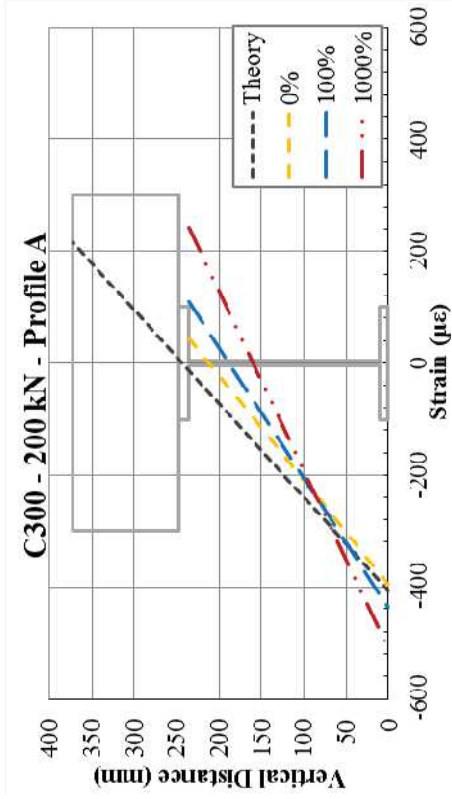
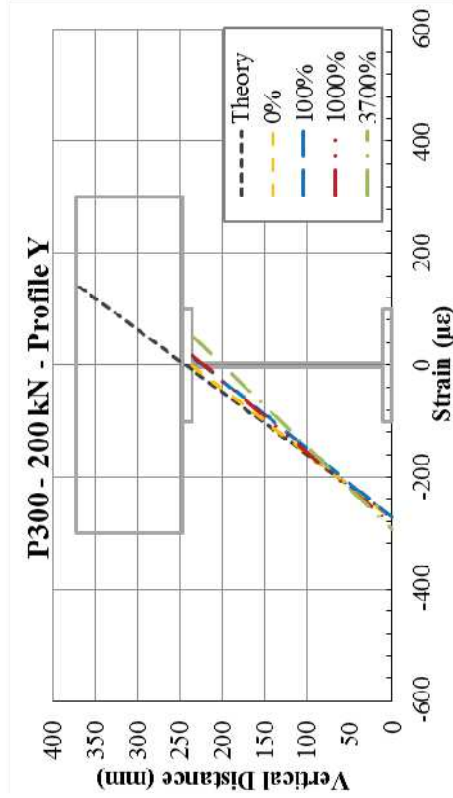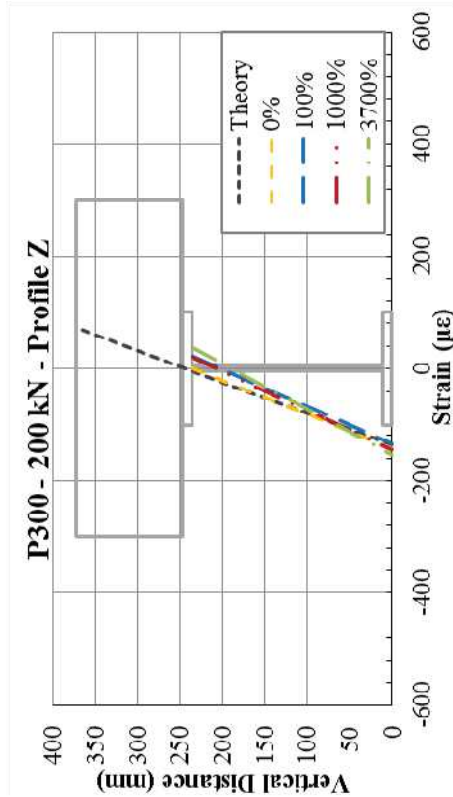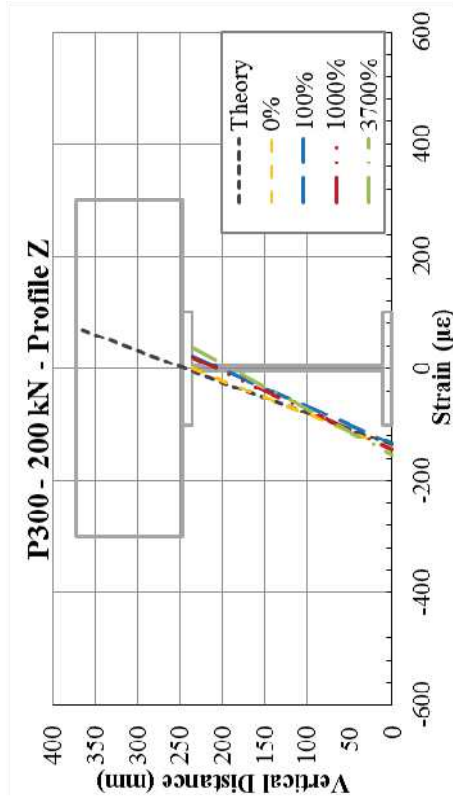**Figure E3-11:** C300 – Strain Profiles (P = 200 kN)

210

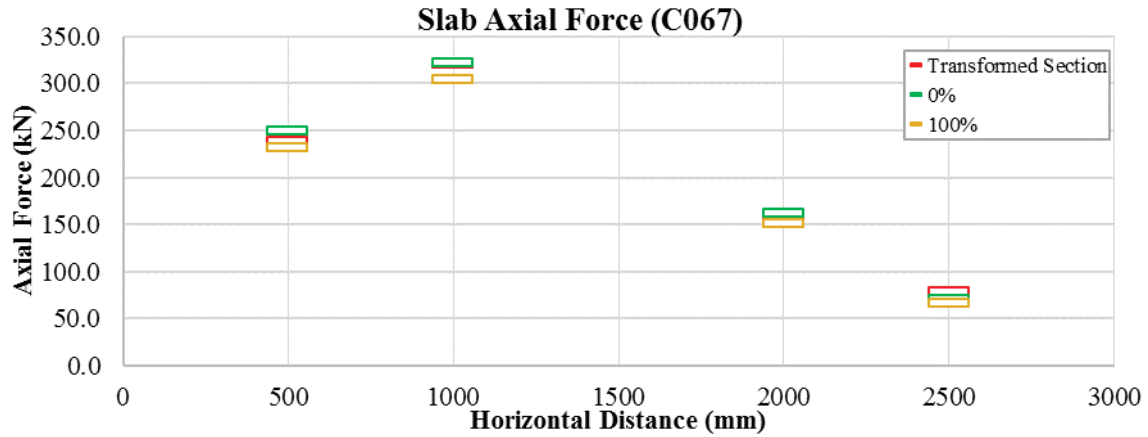**Figure E3-12:** P300 – Strain Profiles (P = 200 kN)

211

Figure E3-13: C067 – Slab Axial Force (P = 200 kN)

Figure E3-14: P067 – Slab Axial Force (P = 200 kN)

Figure E3-15: C100 – Slab Axial Force (P = 200 kN)

212

Figure E3-16: P100 – Slab Axial Force (P = 200 kN)
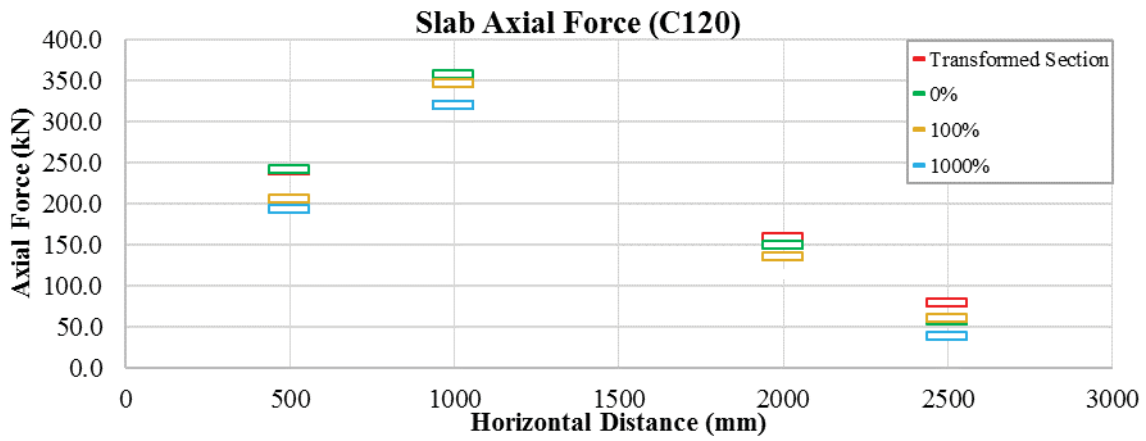
Figure E3-17: C120 – Slab Axial Force (P = 200 kN)
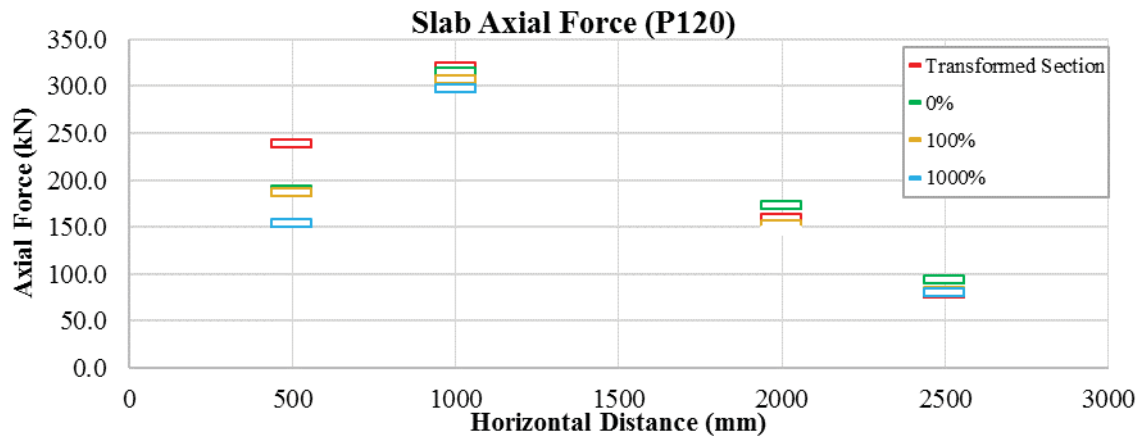
Figure E3-18: P120 – Slab Axial Force (P = 200 kN)

213
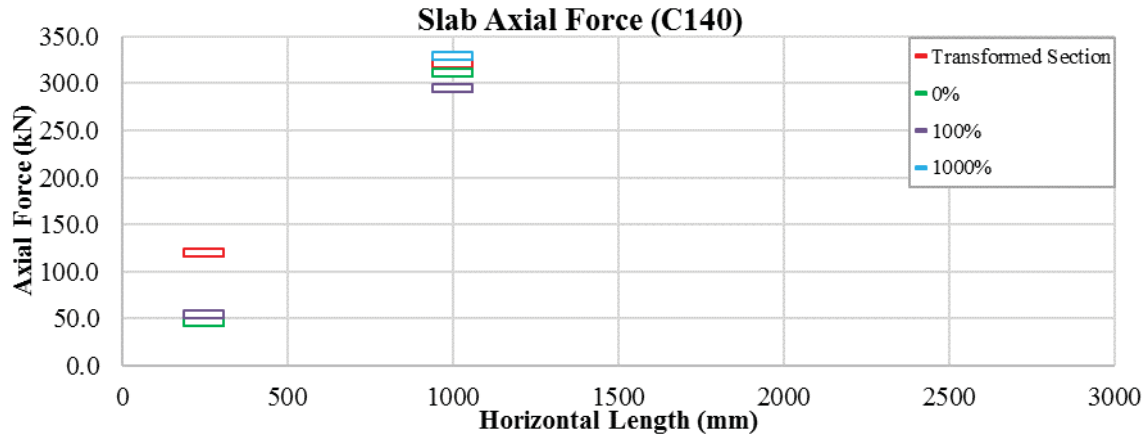
Figure E3-19: C140 – Slab Axial Force (P = 200 kN)
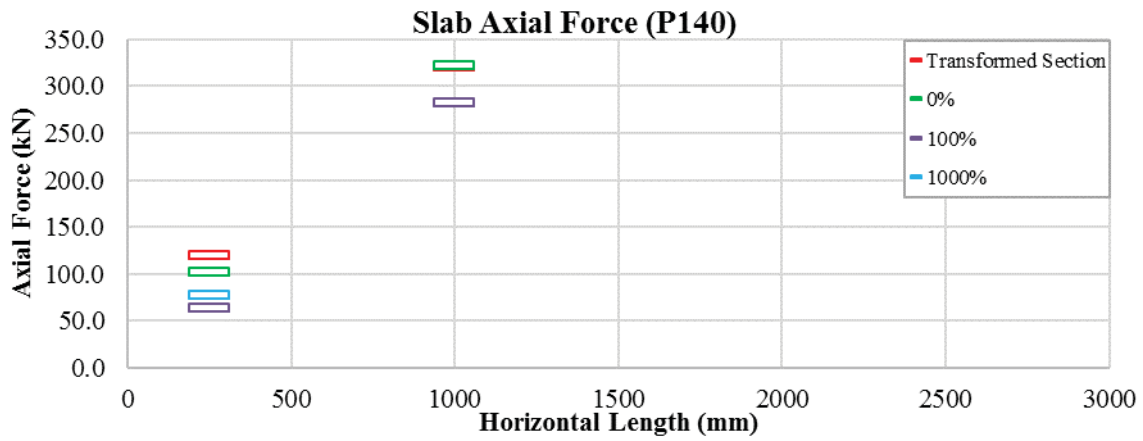
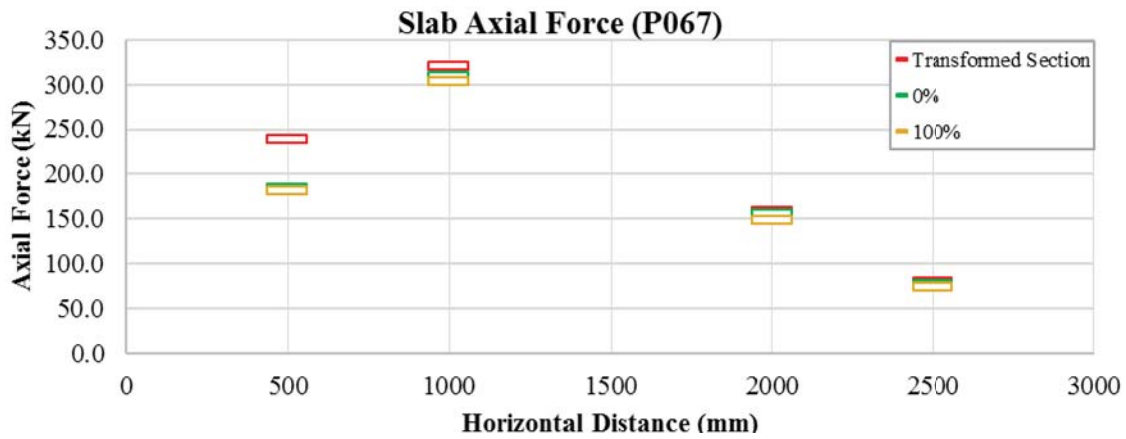**Figure E3-20:** P140 – Slab Axial Force (P = 200 kN)
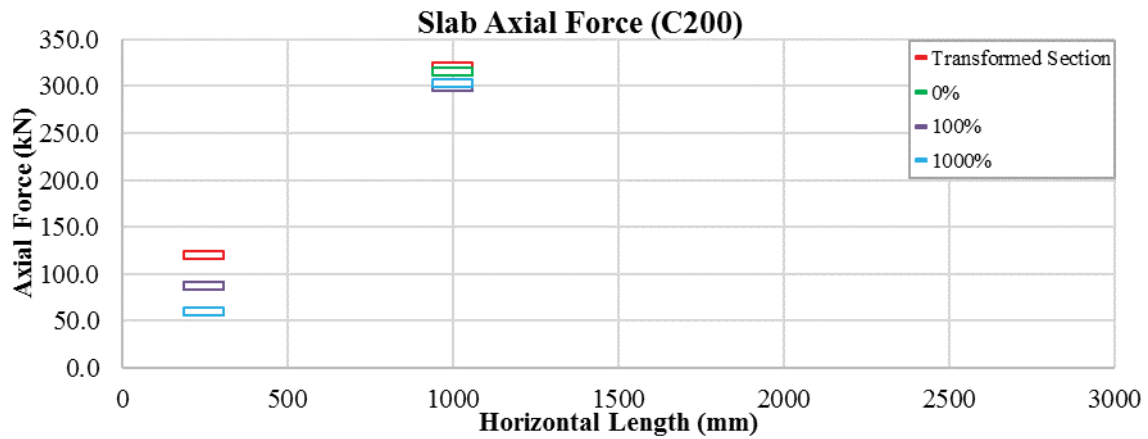
Figure E3-21: C200 – Slab Axial Force (P = 200 kN)

214

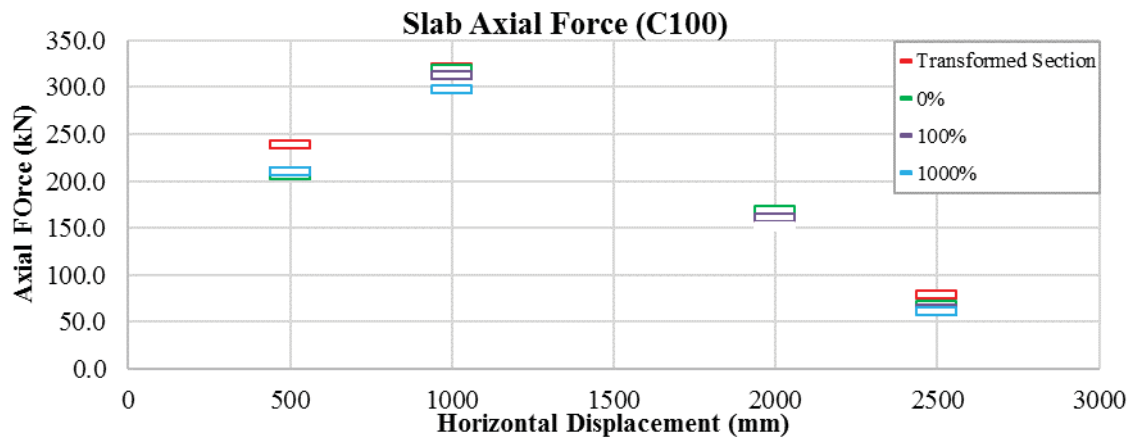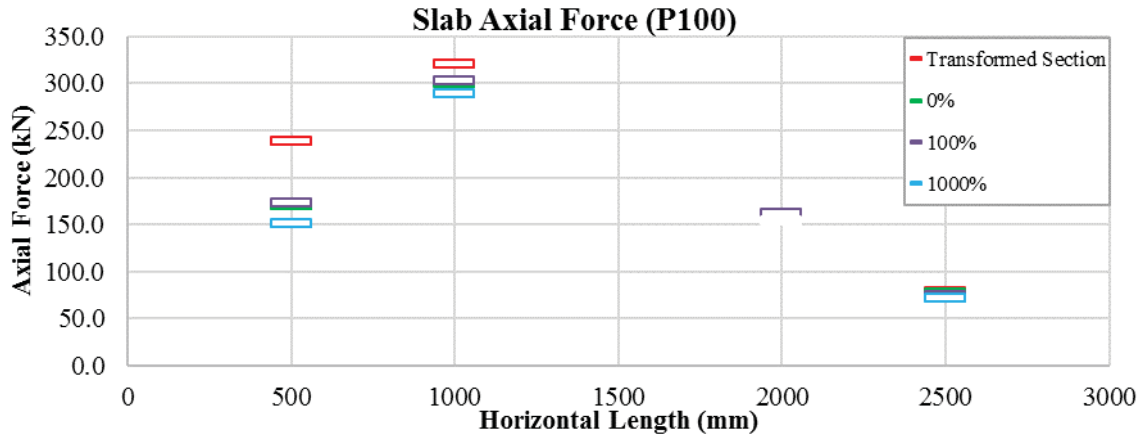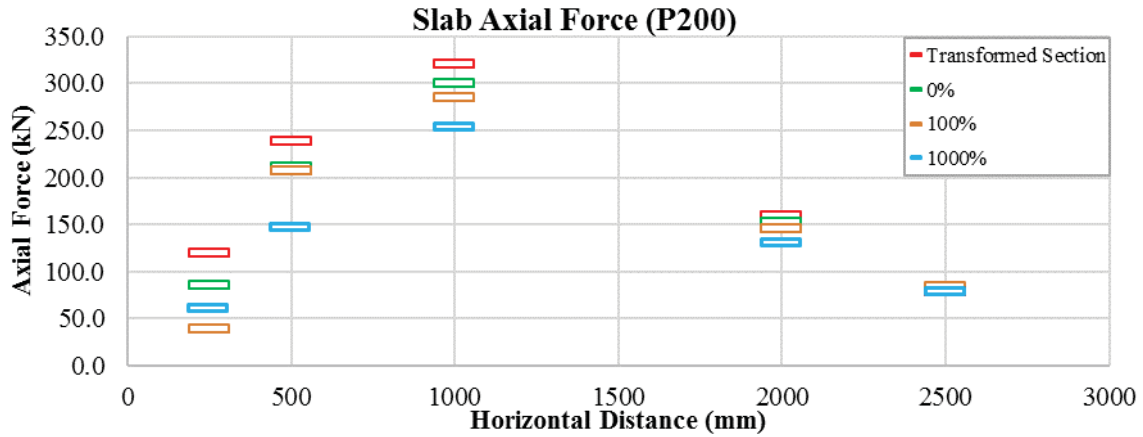**Figure E3-22:** P200 – Slab Axial Force (P = 200 kN)
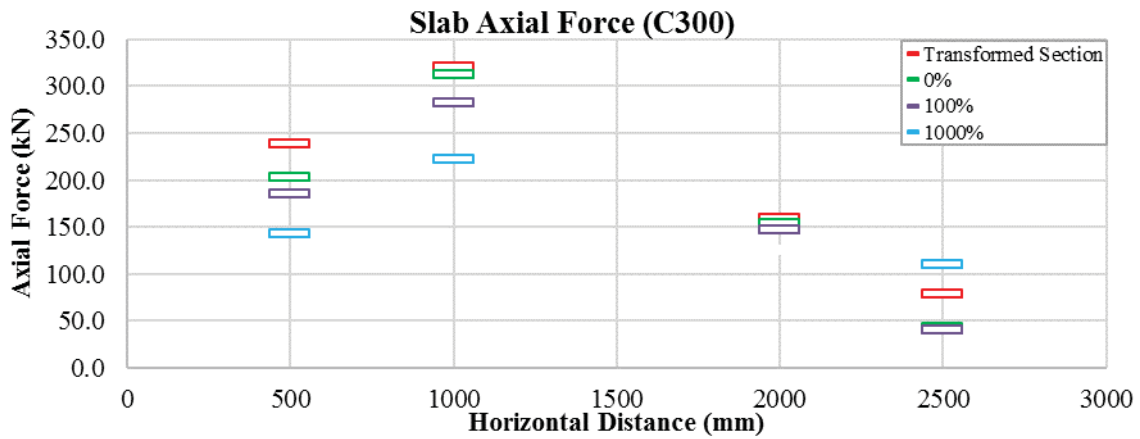
Figure E3-23: C300 – Slab Axial Force (P = 200 kN)
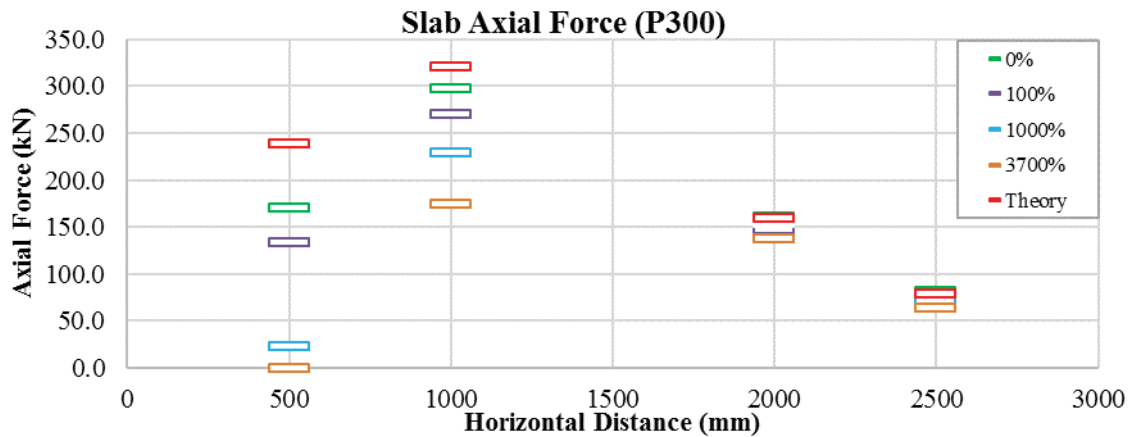
Figure E3-24: P300 – Slab Axial Force (P = 200 kN)

215

Appendix F: Fatigue Test Data

Appendix F1: Deflection versus Cycles
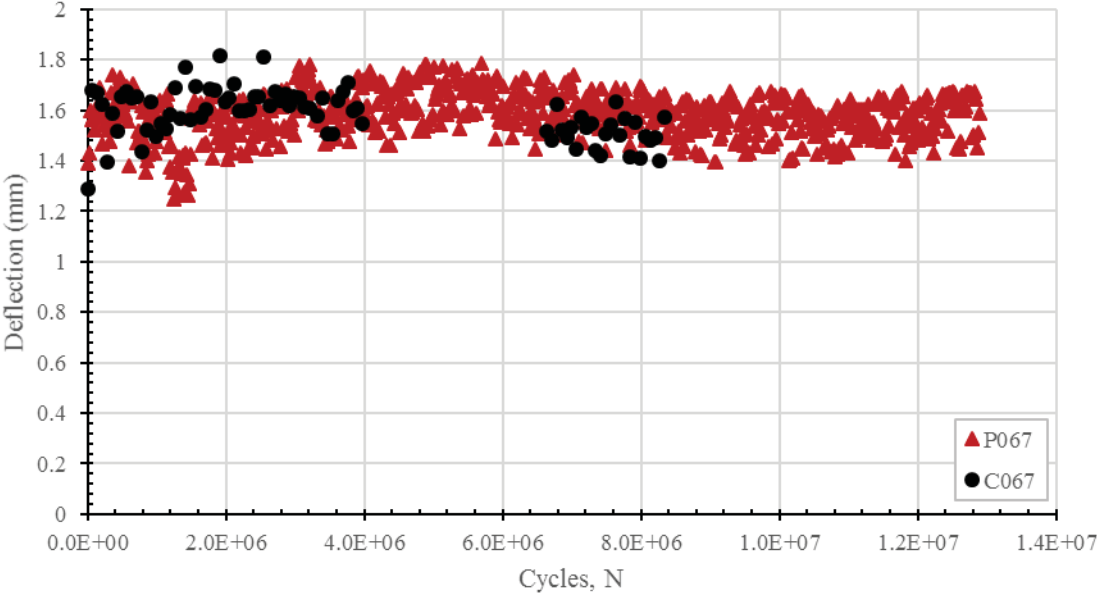
Figure F1-1: C067 & P067 – Deflection Data
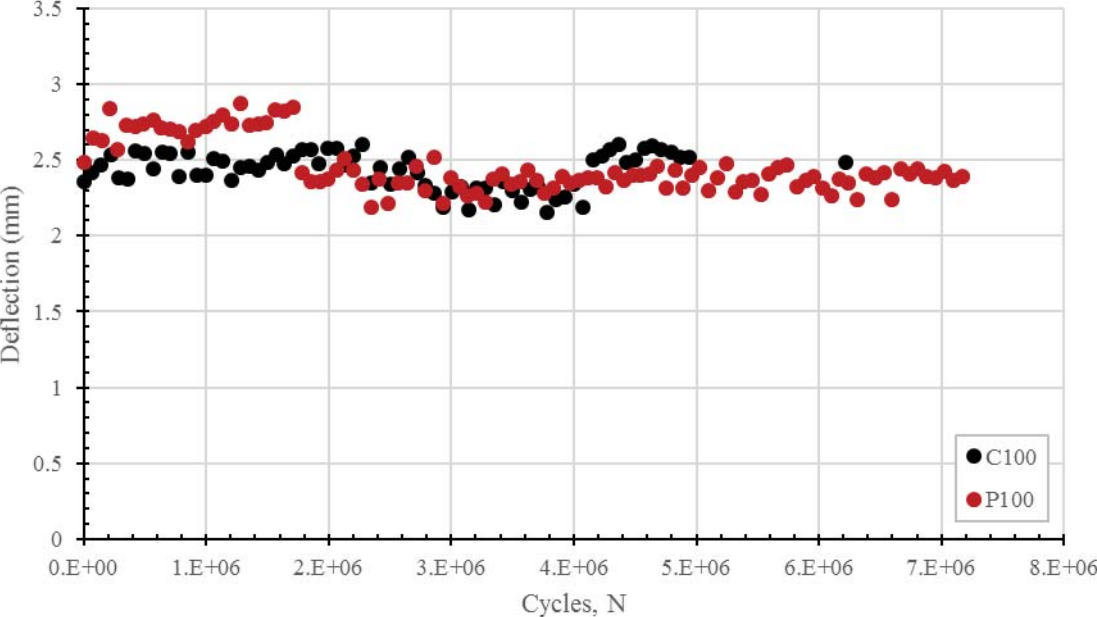
Figure F1-2: C100 & P100 – Deflection Data
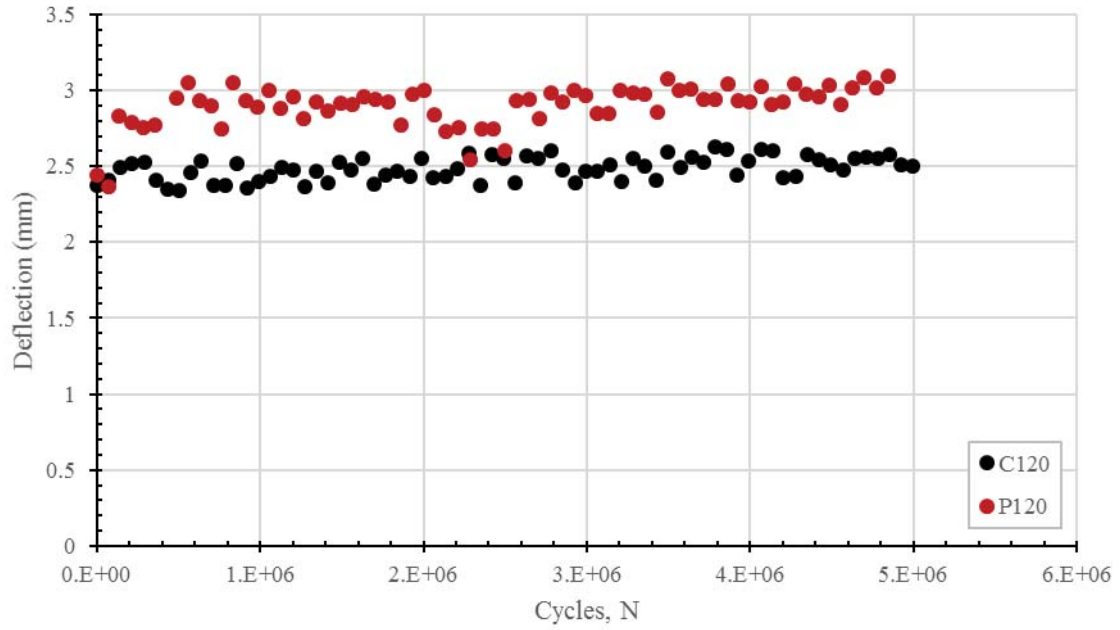
Figure F1-3: C120 & P120 – Deflection Data
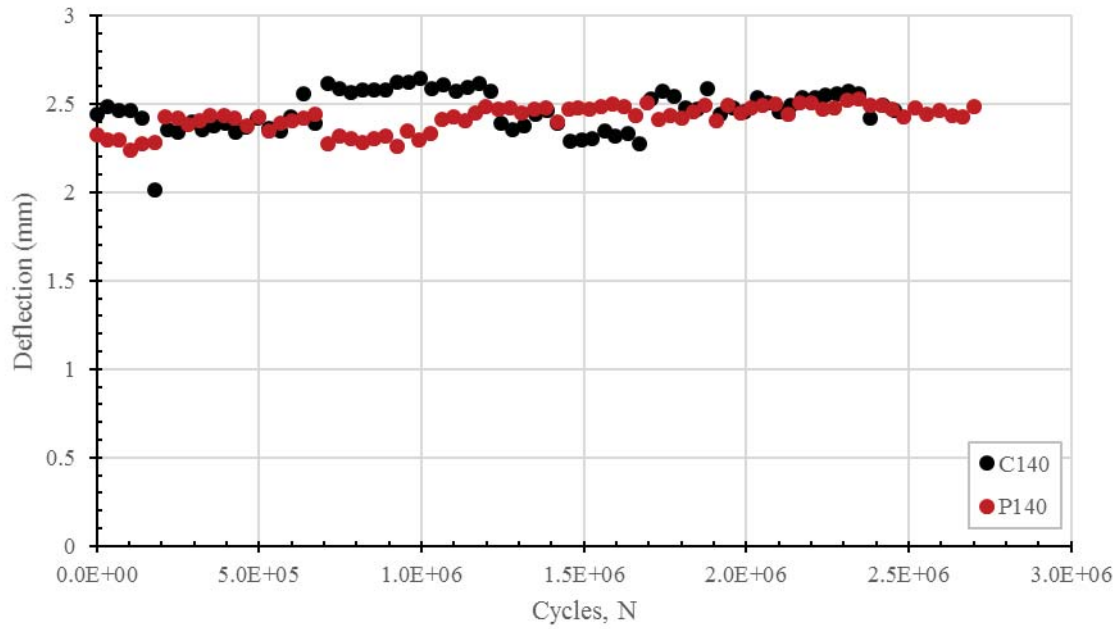
Figure F1-4: C140 & P140 – Deflection Data
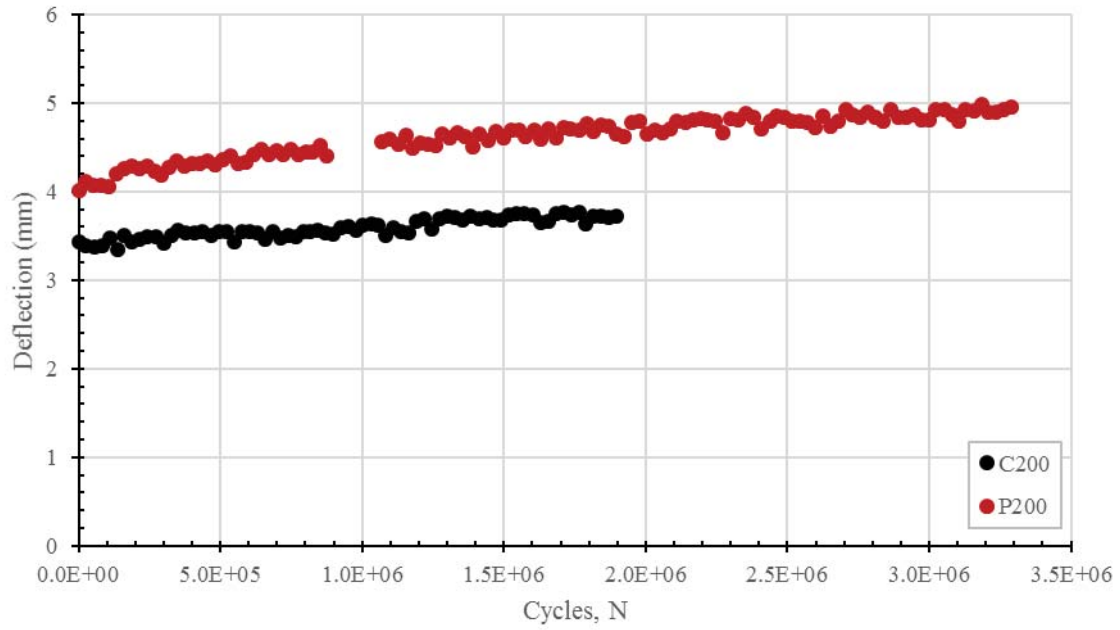
Figure F1-5: C200 & P200 – Deflection Data
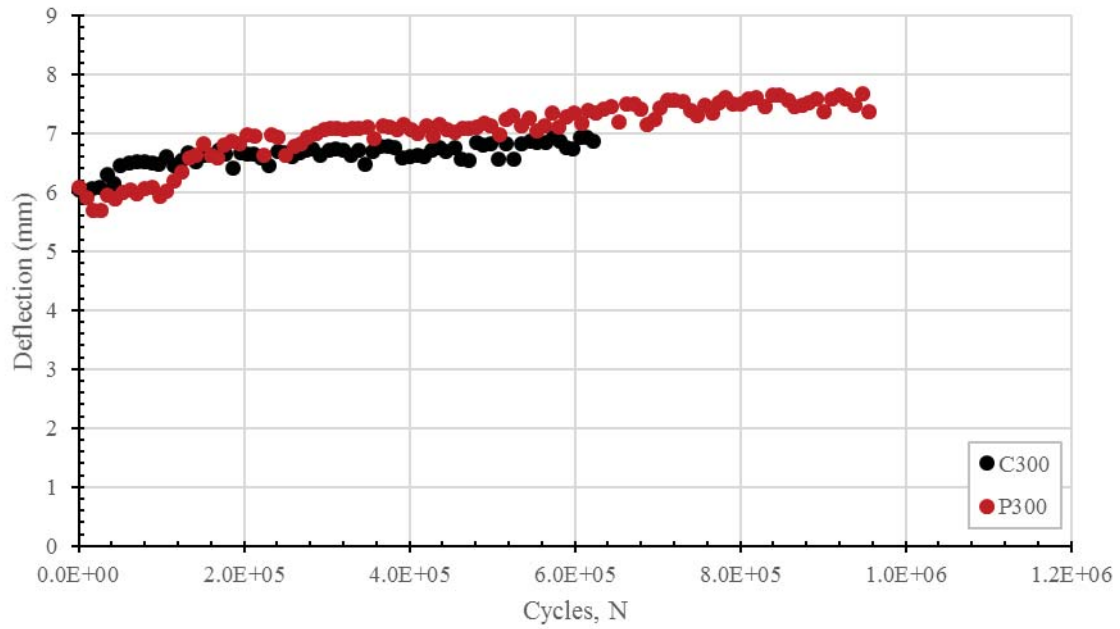
Figure F1-6: C300 & P300 – Deflection Data

219

Appendix F2: Interfacial Slip versus Cycles

Figure F2-1: C067 – Interfacial Slip Data

Figure F2-2: P067 – Interfacial Slip Data
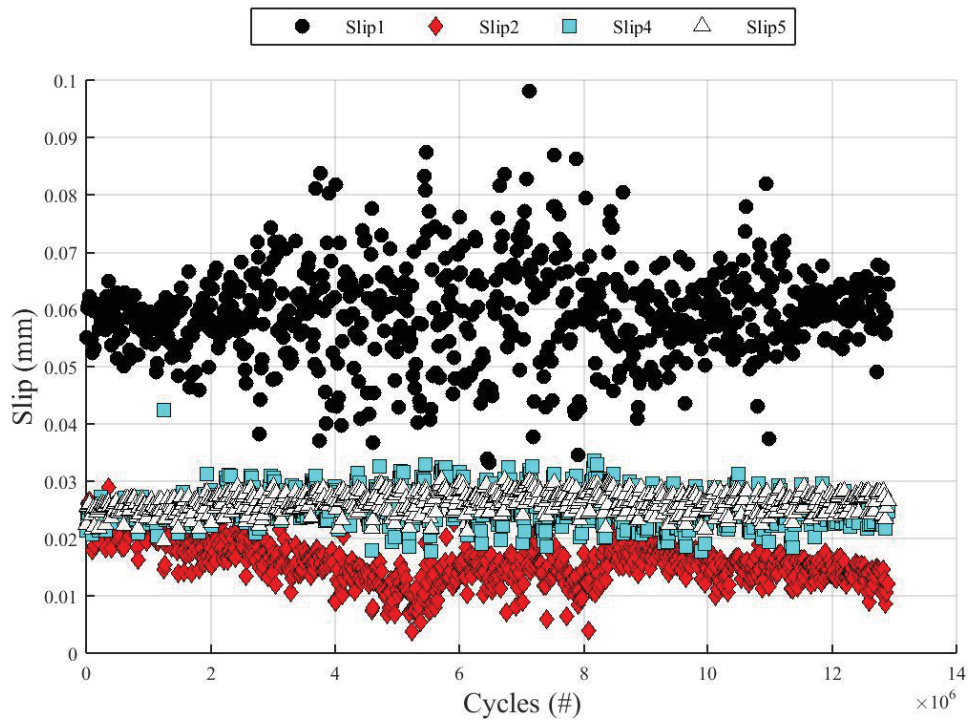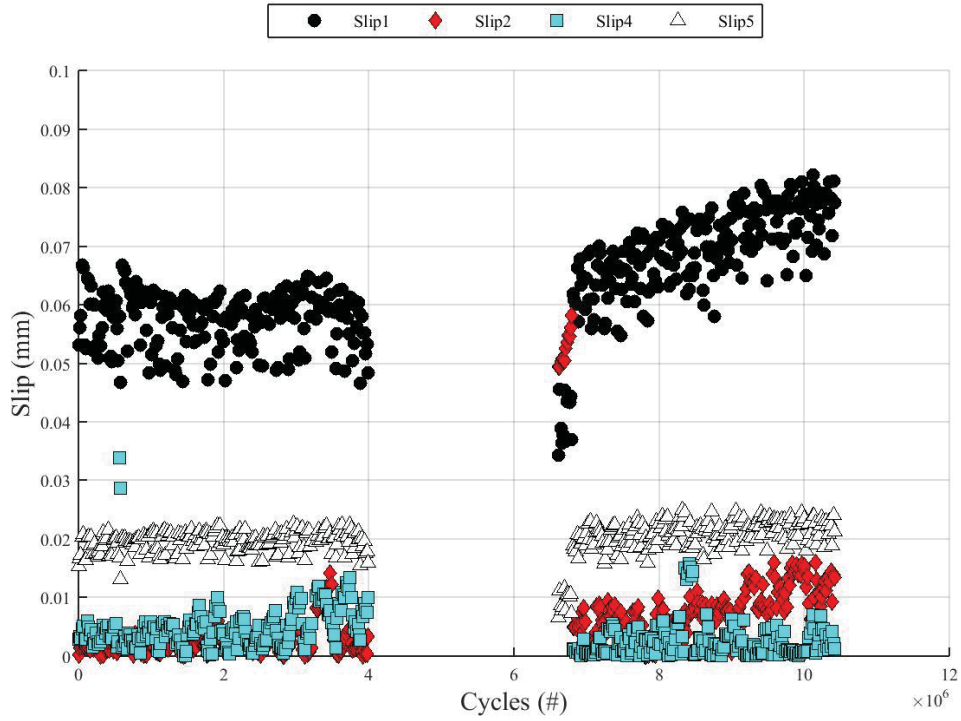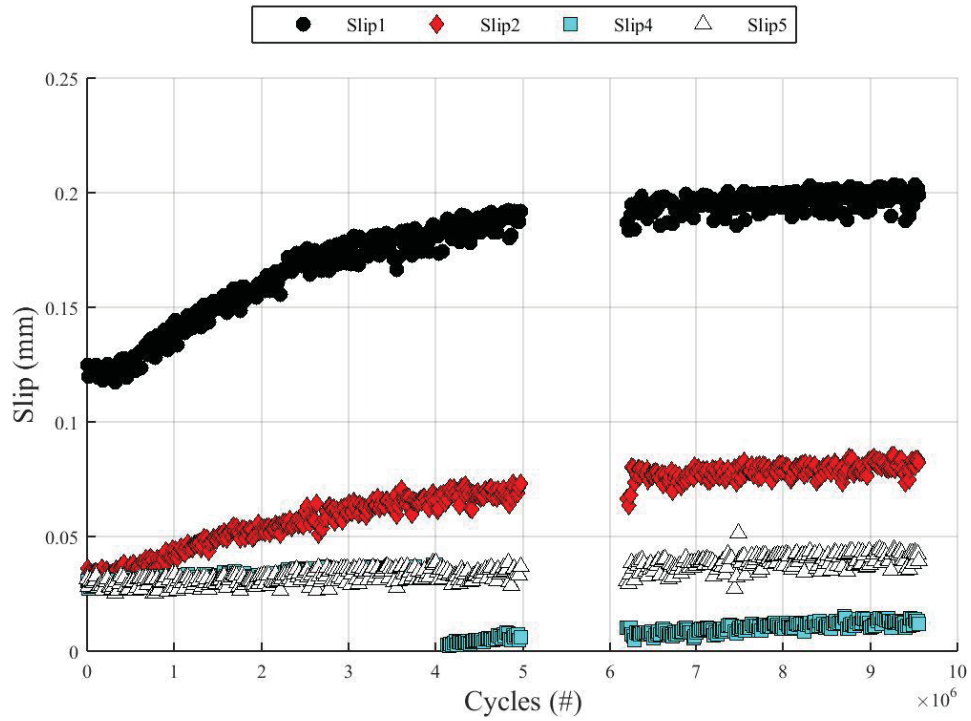
Figure F2-3: C100 – Interfacial Slip Data
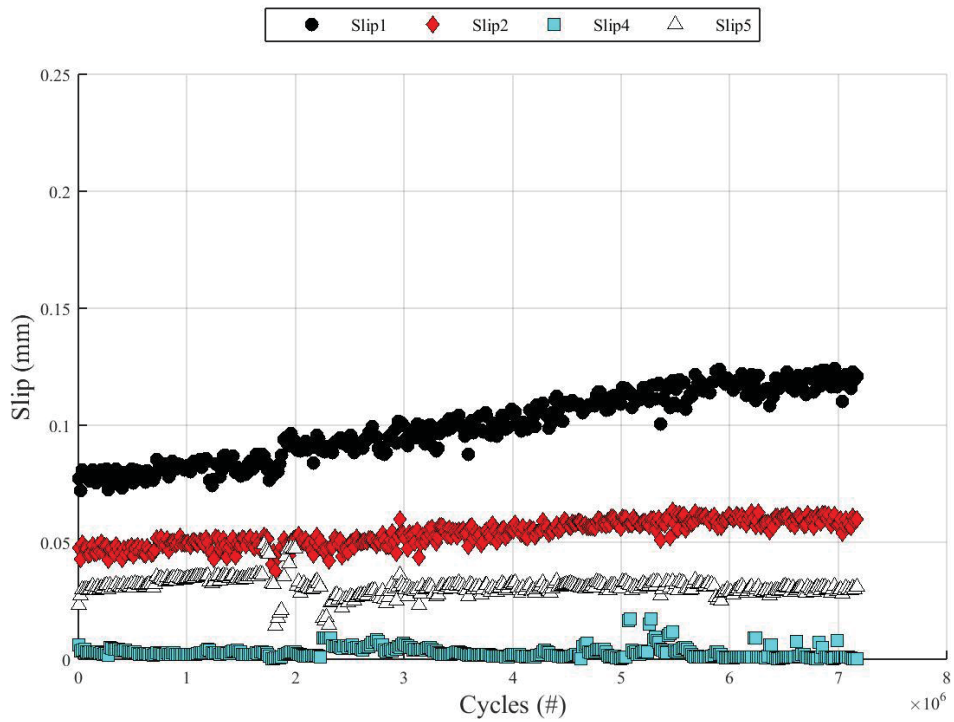
Figure F2-4: P100 – Interfacial Slip Data
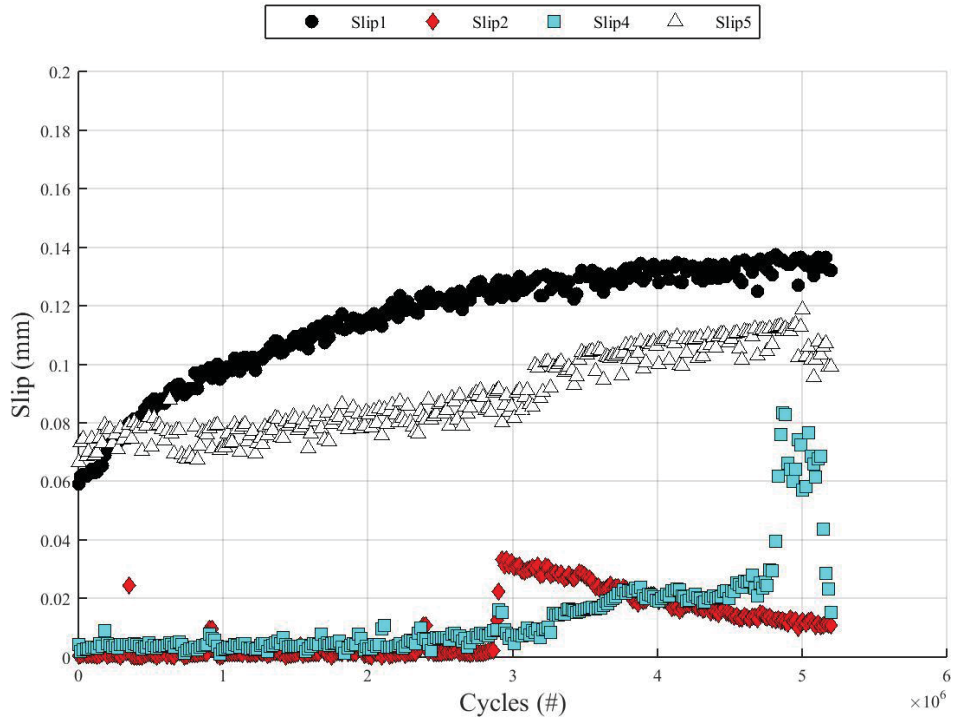
Figure F2-5: C120 – Interfacial Slip Data
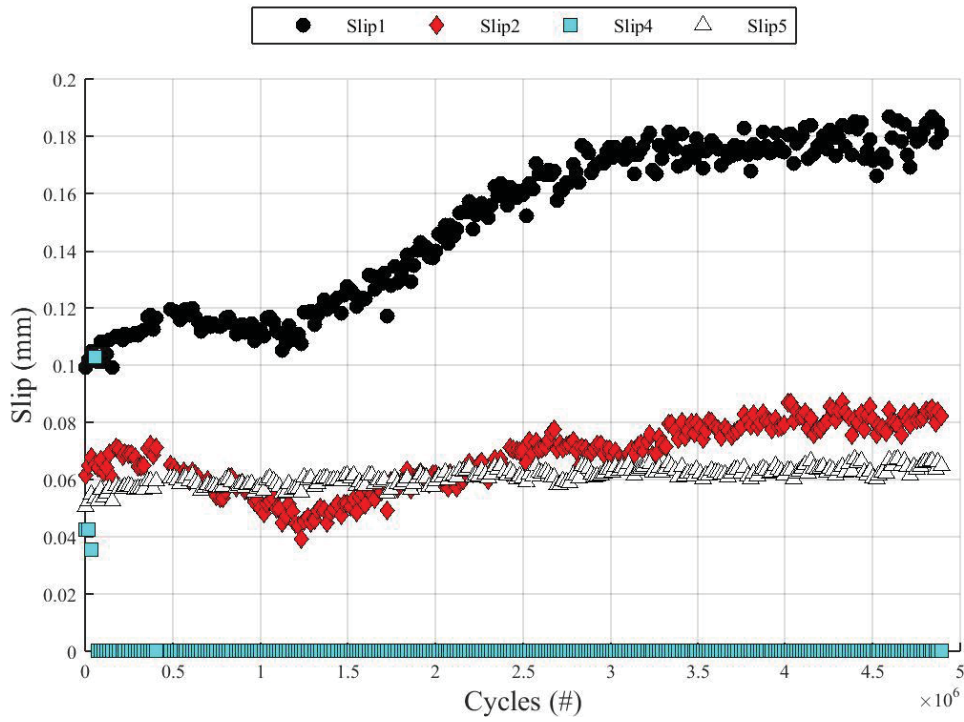
Figure F2-6: P120 – Interfacial Slip Data
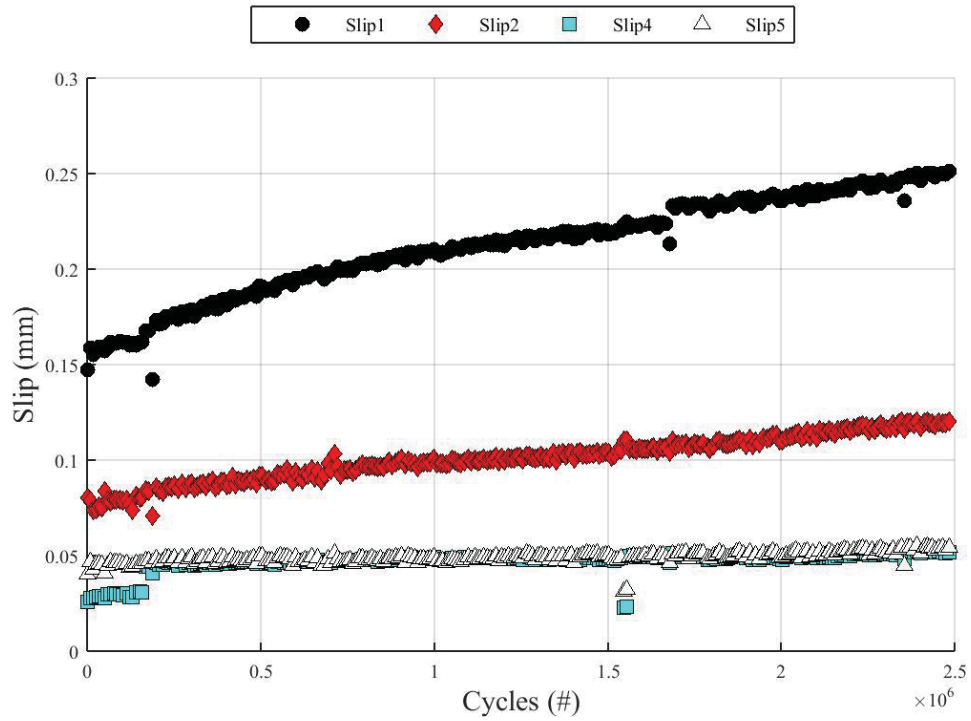
Figure F2-7: C140 – Interfacial Slip Data
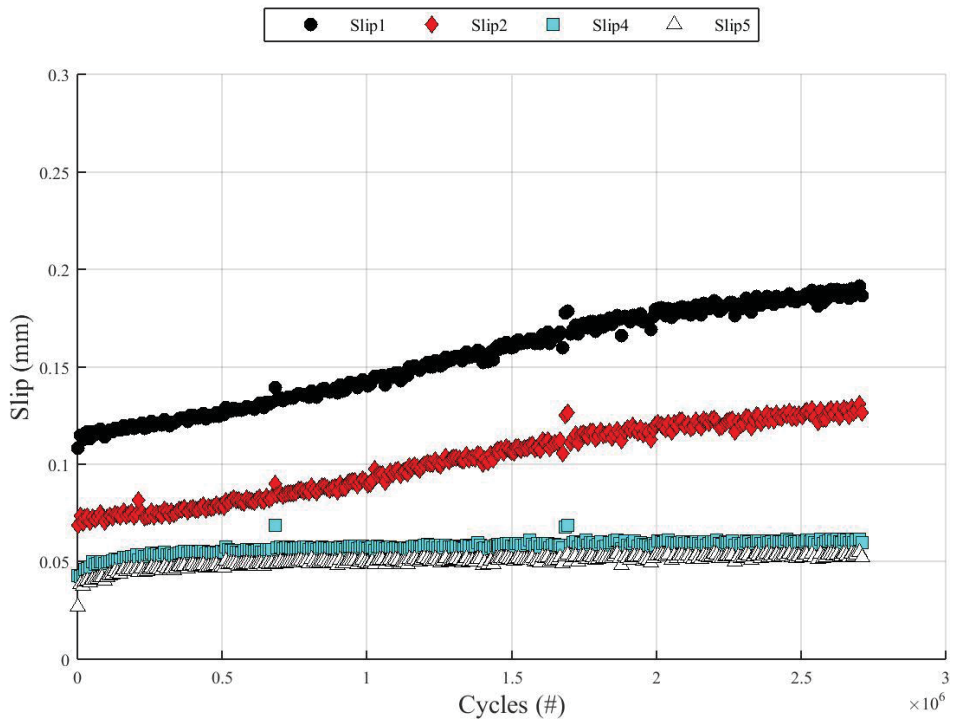
Figure F2-8: P140 – Interfacial Slip Data
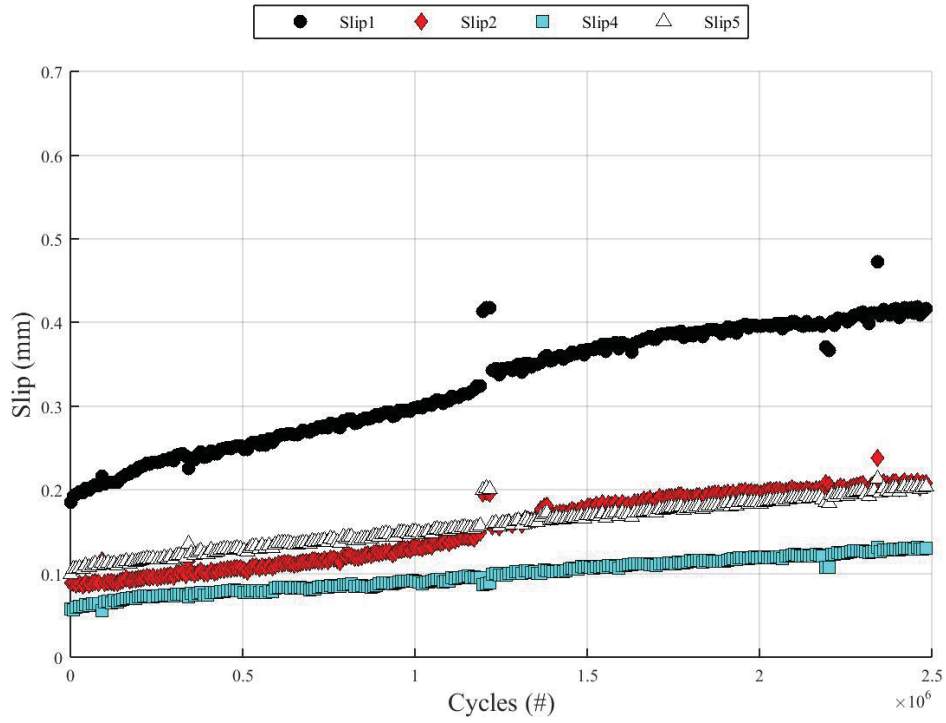
Figure F2-9: C200 – Interfacial Slip Data
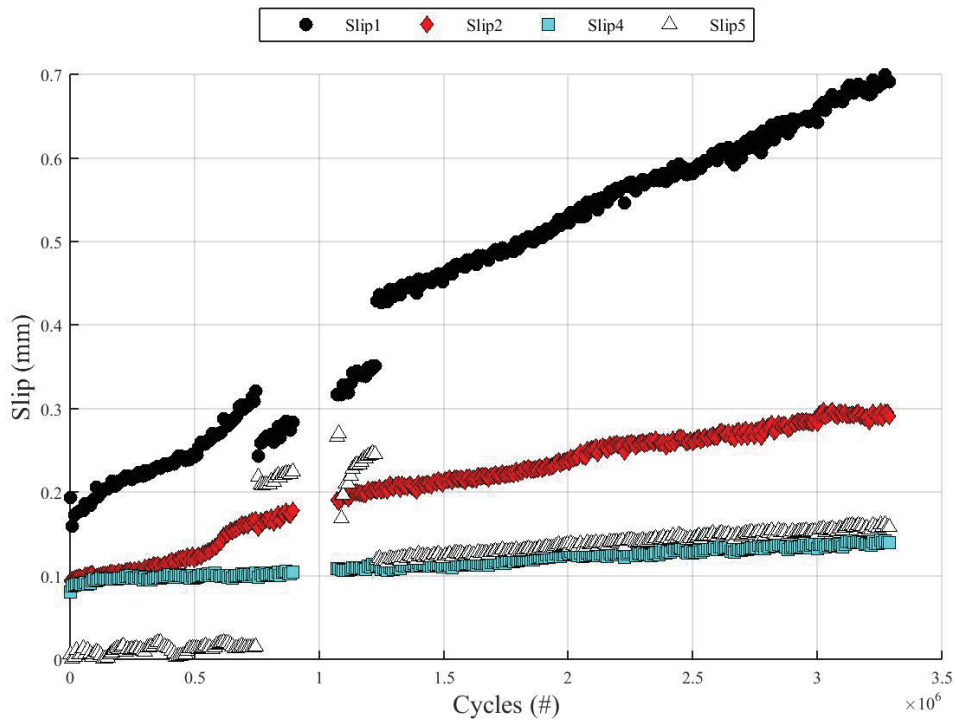
Figure F2-10: P200 – Interfacial Slip Data

224
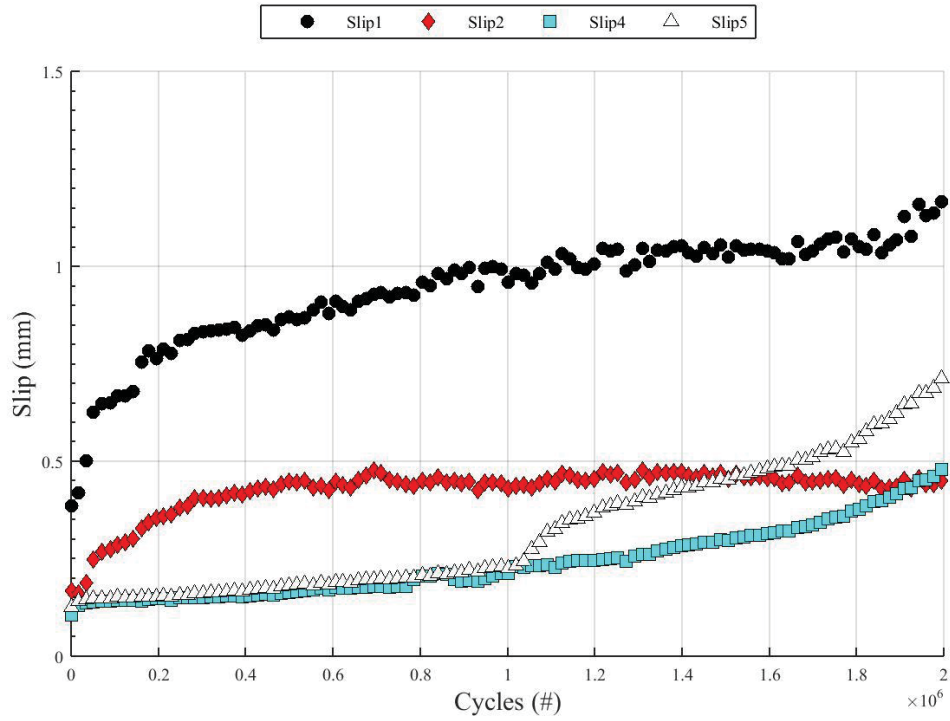
Figure F2-11: C300 – Interfacial Slip Data
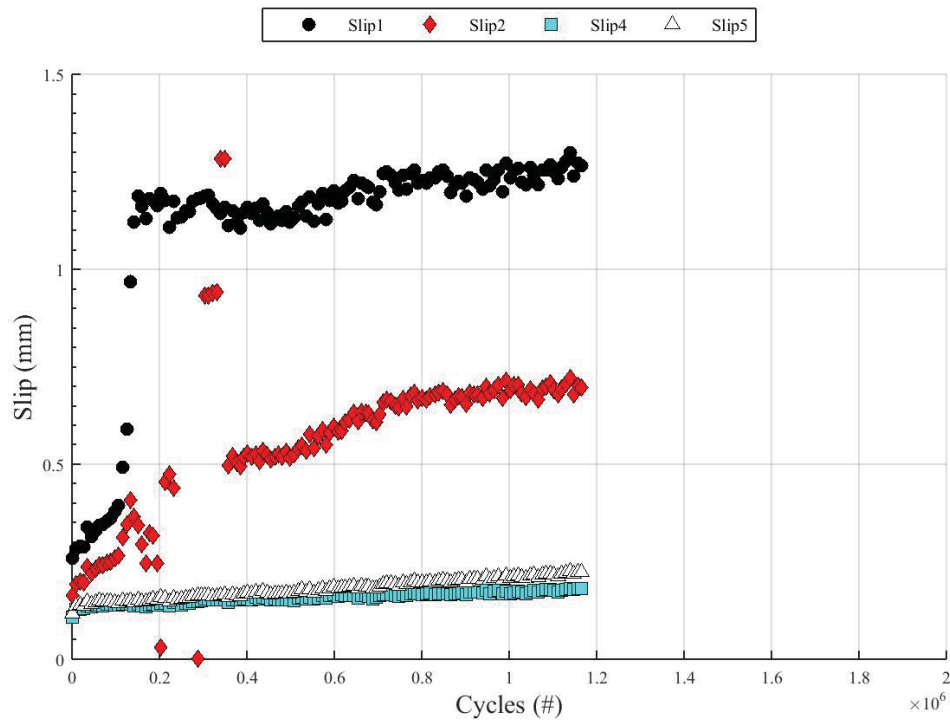
Figure F2-12: P300 – Interfacial Slip Data

225

Appendix F3: Local Distortion Strain versus Cycles

(a)

(b)

(c)
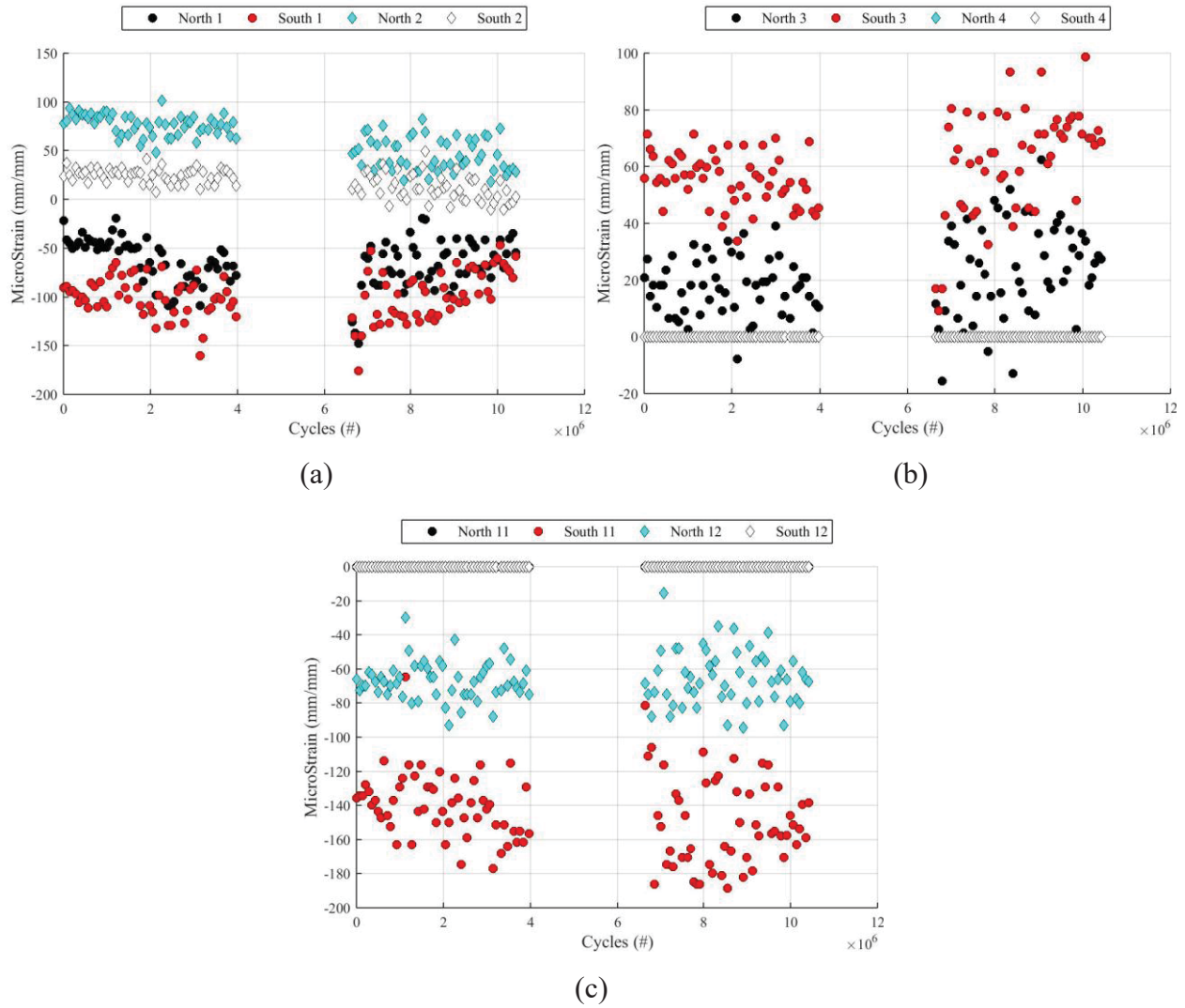
Figure F3-1: C067 – Local Distortion Data
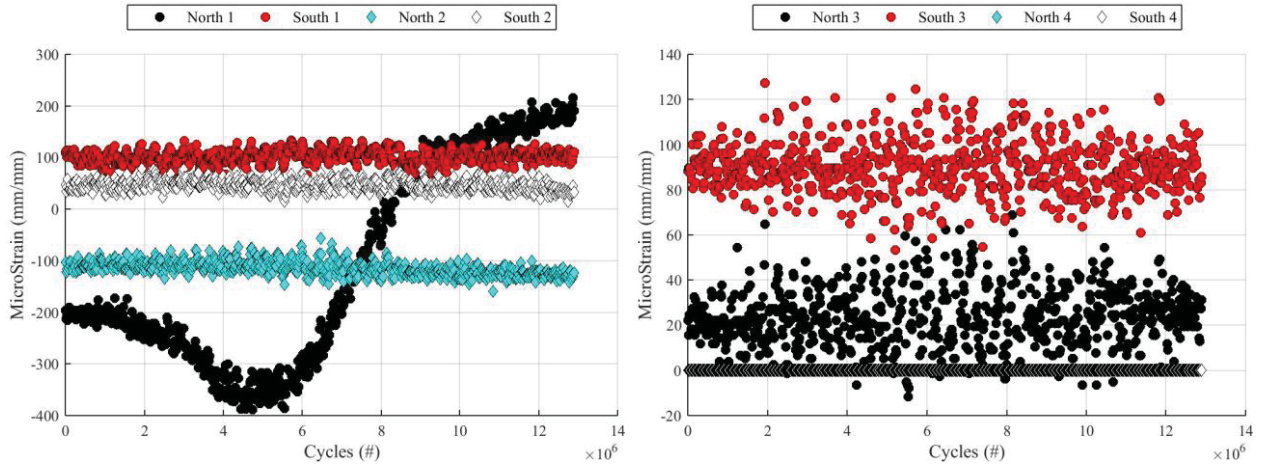
(a)

(b)
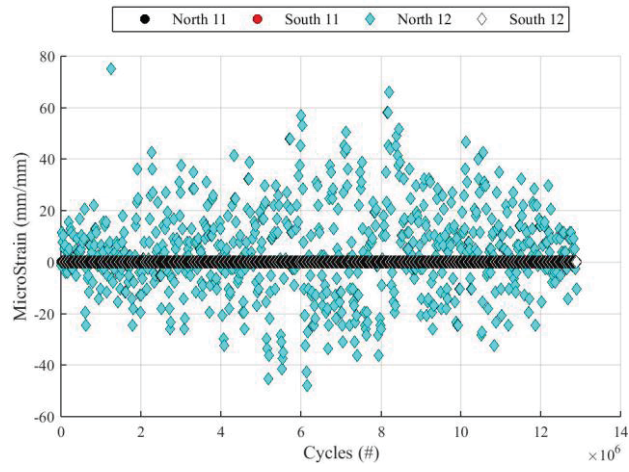
(c)

Figure F3-2: P067 – Local Distortion Data

227
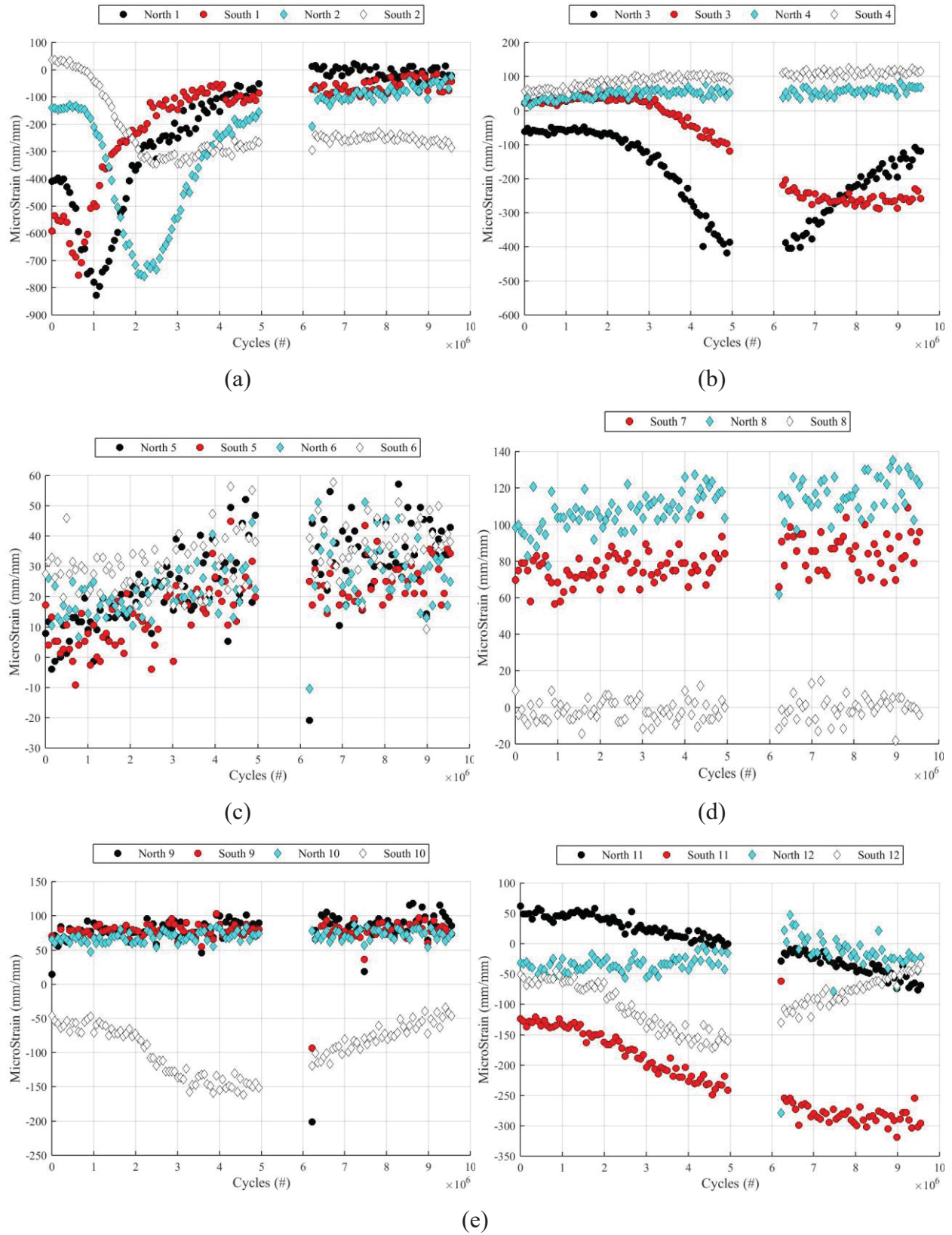
Figure F3-3: C100 – Local Distortion Data
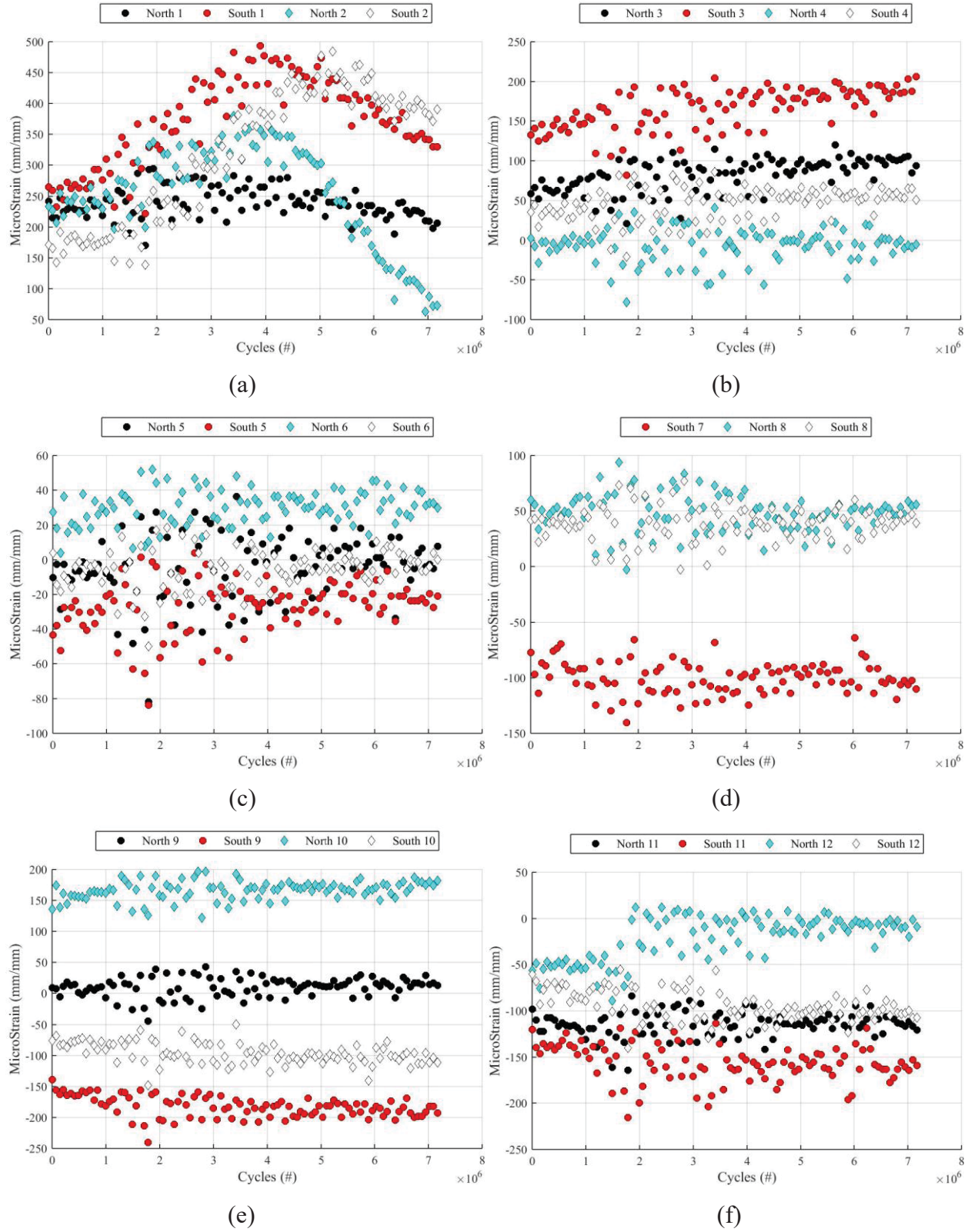
Figure F3-4: P100 – Local Distortion Data
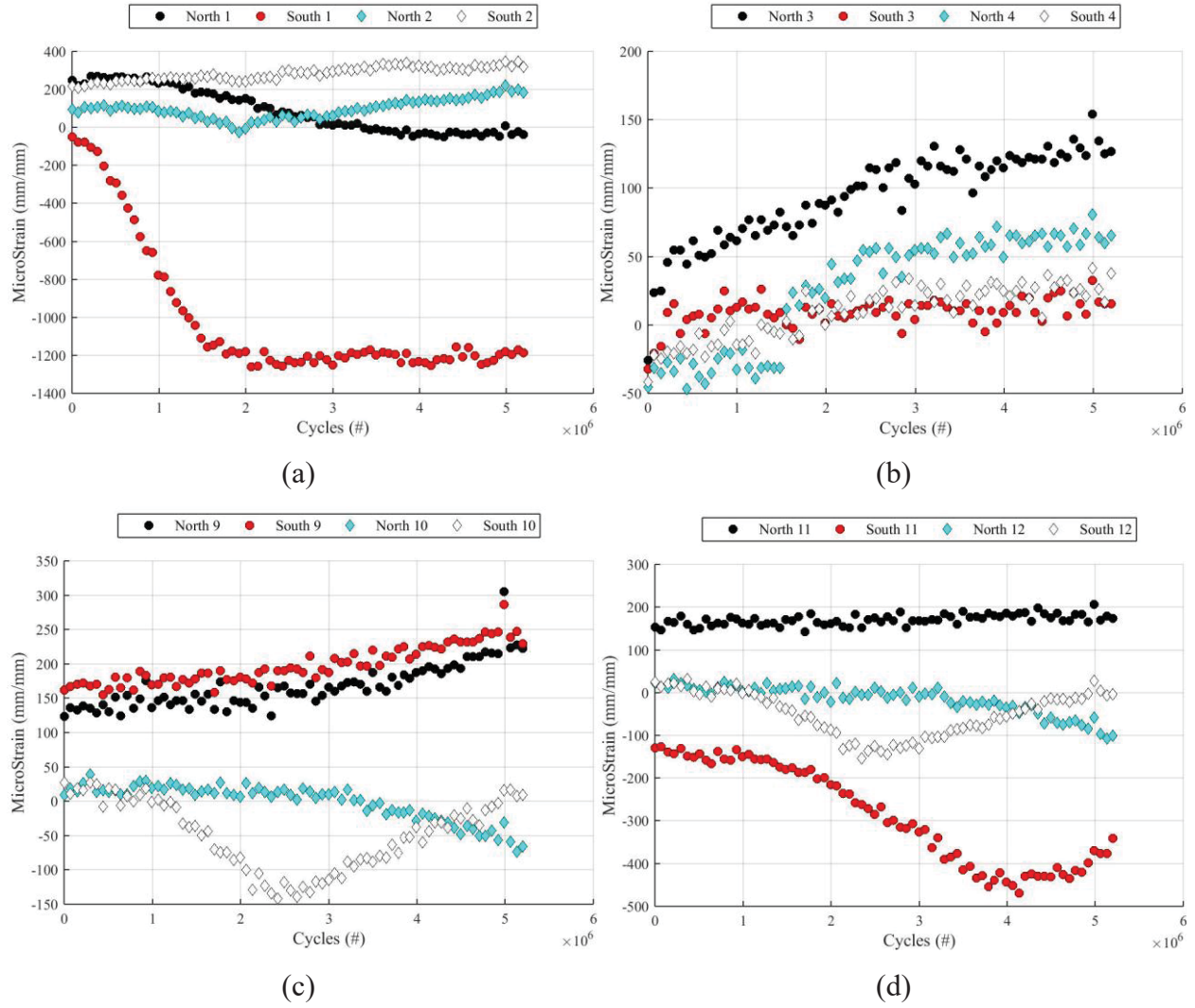
Figure F3-5: C120 – Local Distortion Data
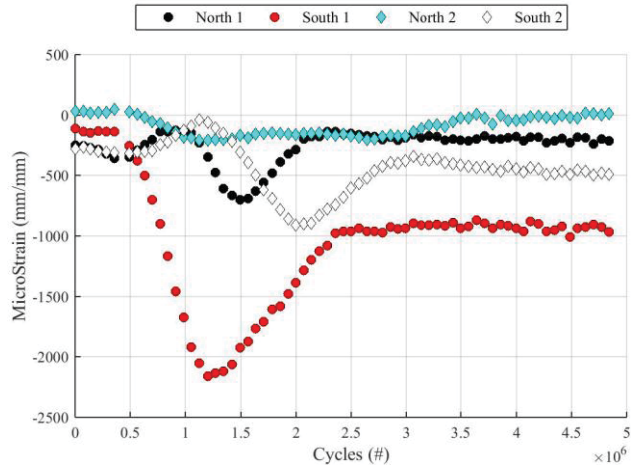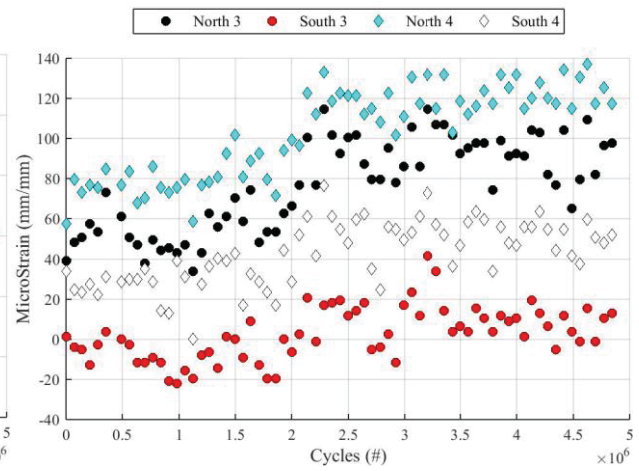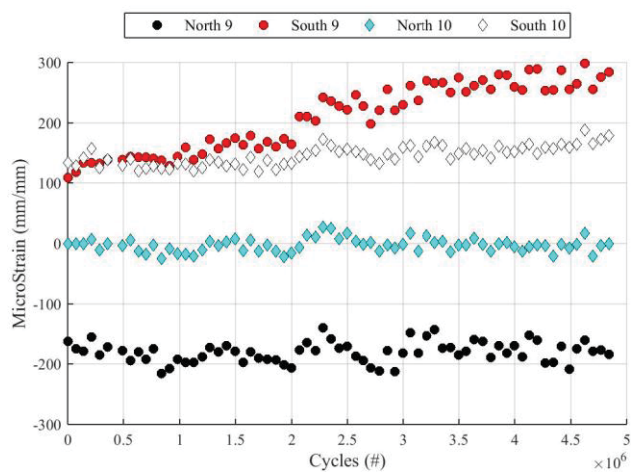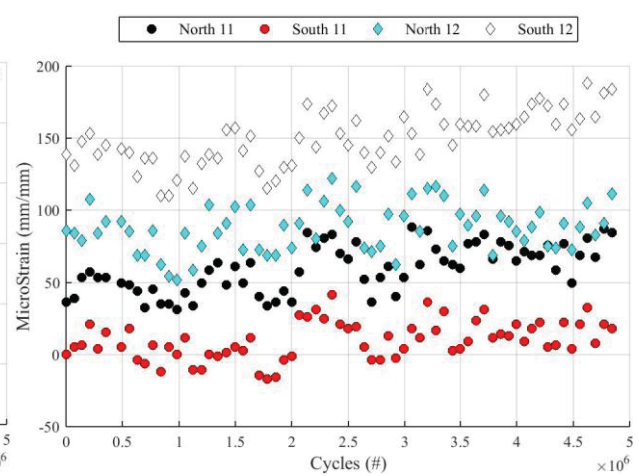
Figure F3-6: P120 – Local Distortion Data

231
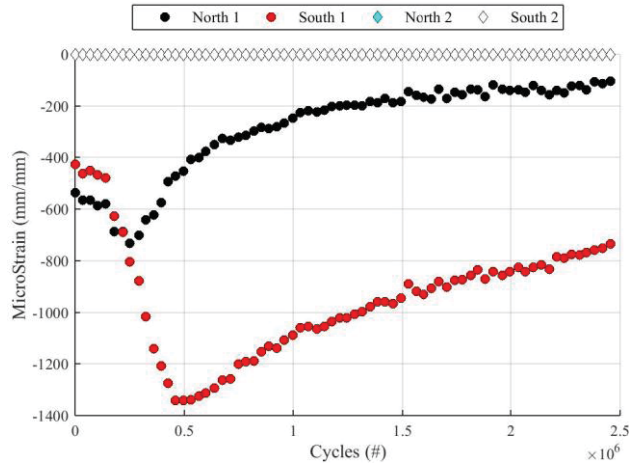
Figure F3-7: C140 – Local Distortion Data

(a)

(b)
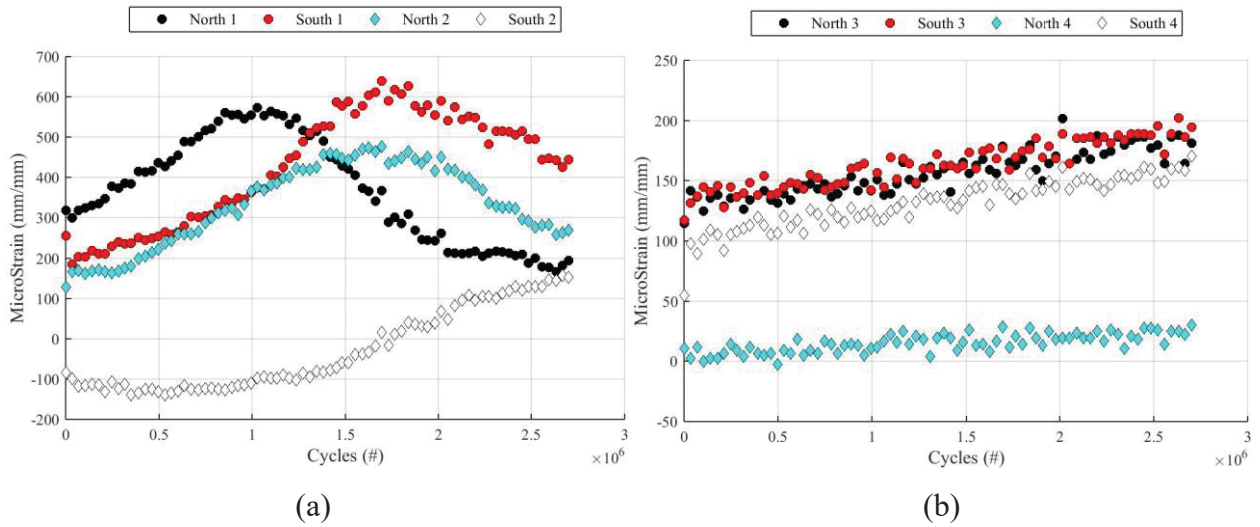
Figure F3-8: P140 – Local Distortion Data

(a)

(b)
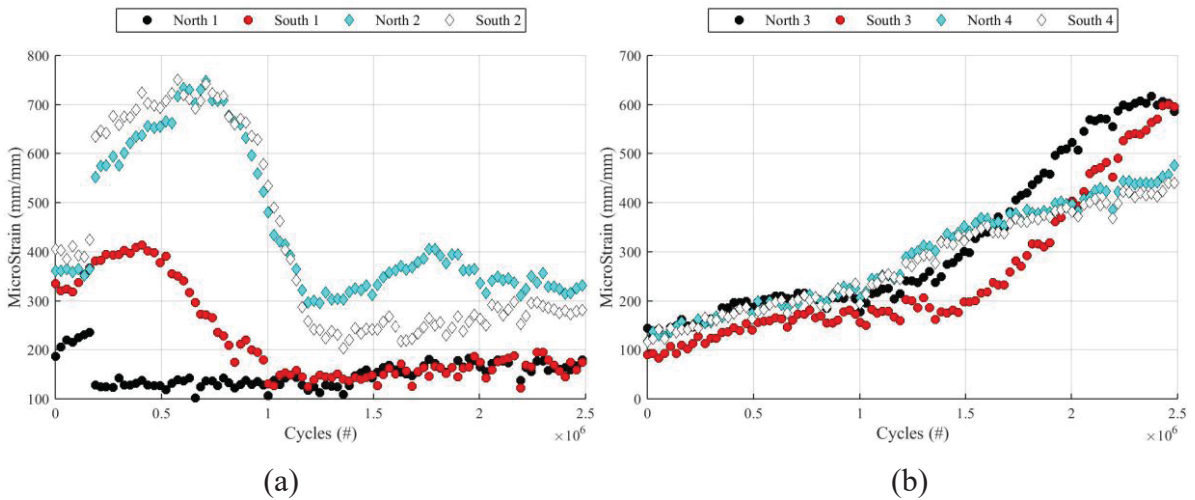
Figure F3-9: C200 – Local Distortion Data
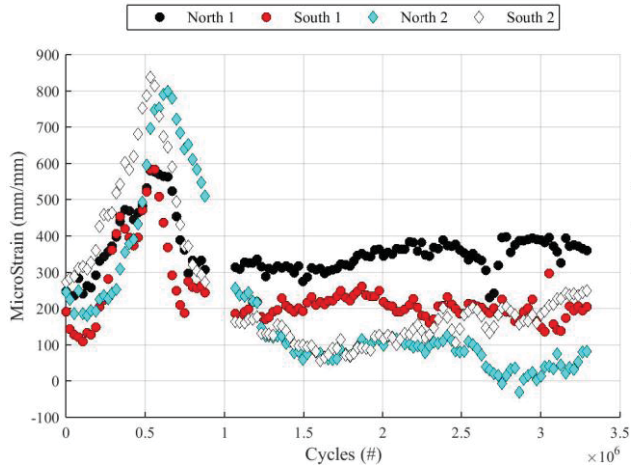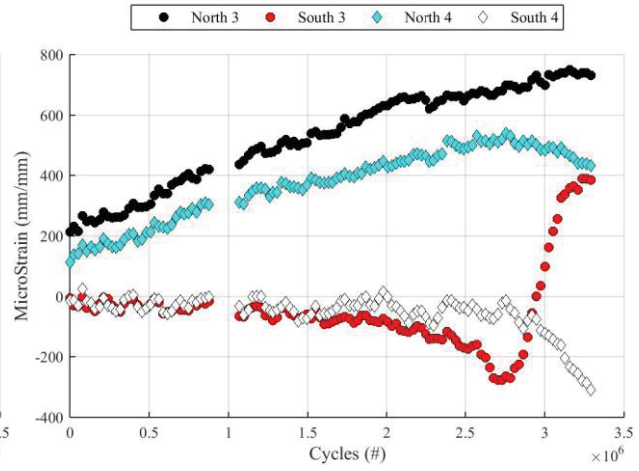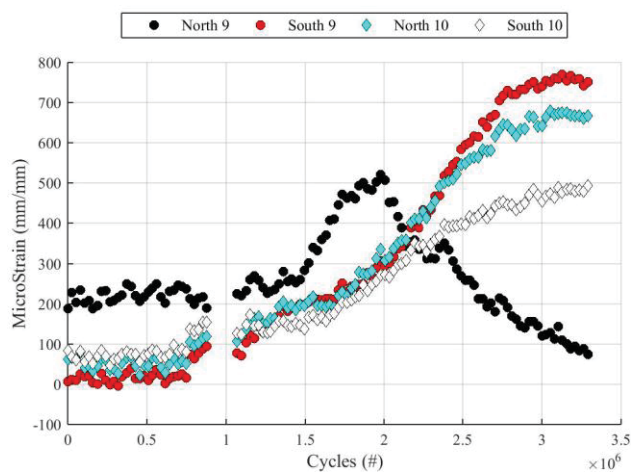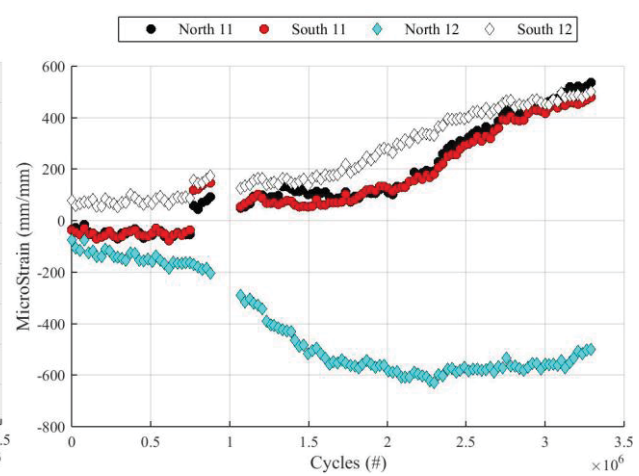
Figure F3-10: P200 – Local Distortion Data

233
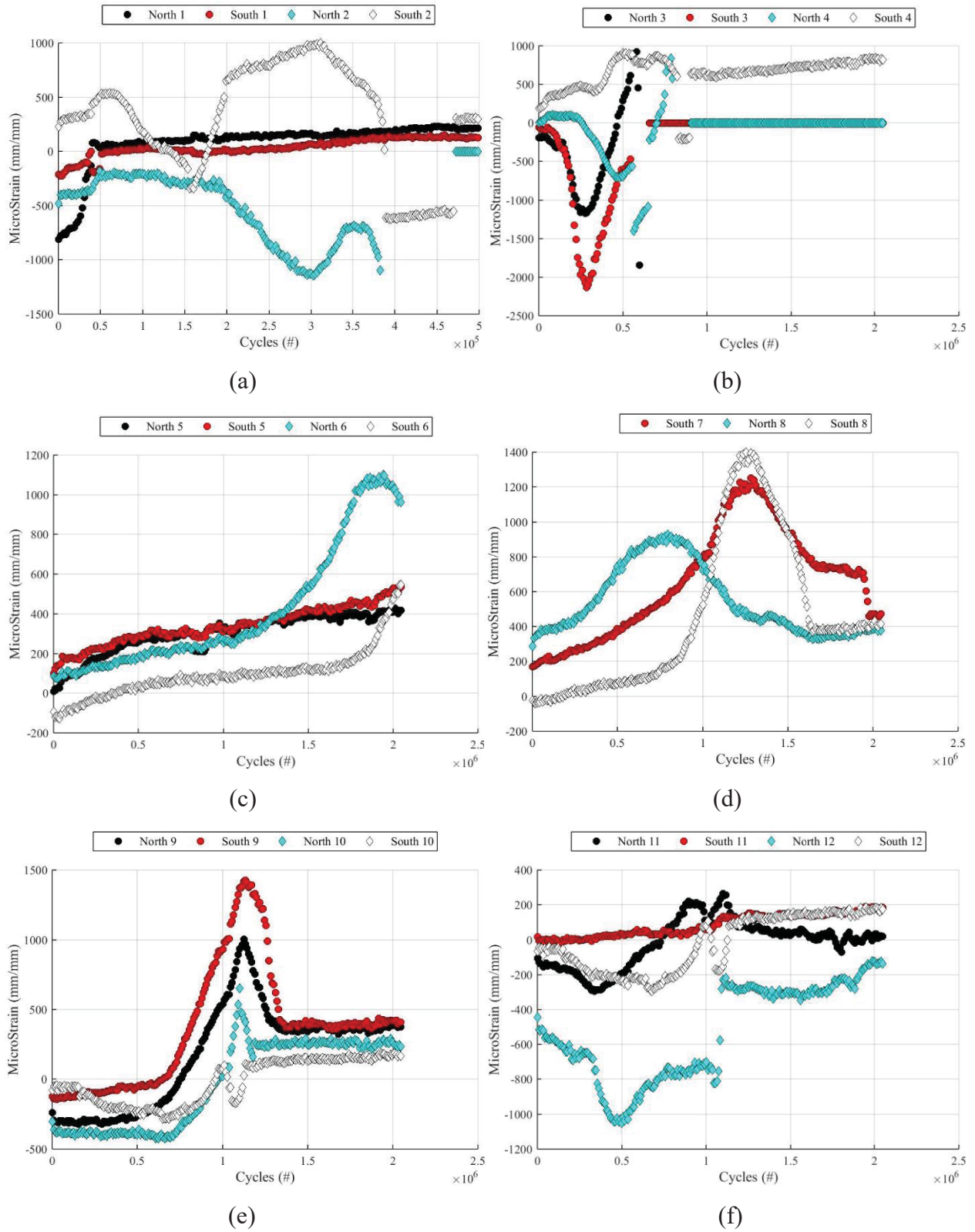
Figure F3-11: C300 – Local Distortion Data

234
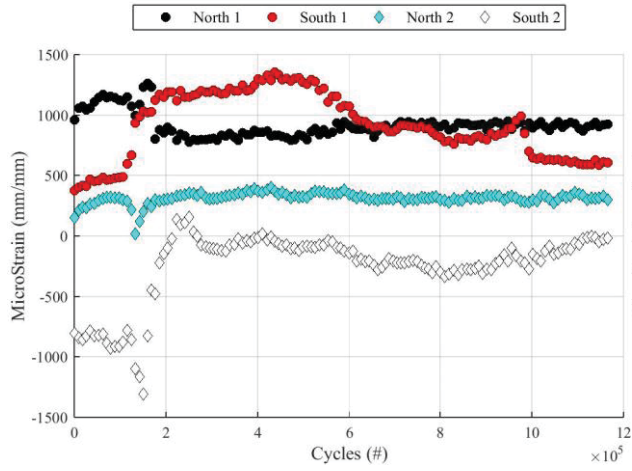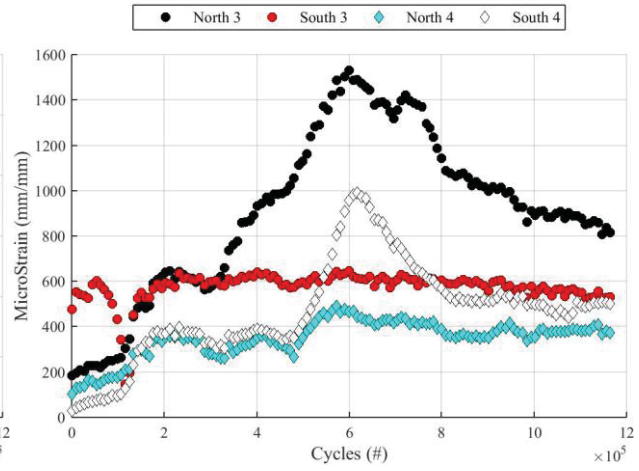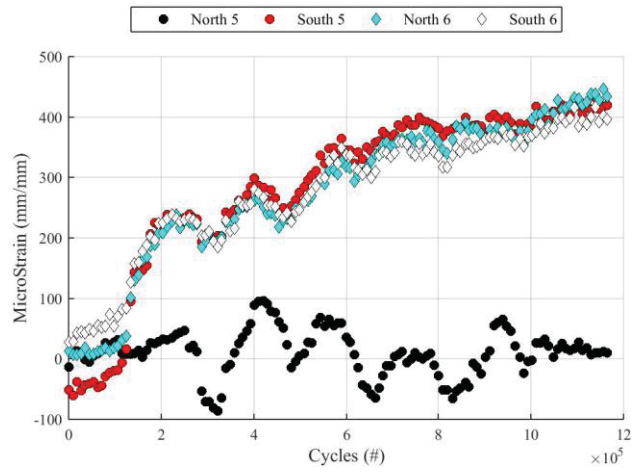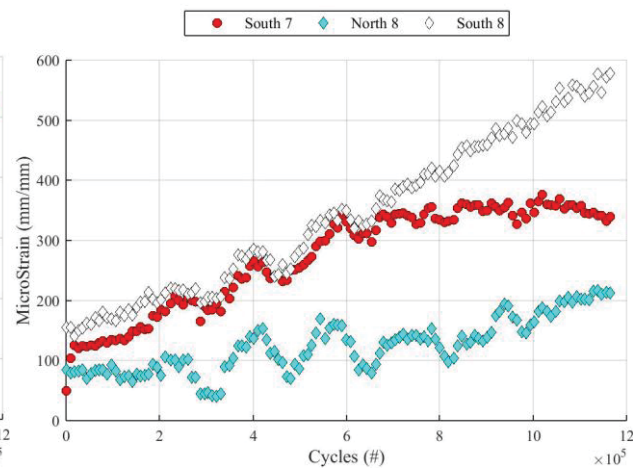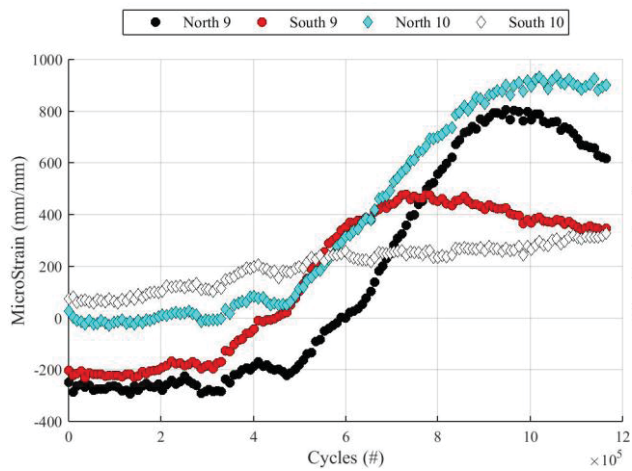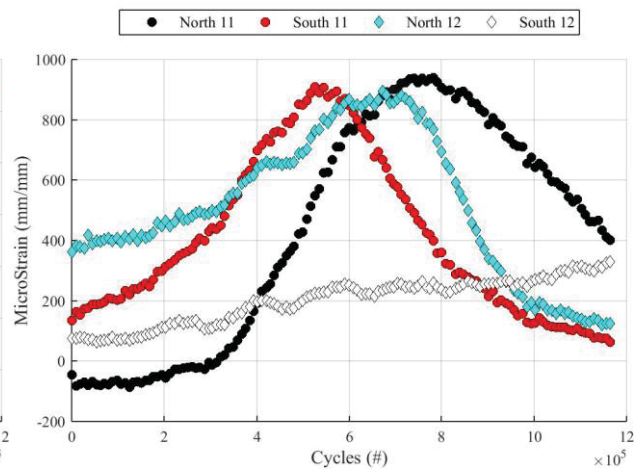
Figure F3-12: P300 – Local Distortion Data

235

Appendix G: Autopsy Results

Autopsy Results C067

Shear Experienced (%)	100%	100%	33.3%	33.3%	33.3%	33.3%	33.3%	33.3%	33.3%	33.3%	33.3%	33.3%
Shear Range (MPa)	67	67	22	22	22	22	22	22	22	22	22	22
Stud ID	N1	N2	N3	N4	N5	N6	N7	N8	N9	N10	N11	N12
Local Strain Behaviour	Post Peak	No Response	No Response									No Response
Cracking (Vis. | X-Sec)	>	NI	NI	NI	NI	NI	NI	NI	NI	NI	NI	No
Bend Test	Passed	NI	NI									Passed
Remaining Area (%)												
Length (mm) (W|E)												
Depth (mm) (W|E)												
Additional Notes	small crack in shank and flange											Zip cut revealed no cracking

Shear Experienced (%)	100%	100%	33.3%	33.3%	33.3%	33.3%	33.3%	33.3%	33.3%	33.3%	33.3%	33.3%
Shear Range (MPa)	67	67	22	22	22	22	22	22	22	22	22	22
Stud ID	S1	S2	S3	S4	S5	S6	S7	S8	S9	S10	S11	S12
Local Strain Behaviour	Post Peak	No Response	No Response									No Response
Cracking (Vis. | X-Sec)	>	NI	NI	NI	NI	NI	NI	NI	NI	NI	NI	No
Bend Test	Passed	NI	NI									Passed
Remaining Area (%)												
Length (mm) (W|E)	10 | 0											
Depth (mm) (W|E)	5											
Additional Notes	small crack in shank and flange											

BEND TESTS

● Failed ○ Passed ○ Not Investigated ○ Shaft Failed

LOCAL STRAINS

● Post Peak ○ Rising ○ No Response ○ Not Instrumented

CRACK DIRECTION

● Cracked Stud ○ Dominant Crack Direction

237

Autopsy Results C067

Figure G-2

Figure G-1

238

Autopsy Results P067

Shear Experienced (%)	100%	100%	33.3%	33.3%	33.3%	-33.3%	-33.3%	-33.3%	-33.3%	-33.3%	-33.3%	-33.3%
Shear Range (MPa)	67	67	22	22	-22	-22	-22	-22	-22	-22	-22	-22
Stud ID	N1	N2	N3	N4	N5	N6	N7	N8	N9	N10	N11	N12
Local Strain Behaviour												
Cracking (Vis. | X-Sec)												
Bend Test												
Remaining Area (%)												
Length (mm) (W|E)												
Depth (mm) (W|E)												
Additional Notes												

Stud ID	S1	S2	S3	S4	S5	S6	S7	S8	S9	S10	S11	S12
Local Strain Behaviour												
Cracking (Vis. | X-Sec)												
Bend Test												
Remaining Area (%)												
Length (mm) (W|E)												
Depth (mm) (W|E)												
Additional Notes												

Not Autopsied

Autopsy Results C100

Stud ID	N1	N2	N3	N4	N5	N6	N7	N8	N9	N10	N11	N12
Shear Experienced (%)	100%	100%	33.3%	33.3%	-33.3%	-33.3%	-33.3%	-33.3%	-33.3%	-33.3%	-33.3%	-33.3%
Shear Range (MPa)	100	100	33	33	-33	-33	-33	-33	-33	-33	-33	-33
Local Strain Behaviour	Post Peak	Post Peak	Rising	No Response	No Response	No Response	No Response	No Response	No Response	No Response	Rising	Rising
Cracking (Vis. | X-Sec)	>	>	NI	NI	NI	NI	NI	NI	NI	X	NI	NI
Bend Test	Passed	Passed	NI	NI	NI	NI	NI	NI	NI	NI	NI	NI
Remaining Area (%)												
Length (mm) (W|E)		12 | 0								0 | 3		
Depth (mm) (W|E)		9										
Additional Notes										Crack in shank		

Stud ID	S1	S2	S3	S4	S5	S6	S7	S8	S9	S10	S11	S12
Local Strain Behaviour	Post Peak	Post Peak	Rising	No Response	No Response	No Response	No Response	No Response	No Response	No Response	Rising	Rising
Cracking (Vis. | X-Sec)	>	>	NI	NI	NI	NI	NI	NI	NI	No	X	NI
Bend Test	Passed	Passed	NI	NI	NI	NI	NI	NI	NI	NI	Passed	NI
Remaining Area (%)												
Length (mm) (W|E)											0 | 9	
Depth (mm) (W|E)											5	
Additional Notes	Transverse X-section taken											

BEND TESTS

● Failed ◐ Passed ○ Not Investigated ○ Shaft Failed

W — N / S (1–12)

LOCAL STRAINS

● Post Peak ◐ Rising ○ Not Instrumented ○ No Response

W — N / S (1–12)

CRACK DIRECTION

○ Cracked Stud ◐ Dominant Crack Direction

W — N / S (1–12)

1 2 3 4 5 6 7 8 9 10 11 12

Autopsy Results C100

Figure G-4

Figure G-8

Figure G-3

Figure G-5

Figure G-7

Figure G-6

Autopsy Results P100

Stud ID	N1	N2	N3	N4	N5	N6	N7	N8	N9	N10	N11	N12
Shear Experienced (%)	100%	100%	33.3%	33.3%	33.3%	33.3%	33.3%	33.3%	33.3%	33.3%	33.3%	33.3%
Shear Range (MPa)	100	100	33	33	33	33	33	33	33	33	33	33
Local Strain Behaviour	Post Peak	Post Peak	No Response	No Response	No Response	No Response	NI	No Response	No Response	No Response	No Response	No Response
Cracking (Vis. | X-Sec)	>	>	NI	NI	NI	NI	NI	NI	NI	NI	NI	NI
Bend Test	Passed	Passed										
Remaining Area (%)												
Length (mm) (W|E)												
Depth (mm) (W|E)												
Additional Notes												

Stud ID	S1	S2	S3	S4	S5	S6	S7	S8	S9	S10	S11	S12
Local Strain Behaviour	Post Peak	Post Peak	No Response	No Response	No Response	No Response	NI	No Response	No Response	No Response	No Response	No Response
Cracking (Vis. | X-Sec)	>	>	NI	NI	NI	NI	NI	NI	NI	NI	NI	NI
Bend Test	Passed	Passed										
Remaining Area (%)												
Length (mm) (W|E)												
Depth (mm) (W|E)												
Additional Notes												

BEND TESTS

Legend: Failed ● | Passed ◐ | Not Investigated ○ | Shaft Failed ○

W / N / S — positions 1 2 3 4 5 6 7 8 9 10 11 12

LOCAL STRAINS

Legend: Post Peak ● | Rising ◐ | Not Instrumented ○ | No Response ○

W / N / S — positions 1 2 3 4 5 6 7 8 9 10 11 12

CRACK DIRECTION

Legend: Cracked Stud ○ | Dominant Crack Direction ◈

W / N / S — positions 1 2 3 4 5 6 7 8 9 10 11 12

Autopsy Results P100

Figure G-9

Autopsy Results C120

Shear Experienced (%)	100%	100%	33.3%	33.3%	-33.3%	-33.3%	-33.3%	-33.3%	-33.3%	-33.3%	-33.3%	-33.3%
Shear Range (MPa)	120	120	40	40	-40	-40	-40	-40	-40	-40	-40	-40

Stud ID	N1	N2	N3	N4	N5	N6	N7	N8	N9	N10	N11	N12
Local Strain Behaviour	Post Peak	Rising	Rising	Rising	NI	NI	NI	NI	Rising	Rising	No Response	Rising
Cracking (Vis. | X-Sec)	>	>	No	No	NI	NI	NI	NI		No	X	>
Bend Test	Fail	Passed	Passed	Passed	NI	NI	NI	NI		Pass	Pass	Pass
Remaining Area (%)	10%											
Length (mm) (W|E)	17.3 | 0										0 | 2	
Depth (mm) (W|E)	7.8										2	
Additional Notes												

Stud ID	S1	S2	S3	S4	S5	S6	S7	S8	S9	S10	S11	S12
Local Strain Behaviour	Post Peak	Rising	Rising	Rising	NI	NI	NI	NI	Rising	Post Peak	Post Peak	Post Peak
Cracking (Vis. | X-Sec)	>	>	No		NI	NI	NI	NI		X	>	>
Bend Test	Fail	Pass	Pass	Fail	NI	NI	NI	NI		Pass	Fail	Fail
Remaining Area (%)	10%										50	30
Length (mm) (W|E)	16.1 | 0									0 | 3	0 | 10.2	0 | 15
Depth (mm) (W|E)	7.2									3	6.5	5.8
Additional Notes												

BEND TESTS

Legend: ● Failed ◑ Passed ○ Not Investigated (grey) Shaft Failed

	1	2	3	4	5	6	7	8	9	10	11	12
W (N/S)												

LOCAL STRAINS

Legend: ● Post Peak ◑ Rising ○ Not Instrumented (grey) No Response

	1	2	3	4	5	6	7	8	9	10	11	12
W (N/S)												

CRACK DIRECTION

Legend: ○ Cracked Stud ⬆ Dominant Crack Direction

	1	2	3	4	5	6	7	8	9	10	11	12
W (N/S)												

Autopsy Results C120
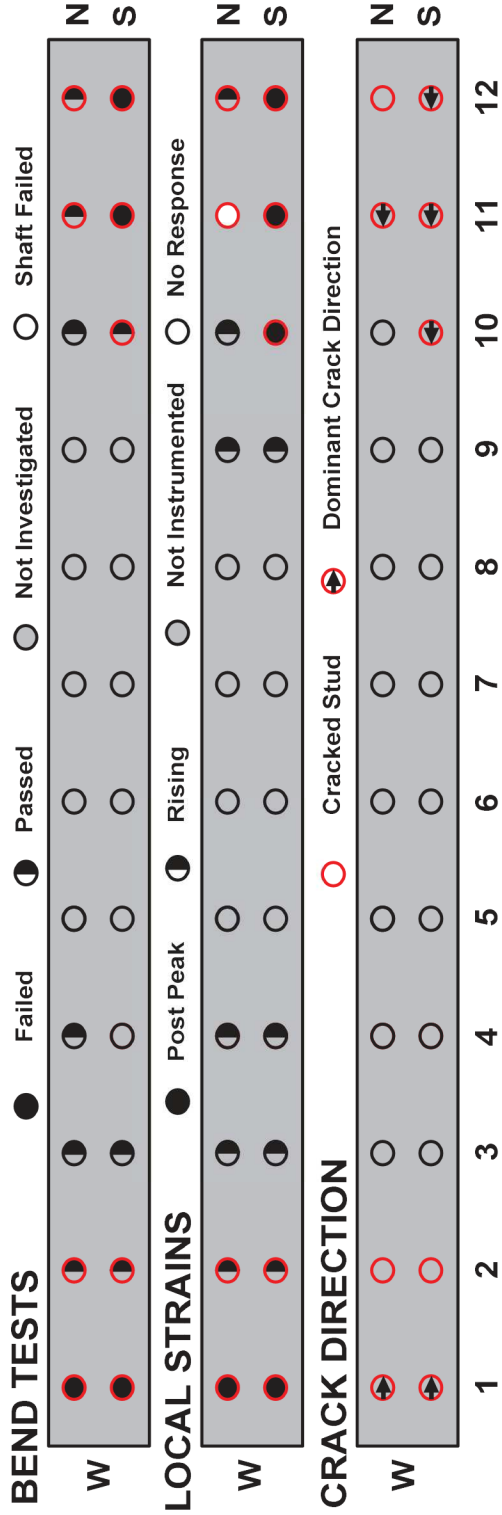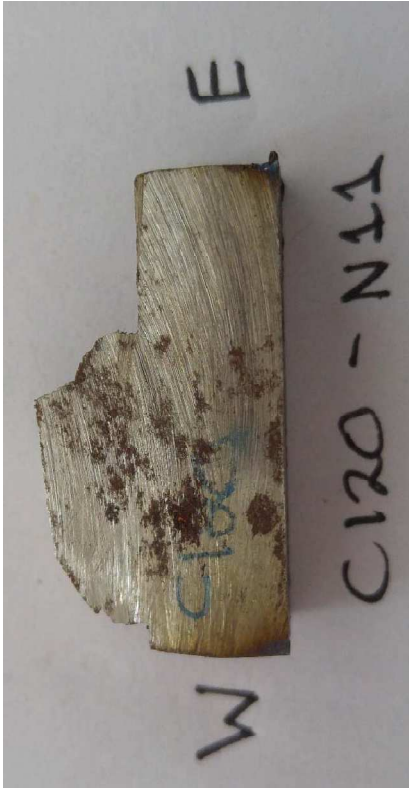
Figure G-11

Figure G-10

Autopsy Results P120

Shear Experienced (%)	100%	100%	33.3%	33.3%	-33.3%	-33.3%	-33.3%	-33.3%	-33.3%	-33.3%	-33.3%	-33.3%
Shear Range (MPa)	120	120	40	40	-40	-40	-40	-40	-40	-40	-40	-40
Stud ID	**N1**	**N2**	**N3**	**N4**	**N5**	**N6**	**N7**	**N8**	**N9**	**N10**	**N11**	**N12**
Local Strain Behaviour	Post Peak	Post Peak	Rising	Rising	NI	NI	NI	NI	No Response	No Response	No Response	No Response
Cracking (Vis. | X-Sec)	>	>	NI	NI	NI	NI	NI	NI	NI	NI	NI	NI
Bend Test	Fail	Fail	NI	NI	NI	NI	NI	NI	NI	NI	NI	Pass
Remaining Area (%)	10%	10%										
Length (mm) (W|E)	11.7 | 10.7	10.1 | 10.2										
Depth (mm) (W|E)	8.2	7.9										
Additional Notes												

Stud ID	**S1**	**S2**	**S3**	**S4**	**S5**	**S6**	**S7**	**S8**	**S9**	**S10**	**S11**	**S12**
Local Strain Behaviour	Post Peak	Post Peak	No Response	No Response	NI	NI	NI	NI	Rising	No Response	No Response	No Response
Cracking (Vis. | X-Sec)	>	>	NI	NI	NI	NI	NI	NI	NI	NI	NI	NI
Bend Test	Passed	Fail	NI	NI	NI	NI	NI	NI	NI	NI	NI	Pass
Remaining Area (%)		20%										
Length (mm) (W|E)	3 | 10	10.6 | 11.8										
Depth (mm) (W|E)	9.5	8.3										
Additional Notes	E crack almost penetrated entire flange depth											

BEND TESTS

● Failed ◑ Passed ◯ Not Investigated ◯ Shaft Failed

W — N / S grid (1 2 3 4 5 6 7 8 9 10 11 12)

LOCAL STRAINS

● Post Peak ◑ Rising ◯ Not Instrumented ◯ No Response

W — N / S grid (1 2 3 4 5 6 7 8 9 10 11 12)

CRACK DIRECTION

◯ Cracked Stud ⬆ Dominant Crack Direction

W — N / S grid (1 2 3 4 5 6 7 8 9 10 11 12)

Autopsy Results P120

Figure G-12

247
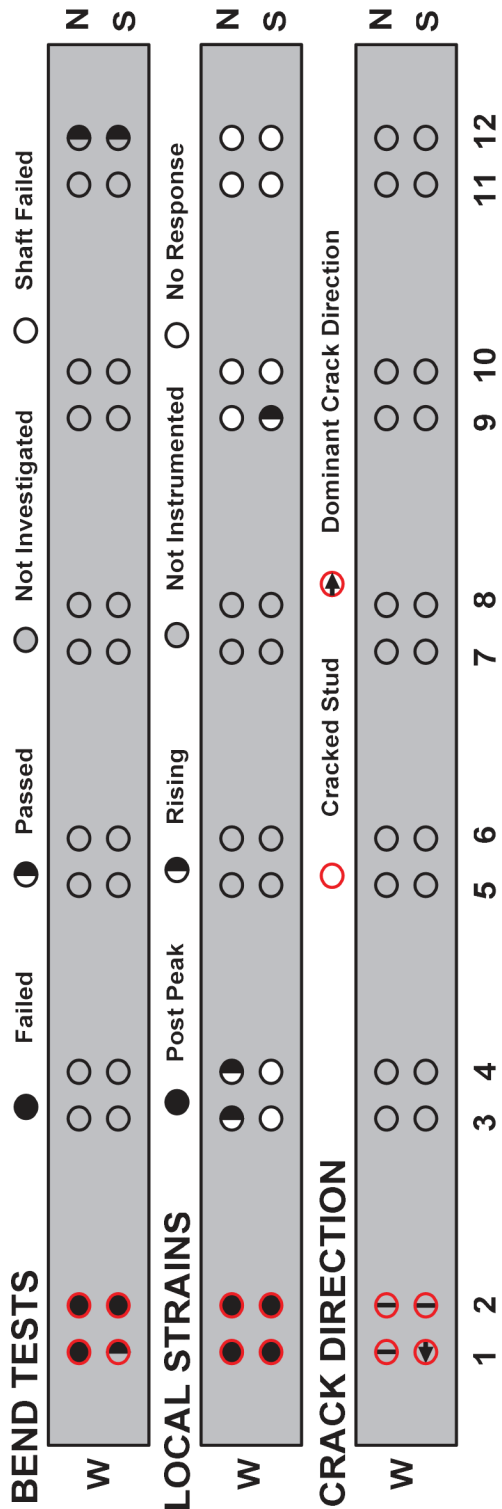
Autopsy Results C140

Shear Experienced (%)	100%	100%	33.3%	33.3%	-33.3%	-33.3%	-33.3%	-33.3%	-33.3%	-33.3%	-33.3%	-33.3%
Shear Range (MPa)	140	140	47	47	47	47	47	47	47	47	47	47
Stud ID	N1	N2	N3	N4	N5	N6	N7	N8	N9	N10	N11	N12
Local Strain Behaviour	Post Peak	NI	NI	NI	NI	NI	NI	NI	NI	NI	NI	NI
Cracking (Vis. | X-Sec)	>	No	NI	NI	NI	NI	NI	NI	NI	NI	NI	NI
Bend Test	Failed	Passed	NI	NI	NI	NI	NI	NI	NI	NI	NI	NI
Remaining Area (%)	10%											
Length (mm) (W|E)	14.0 | 9.0											
Depth (mm) (W|E)	10..5											
Additional Notes												

Stud ID	S1	S2	S3	S4	S5	S6	S7	S8	S9	S10	S11	S12
Local Strain Behaviour	Post Peak	NI	NI	NI	NI	NI	NI	NI	NI	NI	NI	NI
Cracking (Vis. | X-Sec)	>	No	NI	NI	NI	NI	NI	NI	NI	NI	NI	NI
Bend Test	Failed	Passed	NI	NI	NI	NI	NI	NI	NI	NI	NI	NI
Remaining Area (%)	10%											
Length (mm) (W|E)	18.8 | 5											
Depth (mm) (W|E)	9.0											
Additional Notes												

BEND TESTS

● Failed ● Passed ○ Not Investigated ○ Shaft Failed

LOCAL STRAINS

● Post Peak ● Rising ○ Not Instrumented ○ No Response

CRACK DIRECTION

○ Cracked Stud ⊕ Dominant Crack Direction

248
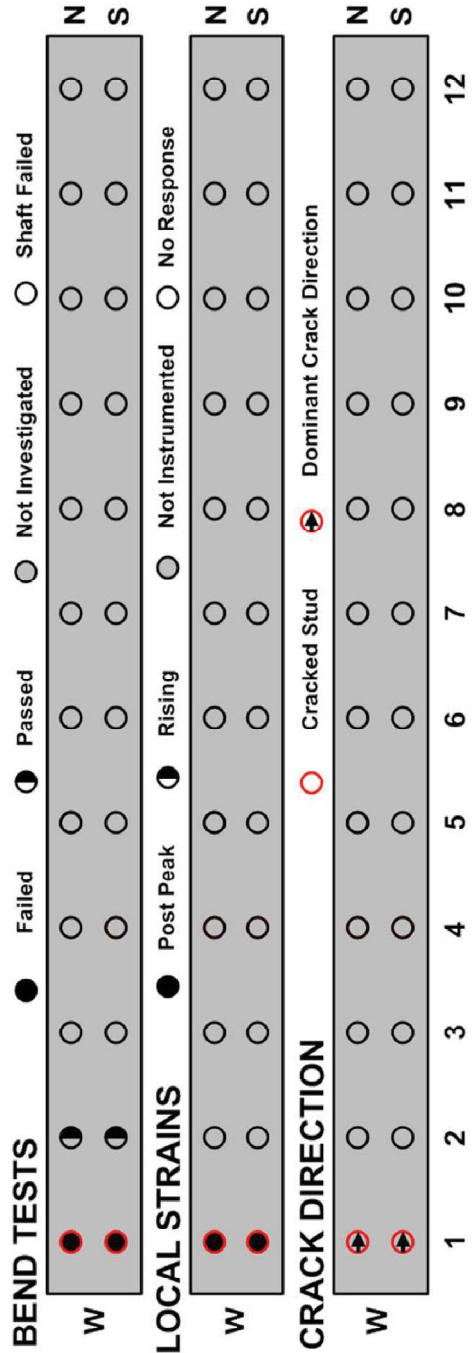
Figure G-13

Autopsy Results P140

Shear Experienced (%)	100%	100%	33.3%	33.3%	-33.3%	-33.3%	-33.3%	-33.3%	-33.3%	-33.3%	-33.3%	-33.3%
Shear Range (MPa)	140	140	47	47	-47	-47	-47	-47	-47	-47	-47	-47
Stud ID	N1	N2	N3	N4	N5	N6	N7	N8	N9	N10	N11	N12
Local Strain Behaviour	Post Peak	Post Peak	Rising	Rising	NI	NI	NI	NI	NI	NI	NI	NI
Cracking (Vis. | X-Sec)	>	>	NI	NI	NI	NI	NI	NI	NI	NI	NI	NI
Bend Test	Failed	Failed										
Remaining Area (%)	10%	50%										
Length (mm) (W|E)	10.7	12.5	2.0	11.5								
Depth (mm) (W|E)	6.5	3.8										
Additional Notes												

Stud ID	S1	S2	S3	S4	S5	S6	S7	S8	S9	S10	S11	S12
Local Strain Behaviour	Post Peak	Post Peak	Rising	Rising	NI	NI	NI	NI	NI	NI	NI	NI
Cracking (Vis. | X-Sec)	>	>	NI	NI	NI	NI	NI	NI	NI	NI	NI	NI
Bend Test	Failed	Failed										
Remaining Area (%)	20%	50%										
Length (mm) (W|E)	10.3	11	3.0	11.2								
Depth (mm) (W|E)	8.7	4.1										
Additional Notes												

BEND TESTS

LOCAL STRAINS

CRACK DIRECTION

Legend:
- ● Failed
- ◗ Passed
- ● Not Investigated
- ○ Shaft Failed
- ● Post Peak
- ◗ Rising
- ○ Not Instrumented
- ○ No Response
- ○ Cracked Stud
- ⊕ Dominant Crack Direction

1 2 3 4 5 6 7 8 9 10 11 12

N
S

250
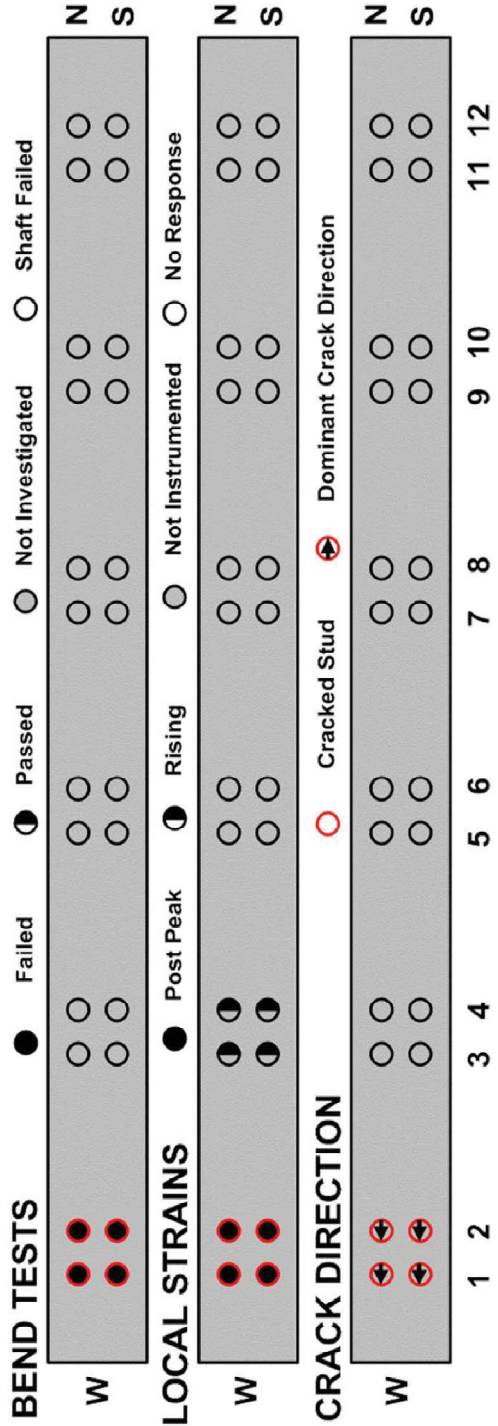
Autopsy Results P140

Figure G-18

Figure G-17

Figure G-16

Figure G-15

Figure G-14

Figure G-21

Figure G-20

Figure G-19

Autopsy Results C200

Shear Experienced (%)	100%	100%	33.3%	33.3%	-33.3%	-33.3%	-33.3%	-33.3%	-33.3%	-33.3%	-33.3%	-33.3%
Shear Range (MPa)	200	200	67	67	-67	-67	-67	-67	-67	-67	-67	-67
Stud ID	N1	N2	N3	N4	N5	N6	N7	N8	N9	N10	N11	N12
Local Strain Behaviour	Post Peak	Post Peak	Post Peak	Rising	NI	NI	NI	NI	NI	NI	NI	NI
Cracking (Vis. | X-Sec)	>	>	>	No	No	No	>	>	>	>	>	>
Bend Test	Failed	Failed	Passed	Passed	NI	Passed	Failed	Failed	Failed	Failed	Failed	Failed
Remaining Area (%)	0%	10%					30%	10%	10%	0%	0%	0%
Length (mm) (W|E)	13.8 | 16.3	8.5 | 11.9					10.3 | 7.8	12.8 | 9.0	16.3 | 12.8	14.3 | 12.6	12.1 | 12.8	6.5 | 16.3
Depth (mm) (W|E)	6.6	7.4					4.6	6.3	8.7	7.0	5.7	5.3
Additional Notes												

Stud ID	S1	S2	S3	S4	S5	S6	S7	S8	S9	S10	S11	S12
Local Strain Behaviour	Post Peak	Post Peak	Post Peak	Rising	NI	NI	NI	NI	NI	NI	NI	NI
Cracking (Vis. | X-Sec)	>	>	No	No	No	No	>	>	>	>	>	>
Bend Test	Failed	Failed	Passed	NI	NI	Passed	Failed	Failed	Failed	Failed	Failed	Failed
Remaining Area (%)	0%	10%					30%	20%	0%	0%	0%	0%
Length (mm) (W|E)	13.7 | 16.3	11.0 | 11.8					10.00 | 6.4	13.1 | 7.5	13.9 | 11.00	14.1 | 11.5	10.8 | 13.0	7.2 | 16.4
Depth (mm) (W|E)	6.3	6.6					4.8	4.7	7.2	5.4	5.8	6.1
Additional Notes												

BEND TESTS

Legend: Failed ● | Passed ◑ | Not Investigated ◯ | Shaft Failed ◯

LOCAL STRAINS

Legend: Post Peak ● | Rising ◑ | Not Instrumented ◯ | No Response ◯

CRACK DIRECTION

Legend: Cracked Stud ◯ | Dominant Crack Direction | Not Investigated

Columns: 1 2 3 4 5 6 7 8 9 10 11 12 (N, S rows for each figure)
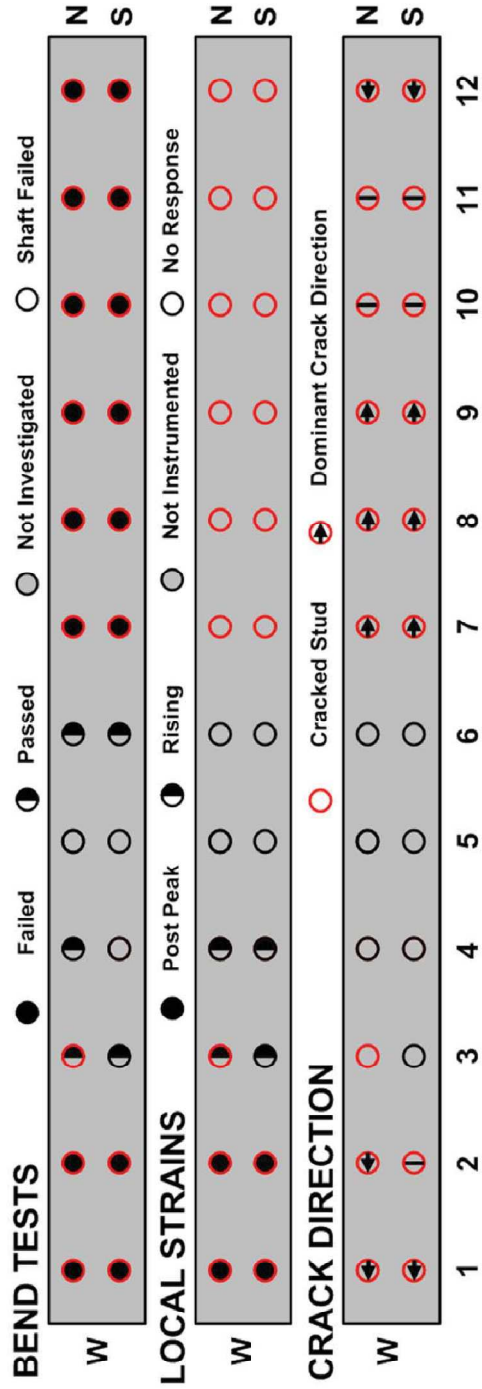
Autopsy Results C200

Figure G-22

Figure G-23

Figure G-24

Figure G-25

Figure G-26
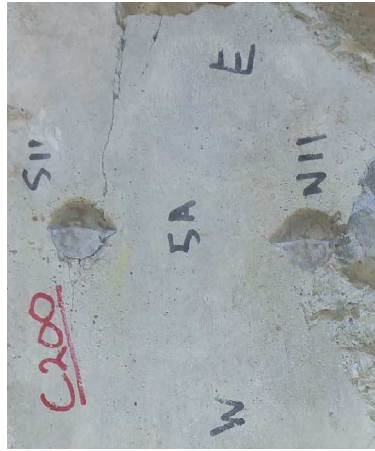
Figure G-27

Autopsy Results P200

Stud ID	N1	N2	N3	N4	N5	N6	N7	N8	N9	N10	N11	N12
Shear Experienced (%)	100%	100%	33.3%	33.3%	-33.3%	-33.3%	-33.3%	-33.3%	-33.3%	-33.3%	-33.3%	-33.3%
Shear Range (MPa)	200	200	67	67	-67	-67	-67	-67	-67	-67	-67	-67
Local Strain Behaviour	Post Peak	Post Peak	Post Peak	Post Peak	NI	NI	NI	NI	Post Peak	Post Peak	Post Peak	Post Peak
Cracking (Vis. | X-Sec)	>	>	>	>	No	No	>	No	>	>	>	>
Bend Test	Failed	Failed	Passed	Passed	Failed	Passed	Failed	Failed	Failed	Failed	Failed	Failed
Remaining Area (%)	0%	0%					40%		20%	40%	10%	10%
Length (mm) (W|E)	8.0 | 17.4	7.4 | 17.0					9.6 | 5.4		13.3 | 5.3	11.8 | 0	12.4 | 7.0	10.6 | 10.4
Depth (mm) (W|E)	5.5	3.1					5.6		4.6	5.1	6.8	5.3
Additional Notes	Complete Static Failure	Complete Static Failure	Crack through flange at outer face		Failed through shank. Very strange fracture plane. Weld air			Bad weld or fatigue crack through shank				

Stud ID	S1	S2	S3	S4	S5	S6	S7	S8	S9	S10	S11	S12
Local Strain Behaviour	Post Peak	Post Peak	Post Peak	Rising	NI	NI	NI	NI	Post Peak	Post Peak	Post Peak	Post Peak
Cracking (Vis. | X-Sec)	>	>	>	>	No	No	>	No	>	>	X	>
Bend Test	Failed	Failed	Passed	Passed	Passed	Passed	Failed	Failed	Failed	Failed	Failed	Failed
Remaining Area (%)	0%	0%					40%		30%	50%	10%	70%
Length (mm) (W|E)	9.0 | 17.4	7.0 | 17.6					9.6 | 5.4		12.8 | 4.6	10.8 | 0	11 | 7.5	8.1 | 0
Depth (mm) (W|E)	6.3	4.3					4.0		4.6	4.8	5.0	5.7
Additional Notes	Complete Static Failure	Complete Static Failure	Crack through flange at outer face					Small fatigue crack in shank			Cut Open	

BEND TESTS

- ● Failed
- ◖ Passed
- ◐ Not Investigated
- ○ Shaft Failed

W   N   S

1 2 3 4 5 6 7 8 9 10 11 12

LOCAL STRAINS

- ● Post Peak
- ◖ Rising
- ○ No Response
- ◐ Not Instrumented

W   N   S

CRACK DIRECTION

- ○ Cracked Stud
- ⊕ Dominant Crack Direction

W   N   S
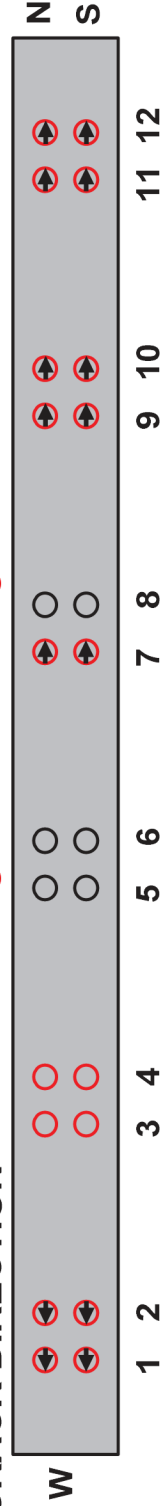
Autopsy Results P200

Figure G-28

Figure G-30

Figure G-29
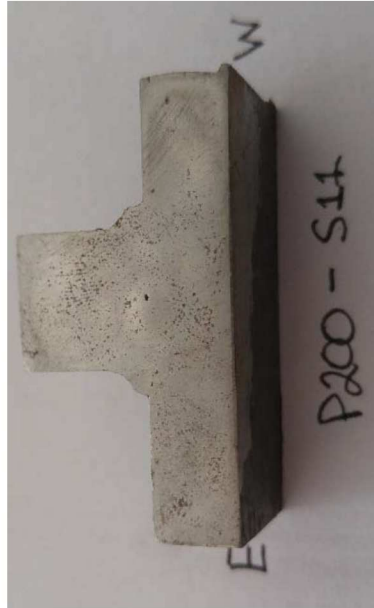
Autopsy Results P200

Figure G-31

Figure G-32
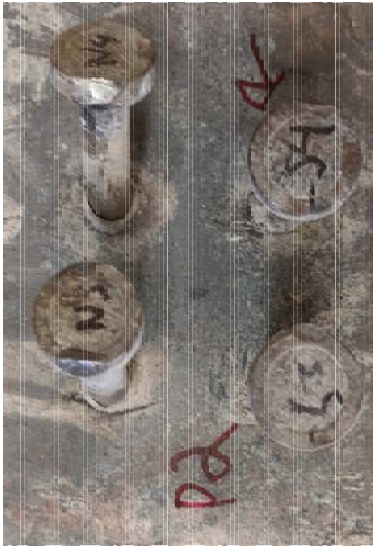
Figure G-33

Figure G-34

Figure G-35

Figure G-36

Autopsy Results C300

	N1	N2	N3	N4	N5	N6	N7	N8	N9	N10	N11	N12
Shear Experienced (%)	100%	100%	33.3%	33.3%	33.3%	33.3%	33.3%	33.3%	33.3%	33.3%	33.3%	33.3%
Shear Range (MPa)	300	300	100	100	100	-100	-100	-100	-100	-100	-100	-100
Stud ID	N1	N2	N3	N4	N5	N6	N7	N8	N9	N10	N11	N12
Local Strain Behaviour	Post Peak	Post Peak	Post Peak	Post Peak	Rising	Post Peak	NI	Post Peak	Post Peak	Post Peak	Post Peak	Post Peak
Cracking (Vis. | X-Sec)	v	v	v	v	No	v	v	v	v	v	v	v
Bend Test	Failed	Failed	Failed	Pass	Pass	Failed	Failed	Failed	Failed	Failed	Failed	Failed
Remaining Area (%)			0%			40%	0%	0%	0%	0%	0%	0%
Length (mm) (W|E)			7.3 / 17.6	11		12.5 / 0	19.3 / 6.6	16.3 / 4.9	15.4 / 5.9	13.8 / 7.6	12.5 / 14.5	5.9 / 15.6
Depth (mm) (W|E)			5.1	11		4	5.8	5.8	3.5	5.2	5.9	4.6
Additional Notes	Complete Failure almost immediately	Complete Failure almost immediately, fatigue crack	Complete Failure, cracking across flange	Crack through flange on outside face								

	S1	S2	S3	S4	S5	S6	S7	S8	S9	S10	S11	S12
Stud ID	S1	S2	S3	S4	S5	S6	S7	S8	S9	S10	S11	S12
Local Strain Behaviour	Post Peak	Post Peak	Post Peak	Post Peak	Rising	Rising	Post Peak	Post Peak	Post Peak	Post Peak	Post Peak	Post Peak
Cracking (Vis. | X-Sec)	v	v	v	v	x	v	v	v	v	v	v	v
Bend Test	Failed	Failed	Failed	Pass	Pass	Failed	Failed	Failed	Failed	Failed	Failed	Failed
Remaining Area (%)			0%			50%	0%	0%	0%	0%	0%	0%
Length (mm) (W|E)			6.4 / 17.9	11 / 3	1.1 / 0	9.4 / 0	15.1 / 7.3	16.6 / 7.2	14.5 / 7.2	14.5 / 11.5	13.3 / 12.5	6.2 / 14.6
Depth (mm) (W|E)			4.3	11 / 1	1	3.3	4.0	4	4.9	6	5.6	4.9
Additional Notes	Complete Failure almost immediately	Complete Failure almost immediately, fatigue crack	Complete Failure, cracking across flange	Cut revealed failure thru flange	Cut revealed small crack (2mm) on W side							

BEND TESTS — ● Failed ◐ Passed ○ Not Investigated ◯ Shaft Failed

LOCAL STRAINS — ● Post Peak ◐ Rising ○ Not Instrumented ◯ No Response

CRACK DIRECTION — ○ Cracked Stud ⊕ Dominant Crack Direction

6
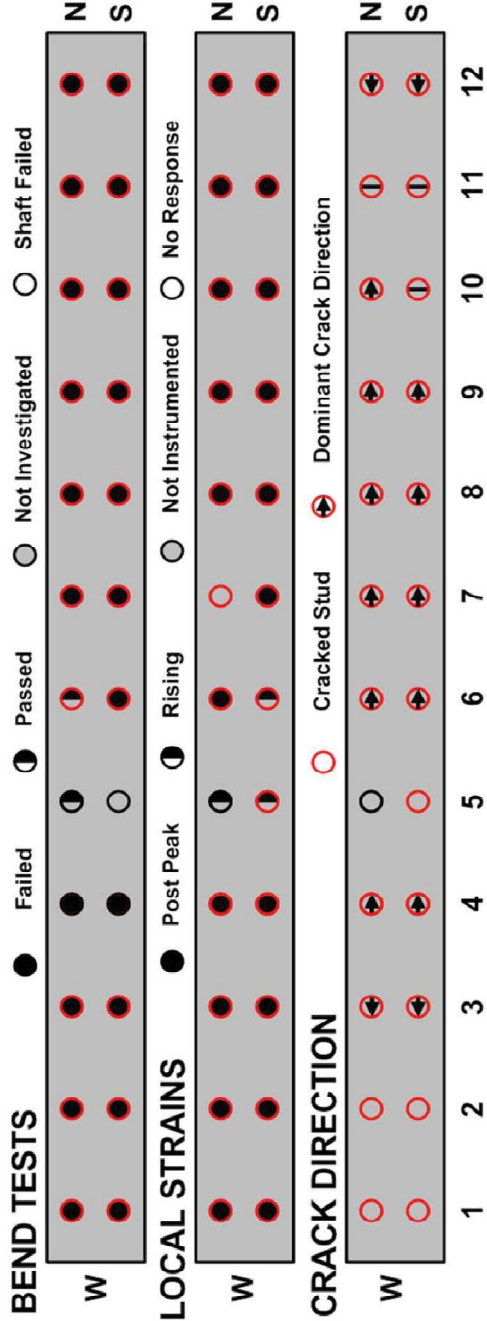
Autopsy Results C300

Figure G-38

Figure G-37

Figure G-40

Figure G-39

Autopsy Results C300

Figure G-46

Figure G-45

Figure G-44

Figure G-43

Figure G-42

Figure G-41

Figure G-52

Figure G-51

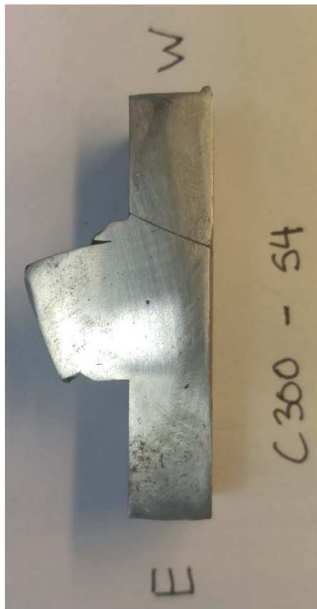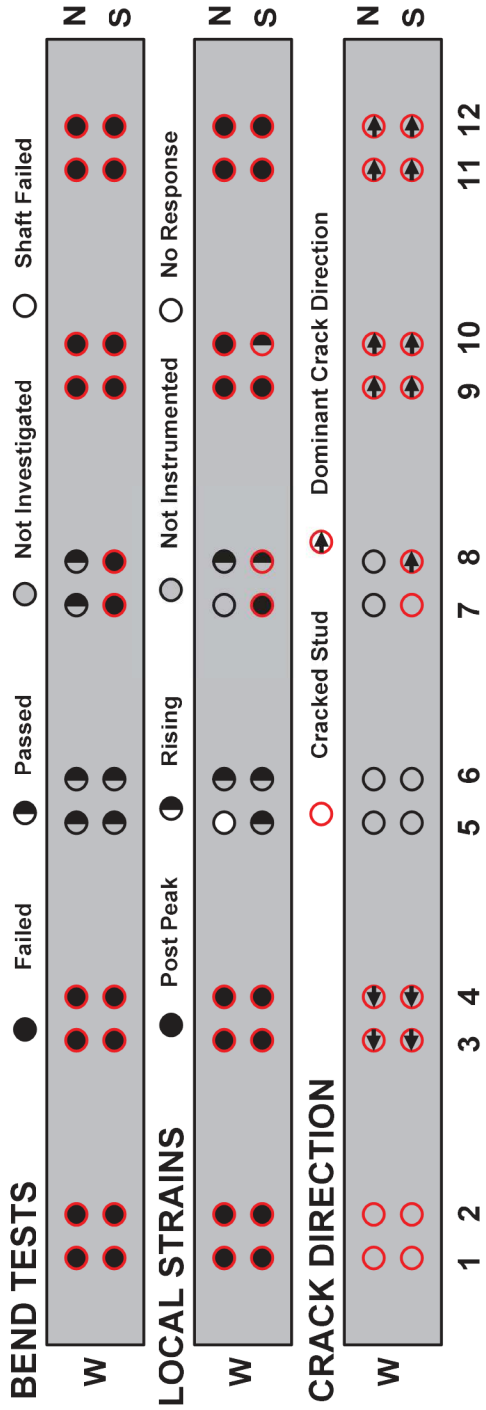Figure G-50

Figure G-49

Figure G-48

Figure G-47

Autopsy Results P300

Shear Experienced (%)	100%	100%	33.3%	33.3%	-33.3%	-33.3%	-33.3%	-33.3%	-33.3%	-33.3%	-33.3%	-33.3%
Shear Range (MPa)	300	300	100	100	-100	-100	-100	-100	-100	-100	-100	-100
Stud ID	N1	N2	N3	N4	N5	N6	N7	N8	N9	N10	N11	N12
Local Strain Behaviour	Post Peak	Post Peak	Post Peak	Post Peak	No Response	Rising	NI	Rising	Post Peak	Post Peak	Post Peak	Post Peak
Cracking (Vis. | X-Sec)	>	>	>	>	No	No	No	No	>	>	>	>
Bend Test	Failed	Failed	Failed	Failed	Passed	Passed	Passed	Passed	Failed	Failed	Failed	Failed
Remaining Area (%)			0%	0%					20%	50%	10%	10%
Length (mm) (W|E)			4.4 | 15.3	3.5 | 17.1					16.4 | 0	13.0 | 0	13.7 | 8.5	13.3 | 9.7
Depth (mm) (W|E)			3.8	3.5					4.5	4.9	6.0	6.3
Additional Notes	Complete Failure (fell off embedded in a group of 4)	See N1, polished through mechanical interaction	Complete Failure, cracking across flange	Complete Failure			Cracking seen after bend test	cracking seen after bend test				

Stud ID	S1	S2	S3	S4	S5	S6	S7	S8	S9	S10	S11	S12
Local Strain Behaviour	Post Peak	Post Peak	Post Peak	Post Peak	Rising	Rising	Post Peak	Rising	Post Peak	Rising	Post Peak	Rising
Cracking (Vis. | X-Sec)	>	>	>	>	No	No	>	>	>	>	>	>
Bend Test	Failed	Failed	Failed	Failed	Passed	Passed	Failed	Failed	Failed	Failed	Failed	Failed
Remaining Area (%)			0%	0%				80%	30%	40%	20%	40%
Length (mm) (W|E)			4.8 | 19.0	4.6 | 20.5				6.6 | 0	16.1 | 0	14.4 | 0	12.3 | 3.3	10.0 | 2.2
Depth (mm) (W|E)			4.0	4.6				4.1	5.0	5.0	5.7	5.2
Additional Notes	Complete Failure (fell off embedded in a group of 4)	See S1, polished through mechanical interaction	Complete Failure, cracking across flange	Complete Failure				Failed through shank. Very strange fracture plane. Weld air pocket. Possibly carrying all load on the south side for this pocket				

BEND TESTS

● Failed   ● Passed   ○ Not Investigated   ● Shaft Failed

LOCAL STRAINS

● Post Peak   ● Rising   ○ Not Instrumented   ○ No Response

CRACK DIRECTION

○ Cracked Stud   ⬤ Dominant Crack Direction

1

Autopsy Results P300
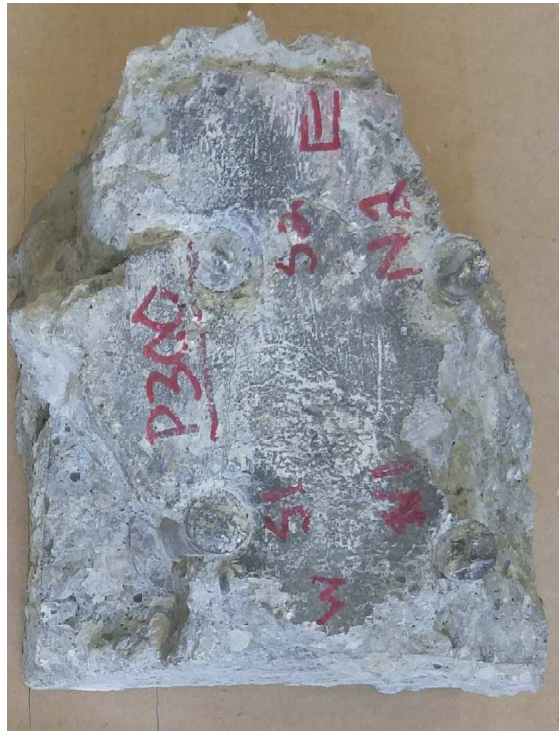
Figure G-53

Figure G-54

261

Appendix H: Stud Failure Data

Table H-1: Precast stud fatigue failures utilized in S-N analysis.

Test	Type	Beam	Stud	Theory Stress (MPa)	FEA Stress (MPa)	Data Stress (MPa)	N Failure
2	Precast	S3	N1	140.6	83.0	108.3	1,091,000
			S1	140.6	83.0	108.3	1,692,000
			N2	140.6	85.8	108.3	1,640,000
4	Precast	S2A	N1	202.3	119.4	155.8	568,000
			S1	202.3	119.4	155.8	400,000
			N2	202.3	123.4	155.8	614,000
			S2	202.3	123.4	155.8	543,000
			N4	67.4	43.2	101.8	2,761,000
			N9	67.4	68.8	65.4	1,991,000
			S9	67.4	68.8	65.4	3,074,000
			N10	67.4	65.4	65.4	3,109,000
			N11	67.4	65.4	69.5	2,750,000
6	Precast	S1	N1	301.9	178.1	232.5	83,380
			S1	301.9	178.1	232.5	138,000
			N2	301.9	184.2	232.5	92,590
			S2	301.9	184.2	232.5	146,600
			N3	100.6	76.5	152.0	626,300
			N4	100.6	64.4	152.0	606,000
			S4	100.6	64.4	152.0	684,300
			N9	100.6	102.6	97.6	961,800
			S9	100.6	102.6	97.6	750,500
			N10	100.6	97.6	97.6	1,071,000
			N11	100.6	97.6	103.7	762,100
			S11	100.6	97.6	103.7	568,600
			N12	100.6	90.6	103.7	727,200
8	Precast	S2	N1	98.6	58.2	75.9	3,140,000
			S1	98.6	58.2	75.9	4,133,000
			N2	98.6	60.1	75.9	4,290,000
			S2	98.6	60.1	75.9	5,710,000
10	Precast	1A	N1	119.9	70.7	92.3	1,515,000
			S1	119.9	70.7	92.3	1,225,000
			N2	119.9	73.1	92.3	1,174,000
			S2	119.9	73.1	92.3	2,078,000
			S9	40.0	40.8	38.8	4,645,000
12	Precast	3A	N1	62.8	37.1	48.4	5,000,000

Table H-2: Cast-in-place stud fatigue failures utilized in S-N analysis.

Test	Type	Beam	Stud	Theory Stress (MPa)	FEA Stress (MPa)	Data Stress (MPa)	N Failure
1	CIP	S4	N1	140.8	94.3	132.4	650,000
			S1	140.8	94.3	132.4	300,000
3	CIP	S5A	N1	202.3	135.5	190.2	161,500
			S1	202.3	135.5	190.2	407,700
			N2	202.3	109.2	190.2	705,000
			S2	202.3	109.2	190.2	705,000
			N3	67.4	60.0	81.6	2,400,000
			S3	67.4	60.0	81.6	2,480,000
5	CIP	S	N2	302.1	163.1	284.0	86,220
			S2	302.1	163.1	284.0	62,850
			N3	100.7	89.6	121.8	236,500
			S3	100.7	89.6	121.8	286,700
			N4	100.7	49.3	121.8	493,800
			S4	100.7	49.3	121.8	722,200
			N6	100.7	73.5	102.7	1,942,000
			S7	100.7	89.6	102.7	1,292,000
			N8	100.7	95.7	102.7	807,500
			S8	100.7	95.7	102.7	1,287,000
			N9	100.7	98.7	123.9	831,400
			S9	100.7	98.7	123.9	809,100
			N10	100.7	99.7	123.9	1,012,000
			S10	100.7	99.7	123.9	810,100
			N11	100.7	98.7	75.5	540,300
			N12	100.7	94.7	75.5	426,800
			S12	100.7	94.7	75.5	812,600
7	CIP	S5	N1	98.8	66.2	92.9	1,000,000
			S1	98.8	66.2	92.9	711,000
			N2	98.8	53.4	92.9	2,200,000
			S2	98.8	53.4	92.9	2,200,000
			N3	32.9	29.3	39.8	5,500,000
			S3	32.9	29.3	39.8	8,700,000
			S10	32.9	32.6	40.5	4,400,000
			S11	32.9	32.3	24.7	9,000,000
			N12	32.9	31.0	24.7	6,480,000
			S12	32.9	31.0	24.7	4,070,000
9	CIP	6A	N1	119.5	80.1	112.3	305,600
			S1	119.5	80.1	112.3	2,224,000
			N2	119.5	64.5	112.3	677,400
			S10	39.8	39.4	49.0	2,589,000
			S11	39.8	39.0	29.9	4,046,000
			S12	39.8	37.4	29.9	2,607,000
11	CIP	4A	N1	63.3	42.4	59.5	6,783,000
			S1	63.3	42.4	59.5	6,783,000